CZECH TECHNICAL UNIVERSITY IN PRAGUE
Faculty of Nuclear Sciences and Physical Engineering

Doctoral Thesis

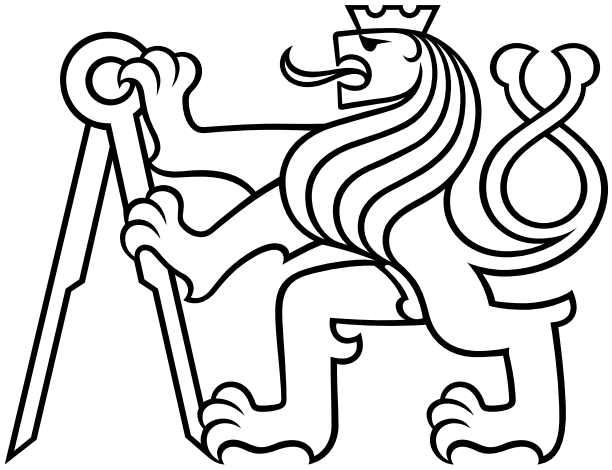

Mgr. Pablo Rodríguez-Ramos

Experimental results in pion induced reaction with carbon and polyethylene targets obtained by HADES-GSI

Prague 2021

Bibliographic Entry

Author:	Mgr. Pablo Rodríguez-Ramos Czech Technical University in Prague Faculty of Nuclear Sciences and Physical Engineering Department of Physics Nuclear Physics Institute of the CAS, p.r.i. Nuclear Spectroscopy Department
Specialization:	Nuclear Engineering
Title of Dissertation:	Experimental results in pion induced reaction with carbon and polyethylene targets obtained by HADES-GSI
Degree Programme:	Applications of Natural Sciences
Supervisor:	RNDr. Andrej Kugler, CSc. Nuclear Physics Institute of the CAS, p.r.i. Nuclear Spectroscopy Department
Supervisor specialist:	Ing. Ondřej Svoboda, Ph.D. Nuclear Physics Institute of the CAS, p.r.i. Nuclear Spectroscopy Department
Academic Year:	2020/2021
Number of Pages:	188
Keywords:	HADES, FAIR, dileptons, baryonic resonance, pion beam, VDM, vector meson

Bibliografický záznam

Autor:	Mgr. Pablo Rodríguez-Ramos České vysoké učení technické v Praze Fakulta jaderná a fyzikálně inženýrská Ústav jaderné fyziky AV ČR, v. v. i. Oddělení jaderné spektroskopie
Specializace:	Jaderné inženýrství
Název práce:	Experimentální výsledky z piony indukovaných reakcí s uhlíkovým a polyethylenovým terčem získané experimentem HADES-GSI
Studijní program :	Aplikace přírodních věd
Školitel:	RNDr. Andrej Kugler, CSc. Ústav jaderné fyziky AV ČR, v. v. i. Oddělení jaderné spektroskopie
Školitel specialista:	Ing. Ondřej Svoboda, Ph.D. Ústav jaderné fyziky AV ČR, v. v. i. Oddělení jaderné spektroskopie
Akademický rok:	2020/2021
Počet stran:	188
Klíčová slova:	HADES, FAIR, dileptony, baryonové rezonance, pionový svazek, VDM vektorový mezon

To my family, who always believed in me

Author's declaration

I hereby declare that this thesis is the result of my own work and only with the cited sources I have used in the bibliography. The thesis has not been submitted to acquire another qualification at this or any other university.

In Prague, ...

Mgr. Pablo Rodríguez-Ramos

(Author's thesis)

Acknowledgements

First of all, I would like to express my sincere gratitude to my supervisor RNDr. Andrej Kugler, CSc. for giving me the excellent opportunity to join the HADES collaboration and work with an outstanding scientific and technical team. To my supervisor specialist Ing. Ondřej Svoboda, Ph.D. for the guidance during my beginnings at Nuclear Physics Institute (NPI). To RNDr. Pavel Tlustý, CSc. to his very broad experience in experimental nuclear physics, help and suggestions were absolutely crucial for me in carrying out this work. I would also like to thank my colleagues from the NPI Mgr. Lukáš Chlad, Ing. Vasily Mikhaylov, and my colleague from the HADES collaboration Ph.D. Jacek Biernat, for our nice discussions and to make more enjoyable our stays at GSI during the pion beam run.

Abstract

In the summer of 2014, HADES collaboration was conducting measurements with secondary pion beam at GSI using carbon and polyethylene targets. The program was devoted to study the electromagnetic baryonic transitions in the time-like region. In particular, the experiment has been carried out in the second resonance region, (N(1520), N(1535)), at $\sqrt{s} = 1.49$ GeV, in that kinematical region the off-shell (ρ, ω) vector meson are expected to play a crucial role. The decay of the baryonic resonance into ρN is of special interest because it is connected with the in-medium modifications of the ρ meson spectral function at finite baryon densities. Using the polyethylene and carbon target allow us to study the inclusive e^+e^- production and the exclusive $\pi^- p \to ne^+e^-$ reaction, in addition to hadronic channels. The normalization of spectra has been done using elastic scattering of pion on polyethylene and carbon. Predictions of the Dalitz decay of the baryonic resonances N(1520) and N(1535) treated as point-like, underestimate the invariant mass yield larger than $M_{e^+e^-} > 300$ MeV/c^2. The description of the excess in the yield is achieved taking into account the time-like electromagnetic form factors using a Vector Dominance Model (VDM) formalism, which generates the off-shell ρ production using the results from the Bonn-Gatchina Partial Waves Analysis (PWA) of two pion production measured during the same experiment. HADES data is the only sample with charged double pion channels and therefore it is sensitive to the ρ production. The add in of the off-shell ρ contribution either in the inclusive or exclusive invariant mass distribution improved significantly the description of the spectra, and therefore, the validity of the VDM formalism for baryon electromagnetic transitions. Current results stimulate further experiments using pion beam to study electromagnetic transitions in the third resonance region, also hyperon Dalitz decay in proton induced reactions are expected.

The second part of the thesis report about a commissioning experiment carried out at MAMI facility in the Johannes Gutenberg Universität, Mainz (Germany), connected with the Electromagnetic CALorimeter (ECAL) which is being developed to complement the dilepton spectrometer HADES. The HADES spectrometer is currently operating on the beam of SIS18 accelerator in GSI, in future, it will be moved to a new location in the CBM cave of the future FAIR complex. Electromagnetic calorimeter (ECAL) enables the HADES experiment to measure data on neutral meson production in heavy ion collisions at the energy range of 2-10 A GeV on the beam of the future accelerator SIS100, but also with the lower energy beam of the current accelerator SIS18. The calorimeter will be based on 978 massive lead glass modules read out by photomultipliers and a novel front-end electronics, it will cover forward angles $12^\circ < \theta < 45^\circ$ and almost full azimuthal angle. Secondary gamma beam with energies ranging from 81 MeV up to 1399 MeV from MAMI-C Mainz facility was used to verify selected technical solutions. The photon beam hit the setup at three different positions (-4 cm, -2 cm, center of the module $= 0$ cm, $+2$ cm) and under three inclinations (angles $0^\circ, 6^\circ$ and 12° with respect to the module's longitudinal axis), in order to study the energy leakage between neighboring modules. Two prototypes of front-end electronics ("Cracow" and PaDiWa AMPS) were tested as well. Relative energy resolution was measured using modules with three different types of photomultipliers.

Abstrakt

V létě roku 2014, skupina experimentu HADES prováděla v GSI měření s pomocí sekundárního pionového svazku s použitím uhlíkového a polyetylénového terče. Experimentální program byl zaměřen na měření elektromagnetických baryonových přechodů v času-podobné oblasti. Konkrétně byl experiment proveden v oblasti sekundárních rezonancí (N(1520), N(1535)) při $\sqrt{s} = 1.49$ GeV. V této kinematické oblasti se očekává výrazná role off-shell vektorových mezonů (ρ, ω). Rozpad baryonové rezonance na ρN je předmětem speciálního zájmu, neboť je spojen s in-medium modifikací spektrální funkce ρ mezonu při konečných baryonových hustotách. Použití polyethylenového a uhlíkového terče nám umožňuje krom hadronových kanálů studovat také inklusivní produkci e^+e^- párů a exkluzivní $\pi^- p \to n e^+ e^-$ reakci. Normalizace spektra byla provedena pomocí elastického rozptylu pionů na polyetylenu a uhlíku. Predikce pro Dalitzův rozpad baryonových rezonancí N(1520) a N(1535) uvažovaných jako bodové, podhodnocuje výtěžek pro invariantní hmoty vyšší než $M_{e^+e^-} > 300$ MeV/c^2. Vysvětlení tohoto přebytku je docíleno započítáním času-podobných elektromagnetických form-faktorů použitím Vector Dominance Model (VDM) formalismu, který generuje off-shell ρ produkci s použitím výsledků Bonn-Gatchinovy analýzy parciálních vln z produkce pionů měřené během daného experimentu. HADES data jsou jediným vzorkem s detekcí nabitých dvou-pionových kanálů, a tudíž je citlivý na produkci ρ mezonu. Přidání off-shell ρ příspěvku buď do inklusivního nebo exklusivního rozdělení invariantní hmoty výrazně zlepšilo popis spektra, a tudíž také zvýšilo validitu VDM formalismu pro baryonové elektromagnetické přechody. Tyto výsledky stimulují další potřebu experimentů s pionovými svazky pro studium elektromagnetických přechodů ve třetí rezonanční oblasti. Krom toho se očekává pozorování Dalitzova rozpadu v protony indukovaných reakcích.

Druhá část této práce popisuje testovací experiment provedený v zařízení MAMI, Univerzita Johanese Gutenberga, Mainz (Německo). Tento experiment byl proveden v souvislosti s vývojem elektromagnetického kalorimetru (ECAL), který je vyvíjen za účelem doplnění dileptonového spektrometru HADES. HADES spektrometr je v současné době provozován s požitím svazku urychlovače SIS18 v GSI. V budoucnosti bude experiment přesunut na novou pozici v hale CBM experimentu v budoucím FAIR komplexu. ECAL kalorimetr umožňuje HADES spektrometru měření dat z produkce neutrálních mezonů při srážkách těžkých iontů při energiích 2-10 AGeV v případě budoucího urychlovače SIS100 avšak i s použitím nižších energií na současném urychlovači SIS18. Kalorimetr je založen na 978 kusech masivních modulů s olovnatým sklem vyčítaných pomocí fotonásobičů a inovativní front-end elektroniky. Pokrytí dopředných úhlů je v rozsahu $12° < \theta < 45°$ a téměř plně pokrývá azimutální úhly. Sekundární gama svazek s energiemi mezi 81 a 1399 MeV byl použit při experimentu v MAMI-C v Mainzu za účelem verifikace vybraných technických řešení. Za účelem studia prosakování“ energie mezi sousedními moduly, zasahoval svazek sestavu modulů na různých místech (-4 cm, -2 cm, střed modulu a $= 0$ cm, $+2$ cm) a také pod třemi různými úhly ($0°, 6°$ and $12°$ ve vztahu k podélné ose modulu). Dva typy front-end elektroniky (“Cracow” a PaDiWa AMPS) byly také otestovány. Relativní energetické rozlišení bylo změřeno s použitím modulů s třemi různými typy fotonásobičů.

Contents

Part I

Pion induced reaction on carbon and polyethylene targets obtained by HADES-GSI

Chapter 1

Introduction

The properties of hadrons when they are surrounded by nuclear matter in extreme conditions, i.e. (high densities and temperatures), give us clues to understand processes as, for instance, the origin of the Universe in the Big Bang and its later evolution. A reason why it is relevant to study the strongly interacting matter at high temperatures and densities. We can observe this strongly interacting matter in neutron stars during crucial moments in the development of supernovae, or since the invention of particle accelerators, it was possible to study the nuclear matter systematically at high temperature and density in the laboratory. This research also contributes to the study of one of the main objectives of current nuclear physics, such as obtaining the equation of state (EOS) of nuclear matter. This knowledge of strongly interacting matter is not only crucial for nuclear physics itself, but also for the understanding of complex systems in general, for instance, the astrophysical processes that take place in the final phase of the evolution of stars. Many questions appear to us like, What are the basics constituents of the Universe? What are the forces between these constituents? Once we know the basic building blocks, the next question will be; Which state of matter can we build with it? Is there a phase transition between them?. The foundation of quantum chromodynamics (QCD) as the fundamental theory describing the strong interaction, has the key to give us many of those answers.

1.1 Structure of QCD matter

1.1.1 Standard Model

The Standard Model is a mathematical theory of particle physics that describes the electromagnetic, weak, and strong interactions between quarks and leptons, which are the basic constituents of the Standard Model. The particles that define the Standard Model are characterized mainly by the mass, electric charge, and spin. Particles with half-integer spin are called *fermions* and with integer spin *bosons*, also the Higgs boson with spin 0, which explains the origin of the mass [1]. All the fundamentals interactions of nature are described with that model, except the gravitation. The model divided all the elementary particles into three groups, quarks, leptons, and bosons see Fig. 1.1. Quarks, which now are defined as point-like, with any excited states or internal structure, cannot be observed as a single particle, they are *confining*, which is an important property of quarks that will be discussed later. The quarks are listed in Fig. 1.1, like leptons they are spin 1/2, quarks are divided in three main types or *flavours* (up,down), (charm, strange) and (top, bottom). Quarks u, c, and t have an electric charge (+2/3e), while d, s, and b is equal to (+1/3e). Quarks come with three different possible colors/anticolor:

red, blue or green and anti-red, anti-blue, anti-green. The color charge is a characteristic for strong interactions, and it says that the sum of all color charges must be colorless, also defined as "white". For instance, if we consider a baryon which is a hadron made of three quarks, it must have different colors (red, green and blue) or if we consider a meson, an hadron made of two quarks, if the quark has a green color, then the anti-quark must have anti-green color. Leptons as quarks are particles spin 1/2, there are six leptons, and they appear in pairs, also called generations, each generation is made of a charged lepton and a neutral neutrino, the three charged leptons are (e^-, μ^-, τ^-) electron, muon, tauon; and the pairs of neutrinos, $(\nu_e, \nu_\mu, \nu_\tau)$, besides, it corresponds another six pairs of antileptons.

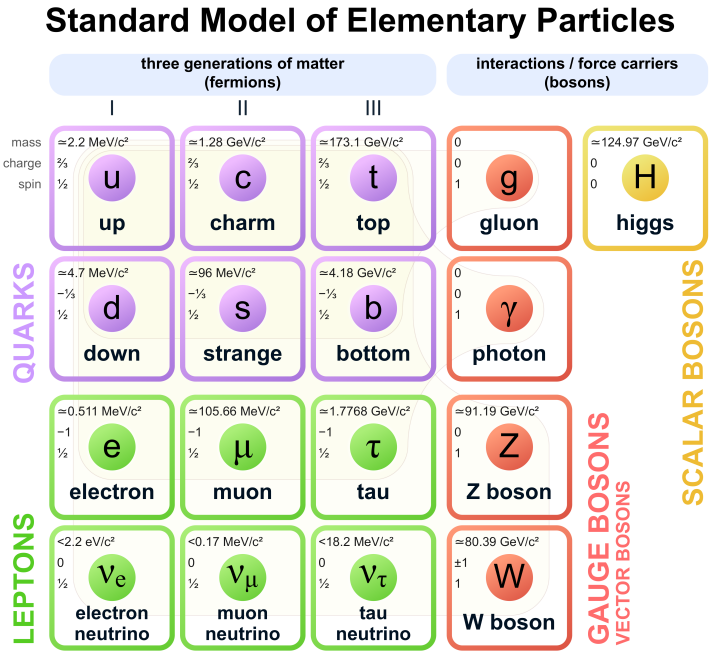

Figure 1.1: Elementary particles and their basic properties [2].

In Nature, four types of interactions field have been observed. On the scale of particle physics, we can see that the gravitational forces are insignificant compared with the others. As we discussed before, the Standard Model does not describe the gravitational field. The particles associated with the interaction fields are gauge bosons, or "force carriers", it is called gauge because it possesses a fundamental symmetry called *gauge invariance*, all the interactions field share this property. Weak interactions are mediated by W^+, W^- and Z^0 boson, the strong interaction is mediated by gluons which carry color force and can interact with themselves, there are eight gluons, all of them has zero mass and are neutral, the electromagnetic by the exchange of a photon, and there should be one for the gravity, "graviton" but it has never been observed, see Table 1.1. The Higgs boson is a quantum of the field which generates the masses of all fermions, quarks and gauge bosons the $W^\pm$ and Z^0. The mass of the hadrons is determined by the constituent masses of quarks. These are effective masses of quarks dressed-up by virtual quark and gluon condensates appearing due to specific features of QCD. The current ones are always smaller than the constituent masses.

Interaction field	Boson	Spin	Relative strength
Strong	Gluons	1	1
Electromagnetic	Photons	1	10^{-2}
Weak	W^+, W^-, Z^0	1	10^{-7}
Gravity	Gravitons, postulated	2	10^{-39}

Table 1.1: Types of interaction field and strength between two protons.

1.1.2 Asymptotic freedom and color confinement

The sector of the standard model that deals with the strong interaction between quarks and gluons is called quantum chromodynamics (QCD), the interaction of color-charged particles via the exchange of bosons (gluons) play a similar rule as photons in QED. Gluons are massless like photons in QED, as necessary by gauge symmetry, but the difference is that, in opposite to photons, the gluon carry also color charge, hence it can interact with itself, obtaining a new property called *asymptotic freedom* and *color confinement* which will be described in the following sections. The strength of the interactions, are given by the coupling constant $g = \sqrt{4\pi\alpha_s}$ which in QED depends on the fine structure constant $\alpha = e^2/(\hbar 4\pi\epsilon_0) \approx 1/137$ and predicts a logarithmic increase of the interaction strength with increasing momentum transfer. A charged particle in QED like an electron is surrounded by a virtual cloud of photons and e^+e^- pairs, due to the charge attraction the virtual positron is closer to the electron and the electron charge is screened. The similarity with QCD is that the virtual cloud is filled with $q\bar{q}$ pairs, but in contrast with the electrical charged and photons, the strong interaction between quarks is by gluons and the gluons couple with itself. That means that the gluons can split not into a virtual $q\bar{q}$ pair but also a pair of gluons. Therefore, the coupling strength of the strong interaction α_s increase with increasing the distance between the two quarks. For large momentum transfer or small distance the coupling constant decreases resulting in quasi-free quarks and gluons, known as *asymptotic freedom*, see Fig. 1.2. As long $\alpha_s \leq 1$ we can treat the Lagrangian as perturbative, also know as pQCD, because it will allow expansion of α_s around large momentum transfer. However, for $q \simeq 1$ GeV/c momentum transfers the degrees of freedom change rapidly with the scale, at large distances or small momentum transfer the quarks are confined into colorless objects forming meson (two quarks) or baryons (three quarks). In this regime, the perturbative treatment cannot be applied, consequently intractable by the analytical techniques that have led to the well-established understanding of pQCD. The only possible way to study is by lattice QCD (lQCD), which is a discrete space-time lattice numerical implementation of QCD [3].

The potential of QCD is described by the following expression:

$$V_s(r) = -\frac{4}{3}\frac{\alpha_s(r)}{r} + kr \tag{1.1}$$

where $\alpha_s(r)$ is the coupling constant as a function of the quark distance, k the energy density term ($k \approx 1$GeV/fm) and r the distance between quarks. The first part of the QCD potential is similar to a Coulomb force in QED and dominates at small distance, resulting as asymptotic freedom, while the second term, the linear, is related to the color confinement. The vacuum fluctuations in QED correspond to a fermion loop in the photon propagator, this mechanism leads to a screening of the electric charge at a large distance, and as a consequence a decreasing of the strength. In QCD the vacuum fluctuations correspond to boson loops (gluons) which are more abundant than fermion loops, as a result, the running coupling constant α_s increase. For this reason, the binding force between quarks increases within the distance, and any separation of them will lead with the creation of a new $q\bar{q}$, therefore it is impossible to separate pair of

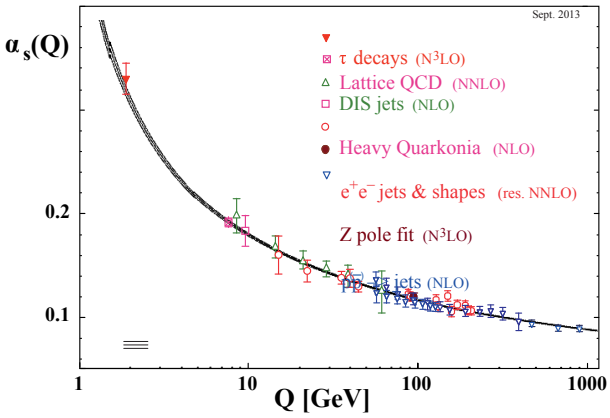

Figure 1.2: Summary of measurements of α_s as a function of the respective energy scale [4].

quarks because it will need an infinite amount of energy.

1.1.3 The origin of hadron masses

Most of the Universe's visible mass is composed of baryons, like protons and neutrons, which make up over 99.94% of atom masses. The mass of the nucleus will be the sum of it's constituents, but unlike we thought, the *confinement* explained in the previous section lead to an ambiguous definition of the quark mass, since we can define it either as a current or constituent mass. The current mass is the mass of quarks from a gluon cloud, for up (u) is ≈ 2.3 MeV/c^2 and down (d) quark is ≈ 4.8 MeV/c^2. The masses of the next quarks rise very quickly: strange (s) ≈ 95 MeV/c^2, charm (c) ≈ 1.27 MeV/c^2, bottom (b) ≈ 4.18 MeV/c^2 and top (t) ≈ 173 MeV/c^2. The constituent mass is determined by the mass of the hadrons. The interaction between a gluon condensates, and the quarks causes that the quarks acquire large effective mass. For instance, protons and neutrons which are bound states of three quarks (ddu) and (uud), respectively. On the other hand the mass of the proton is approximately ~ 1 GeV/c^2 that is ~ 100 times larger than the sum of the current mass of the quarks, $2m_u + m_d \simeq 10$ MeV/c^2. A key feature of QCD is the formation of massive hadrons out of almost massless quarks and gluons.

1.1.4 Chiral symmetry

The structure of the lightest hadron involving u, d and s quarks is determined mainly by the chiral symmetry and its breaking in the physical vacuum where the confinement plays a minor role. The QCD Lagrangian is invariant under gauge transformation $SU(3)_{\text{color}}$, and also shows a global symmetry $U(1)$ which correspond to the conservation of the baryon current and baryon number. The masses of the quarks with an momentum transfer of 1 GeV are:

$$\begin{aligned} m_u &= (5 \pm 2)\text{MeV/c}^2 \\ m_d &= (9 \pm 3)\text{MeV/c}^2 \\ m_s &= (175 \pm 55)\text{MeV/c}^2 \end{aligned} \tag{1.2}$$

The masses of the quarks are small or almost zero compared with an hadronic scale like the proton for instance.

$$\frac{m_u}{M_p} \sim 5 \cdot 10^{-3}, \quad \frac{m_d}{M_p} \sim 10^{-2}, \quad \frac{m_s}{M_p} \sim 0.2 \tag{1.3}$$

Therefore, it makes sense to treat the quark masses as perturbations since $m_u = m_d = m_s = 0$. In that limit, QCD Lagrangian has another symmetry called *chiral symmetry*, which is the conservation of right- or left-handedness for zero mass and spin 1/2 (fermions) and represented by $SU(3)_R \times SU(3)_L$. The symmetry conserves the handedness, which is the projection of the spin on the momentum direction of a quark. Therefore, the left and right-handed quarks do not mixed dynamically. The separate conservation of the right and left currents properly combined lead to the conservation of the vector-axial current according to Noether's theorem [5].

Spontaneous breaking of chiral symmetry

If symmetry the is conserved, a parity multiples in the hadron spectra should appear. We could expect that states that can rotate into each other, which relate positive and negative parity states, like ρ and a_1 will have the same masses. However, this is not the case, as $m_\rho = 770$ MeV/c^2 and $m_{a_1} = 1260$ MeV/c^2. The solution to the problem of the splitting mass of the chiral partners is the spontaneous breaking of chiral symmetry due to a non-vanishing expectation value of the quark condensate in the vacuum $< \bar{q}q > \neq 0$. The Lagrangian is invariant under the vector transformations but not under the axial-vector. Therefore, axial-vector symmetry is spontaneously broken. The Goldstone's theorem says that for any *spontaneous broken global symmetry* of a given Lagrangian exists a massless mode or Goldstone boson. These states are the octet of pseudoscalar mesons with a small mass, $(\pi^\pm, \pi^0, K^\pm, K^0, \overline{K}^0, \eta)$. Goldstone's bosons can be massive or massless depending if the excitation cost energy or not. We can illustrate it with a classical mechanical analogy shown in Fig. 1.3 and with the following potential:

$$V = -\frac{1}{2}\mu^2 \left(\sigma^\dagger\sigma + \pi^\dagger\pi\right) + \frac{1}{4}\nu^2 \left(\sigma^\dagger\sigma + \pi^\dagger\pi\right)^2 \tag{1.4}$$

For $\mu^2 > 0$, the potential shows a rotational symmetric at $\sigma = \pi = 0$, but for $\mu^2 < 0$ this state is unstable because it is a local maximum equilibrium. Hence, taking a ground state, it breaks the symmetry spontaneously.

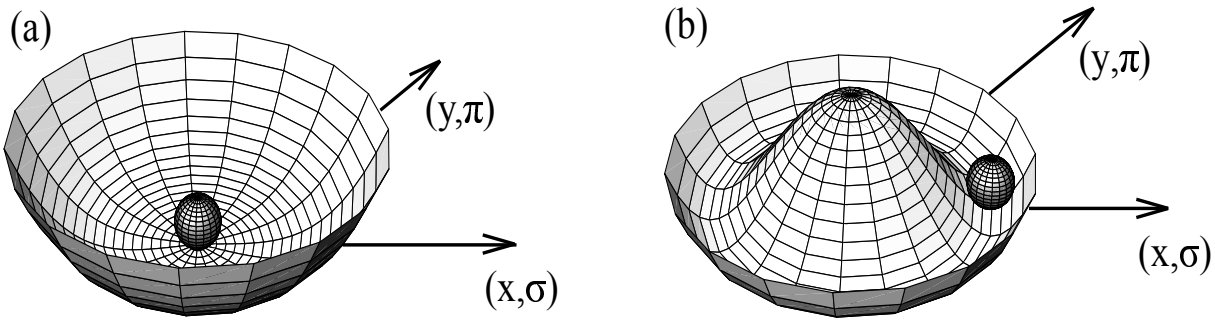

Figure 1.3: Classical mechanics potential model illustrating chiral symmetry breaking. The potential in a) is symmetric. In b), the potential is still symmetric, but the ground state's symmetry is spontaneously broken as the ball rolls to a certain point in the potential and selects a direction, which breaks the symmetry. However, a rotation (moving the ball in the valley) does not cost energy Q [6].

Noether's theorem establish that if a symmetry it is conserved, its current and charged are also conserved and Goldstone's says that for a symmetry breaking there are massless and massive excitations which generate the mass of the hadrons. The mass of the pion is not zero, but is much smaller than the rest of the hadrons that is why it is considered as a Goldstone's boson [6].

Explicit symmetry breaking

The small mass of the pseudoscalar mesons, however non-zero, is due to the *explicit* breaking of the chiral symmetry, which reflects the fact that the mass of the quarks is small but non-zero [7]. This explicit symmetry breaking is a result of slightly tilting in the Mexican hat potential in the σ direction, which breaks the symmetry of the potential, as we can see in Fig. 1.4

$$V = -\frac{1}{2}\mu^2\left(\sigma^\dagger\sigma + \pi^\dagger\pi\right) + \frac{1}{4}\nu^2\left(\sigma^\dagger\sigma + \pi^\dagger\pi\right)^2 - f_\pi m_\pi^2\sigma \tag{1.5}$$

The new minimum value at $\sigma = f_\pi$ preserve the Goldberger-Treiman relation, but the pion now acquire a finite mass, due to explicit symmetry breaking, which is related to the current quark mass by the Gell-Mann-Oakes-Renner (GOR) relation, see Eq. 1.6.

$$m_\pi^2 f_\pi^2 = -\frac{m_u + m_d}{2} < 0|\bar{u}u + \bar{d}d|0 > \tag{1.6}$$

where the f_π is the pion decay constant, m_u and m_d the bare quark masses and $< 0|\bar{u}u + \bar{d}d|0 >$ the expectation value of the ground state, also called quark condensate. Consequently, the mass of the pion $\left(m_\pi \approx 140\ \mathrm{MeV/c^2}\right)$, or any hadron, is the result of an explicit symmetry breaking due to the non zero value of the quark mass, and also due to the non vanishing expectation value of the vacuum. For a value of pion decay constant $f_\pi \approx 92$ MeV we obtain a vacuum expectation value of $< 0|\bar{q}q|0 > \simeq -(240\ \mathrm{MeV})^3 \simeq -1.6\mathrm{fm}^{-3}$ [8]. This is very large compared to the normal nuclear density $\rho_0 \simeq 0.17\ \mathrm{fm}^{-3}$ which indicates a strong dynamical breaking of the chiral symmetry.

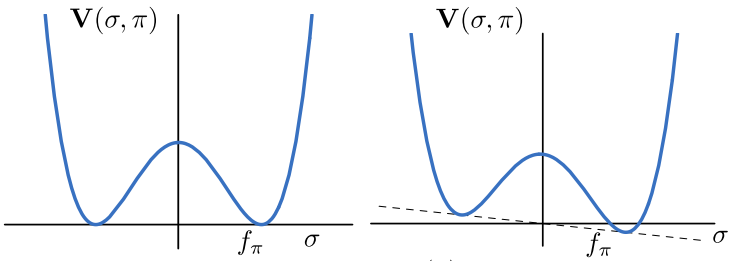

(a) Symmetric Potential (b) Tilted Potential

Figure 1.4: Mexican Hat Potential at $\pi = 0$. In case of (b) the potential is tilted along the σ field breaking explicitly the chiral symmetry [6].

1.1.5 In-medium quark condensate

In conclusion, due to the condensate, the chiral symmetry is spontaneously broken, and hadron masses are determined by the existence of this chiral condensate $< q\bar{q} >$. As the vacuum is populated by a condensate of $< \bar{q}q >$, a quark that propagates in that condensate can change its chirality, and so getting an effective mass that breaks the chiral symmetry. Those quarks which are dressed by a virtual $< \bar{q}q >$ and gluons are called constituent quarks. In other words, we can say that the polarization of the vacuum into a condensate of $< \bar{q}q >$ transform a light quark, with a small bare mass into a massive quasiparticle, and with a finite size. Up to now, we just spoke about the QCD vacuum, but it will be interesting to speak about properties of hadronic matter in the presence of a hot and dense medium that is created in RHIC. At high temperatures and/or densities it is expected a phase transition from hadronic matter, where

quarks are confined into hadrons, to a deconfined phase of quarks and gluons, the (**Q**uark **G**luon **P**lasma) QGP. In Fig. 1.5, it is shown the phase diagram of strongly interaction matter as a function of the temperature and the baryonic net density.

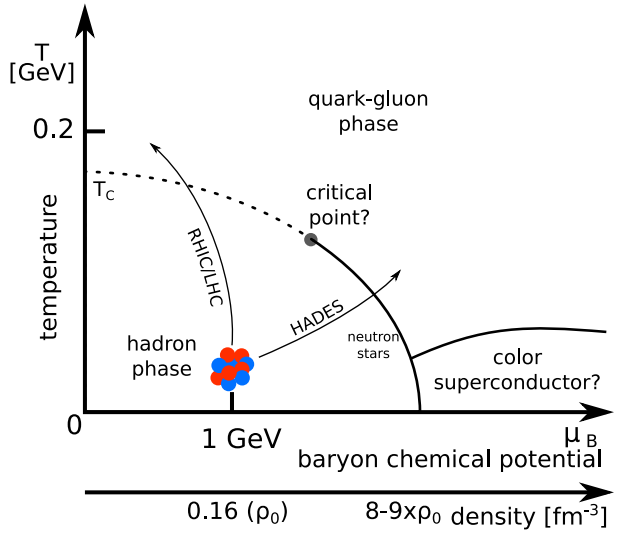

Figure 1.5: Phase diagram (temperature, net baryon density) of QCD matter, ranging from regular nuclear matter to Quark-Gluon Plasma [9].

The melting of the quark condensate $< q\bar{q} >$ indicates the chiral symmetry restoration. In Fig. 1.6 it is shown the values of the chiral condensate $< q\bar{q} >$ as function of the temperature T, and nuclear density ρ/ρ_0 based in the Nambu-Jona-Lasinio model [10]. In the chiral limit, the temperature dependence of the quark condensate is given by Eq. 1.7 [6].

$$< \bar{q}q >_T = < 0|\bar{q}q|0 > \left(1 - \frac{T^2}{8f_\pi^2}\right) \tag{1.7}$$

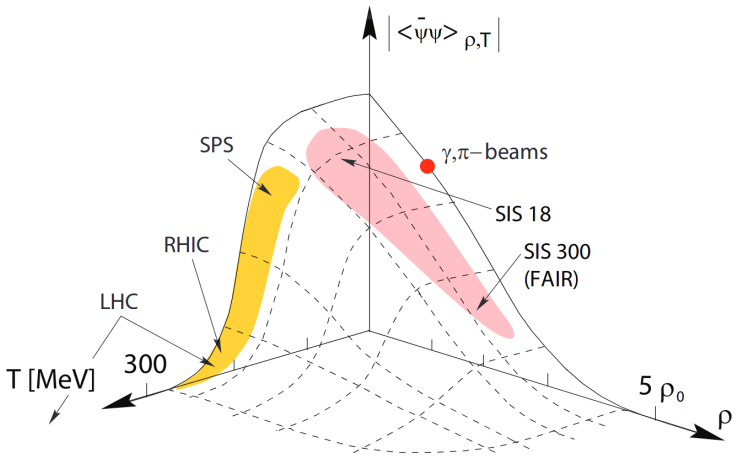

Figure 1.6: Value of two quark condensate as a function of the density and temperature, based on the NJL model [11].

As we can see, the quark condensate drops to like $\sim T^2$, so the change in the condensate is small at low temperatures. Experiments in heavy-ions collisions like LHC and RHIC run at high

temperature but low nuclear densities, therefore they are more sensitive to the QGP phase. In contrast, the quark condensate drops linearly with density. At normal nuclear matter the quark condensate is dropped by 35%.

$$< \bar{q}q >_{\rho} = < 0|\bar{q}q|0 > \left(1 - 0.35\frac{\rho}{\rho_0}\right) \tag{1.8}$$

This calculation predicts a chiral symmetry restoration at temperatures of the order of $T \sim 300$ MeV at 0 density or densities of $\rho \sim 5\rho_0$ at low temperature. At densities of $\rho \sim 5\rho_0$, there is already a decrease of the vale of the $\langle \bar{q}q \rangle$ condensate, which is already the value of nuclear matter density. This region of high density and low temperature is probe by HADES experiment and the future facility FAIR. At normal density matter and moderate temperature, HADES experiment located at SIS18 is able to study heavy-ion at energies between 1 and 4A GeV. Experiments of hadron-hadron and hadron-nucleus reaction, like pion-induced reactions reported in this thesis, allow to constrain the hadron properties in vacuum and cold nuclear matter. Therefore, at energies produced by SIS-GSI, the partial restoration of chiral symmetry might be observed. Brown and Rho [12], proposed that masses of hadrons are related to the quark condensate; they predicted a reduction of hadron masses at finite densities. For instance, the ρ meson mass should drop about $15 - 20\%$ at nuclear matter densities. Finite density is very efficient in reducing the quark condensate, and we should expect that any in medium modification due to a dropping quark condensate should already be observable at nuclear matter density. Different scenarios have been proposed using various models to describe the in-medium modifications of vector mesons which include mixing, broadening and even raising of the spectral functions [6], a detailed description of the different scenario will be described in Section 1.2. However, still is a debate if the mass modification of vector mesons is a clear sign of chiral restoration. A particular interest of the in-medium modification of ρ meson will be discussed in this thesis.

1.2 Medium modifications of vector mesons

A unique opportunity to measure the properties of hadrons in vacuum, in medium and the effects of the chiral symmetry restoration are the light vector mesons ρ, ω, and ϕ [13]. They have a short lifetime, on a time scale of $\tau \approx 10$ fm, which assures their decay or at least part of it inside the hot dense hadronic medium. They decay directly into dilepton pairs, see Table 1.2. The dilepton invariant mass reflects the mass of the vector mesons at the time of the decay, being not affected by the medium since electrons only interact electromagnetically. The coupling between hadrons to dileptons at low energy is explained by the **Vector Dominance Model** (VDM) model [14], which states that the virtual photons can acquire a hadronic character into vector mesons since vector mesons carry the same quantum numbers as a photon $\left(J^P = 1^{--}\right)$ coupling directly to a lepton pair. Therefore, they reflect as well the electromagnetic form factor of the decay. We need to distinguish between virtual and real photons, real photons are massless so they cannot decay, but virtual photons can decay for a short time $\left(\approx 10^{-23}s\right)$ restricted by Heisenberg uncertainty. As we mention before, since the process is not forbidden, the off-shell photon can be converted to a vector meson and then decay to a lepton pair, also called *dileptons*, which are the pair of leptons decaying from virtual photons.

The proposed in-medimum modifications of the vector mesons can be observed in the modifications of the invariant mass distribution of dilepton pairs from ρ decays which is given by the ρ spectral function. The ρ spectral function is defined as the imaginary part of the propagator:

Particle	Mass (MeV/c^2)	Decay width (MeV/c^2)	Lifetime (fm/c)	Main Decay	Branching Ratio e^+e^-
ρ	769	152	1.3	$\pi^+\pi^-$	4.44 x 10^{-5}
ω	783	8.43	23.4	$\pi^+\pi^-\pi^0$	7.07 x 10^{-5}
ϕ	1020	4.43	44.4	K^+K^-	3.09 x 10^{-5}

Table 1.2: Properties of light vector mesons in vacuum [15]

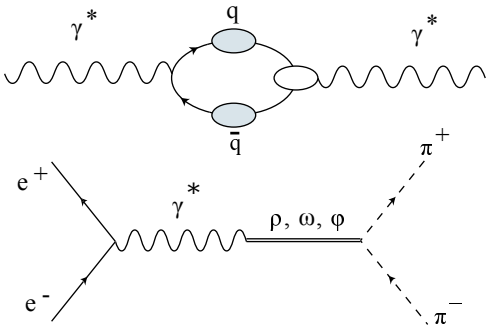

Figure 1.7: Up diagram shows the conversion of virtual photon to quark-antiquark pair forming a vector meson. The low diagram Feynmann diagram shows the Vector Dominance Model (VDM) in dilepton production via e^+e^- annihilation.

$$D_\rho = \left[M^2 - \left(m_\rho^{(0)}\right)^2 - \Sigma_{\rho\pi\pi} - \Sigma_{\rho M} - \Sigma_{\rho B}\right]^{-1} \tag{1.9}$$

The ρ propagator in the hadronic matter is evaluated from the self-energy of different contributions in the case of hadronic many-body, see Fig. 1.8. Where $m_\rho^{(0)}$ is the bare mass, and we classify the self-energy contributions in three types: (i) medium modifications of the pseudoscalar meson cloud $\sum_{\rho\pi\pi}$ throw πNN^{-1} and $\pi\Delta N^{-1}$ which its gives the width already in the vacumm $\Gamma_{\rho\pi\pi}(m_\rho) \simeq 150$ MeV and direct interactions with (ii) mesons encoded in $\sum_{\rho M}$ with the interactions with the most abundant thermal mesons and (iii) baryons in the medium from $\rho N \to B$ interactions ($B = N, \Delta, N(1520)\ldots$) encoded in $\sum_{\rho B}$ [16; 17].

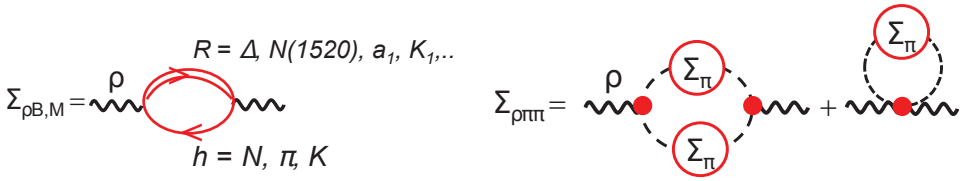

Figure 1.8: ρ-meson self-energy diagrams in-medium. **Left**: Excitation of baryon or meson resonances. **Right**: Formation of pion loops in vacuum.

Studies associated with the ρ meson can be classified in two scenarios, "dropping" and "broadening" of the ρ mass. In a "dropping" scenario which was already introduced in Section 1.1.5, the ρ mass essentially changes without affecting the width of the state, introduced by (e.g. Hatsuda Lee and Brown Rho [18; 12]) also called "BR-scaling". They predicted a reduction of hadron masses at finite densities, for instance, a reduction of the ρ meson mass about $15 - 20\%$ at nuclear matter densities, which has not been confirmed yet. Pisarski [19] studied the critical temperature in the limit of the chiral symmetry, he observed that ρ and a_1

meson become degenerate. Later, Song [20] using a non-linear model of the chiral symmetry found out that with increasing the temperature ρ meson mass increase and a_1 decrease.

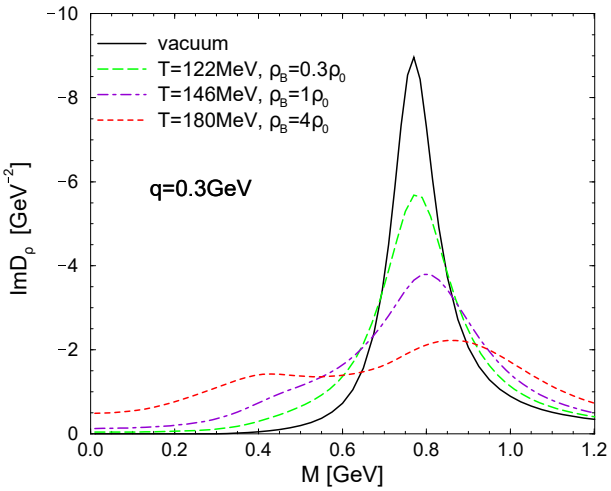

Figure 1.9: ρ meson spectral function (at fixed 3-momentum $q = 0.3$ GeV) in hot and dense hadronic matter in the many-body approach at various temperatures and total baryon densities corresponding to a fixed baryon chemical potential of $\mu_B = 0.408$ GeV and vanishing meson chemical potentials [21].

Hadronic many-body model proposed the "broadening" of the ρ spectral function without modification of the pole mass (e.g. Rapp, Wambach, et al: [21; 22; 23]). They find a strong broadening of the ρ meson spectral function in hot/dense matter, leading to a melting of its resonance structure mostly driven by interactions with baryons and antibaryons, see Fig. 1.9. The broadening is explained by the interactions of the ρ with mesons and baryons in the medium, see Fig. 1.8. The modification of the ρ spectral function, it is not only due to the resonance-hole excitation as we can see in the left panel of Fig. 1.8, but also due to the coupling of baryons and mesons, which increase the yield for lower masses and also a small shift of the pole mass, see Fig. 1.9 [24; 25]. It has been observed that the modification due to baryonic resonances is bigger than the one from pion gas [26; 27]. However, there is no a definite conclusion on the mechanism of the excess, if these effects are independent of each other and whether they are more driven by baryonic density or by temperature (i.e. pion density). The in-medium modification of the vector mesons due the coupling with baryonic resonances is an essential ingredient specially at lower energies, where the hadronic matter is baryon rich. HADES experiments at 1 - 3.5A GeV offers a unique tool to study this in-medium modification. It is important to remark that the in-medium modifications of the ρ spectral function due to the coupling to baryonic resonance, can appear already in elementary nucleon-nucleon collisions (like pion-induced reactions) at low energy where the medium is cold and baryon rich. In that case, the ρ spectral function is modified via the production and decay of these baryonic resonances. In fact, both of them are related by the same physical phenomenon: The coupling of the ρ vector mesons to baryonic resonance [28].

1.2.1 The electromagnetic structure of hadrons

The studies of the electromagnetic structure of hadrons are directly related to the form factors. An effective tool to study subatomic structures with electromagnetic probes is the scattering of a charged probed in the electromagnetic field of the object under investigation. In

the scattering of high energy pions on electrons in a target, the cross section for $\pi^{\pm}+e^{-} \rightarrow \pi^{\pm}+e^{-}$ is directly measured. In Fig. 1.10 it is shown the mechanism of the interaction, which it is mediated by the emission and absorption of a virtual photon. We can categorized the virtual photons in *space-liked* and *time-liked* photons. The momentum transferred by a virtual photon is given by:

$$q^2 = (\Delta E_l)^2 - (\Delta p_l)^2 \tag{1.10}$$

where Δp_l is the momentum of a lepton and ΔE_l is the energy. For elastic scattering processes $q^2 < 0$ momenta by no energy transfer, the region is called *space-liked*, and for annihilation processes $q^2 > 0$ only energy transfer but no momenta, the region is called *time-liked*, see Fig. 1.10.

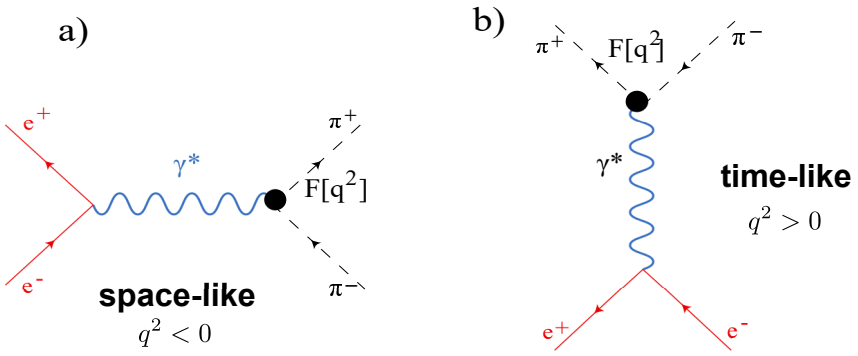

Figure 1.10: **a)** Space-like pion scattering. **b)** Time-like $e^{+}e^{-} \rightarrow \pi^{+}\pi^{-}$ annihilation.

The differential cross section for the scattering of an electron by a non-point particle with a specific spacial structure is given by the Rosenbluth formula [29]:

$$\frac{d\sigma}{d\Omega} = \left[\frac{d\sigma}{d\Omega}\right]_{Mott} \cdot \left[\frac{G_E^2\left(Q^2\right) + G_M^2\left(Q^2\right)}{1+\tau} + 2\tau G_M^2\left(Q^2\right)\left(\tan\frac{Q}{2}\right)^2\right] \tag{1.11}$$

where $\left(\frac{d\sigma}{d\Omega}\right)_{Mott}$ is the Mott differential cross section, $Q^2 = -q^2 = \left(\frac{E}{c}\right)^2 - p^2$ is the 4-momentum transfer, $\tau = \frac{Q^2}{4M^2c^2}$, G_E^2 is the electric and G_M^2 is the magnetic form factor of the non-point-like particle. The point object term describes a point-like object for a given parity and spin, the term $\left[F\left(q^2\right)\right]^2$ it is the form factor, in general, is a complex quantity also depending on spin and parity. The form factor describes the deviation of the differential cross section from a point-like charge distribution from a Fourier transformation of $\left[F\left(q^2\right)\right]^2$, it gives a characterization of the charge and current spatial distributions of an extended object, and it can be obtained comparing the theoretical predictions for a point-like with the experimental data. In Fig. 1.11 it is shown the pion form factor as a function of the 4-momentum transfer. Besides the *time-liked* and *space-liked* region there is a kinematically forbidden region in the time-like $0 < q^2 < (2m_\pi)^2$ because there is not enough energy to generate the two outgoing pions [30]. The right part of Fig. 1.11 shows that experimental data in the *space-like* region, the pion form factor decrease as increasing q^2 because the place where the scattering process occurs is decreasing and the interaction of the virtual photon with the hadron is getting smaller.

In the *time-like* region this argument can be valid also, but there is another mechanism which plays an important role since the virtual photon interacts with the hadrons with a transition to a vector meson (ρ, ω, ϕ) when the value q^2 is approach the vector meson mass, this process become dominant with the so-called Vector Dominance Model (VDM), as we already introduced

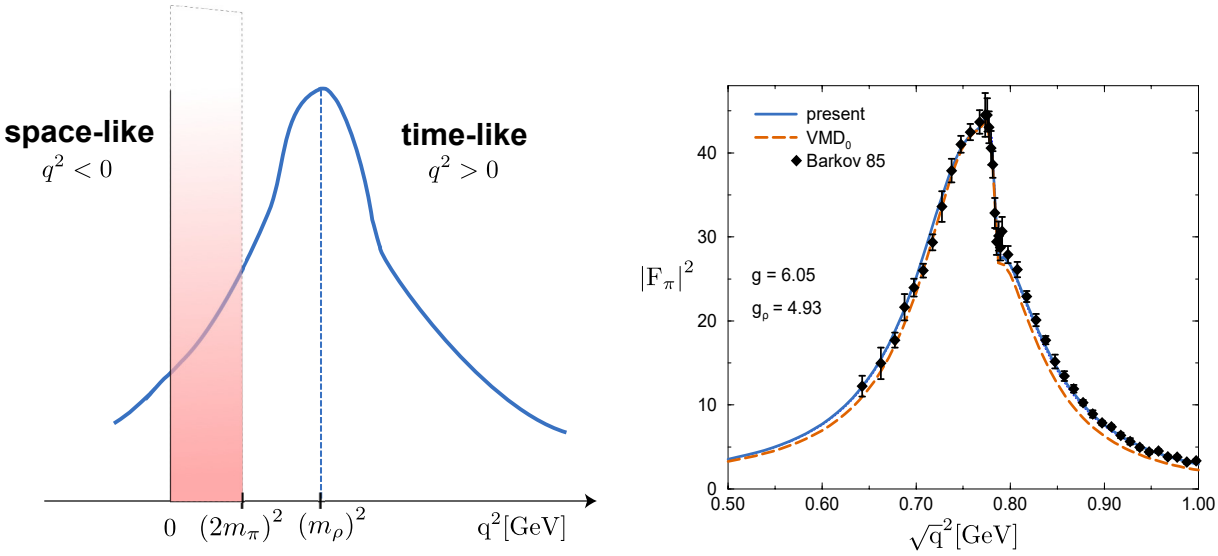

Figure 1.11: **Left**: Dependence of the pion form factor on the 4-momentum transfer. The dashed rose area is a nonphysical domain which is kinematically prohibited [30]. **Right**: Form factor of pion in *time-like* region for $e^+e^- \to \pi^+\pi^-$. The resonance at ρ and ω is explained with the VDM (solid line) and the $\rho - \omega$ mixing [31].

at the beginning of this chapter. This also explain the resonant q^2 dependence in the *time-like* region. The coupling of ω meson with two pions that happen only in the presence of hadronic matter explain the fall of the curve around ω mass, and it is known as $\rho - \omega$ mixing [31]. For instance, the pion form factor extracted from the pion annihilation process from Fig. 1.11 can be approximated by a Breit-Wigner function:

$$\left|F_\pi\left(q^2\right)\right|^2 = \frac{m_\rho^4}{\left(q^2 - m_\rho^2\right)^2 + m_\rho^2\Gamma_\rho^2} \tag{1.12}$$

where m_ρ and Γ_ρ are respectively the mass and the decay width of ρ meson.

1.2.2 Baryon electromagnetic decays

The low energy part of a nucleon-nucleon collision is determined by a resonance model in which all collision cross section is assumed to be dominated by the excitation of baryonic resonance. Depending on energy, different resonance are produced, which coupled differently with meson production. For instance, the $\Delta(1232)$ resonance it is the most produced and its very important for pion production, the N(1535) couples with the η meson and the N(1520) is crucial for the ρ production. The main contribution of the absorption of the ρ meson is from $\rho N \to R$ which produced a broadening of the spectral function, where R here is a N^* or Δ^* resonance. The ρ spectral function does not only broader due to the coupling to baryonic resonance, other structures and secondary peaks appears, and deviate the spectral function from a Breit-Weiger form, see Fig. 1.13. This structure is generated by the strong coupling of N(1520) which plays an important role in the medium spectral function.

One source for vector mesons in the dilepton spectrum is the Dalitz decay of baryonic resonances $R \to N\rho \to Ne^+e^-$ see Fig. 1.12, the description of the baryonic resonance $R \to Ne^+e^-$ is based on the VDM model in its monopole form with one virtual vector meson V, so the model describes the radiative $R \to N\gamma$ and mesonic $R \to NV$ decays.

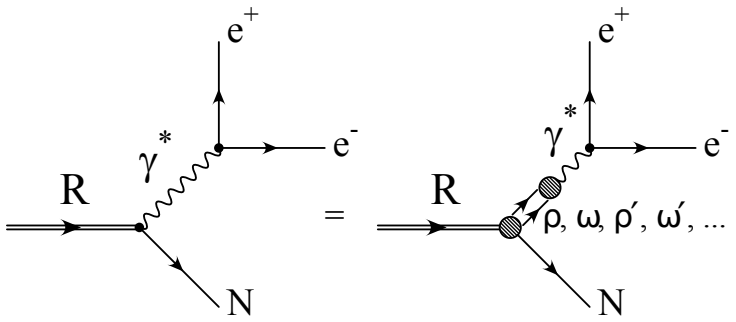

Figure 1.12: Decay of baryonic resonance to dileptons in the extend VDM model [32].

A similar approach to the studies of electromagnetic structure of hadrons in Section 1.2.1 with a lepton-hadron interaction can be done for baryonic Dalitz decay. The investigation of a Dalitz decay of a baryon resonances R into a nucleon N and a virtual photon give us information about the structure of the resonance throw the electromagnetic transition form factor (eTFF) in the time-like region. In contrast with mesons, there is no data of eTFF in this kinematical region. Also, there is a problem with the separation of the different resonance produced because their width is too large. Fortunately, pion-induced reaction allow us to separate each individual contribution by the available pion energy. The eTFF for baryonic resonances are well characterize by the four-momentum transfer $q = \vec{p}_N - \vec{p}_B$ with $\vec{p}_N$ and $\vec{p}_B$ the nucleon and baryon four momenta. The VDM is also use in a the Dalitz decay process, called as extended VDM (eVDM). Therefore, the momentum transfer or invariant mass by a virtual photon is equal to

$$M_\gamma^2 = q^2 = (E_B - E_N)^2 - (\vec{p}_B - \vec{p}_N)^2 \tag{1.13}$$

where $E_B, E_N, \vec{p}_B$ and $\vec{p}_N$ are the energies and momentum of the baryon and nucleon respectability. We can observe in Fig. 1.13 that different regions can be explored.

- *Time-like* baryon transition for a $q^2 = M_{inv}^2\,(e^+e^-) = M_{\gamma^*}^2 > 0$ with a maximum $q_{\max}^2 = (M_B - M_N)^2$ accessible with Dalitz decay of baryonic resonance. Also with annihilation reaction $e^+e^- \to \bar{B}N$ but in this case the minimum $q^2 = (M_B + M_N)^2$.
- *Space-like* baryon transition for a $q^2 = M_{\gamma^*} = -Q^2 < 0$ is accessible with electron scattering processes limited by the kinetic energy of the incoming electron.
- The *forbidden* region is not accessible experimentally at $(M_B - M_N)^2 < q^2 < (M_B + M_N)^2$.

In Section 8.0.1 a more detailed study of Dalitz decay of baryonic resonance will be described.

1.2.3 Dilepton spectroscopy

Photons and dilepton (e^+e^- or $\mu^+\mu^-$ pairs) are not affected by the strong force and also the QED coupling constant is very small, since they can leave the reaction volume undistorted they carry information about the in-medium modifications of vector mesons properties. The decays of vector mesons to virtual photon decaying after to e^+e^- or $\mu^+\mu^-$ dilepton pairs have been proposed long ago as a signature of a phase transition and also as a probe of chiral symmetry restoration. Unfortunately the branching ration of e^+e^- decay of ρ, ω, ϕ is on the order of $10^{-5} - 10^{-6}$ which translates to a real challenge concerning the detection and data analysis. Additionally, large background sometimes is dominant over the signal, which is something that we need to subtract to determine the ρ signal. The main contribution comes from:

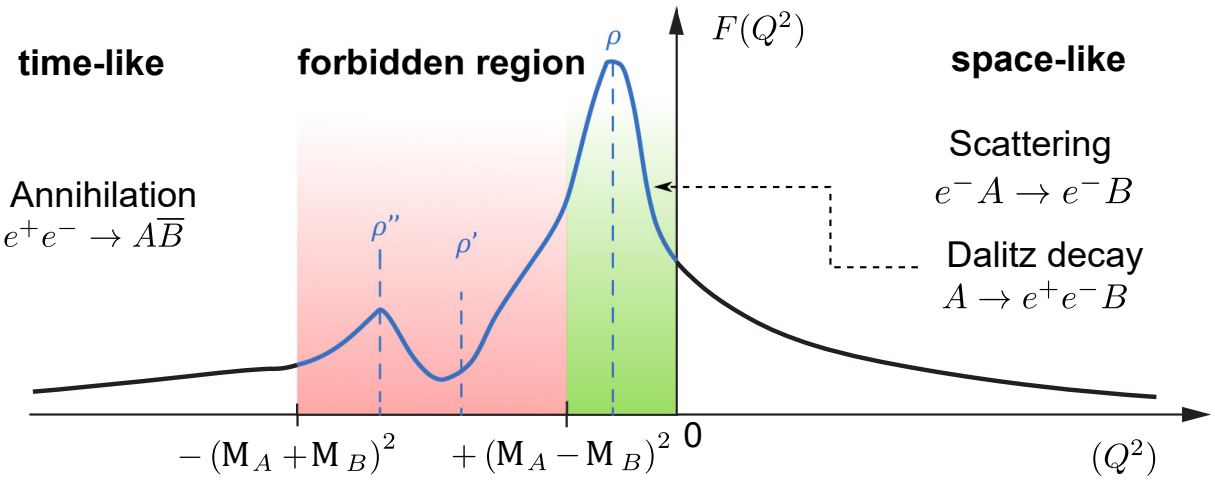

Figure 1.13: Sketch of a generic form factor as a function of ($Q^2 = -q^2$) in the space-like and time-like region for a nucleon excited state. The peaks shows the the different ρ meson poles, (picture taken from [33]).

- Dalitz decay of neutral mesons $\pi^0 \to \gamma e^+e^-; \eta \to \gamma e^+e^-$.
- Nucleon-Nucleon or π-nucleon bremsstrahlung (non resonant $NN \to NNe^+e^-$ or $\pi \to \pi N e^+e^-$ processes).
- Baryon Dalitz decays (N/R $\to$ Ne^+e^-).
- Direct decay of vector meson ($\rho/\omega/\phi \to e^+e^-$).

Vector mesons decay directly into lepton pairs, whose invariant mass reflects the mass of the vector meson at the time of the decay, since their life time is too short. The invariant mass ($M_{l^+l^-}, l = e, \mu$) of the lepton pair is given by:

$$M_{l^+l^-} \cdot c^2 = \sqrt{(E_{l^+} + E_{l^-})^2 - (\vec{p}_{l^+} \cdot c + \vec{p}_{l^-} \cdot c)^2} \tag{1.14}$$

where $E_{l^\pm}$ is the total energy, $p_{l^\pm}$ is the momentum in the laboratory system and c is the velocity of light. The invariant mass can be simplified since the momenta is larger compared with the rest mass

$$M_{l^+l^-} = 2 \cdot \sin\frac{\theta_{l^+l^-}}{2} \cdot \sqrt{p_{l^+} \cdot p_{l^-}} \tag{1.15}$$

the invariant mass depends only on the momenta p_l of decay leptons and opening angle $\theta_{l^+l^-}$. It is more common to use the transverse momentum p_T because is invariance under a boost in the beam direction

$$p_t = \sqrt{(p_{l^+x} + p_{l^-x})^2 + (p_{l^+y} + p_{l^-y})^2} \tag{1.16}$$

And the rapidity

$$y = \frac{1}{2} \cdot ln\frac{(p_{l^+} + p_{l^-}) + (p_{l^+} + p_{l^-})}{(p_{l^+} + p_{l^-}) - (p_{l^+} + p_{l^-})} \tag{1.17}$$

From all the observables the invariant mass is the most important as we can make a distinction between the different sources. Dilepton spectra are usually divided into three region of invariant mass.

- **Low-mass region**: $M_{ee} < 1.1$ GeV/c^2
- **Intermediate-mass region**: 1.1 GeV/c^2 $< M_{ee} <$ 2.7 GeV/c^2
- **High-mass region**: $M_{ee} > 2.7$ GeV/c^2

Each mass region has different mechanism of dilepton production. The high mass region contains dileptons from Drell-Yann annihilation between $q\bar{q}$ pairs as well peaks of J/ψ, in the intermediate mass region the mayor background source come from the decay of open charm formed from the hadronization of $\bar{c}c$ pairs into $\overline{D}D$ and its decay, in the low mass region the main sources are the decay of vector mesons, hadronic resonances and Dalitz decays. The Figure 1.14 schematically illustrates the expected sources of dilepton production as a function of invariant mass in ultrarelativistic heavy ion collisions.

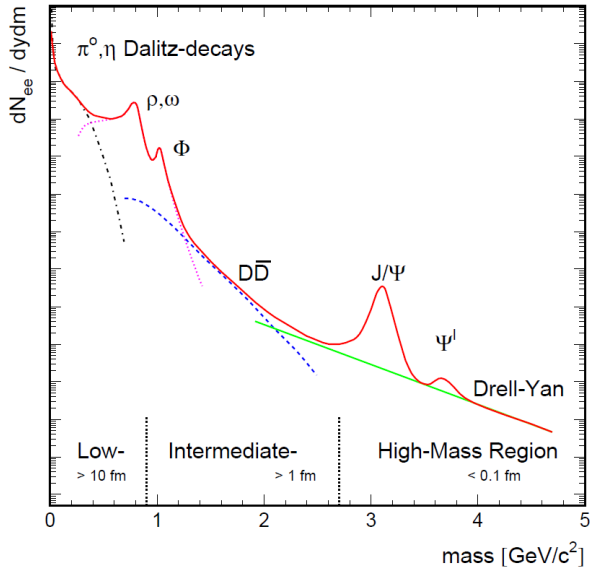

Figure 1.14: Schematic spectral distribution of lepton pairs emitted in ultra-relativistic heavy-ion collisions (picture taken from [21]).

1.3 Experimental results on dilepton production

Many experiments during the last decades have been carried out studying the production of vector mesons, using photon and proton beam, and as well in heavy ion reactions. In-medium modifications of vector mesons can be studied mainly in: *i*) Reconstruction of invariant mass through the dilepton spectra. *ii*) Meson absorption in nuclei and connection to the in-medium decay width $\Gamma^*_{\rm tot}$ by model calculations (this is used for $p(\gamma) + A$ collisions). Dileptons are the ideal candidates since they do not suffer strong interactions with the nuclear matter, on the other hand, the small branching ratio ($\sim 10^{-5}$ s) it is a challenge from an experimental point of view. Results from $p(\gamma) + A$ shows different conclusions: The E325 experiment at KEK [34] observe a dropping mass scenario of the ρ meson in the e^+e^- dilepton spectrum according to

Brown-Rho scaling [12].In contrast, JLAB (CLASS) they observe only a small broadening of the ρ [35]. Measurements of ω at ELSA/MAMI (CBELSA-TAPS) [36] and JLAB [37] and ϕ at COSY (ANKE) [38], LEPS at Spring8 [39] indicates for both mesons a large absorption. For heavy-ions collisions, the studies of in-medium modification of vector mesons spectral functions were carried out by CERES [40] HELIOS [41] collaborations at CERN-SPS and the DLS [42] at BEVALAC. Below the ρ/ω pole it was found a low mass pair excess, see Fig. 1.15. Even there were not enough statistics the results obtained by SPS indicate that the excess is related to the pions annihilation into ρ mesons, therefore it is a direct link to the in-medium modifications of of the spectral function, see Fig. 1.16.

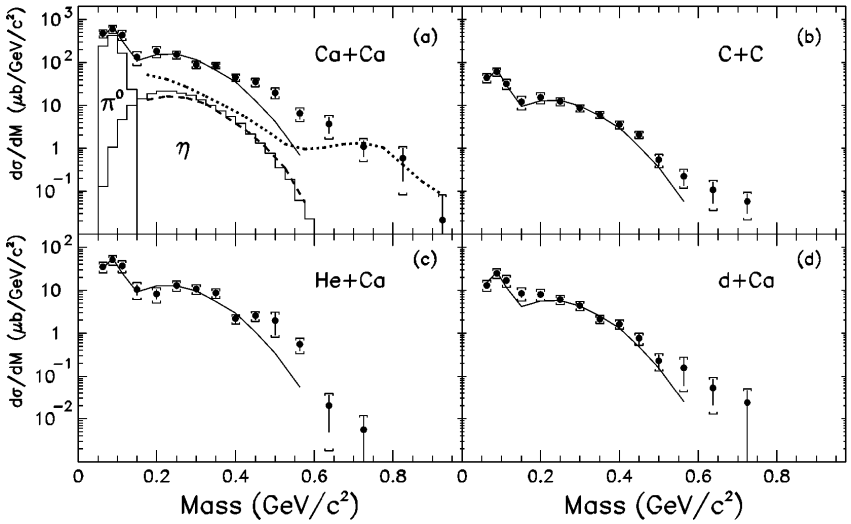

Figure 1.15: DLS measurements of dilectron cross section compared with the BUU model (dotted lines), π^0 and η decay estimated from TAPS measurements and isotropic model (histograms), π^0 and η are in agreement with the data up to a value of 0.4 GeV/c^2 [42].

NA60 reached a milestone with high statics which allowed to to extract the in-medium of ρ spectral function see Fig. 1.16 [43]. It was shown that the modification of the ρ spectral function was affected mainly by two effects from the coupling of the ρ meson to baryonic resonances and the formation of pion loops [16], as it was shown in Fig. 1.8. The first mechanism, the coupling to baryonic resonances plays an important role in the in-medium modifications. At RHIC energies of $\sqrt{s} = 200$ GeV results from PHENIX [44] shows even more excess than results from SPS, but new measurements from STAR [45] does not show this behavior. For the lower energies scale at $1 - 2A$ GeV, DLS [42] experiment could not find an explanation of the dilepton spectra for a light collision of C+C, no models could described the spectra and the excess around $0.15 < M_{e^+e^-} < 0.6$ GeV/c^2. But this energy range is dominated by baryonic matter, so it was not clear if the excess it came from the coupling to baryonic resonances or from true in-medium effects. An explanation of this problem was one of the principal reason to build HADES at GSI [46].

The HADES experiments aims to study dilepton production in heavy-ion collisions in AA, elementary collisions (π+p, p+p, p+d) and cold nuclear matter experiments(p+A, d+A, π+A), see Table 1.3. Measurements of heavy-ion AA collisions are compared with a reference spectra (pp, np, pA) collision system which provides a model independent reference. In the following section it will be shown an overview of the latest results obtained from HADES experiment, (for a detailed review see [47]).

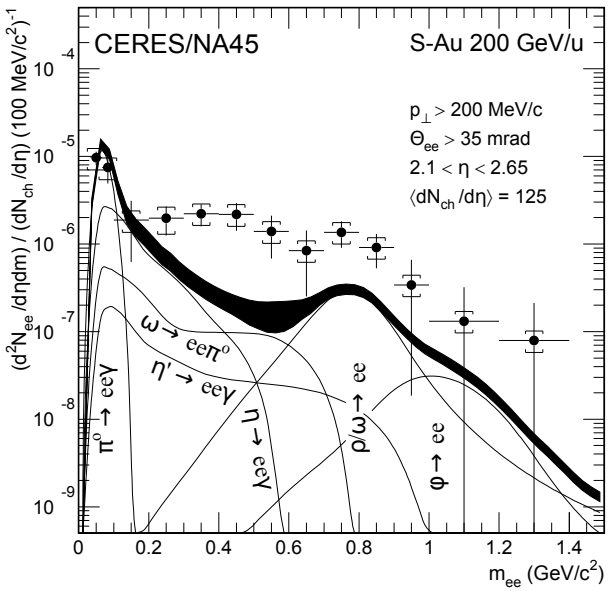

Figure 1.16: Inclusive e^+e^- mass spectra in 200 AGeV in S-Au collisions, data (full circles) compared with various hadron decays, systematic errors on the summed contributions (dashed area) [40].

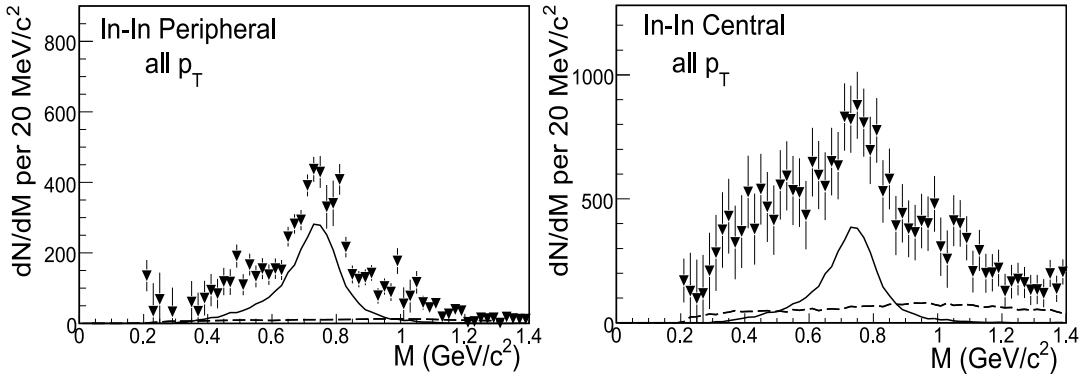

Figure 1.17: Excess mass spectra of dimuons. The cocktail ρ (solid) and the level of uncorrelated charm decays (dashed) are shown for comparison. The excess increase towards central collisions [43].

1.3.1 Results from N-N reaction

Dilepton production in N-N collisions at the beam energy range of 1-2 GeV is mainly dominated by a strong contribution from baryonic sources, Dalitz decays of nucleon resonances $R \to Ne^+e^-$ mainly $\Delta(1232)$) and N-N bremsstrahlung and rising excitation function of η meson production. Above the π^0 mass, at beam energy below $E_{\rm beam}^{\rm thr} = 1.25$ GeV baryonic sources determined completely e^+e^- invariant mass distribution. Vector meson production is small due to the high production threshold $E_{\rm beam}^{\rm thr} = 1.88$ GeV for ω. The exclusive production of ω and η is well know in p+p reaction, but the data for ρ are rared. An important coupling of ρ to low-mass baryonic resonance has been predicted, a detailed understanding of these couplings are necessary for any conclusion on in-medium modification. Fig. 1.18 shows the invariant mass distribution for p+p and p+n reactions, while the p+p reaction can be well described by a

System	E_{kin}(GeV)	$\sqrt{s}$(GeV)	Year
p+p	1.25	2.42	2006
d+p	1.25	2.42	2007
p+p	2.2	2.76	2004
p+p	3.5	3.17	2007
p+Nb	3.5	3.17	2008
C+C	1.0	2.32	2004
C+C	2.0	2.70	2002
Ar+KCl	1.756	2.61	2005
Au+Au	1.23	2.42	2012
$\pi^- + p$	0.656, 0.690, 0.748, 0.800	1.46 - 1.55	2014
$\pi^- + A$	0.656, 0.690, 0.748, 0.800	1.46 - 1.55	2014

Table 1.3: HADES data taking with various collision systems.

superposition of the π^0 and $\Delta(1232)$) Dalitz decays, the p+n do not describe well the data over these two contributions above π^0 mass region. Shaded areas shows the uncertainty due to electromagnetic transition form factors of $\Delta(1232) \rightarrow Ne^+e^-$ decay calculated with the Iachello-Wan model [48]. The solid curve shows the prediction in One Boson Exchange Model (OBE). In special, the unusual form of p+n data is due to the electromagnetic form factor of the charged pion, this is possible because unlike in p+p a charged pion can be exchanged. Clement and Bashkanov [49] described well the production of two pions in p+p and p+n, and explain the enhancement in p+n from the double delta excitation followed by the decay into dielectron in the isospin I=1 channel, which is coupled to off-shell ρ meson. Even if the p+n data is not fully theoretically described, the data allows to construct the N+N reference spectrum which is used for heavy ion reactions to account for baryonic contributions.

1.3.2 Results from p+Nb reaction

In 2008, p+Nb and p+p were measured at a beam energy 3.5 GeV to study in-medium modifications of vector meson in cold nuclear matter [50]. In left of Fig. 1.19 the differential inclusive e^+e^- cross section as a function of e^+e^- invariant mass is shown. A comparison of experimental data and the expected distributions calculated from PYTHIA is shown for p+p. The strength below vector meson production, which is even more pronounced in p+p can be explained as a strong coupling of ρ meson to low-mass baryonic resonances, which are not included in PYTHIA. In order to explain this behavior the exclusive ppe^+e^- channel, see right Fig. 1.19, which are related to two body vector meson decay and the resonance $R \rightarrow pe^+e^-$ were studied including $R \rightarrow pe^+e^-$ where R is $\Delta(1232)$ (black/red solid line), higher mass Δ^+, N^* (grey/green solid line), and the two-body meson $\rho, \omega \rightarrow e^+e^-$ decays. Those calculations underestimated the data which corroborates the hypothesis of a strong off-shell resonance ρ coupling, enhancing dielectron emission below the vector meson pole. To observe the expected excess in the low mass region, a comparison of the p+Nb to the elementary reference was studied in two different pair momenta, in left part of Fig. 1.20 for $P_{ee} > 0.8$ GeV/c no difference is observed in contrast with the right part of Fig. 1.20 at $P_{ee} < 0.8$ GeV/c where the yield of p+Nb is reduced around the ω pole and enhanced at lower masses, this is understood as extra ρ production due to multiparticle collisions. Baryonic resonance influence the ρ production, and as a consequence, the in medium properties of the meson due to the multiple particle collisions which are a new mechanism of ρ production [51]. Results in pion induced reactions presented

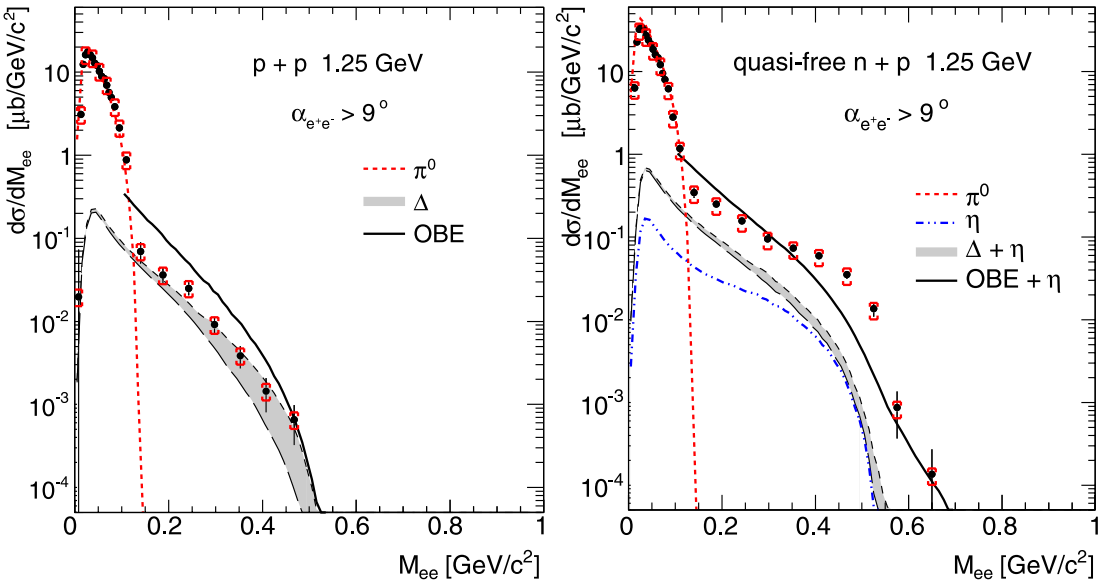

Figure 1.18: **Left**: Differential cross sections as function of invariant mass (full circles) measured in $p+p$. **Right**: $n+p$ at 1.25 GeV. The curves show results of model calculations with PLUTO event generator for π^0 Dalitz decay (red dashed) and baryonic resonances (black long dashed) only due to production threshold. The p+p data is in agreement with theoretical predictions in contrast with n+p which does not agree and shows a cut off at a higher mass. The OBE calculations fail to describe the data above π^0 mass. The η Dalitz is also add to the model (blue dashed-double dotted) [50].

in this thesis and in the future campaigns with the pion beam are expected to clarify this mechanism.

1.3.3 Results from A-A reaction: C+C, Ar+KCl and Au+Au

Particle production in heavy-ion collisions at a beam energy of 1–2 AGeV are mainly dominated by pion production from $\Delta(1232)$ resonance. The e^+e^- invariant mass distributions measured with HADES in the light C+C (at 1.0 AGeV) and the medium heavy Ar+KCl (at 1.756 AGeV) systems are shown in Fig. 1.21.

The differential distributions are compared to the expected mesonic e^+e^- cocktail from the π^0, η Dalitz and ω decays. The e^+e^- The cocktail produced from the meson decays does not describe the measured yields for both collision systems and open a question for a contribution expected from the baryonic sources discussed above: resonance Dalitz decays (mainly $\Delta(1232)$) and nucleon-nucleon bremsstrahlung. In the interest of searching in-medium radiation from dense nuclear phase of collisions, it was compared e^+e^- production from nucleus– nucleus reactions with a proper production rates measured in elementary collisions. In Fig. 1.22 the ratio of the pair multiplicities measured in nucleus–nucleus collisions and for C+C to the averaged $1/2\left(M_{pp}^{e+e^-} + M_{pn}^{e+e^-}\right)/M_{\pi^0}$ is shown.

In Fig. 1.22 we can see that the invariant mass distribution below π^0 mass range is well described for 1 and 2 AGeV. Also the ratio for $M_{e^+e^-} < 0.6$ GeV/c^2 in C+C collision is consistent. Hence, pair production in these mass region can be described by a sum of contributions from baryonic sources, extracted from the N + N collisions, which yield scale as pion production and η, π^0 mesons accounting for the radiation after freeze-out. These results solve the unexplained

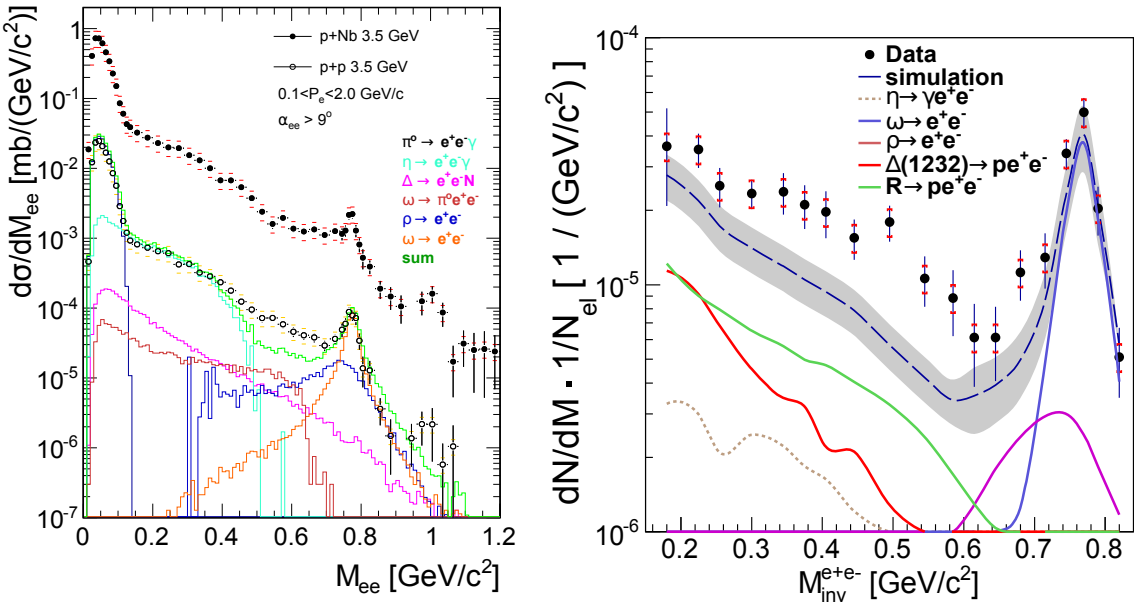

Figure 1.19: **Left**: Comparison of dielectron cross sections as a function of the invariant mass measured in p+p and p+Nb collisions at the kinetic beam energy of 3.5 GeV. For the p+p data a PYTHIA dilepton cocktail is displayed in addition. [51]. **Right**: e^+e^- invariant mass distributions compared to the simulation result assuming a point-like $RN\gamma^*$ coupling (QED-model) [52].

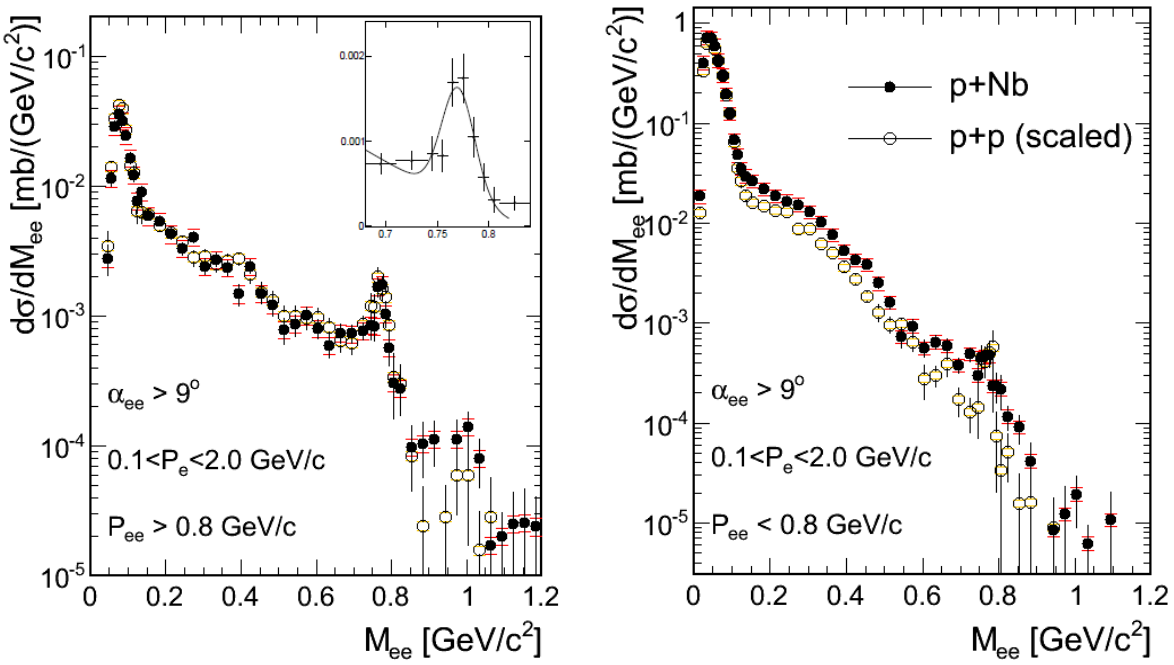

Figure 1.20: Invariant mass spectra yield in p+Nb collisions.**Left**: Pair momenta e^+e^- are limited to $P_{ee} > 0.8$ GeV/c. **Right**: Pair momenta e^+e^- are limited to $P_{ee} < 0.8$ GeV/c. Low momenta pairs are moving slowly so a higher medium modification is expected [51].

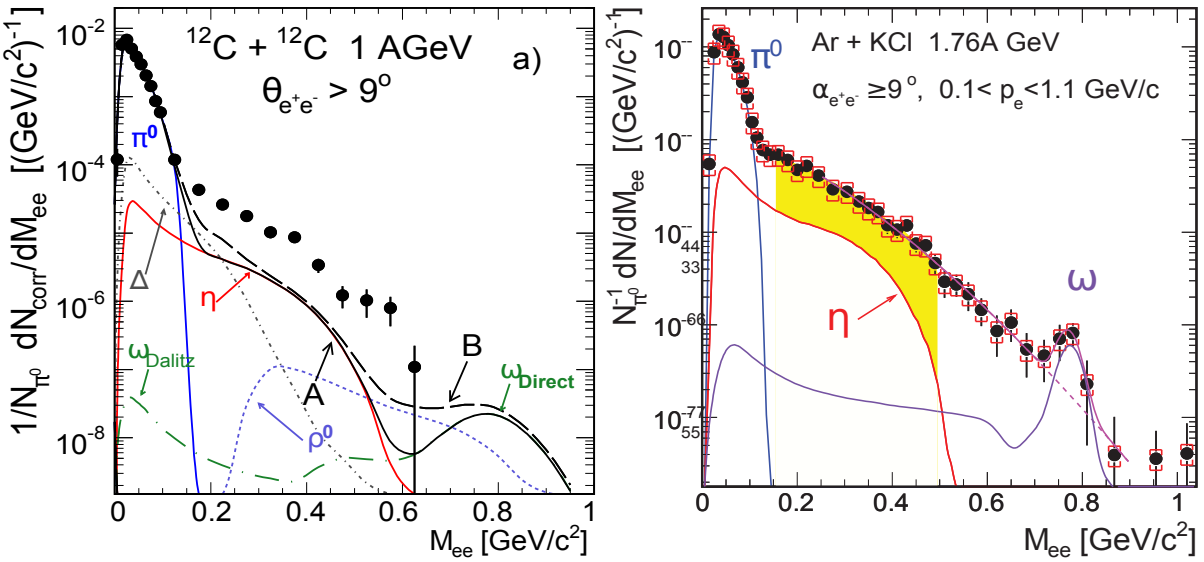

Figure 1.21: **Left**: e^+e^- production rates normalized to the π^0 yield as a function of the invariant mass distribution measured in C+C collisions at 1 AGeV compared to thermal dielectron cocktail of mesonic sources (π^0, η, ω) after freeze-out [53].**Right**: e^+e^- distributions for Ar+KCl collisions at 1.756 AGeV. Shaded area shows invariant mass region where the pair excess from in-medium radiation has been identified [54].

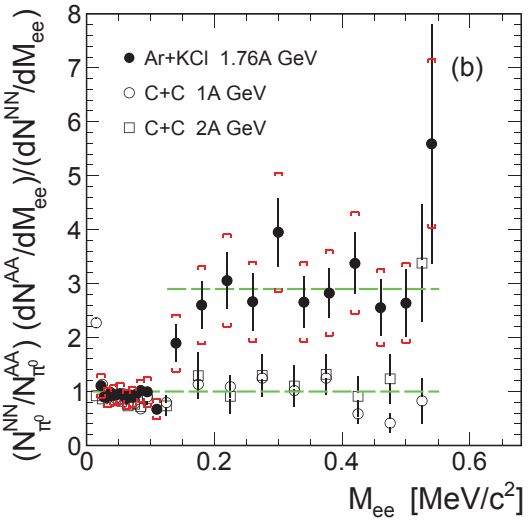

Figure 1.22: Ratio of e^+e^- invariant mass distributions measured in Ar+KCl and C+C with subtracted η meson contribution to the N+N reference spectrum [54].

"DLS puzzle" yield measured in C+C by not accounted for baryonic contributions [49]. In contrast, we can observe a significant excess (2.5–3) concerning the N+N reference for Ar+KCl above the π^0 mass showing that there should be another contribution that is not included in the model. An explanation from this undescribed yield, it comes from the contributions of multibody and multi-steps process created in the collisions of large size nuclei. In this case, short-lived baryonic resonances seem to play a major role. A further important test of this scenario is provided by data obtained from Au+Au collisions at 1.25 AGeV. In top of Fig. 1.23

we can observe that the excess is increasing along with the size of the system. The excess yield indicates a strong medium modification of the ρ meson, probably induced by the high baryon density, where the meson is modified by in-medium effects.

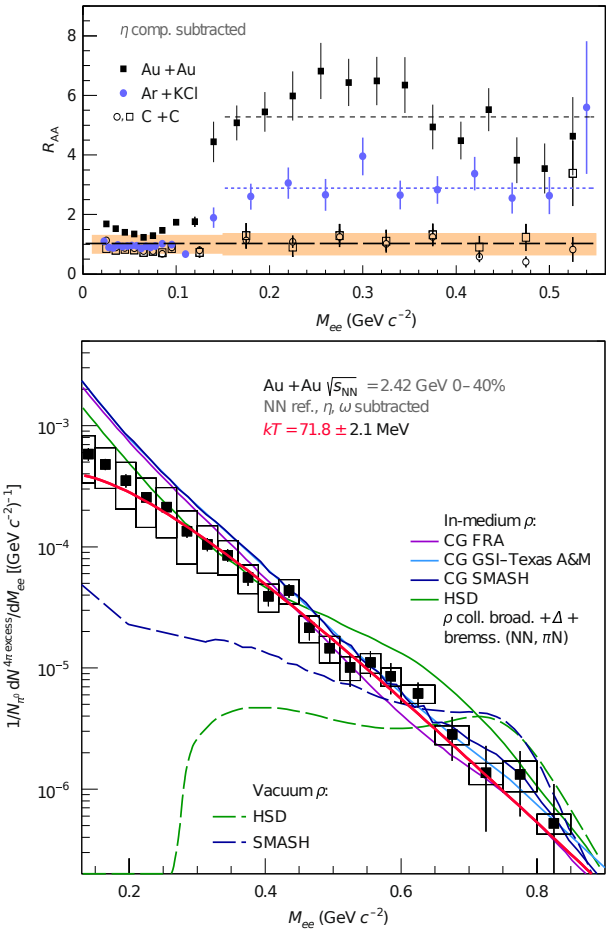

Figure 1.23: **Top:** Ratio of e^+e^- invariant mass distributions measured in A+A compared to N+N reference. The η contribution subtracted from the spectra. **Bottom:** Acceptance-corrected dilepton excess yield, subtracted the η and ω contribution as well as the N+N reference normalized to the number of neutral pions. Dashed curves: ρ ('free' spectral function) contribution from HSD and SMASH transport model calculations normalized to the respective number of neutral pions. The dark-blue, blue and pink curves show the results of three versions of coarse-grained calculations using different concepts to obtain the local thermal parameters. [55].

1.4 Motivation for pion-induced reactions at HADES

Pion-induced reaction is a good supplementary source of information besides proton-induced and heavy-ions reactions, which we already discussed in the previous section. One of the advantages is that they are more suitable for studying individual resonance than other nuclear projectiles. When the N-N collision gives a broad variety of resonance, the energy in collision can be modified by the energy of the pion beam, and scan the mass of the resonance we want to produce. Of course, there will be overlapping resonances but much less than in N-N and A+A.

Moreover, the process $\pi N \to Ne^+e^-$ is related to the time inverse of pion photo or electroproduction $\gamma^* N \to \pi N$, which is the key experiment determining the electromagnetic properties of baryonic resonances and it was studied deeply experimentally and theoretically [28; 56]. Partial wave analysis (PWA) of the measured data is required to extract the amplitudes and separate the different contributions. It was already mentioned that resonance contributions are an important ingredient to described the dilepton spectra measured from HADES, pion-induced reactions will give additional information on these resonance contributions. Therefore, the study of the exclusive $\pi^- p \to ne^+e^-$ reaction below the ω threshold gives a novel opportunity to measure the coupling of baryonic resonances to off-shell vector mesons, which is of fundamental importance for the understanding of medium effects in hadronic matter. These couplings are indeed thought to be at the origin of the in-medium modifications of the vector meson spectral function in hadronic matter [57]. We can measure directly the dilepton spectra from pion-induced reactions tuning the beam energy range of the resonance peak we want to excite to get the maximum contribution from it. In Fig. 1.24 it is shown the dilepton excitation function for $\pi^- p$ reaction, we can see clearly that the π^0 Dalitz decay dominate the total dilepton production, which fortunately can be identified very well since it is limited by its low invariant mass ($m_{ee} < m_\pi$). The π^0 Dalitz decay followed by the π^0 production cross section shows resonance structures like the $\Delta(1232)$ and also some peaks in the second resonance region. The η Dalitz decay appears for beam energies above 500 MeV, just below we can find the resonance contributions, Δ Dalitz and resonances trough $R \to \rho N$ decay, those resonances throw the ρ decay are well known due to its strong coupling, in particular with the $D_{13}(1520)$ gives the largest contribution which dominates at lower energies. It is clear that the peak of $N(1520)$ is larger in magnitude than the Δ which confirm the important role that takes into the dilepton production where we already observe in NN collisions [28]. The production of baryonic resonance in $\pi^- p \to ne^+e^-$ reaction can be described in two ways that we already discussed in Section 1.2.2; direct decay of baryonic resonance to e^+e^- throw a ρ or ω meson or a Dalitz decay ($R \to ne^+e^-$) of the baryonic resonance R, see Fig. 1.12. In the second case, time-like electromagnetic form factors are considered with the aim to described the electromagnetic structure of this baryonic transition. When using Vector Dominance Model form factors, the two ways are equivalent.

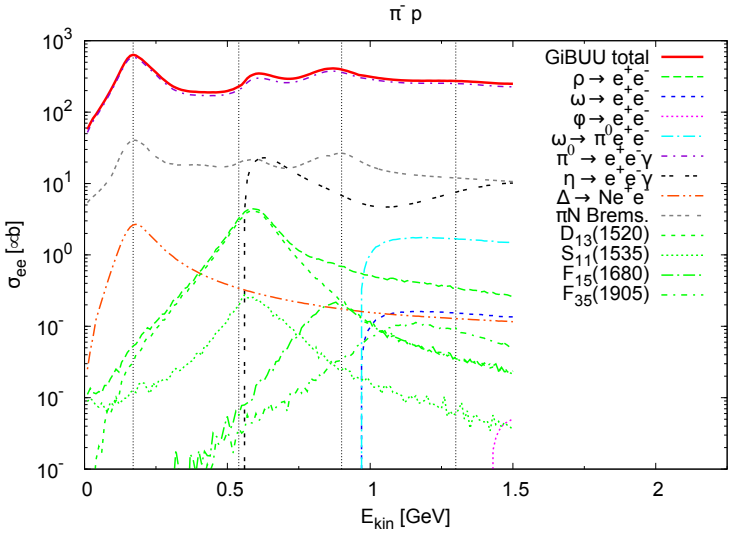

Figure 1.24: $\pi^- p \to e^+e^- X$ excitation function [28].

Last but not least, a measurement from pionic final states 2π over a beam energy range

can improve the existing database which is very important, as an input for the analysis of PWA, also useful for the description of the dielectron channels. Based on theoretical predictions aforementioned, in 2014 HADES experiment has been operating a pion beam induced reactions, for a data taking period of two weeks with an incident pion beam momenta between $p_\pi = 0.650 - 0.800$ GeV/c corresponding to $\sqrt{s} = 1.460 - 1.550$ GeV. Between this range, four different pion beam momenta were chosen (0.656, 0.690, 0.748 and 0.800 GeV/c). The pion induced reactions were carried out on two targets: polyethylene $(C_2H_4)_n$ and carbon C, the normalization of spectra has been done using elastic scattering of pion on polyethylene and carbon. It was planned to subtract carbon events from polyethylene one and get pure pion proton contribution, lately in the following chapter we will inform that it was only possible for the pion production channels because there were not enough statistics collected for dilepton production with the carbon target.

First run was devoted to strangeness production in pion-induced reactions on light $\left({}^{12}\mathrm{C}\right)$ and heavy $\left({}^{74}\mathrm{W}\right)$ nuclei at a beam momentum of 1.7 GeV/c. The second run was devoted to the analysis presented in this Ph.D. thesis, which is to measure the dilepton production e^+e^- for a pion beam momentum of 0.69 GeV/c where the largest statistics were collected. At this fixed pion beam energy, we can excite the region of N(1520) that couples strong to the ρN giving information of in-medium modifications of ρ meson, and also we can check the verification of the VDM where the contribution of vector mesons is not described explicitly but is embedded in the VDM form factors [56]. The data were taken for an energy range of 0.656, 0.690, 0.745 and 0.800 GeV/c was devoted to measuring the excitation function of two-pion production which was used as a new input to the Partial Waves Analysis (PWA) which are very useful to describe the resonance contributions.

1.5 Existing database for pion-induced reactions

Database for pion nucleon reaction is very limited, in particular for differential distributions the e^+e^- production in pion induced reactions has never been measured. Nevertheless, there is some data for meson production which can be useful in the description of our data. Since the measurement was done with two different targets of $(C_2H_4)_n$ and carbon C to subtract carbon contribution to obtain the pure contribution on protons, therefore a detailed study of pion reactions on C target it is necessary.

1.5.1 Review of experimental data for $\pi^- p$ reaction

As we can see in Fig. 1.25, pion-induced reactions excited a various number of hadronic channels, in the context of this thesis the analysis was performed for the study of dilepton production e^+e^- at $\sqrt{s} = 1.49$ GeV. Unfortunately, there is no information of dilepton production in this energy range, only a few information about meson production which can be used to interpret the data. I am only interested in the $\pi^- p \to n e^+ e^-$ and $\pi^- p \to n\eta$ reaction channels that decays into a e^+e^-, those are baryonic resonance $R \to N e^+ e^-$ and Dalitz decay of mesons $\pi^0 \to \gamma e^+ e^-; \eta \to \gamma e^+ e^-$

$\pi^- p \to n\pi^0$ reaction

The exclusive charge exchange of $\pi^- p \to n\pi^0$ reaction gives the largest production of π^0. SAID Partial Wave Analysis (PWA) [59] has recorded many of these cross sections and angular distributions from many experiments. Two experiments are not included in SAID analysis because they use only differential distributions, those experiments are at BNL [60; 61]. The

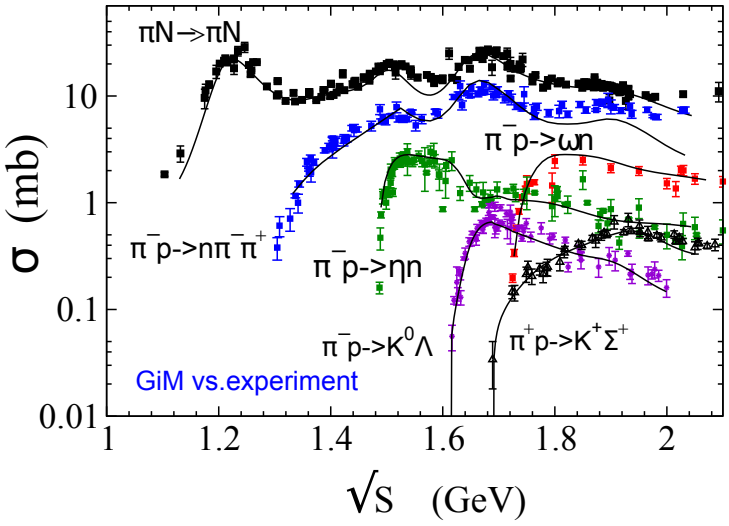

Figure 1.25: Total cross section for pion-induced reactions calculated in Giessen model vs. experimental data. $\pi^- p \to e^+ e^- X$ excitation function [58].

comparison of different PWA from the SAID database and the two experimental data from BNL are shown in see Table 1.4

Energy (MeV)	PWA Solutions	Cross Section (mb)
564	KH80	8.99
	KA84	9.49
	CMB	9.71
	WI08	9.77
565	BNL [60]	7.71±0.62
568.3	BNL [61]	8.33±0.56

Table 1.4: Cross section for $\pi^- p \to n\pi^0$ reaction at E= 564 MeV for differents PWA solutions and data from BNL experiments.

In Fig. 1.26 we can see the differential cross section as a function of π^0 polar angle for a range of pion beam energies close to HADES experiments. The latest results are the one labeled as St[05], measured with the Crystal Ball (CB) at BNL [62]. Even there are not enough measurements for angles below 20° we can note that the π^0 angular distribution increase in forwards direction. The best agreement is obtained with the most recent solution WI08. The information obtained with that results is that cross section of the π^0 production at our beam energies is a strong forward peak for angles below 20° and can decrease about factor 2 for angles between 20° and 40°, this is something we need to take into account for the HADES acceptance and also in the simulations.

The $\pi^- p \to \pi^0 \pi^- p$ reaction

Only old data is found for this reaction, results from BNL [63] gives a cross section of 3.99 ± 0.5 mb at an incident beam energy of 683 MeV/c and at Berkley [64] at beam energy of 713 MeV/c gives a value of 3.98 ± 0.35 mb. Both values shows a good agreement.

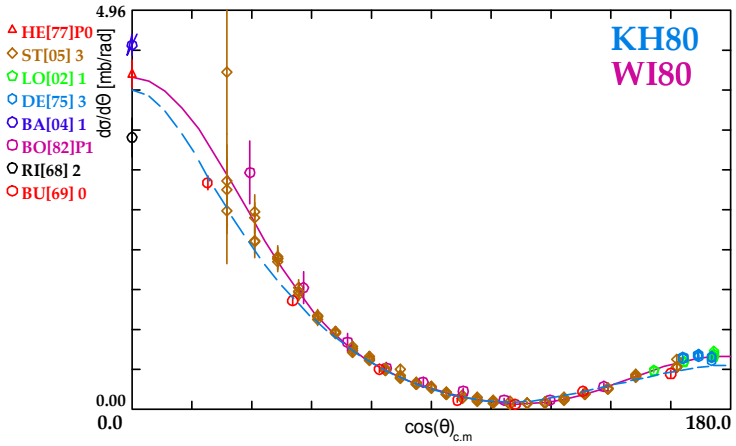

Figure 1.26: SAID database of $\pi^- p \to n\pi^0$ reaction for a pion beam energy range between [554 - 564 MeV] compared with the WI08 (pink) and KH80 (blue) PWA solutions [59].

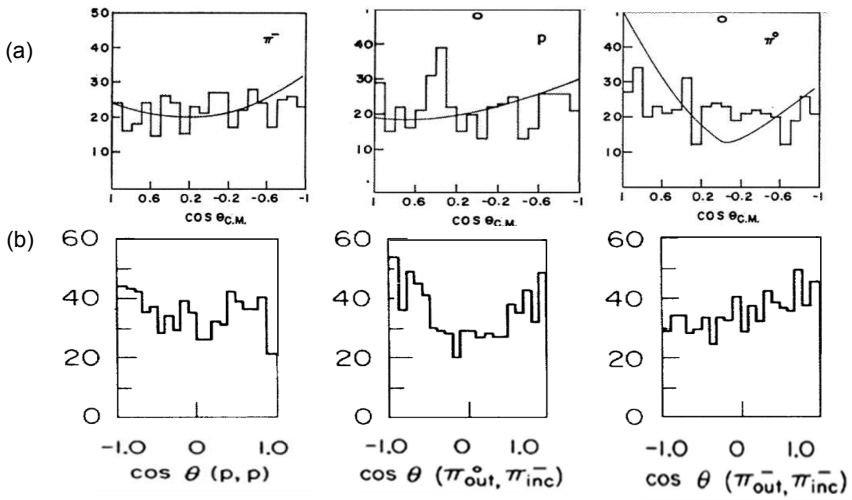

Figure 1.27: Center of mass angular distribution for π^-, p and π^0 at incident energy **a)** E= 683 MeV/c [63] and **b)** E=763 MeV/c [64].

The $\pi^- p \to \pi^0\pi^0 n$ reaction

Crystal Ball collaboration (CB) has measured the cross section for $\pi^- p \to \pi^0\pi^0 n$. As we can see in Fig. 1.28 for our energy range we obtain a value of $\sigma = 1.880 \pm 0.015$ mb. Differential cross sections for the $2\pi^0$ at different beam energies is shown in Fig. 1.29, for forward and backward directions there is an increment in the production of the $2\pi^0$, specially for the forward directions.

The $\pi^- p \to n\eta$ reaction

The η production measurements for the total cross section compared with the analysis of the GiBUU group [66] are shown in Fig. 1.30. As we can observe the energy threshold for η production is $\sqrt{s} = 1.481$ GeV or $p_\pi = 0.697$ GeV/c. In our energy range the η production is dominated by the contribution of $N(1535)S_{11}$ resonance. For our experiments the most important measurements are the threshold data from BNL E909 experiment (red circles) [67].

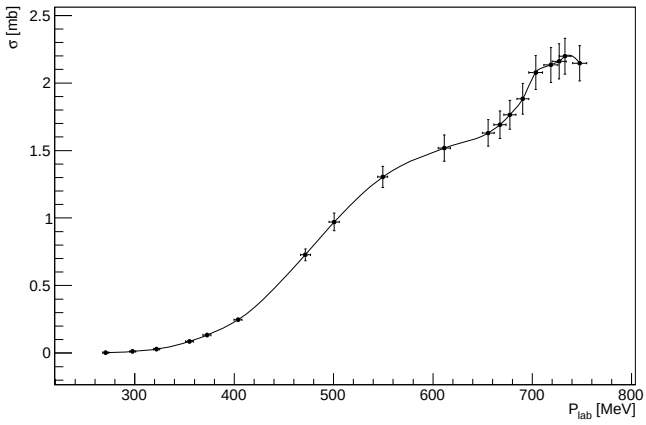

Figure 1.28: Summary of the main results for the total cross section of $\pi^- p \to \pi^0\pi^0 n$ reaction [65].

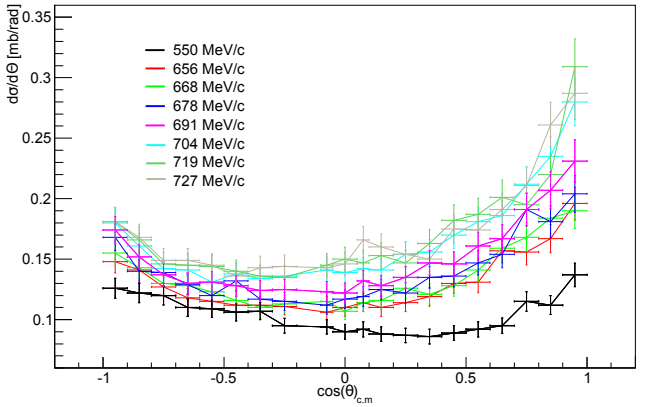

Figure 1.29: Differential cross sections as a function of the polar angle for $2\pi^0$ system produced in $\pi^- p \to \pi^0\pi^0 n$ at eight different beam momenta [65].

1.5.2 Cross section contribution of n and p in $\pi^{-12}C$ reaction

For pion induced reactions on ^{12}C we need to consider that pions can interact either with protons $\pi^- p$ and neutrons $\pi^- n$, so it is necessary to study the cross section for the different reactions to observe how strong are these contributions. Fig. 1.31 shows the total cross sections for $\pi^- p$ and $\pi^+ p$ (analog to $\pi^- n$) against pion beam momentum. We can see that in the region of $\Delta(1232)$ resonance the $\pi^+ p$ is larger than the $\pi^- p$ about one order of magnitude due to different isospin factors. For the second and third resonance region, the $\pi^- p$ is much larger, especially in our energy range at pion beam momenta of 0.690 GeV/c the ratio between both reactions equal to $\sigma_{\pi^- p}/\sigma_{\pi^+ p} = 3$, which indicates the $\pi^{-12}C$ reaction it is dominated by $\pi^- p$ interaction rather than $\pi^- n$.

1.5.3 Review of experimental data for $\pi^{-12}C$ reaction

The physics of pion-nuclear interactions can be separated in three different regions according to pion kinetic energy: the low-energy $0 < T_\pi \leq 80$ MeV, the $\Delta-$resonance region with

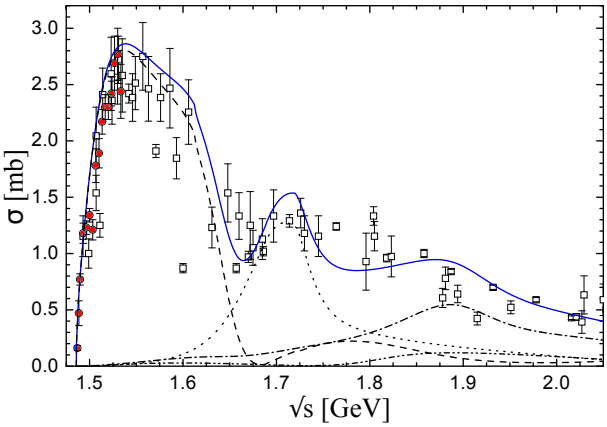

Figure 1.30: $\pi^- p \to \eta n$ total cross section. The new threshold data are denoted by red circles. Partial-wave decomposition of the total cross section. $J^P = \frac{1}{2}^-\,(S_{11})$: dashed line; $\frac{1}{2}^+\,(P_{11})$: dotted line; $\frac{3}{2}^+\,(P_{13})$: dash-dotted line; $\frac{3}{2}^-\,(D_{13})$: dash-double-dotted line (in brackets the πN notation is given). The sum of all partial waves is given by the solid blue line [66].

80 MeV $\leq T_\pi \leq$ 400 MeV and the high-energy region $T_\pi \geq$ 400 MeV. A difference between energies comes with the study of the mean free path, in the low-energy region, long wavelength, the mean free path is large which implies that the interaction is weak and the pion can penetrate deeply into the nuclear interior. In passing from low energies to the region of $\Delta(1232)$ resonance the pion-nucleus interaction changes drastically, the pion mean free path is short compared with the inter-nucleon distance so the scattering consequently short wavelengths for pions which should allow the use of a simple eikonal(optical) reaction model. There are many studies for $\Delta-$resonance region in pion beam experiments like in LAMPF, TRIUMPF and PSI [68; 69; 70]. The main process for π^--nucleus reaction at this energy range is the quasi-free scattering, which is modified by several medium effects as Fermi motion, absorption,...One of the key results of pion nuclear physics at intermediate energies is that the $\Delta-$isobar survives as a distinct baryonic species in a strongly interacting nuclear environment, it can be treated as a quasiparticle, just like a nucleon. Measurements of total and absorption cross section of pion nucleus reaction from an energy beam between 0.6-1.2 GeV are provided by [71] Cosmotron, and between 0.5-1.3 GeV at Saturne [72].

The $\pi^{-12}C \to (\pi, \pi^0)$ reaction

Inclusive pion scattering (π, π') [73] and charge exchange (π^-, π^0) [74; 75; 76] were carried out by LAMPF experiment. In Fig. 1.32 we can clearly see for forward reactions a peak which coincide with the red dotted lines that represent the pion kinetic energies for the corresponding free $\pi^- p$ reaction, which at larger angles it disappear. The π^0 production in $\pi^{-12}C$ reactions is similar to $\pi^- p$ reaction, therefore we can confirm the hypothesis of a participant-spectator procedure for the π^0 production.

Measurements of two-pion production were carried out by PSI [78] and TRIUMPF [79] for $^{12}C\,(\pi^-, \pi^-\pi^+)$ and $^{12}C\,(\pi^-, 2\pi^-)$ processes for a energy beam up to 320 MeV. As well, for the same energy range, other experiments like Crystal Ball collaboration at BNL for $(\pi^-, \pi^0\pi^0)$ and TRIUMPF by the CHAOS collaboration for the $(\pi^+, \pi^+\pi^-)$ and $(\pi^+, \pi^+\pi^+)$ measured differential cross section for different nuclei [80; 81; 82]. Above the $\Delta-$ resonance region there are scare information for pion production on nuclei in our energy range, but it can be assumed that the process of two-pion production it follows by a quasi-free reaction, like in the charge-

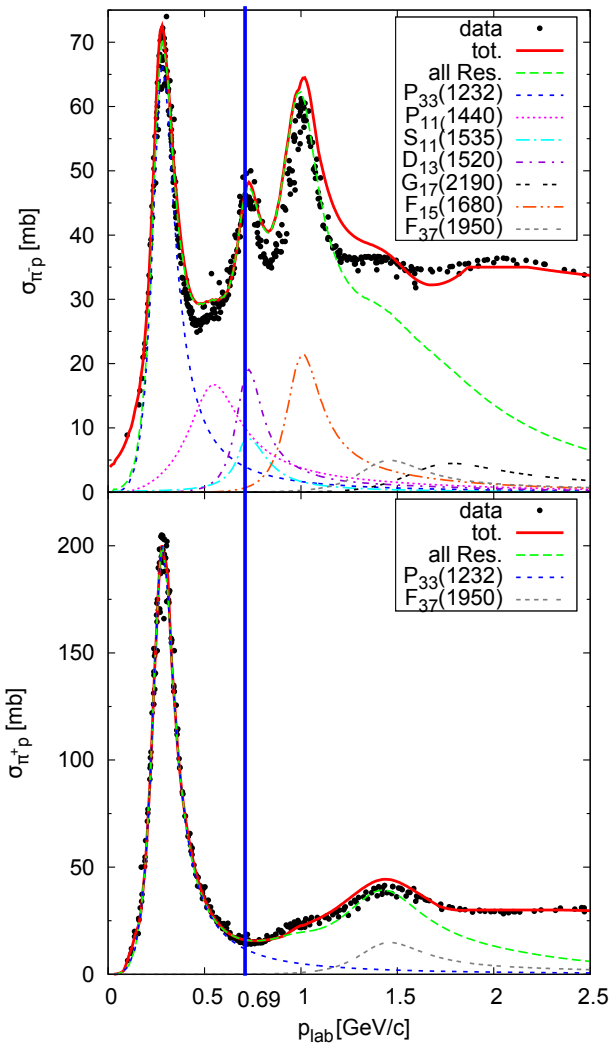

Figure 1.31: Total cross section for $\pi^- p$ **Top** and $\pi^+ p$ **Bottom** with the contributions of the most important resonances. [28]. Blue line indicates a pion beam momenta of 0.69 GeV/c.

exchange reaction.

The $\pi^- C \to n\eta$ reaction

Experimental information on the η-nucleus has been carried out from different experiments. Pion induced η production in light nuclei like $\pi^- + {}^3He \to \eta$+t has been detected at LAMPF and in d+p experiments at SATURNE [83]. For the pion scattering data on ^{12}C it was used a Glauber model for a better prediction of the multiple scattering of the π from the nucleus [84; 85; 86]. Calculations from different authors shows that the reaction $\pi + N \to \eta + N$ is dominated by an intermediate N(1535)resonance. It is also found that proton final state interaction reduces the cross section by a factor of 2. All the previous results have to be taken into account in our analysis as we are using a participant-spectator model for the $\pi^- C$ reaction.

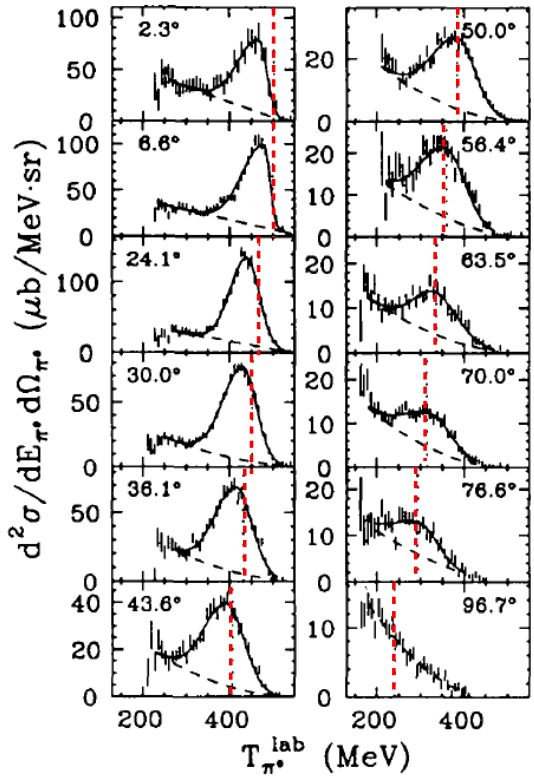

Figure 1.32: Pion SCX cross sections for C (π^-, π^0) at 500 MeV. The red dotted lines mark the pion kinetic energies for the corresponding $\pi^- p \to \pi^0 n$ reaction [77]

1.6 Overview of the present work

In the Chapter 1 will be introduced the general physics background, results from different experiments which use electromagnetic probes to study the properties of vector mesons, and finally, a review of the most recent results of the HADES collaboration which reenforce the motivation for the actual pion beam experiment. In particular, I have done a detailed review from many experiments related to pion-induced reactions in proton and carbon targets in the energy range of my interest, since these results provides cross section values which are crucial to describe the dilepton spectra in the simulations. In the Chapter 2 will be presented the HADES spectrometer, the performance of all the subdetectors, the properties of the targets used during the experiment, and a description of the secondary pion beam. The Chapter 3 will describe the analysis strategy, the reconstruction procedure of a single lepton track and the different quality cuts applied for the lepton identification. The calibration procedure of the TOF detector will be presented in Chapter 4, which was one of my duties during the commissioning of the pion-beam experiment in 2014. The efficiency corrections and the systematic errors will be calculated in Chapter 5 along with studies of the relative carbon contribution in the polyethylene target. In Chapter 6 the pair reconstruction analysis will be described, also the background rejection procedure and the comparison between Backtracking analysis and RICH ring finder procedure. A first approach to subtract the carbon contribution from the polyethylene target was developed in Chapter 7, also the procedure to obtain the normalization factor in order to scale the experimental yield is described in this chapter. In Chapter 8 the theoretical models of baryonic Dalitz decays and the electromagnetic form factors (EMFF's), using a QED calculation

and VDM form factors is described. Results from HADES PWA analysis of the two pion channels shown in this chapter were carried out by the Cracow team from HADES collaboration. The final results and main contributions of the current analysis are discussed in Chapter 9. The Chapter 10 described the results from a commissioning experiment at MAMI facility connected with the Electromagnetic CALorimeter (ECAL). The PhD thesis is summarizes with the final conclusions and the outlook in the Chapter 11 and Chapter 12.

Chapter 2

The HADES spectrometer

HADES is a fixed target experiment installed at SIS18 synchrotron located in GSI Helmholtzzentrum für Schwerionenforschung in Darmstadt (Germany). The goal of the HADES experiments is to measure the spectral properties of vector mesons as their in-medium masses and widths throw their leptonic decays to e^+e^-. It is designed to systematically measure the production of electron-positron pairs coming from nucleon-nucleon, heavy-ions collisions, and pion-nucleon produced at SIS18 with maximum kinetic energy protons and ions of 4.5 GeV and 2 AGeV respectively. It consists of six identical sectors covering the full azimuthal range and polar angles from 18° to 85° with respect to the beam direction. Each sector contains: A Ring Imaging CHerenkov (RICH) detector used for electron identification; two Mini-Drift Chambers (MDC) placed in front and two (MDC) placed behind the toroidal magnetic field to determine momenta of charged particles; Multiplicity and Electron Trigger Array (META) composed of Time-Of-Flight detectors (TOF+RPC) and Pre-Shower detector improving the electron identification. Two-stage trigger system is employed to select events within a predefined charged particle multiplicity interval (first-level trigger LVL1), as well as electron candidates (second-level trigger LVL2). Also, a START detector is located in front of the target for the reaction time measurement [46]. A section of the detector in the vertical plane containing the beam axis is shown in Fig 2.1.

The main features of the HADES detector are shown below:

- A di-electron invariant mass resolution at the ω peak of $\sim$2.7% and a momentum resolution for protons of 4% can be achieved.
- Large geometrical acceptance to register rare dielectron decays with a large opening angle like ω or small like π^0Dalitz decay.
- High trigger rate of the order of 10-40 kHz makes HADES detector unique among other heavy-ion experiments studying hadronic matter.
- Low background due to the reduce material budget $/X_0 \sim 2 \cdot 10^{-3}$ which is very important to increase the high resolution in the electron identification.

In the following sections, all the sub-detectors will be described briefly. More detailed information can be found in [46]. Also, a detailed description of the dedicated pion beam and targets will be described in this chapter.

2.1 Target

HADES is a fixed target experiment, which demands experiments with multiple beam-target combinations. Studies of elementary reactions are carried out with proton, deuteron and pion beams incident in liquid hydrogen targets. In the analysis of pion induced reaction in 2014

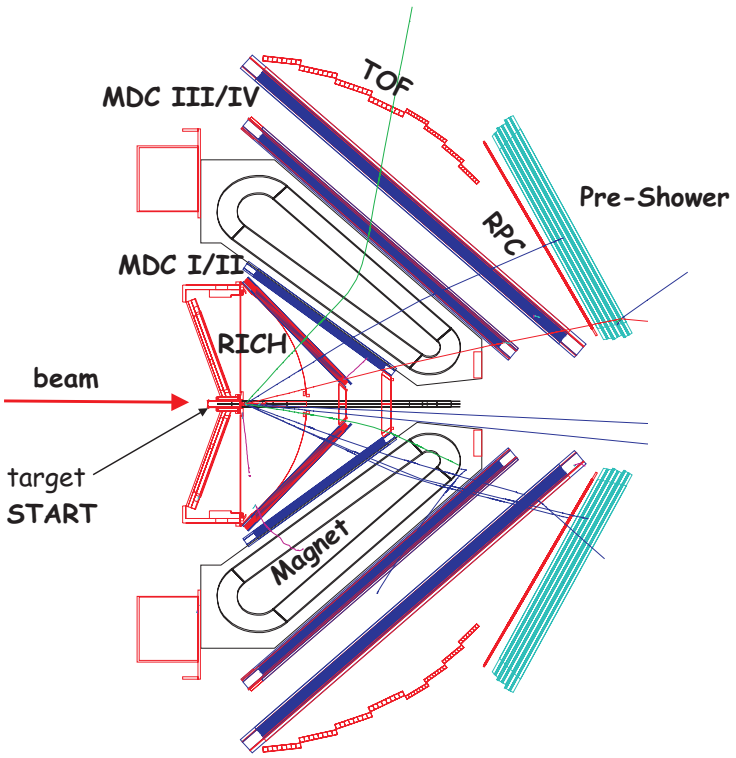

Figure 2.1: **Left**: Schematic layout of the HADES detector.

polyethylene and carbon targets were used, see Fig. 2.2. The usual liquid hydrogen target was replaced for a thick polyethylene target to avoid problems with the cooling of the liquid hydrogen below 20K. Also the solid polyethylene target has a larger density of protons $\left(4 \cdot 10^{23}/\mathrm{cm}^2\right)$ (factor 2) in contrast with the LH_2 target, and last, the thickness of the surrounding material produces less secondary particles. In-medium modifications of hadron properties are done with light projectiles on heavy targets, and for the studies at high temperature/densities requires reactions with heavy projectiles [46].

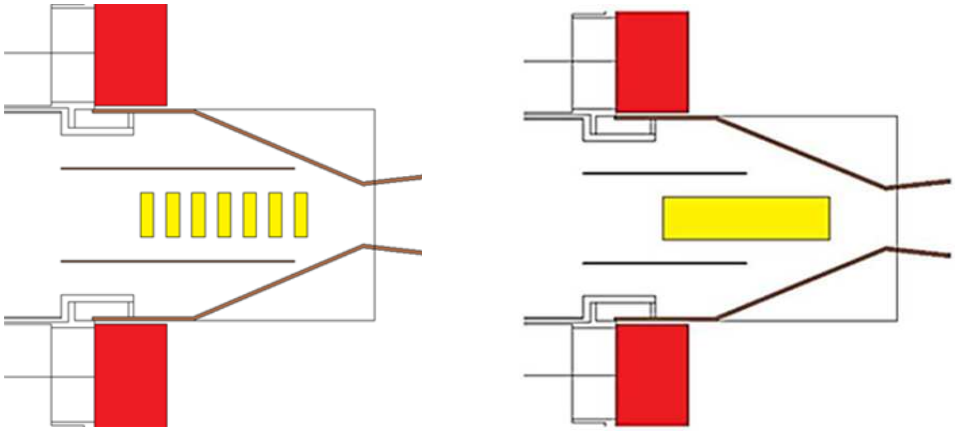

Figure 2.2: The scheme drawing of targets used in July/August 2014 the yellow part correspond to the target, the red is the RICH flange and the black is the supportingg structure. **Left:** Carbon target. **Right:** Polyethylene target.

The carbon target is divided into seven segments of cylinders that are glued to a foil and placed inside a support structure made of carbon, each segment has a diameter of 12 mm, with a length of 7.2 mm. The reason for a segmented target, is to avoid the bremsstrahlung radiation created when a high energy particle is decelerated. All of this is then placed into the beam pipe, and the vacuum is made inside. The probability of interaction beam particles with the target is approximately 1%. Depending on the HADES physics program, targets like LH_2, carbon, polyethylene, niobium, tungsten, or gold are utilized. In our case, carbon and polyethylene target was used. Properties of the targets we used are shown in Table 2.1.

Targets	Carbon	Polyethylene
Diameter (mm)	12	12
Length (mm)	46	46
Lab position center (mm)	-32.6	-32.7
Number of segments	7	-
Thickness of segments (mm)	3.6	-
Distance between segments center (mm)	7.1	-
Molar mass (g/mol)	28	12
Density (g/cm^3)	0.93	1.85

Table 2.1: Dimensions of the targets.

2.2 The Ring Imaging CHerenkov detector (RICH)

The HADES Ring Imaging CHerenkov detector (RICH), see Fig. 2.3, constitutes the innermost part of the spectrometer and is built to identify e^+e^- pairs with momenta betwenn 0.1 GeV/c $\leq p \leq$ 1.5 GeV/c. It is based in a Cherenkov effect, electromagnetic radiation is emitted when a charged particle travel with a velocity higher than the speed of light in a medium of refraction index n, (so $v > c/n$). Cherenkov photons are emitted in a polar angle related to the velocity of the particle. The opening angle is given by:

$$\cos\theta = \frac{1}{\mathrm{n}\beta} \tag{2.1}$$

$$\beta = \sqrt{1 - \frac{1}{\gamma^2}} \tag{2.2}$$

where θ is the opening angle, β and γ are the velocity and Lorentz factor of the particle respectively. We guarantee that only leptons radiate in RICH, using an appropriate gaseous C_4F_{10} radiator, with a refraction index of $n = 1.00151$ corresponding to a Cherenkov threshold $\gamma > 18.2$ allow to radiate only leptons, while hadrons with the same momentum have velocities below the threshold. For instance, to produce the Cherenkov light, the velocity β of a particle should be greater than 0.9985, which corresponds to 0.009 GeV/c for an electron, 2.5 GeV/c for pion and 17 GeV/c for a proton. The emitted Cherenkov radiation is reflected by a segmented spherical VUV-mirror and after focused onto a photon detector with CaF_2 entrance window to form rings of almost constant radius. To manage the high event rates, the photon detector consists of six MWPC operated with CH_4 and cathode pads covered by the CsI photon converter [87]. In the energy range of our experiment, i.e., 1-2 GeV, electrons have velocities close to the speed of light in vacuum, while most of the hadrons have much lower velocities and do not radiate photons in

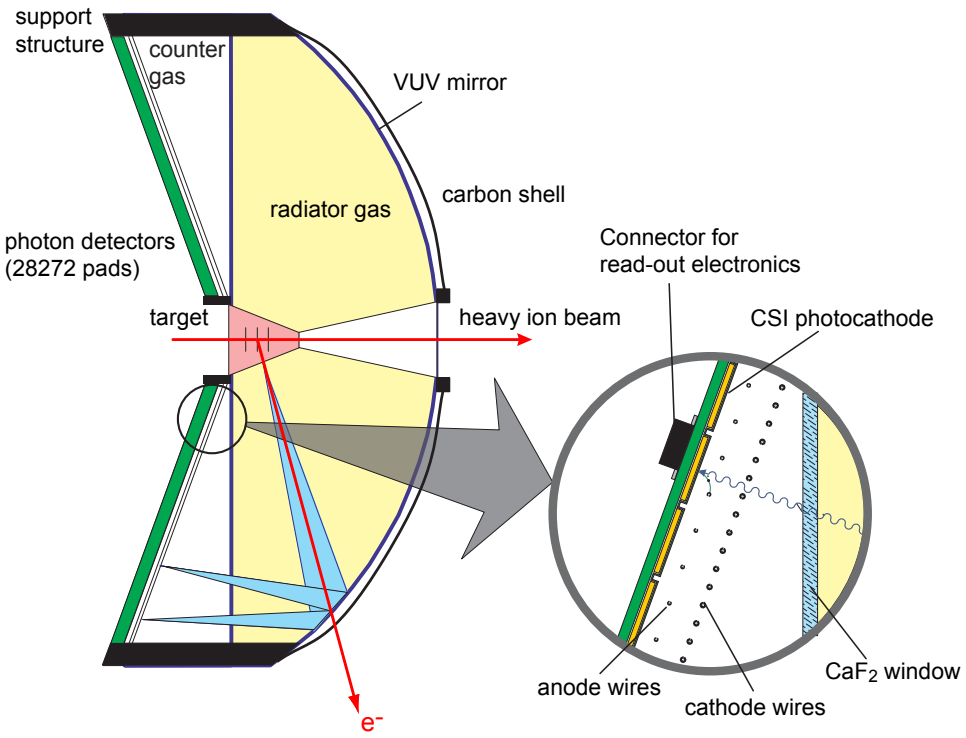

Figure 2.3: Schematic layout of the RICH, consisting of a Carbon shell mirror, a C_4F_{10} window and a photon detector.

our RICH detector. By choosing an appropriate refraction index, the Cherenkov effect becomes a reliable tool to discriminate leptons from hadrons.

The radiator gas also offers high transparency to the wavelengths down to $\lambda \geq 145$ nm, which is well suited since the produced photons are mostly at ultra-violet frequencies. The spherical carbon mirror is placed downstream of the gas radiator and reflects the Cherenkov light (average reflectivity is $\sim 80\%$) to the photon detector, which is able to detect a single photon providing information about the position. Typically, an electron with a momentum of 0.1 GeV/c produces about 110 photons along its trajectory in the radiator, but only about 20 are detected.

2.3 Tracking system

The design and performance of HADES tracking system was based in the required high resolution spectroscopy of vector mesons via decay to dileptons of $\left(\sigma_{M_{e^+e^-}}/M_{e^+e^-} \simeq 2.5\%\right)$. Also a low mass materials in order to reduce the multiple scattering and γ conversion and a high event rate to be capable of managing the large charged particles multiplicities. To satisfy these specifications, the tracking system of HADES consists of a toroidal field given by the superconducting coils and four planes of low-mass mini drift chambers (MDC) (see left panel of see Fig 2.5). It enables us to reconstruct the particle trajectories in a large range of polar angles (θ from 14° to 86°) and to determine the particle momentum with a resolution of $\Delta p/p \sim 4\%$ for protons.

2.3.1 The superconducting Magnet

The Iron-Less Superconductive Electromagnet (ILSE), see Fig. 2.4, consists of 6 superconducting coils, producing an inhomogeneous magnetic field up to a maximum value of 0.7 T within the acceptance region. This value corresponds to:

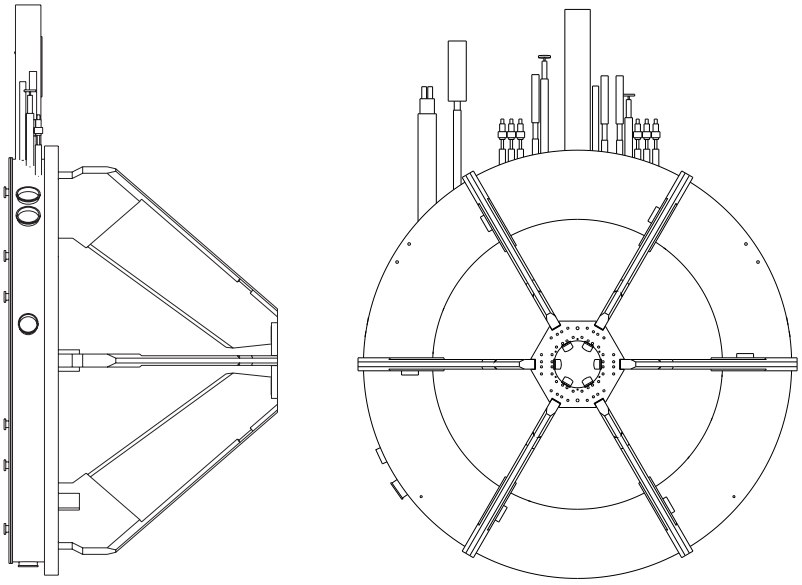

Figure 2.4: **Left:** Side view of the superconducting HADES magnet. The outer diameter of the support ring amounts to 3.56 m. **Right:** Back view

$$\int B \cdot dl \simeq 0.3\,T \;\; at\; \theta = 20^{\circ} \tag{2.3}$$

$$\int B \cdot dl \simeq 0.12\,T \;\; at\; \theta = 70^{\circ} \tag{2.4}$$

where $\int B \cdot dl$ is the integrated magnetic field. To not harm measurements of RICH and TOF detectors, the magnetic field required is below (below $5 \cdot 10^{-3}$ T) . At the maximum field, the transverse momentum kick p_k ranges between 0.03 and 0.1 GeV/c, where p_k is the difference between the incoming and outgoing momentum vectors in the plane perpendicular to the field. For instance, a charged particle ± 1 with a momentum of p = 1 GeV/c and emitted at $\theta = 20^{\circ}$, its momentum kick p_k amounts to 0.1 GeV/c (so the defection angle is $\Delta\theta = 5.7^{\circ}$).

2.3.2 The MDC detector

Like RICH detector, also the mini-drift chambers (MDC) was designed with a low material budget. Moreover, to achieve the invariant mass resolution of $\left(\sigma_{M_{e^+e^-}}/M_{e^+e^-} \simeq 2.5\%\right)$ needs a precision of $\frac{\sigma_p}{p} = 1.5 - 2\%$ in the momentum [88]. The tracking is performed by 24 trapezoidal Mini-Drift Chambers(MDC), which are symmetrically arranged in six identical sectors providing a polar angle (θ from 14° to 86°) around the beam axis, forming four tracking planes of increasing size. In each sector there are two planes in front of and two behind the magnetic field. Each chamber is composed of six sense/field wire layers (called anode planes) oriented in different stereo angles from the inner layer to the outer: +40°, -20°, +0°, -0°, +20°, -40° to have a better resolution on the polar angle respect with the azimuthal one, (see right panel of Fig. 2.5).

There are also seven cathode wire layers (called cathode planes) so that each sense/field wire layer is in between two cathode planes. For MDC IV, the gap between the anode plane and the cathode plane is 5 mm. The space between anode and field wires defines a drift cell. All four chambers contain about 1100 drift cells, each with size on average varying from 5 x 5 to 14 x 10 mm^2 from the plane I to plane IV to achieve a constant detector occupancy. In each chamber, the windows consist of aluminized Mylar foils. Inside the chamber, a different gas mixture is circulated during operation with an overpressure below one millibar, see Table 2.2.

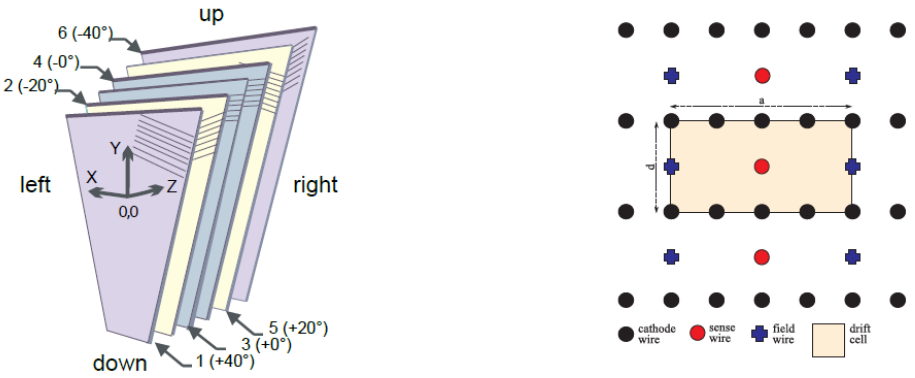

Figure 2.5: Schematic layout of the HADES tracking system. **Left**: Arrangement of the MDC chamber with respect to the magnetic coils. **Right**: View of the six anode wire frames inside a HADES MDC, with the respective wire angles.

MDC Plane	I	II	III	IV
Counting gas	Ar:CO_2 = 70:30	Ar:CO_2 = 70:30 + H_2O	Ar:Isobutane = 84:16	Ar:Isobutane = 84:16
Gas flow	~15 l/h	~15 l/h	~25 l/h	~25 l/h

Table 2.2: Gas mixture for each MDC plane.

A drift cell is defined by the space between the anode and the cathode wires, when a charged particle passes these drift cells, it ionizes the gas and produces electron/positive ion pairs along its trajectory. The electrons move towards the anode wires and produce further ionization especially close to the anode wire. The collected charges induce a signal on the anode wires. For each hit wire, the corresponding drift times depend on the minimum distance of the particle trajectory from the wire. Note that the relation between drift time and the drift distance is not linear in our case since the electric field is not constant in the drift cells, and it is calculated by a Garfield simulation [89].

2.4 META detectors

The Multiplicity Electron Trigger Array (META) system is positioned downstream behind the outer MDC's and is used for particle identification and triggering. The system is formed by two sets of time-of-flight detector (TOF+RPC) and an electromagnetic shower detector.

2.4.1 TOF wall

Time-of-Flight wall TOF subdetector was developed to select rare events of dileptons pair. The TOF wall is denoted to three main objectives:

- Fast determination of the charged particle multiplicity of the event to select central collisions.
- Fast tracking, by determining the impact position of each hitting particle, to allow a fast second level trigger decision about the event.
- Measurement of the TOF of each particle detected, to separate electrons and positrons from the more massive particle.

The TOF detector covers polar angles from 44° to 88°. Its functionality is based on a scintillating rod element structure. It consists of 384 scintillator rods (6 sectors, each consisting of 64 rods), each rod is read-out at its two ends by a photomultiplier (PMT). The selected scintillating material is BC408 from Bicron, mainly due to its good attenuation length combined with high scintillation efficiency ($\approx 10^4$ photons/MeV) and speed (2.1 ns decay time). The lengths of the rods go from 100 mm to 200 mm, for the 200 mm a cross section of 30 x 30 mm^2 with a bending angle of 65°, and for the 100 mm a cross section of 20 x 20 mm^2 with a bending angle of 67.5°. TOF granularity has been paired to the charged-particle multiplicity angular distribution reducing the probability of double hits (two particles emitted in the same direction hit the same rod) to less than 10%. With this setup a TOF and position resolution of $\sigma_{\mathrm{TOF}} \leq 150$ ps and $\sigma_x \leq 25$ ps is achieved [90].

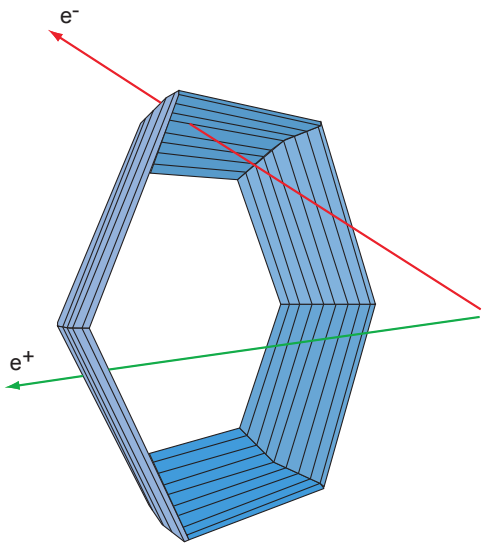

Figure 2.6: Layout of the TOF detector showing the detection of an electron and a positron in two different sectors

From the measured signals the time-of-flight (t_{tof}) of a particle, its hit position (x) along the rod the and the deposited energy (ΔE) can be extracted:

$$t_{tof} = \frac{1}{2}\left(t_L + t_R - \frac{L}{v_{group}}\right) \tag{2.5}$$

$$x = \frac{1}{2}\left(t_R - t_L\right) v_{group} \tag{2.6}$$

$$\Delta E = k\sqrt{a_L \cdot a_R \cdot e^{L/\lambda_{att}}} \tag{2.7}$$

Where t_L and t_R are the time interval between the signal in the start detector and the signal generated in one of the two multipliers a_L and a_R are the corresponding light signal amplitudes, v_{group} is the average group velocity of the light in the rod, λ_{att} is its attenuation

length, L is the length of the rod and k a proportionality constant. TOF information is used to distinguish between particles with the same momentum but different mass. In Section 4 a detailed description of the time-of-flight measurement and the calibration procedure will be described.

2.4.2 RPC wall

A Resistive Plate Chamber (RPC) was installed at HADES in 2008 to replace the low granularity scintillator TOFino, which covered the low polar angles missed by TOF. It measures the time-of-flight measurements at forwarding polar angles between 18° to 45°. The requirements of its design are listed below:

- Divided into six RPC sectors to cover the HADES geometry.
- Efficiency above 95% for single hits.
- Time resolution below 100 ps for minimum ionizing particles MIP, to allow separation between $e^{\pm}$, $\pi^{\pm}$ and K^{+}.
- Rate capability up to 1 kHz/cm^2 in the innermost part.
- Low probability of secondary particle production.
- High granularity and highest hit loss probability under 20% for the heaviest system's central collisions.

Each sector consists of two layers of overlapping RPC cells with different lengths. In total, 1116 cells are installed. A single RPC cell consists out of a sandwich of three Aluminum and two glass electrodes, which carry a potential of 5 kV. They are enclosed in an Aluminum box. The cell is filled with a gas mixture of SF_6 and $C_2H_2F_4$. The cell layout of the HADES-RPC and a schematic drawing of a RPC sector are shown in Fig. 2.7 [91]. Charged particle crossing the detector interact trough Coulomb force with the electron of the gas. The energy transferred to the atoms gives them a state of ionization or excitation. The applied high electric field between the electrodes in the detectors accelerates the unbound electrons producing an avalanche, then ions and electrons drift to the electrodes creating an induced current that can be registered by the acquisition equipment. It was observed that the efficiency rate capability and time resolution could be improved, combining several RPC layers to a so-called multi-gap RPC. Each cell was electrically shielded, allowing an excellent multi-hit capability.

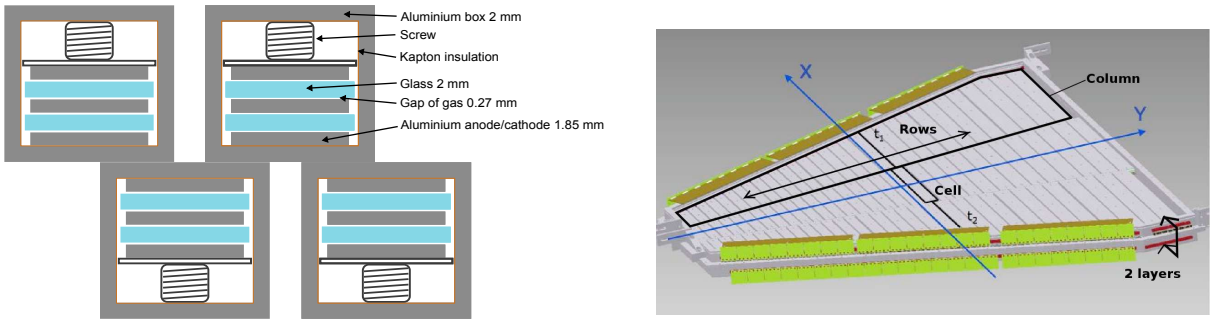

Figure 2.7: **Left**: The HADES multi-gap RPC cell layout and their ingredients. The cells are aligned in two overlapping rows. **Right**: A schematic drawing of a RPC sector. The cells have smaller sizes at smaller polar angles and fill the trapezoidal support frame.

2.4.3 Pre-Shower detector

The main propose of the Pre-Shower detector is to identify dileptons by its electromagnetic shower. The Pre-Shower detector is mounted behind the RPC detector and covers polar emission angles from 18° to 44°. It is composed of a stack of three trapezoidal wire chambers with a pad read-out separated by two lead converters. As shown in the left part of Fig. 2.8, when a charged particle goes throw the gasses, it ionizes producing an ionization avalanche, where the electrons drift to the nearest anode wire. Lepton/hadron discrimination is performed by comparing the number of particles measured in the front and behind the lead converters. The wire chambers are filled with an isobutane-based gas mixture and are operated in the limited self-quenching streamer (SQS). The SQS mode ensures that an avalanche charge depends weakly on the particle specific energy loss because of the charge saturation effect limiting the chamber gain. In this mode, the avalanche charge does not depend on the particle energy loss, but it is only proportional to the number of particles crossing the chambers [92]. The pads are settled into rows, 32 per chamber, which are connected to front-end electronics boards, based on a dedicated ASIC chip, which represents a 32-channel charge amplifier/shaper with output multiplexer, and digitization with an 8-bit ADC. For future experiments, the Pre-Shower detector will be replaced by an Electromagnetic Calorimeter. A detailed description is shown in Section 10.

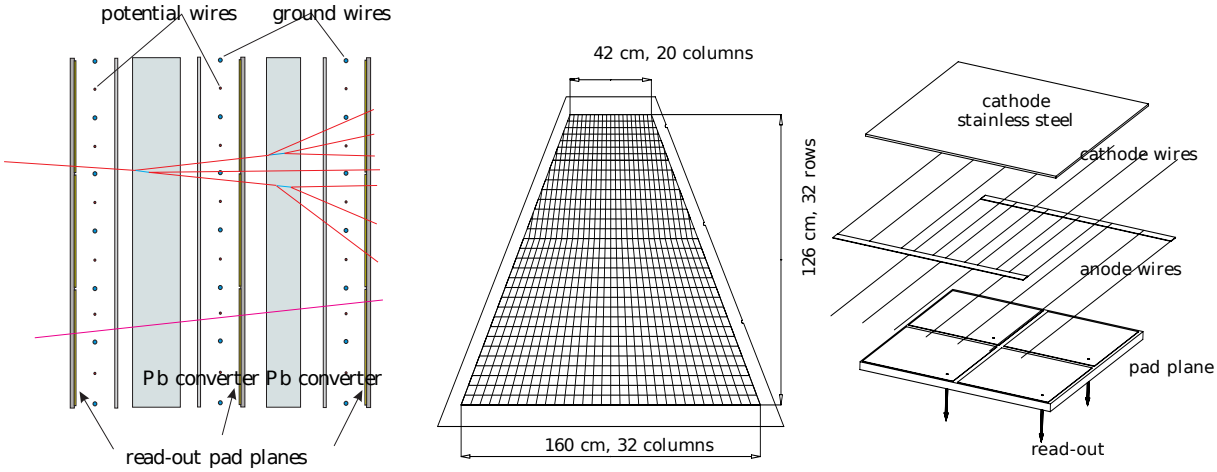

Figure 2.8: **Left**: Schematic drawing of a chamber of the Pre-Shower detector. The position sensitive pad plane with 942 pads is shown. **Right**: Side view of the Pre-Shower detector. Three gas chambers and two lead converters (one sector) are shown. Lepton/hadron discrimination is performed by comparing the charge signal measured in the front and behind the lead converters [92].

2.5 Pion beam

The pion beam is a secondary beam added to the already available primary beam of proton and heavy ions at GSI. The pions are produced with the collision of a proton or heavy-ion from the SIS18 with the production target. After the produced pions are transported from the production target to the HADES target by a beam line composed by 9 quadrupole and 2 dipoles magnets, located 33 m downstream, see Fig. 2.10. In our case, the SIS18 synchrotron provided a primary N_2 beam at E_{kin} = 2A GeV which generated the pions in a 10 cm thick target of beryllium, with an intensity close to the space-charge limit of $0.8 - 1.0 \cdot 10^{11}$ ions/spill. The pion

current after the last quadrupole, before HADES target, has a maximum of about 10^6 ions/spill at $p_0 = 1.0$ GeV/c and decrease a factor 2 for $p_0 = 0.7$ GeV/c and $p_0 = 1.3$ GeV/c. Therefore, the pion beam momenta depend on the primary beam momentum and on the production target and its geometry [93].

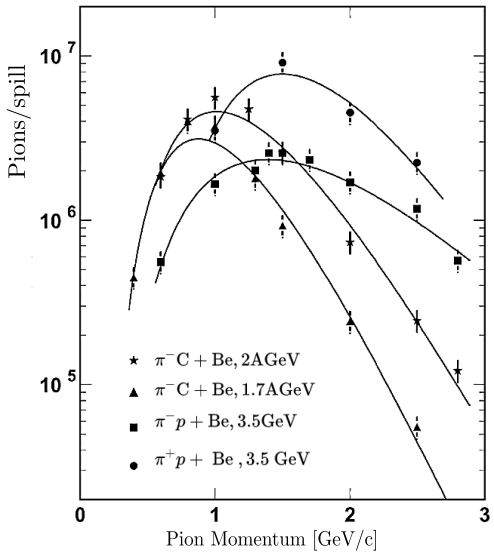

Figure 2.9: Pion intensity measured for p and ^{12}C targets with different primary beams energies as a function of the central momentum of the beam-line. The primary beam intensities correspond to the maximum intensity to be extracted from SIS, i.e.1.7×10^{11} protons/spill and 5×10^{11} carbon ions/spill, respectively. The solid curves represent fits to the data [94].

Along with the pions, other particles are produced, like electrons, muons, and kaons, which constitute the secondary beam's dominant contamination. Electrons with certain momentum are mainly created by the decay of neutral pions at the production target. The pions can decay by Dalitz decay ($\pi^0 \rightarrow \gamma e^+ e^-$) $BR = 1.17\%$ or via the two photon channel ($\pi^0 \rightarrow \gamma\gamma$ with $BR = 98.8\%$) followed by pair conversion. To find the fraction of photons that could convert a simulation of the reaction N+Be was carried out to find out the electron/pion ratio. It was found that electron contamination by at HADES target position was 9.6% and 0.84% for 0.7 GeV/c and 1.7 GeV/c pion beam momenta respectively. Muon directly decay from in-flight leptonic decay ($\pi^- \rightarrow \mu\bar{\nu}_\mu, BR = 99.99\%, c\tau = 7.8\text{m}$). The effective decay lenght for 0.7 GeV/c and 1.7 GeV/c are 39.3m and 95.4m, therefore many pions decay before the target position. For both pion beam momenta an estimation of muon/pion ratio of 0.65% and 0.75% was found out. Negative kaons can be produced through the reaction $NN \rightarrow NNK^+K^-$; the kinematical threshold of this reaction is 2.5 GeV, so the production is very rare. Moreover, due to its high mass, most of the kaons will decay before the pion tracking detectors and finally, HADES [93]. The contribution of lepton-induced nuclear interaction does not contribute significantly to the HADES data, due to the small cross-section compared with the pions. However, their interaction with the START detector may affect the normalization and cross-section determination for the reaction rate of interest, which it is an information we need to consider if it is used in the experiment [93].

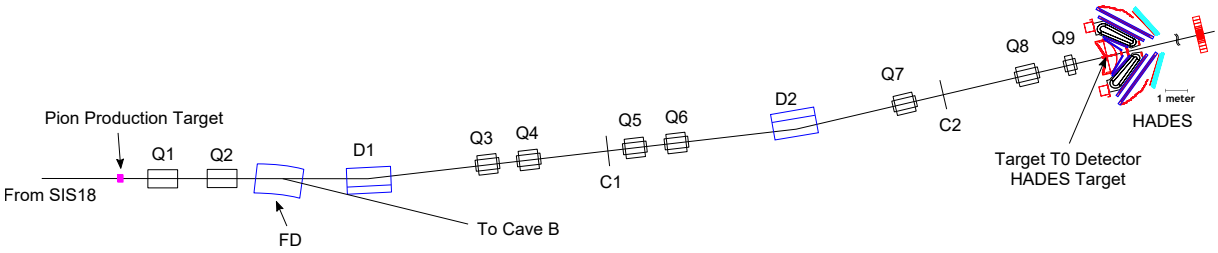

Figure 2.10: Schematic drawing of the pion beam-line between the pion production target and the HADES cave. All magnets and detectors are indicated by: dipole magnets (D), quadrupoles (Q), tracking detectors (C1,C2) and the target T0 detector [93].

2.5.1 Beam detectors

In all HADES experiments a target T_0 detector is required for a beam profile optimization and to provide a fast timing signal to trigger objective, and last, for measurement of time-of-flight. The detector is located close to the target (START) to minimize beam interaction and resulting in charged particle hitting the sensitive RICH photoelectron detector. In some configuration also in the exit of the RICH (VETO), just behind the target which is used as a trigger logic for event selection [93]. In special, for the pion-beam experiment the detector needs to satisfy the next specifications:

- Good timing precision $\delta t \leq 100$ ps for particle identification via time-of-flight.
- Operation stability for particle fluxes $J \geq 10 \times 10^6$ cm^{-2}s^{-1}
- Detection efficiency for MIPS $\epsilon \simeq 100\%$
- Low material budget
- Reasonable position resolution of $\delta x <$ 1mm for tracking support and vertex reconstruction
- Vacuum operation
- Active area $A = 1$ cm^2

START detector

A mono-crystalline diamond material produced with the process of Chemical Vapor Deposition (CVD) matches the criteria of a detector establish above. The START detector, see Fig. 2.11, consists of nine diamond sensor array with an active area of $A = 4.3 \times 4.3$ mm^2 support on two boards, each with 5 and 4 sensors. To avoid multiple scattering and the required signal-to-noise, a 300 μm thickness has been chosen.

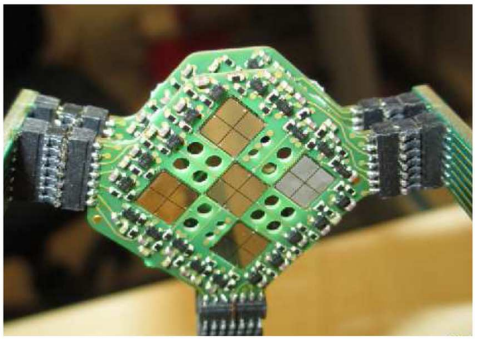

Figure 2.11: Photograph of the T0 detector taken from [93].

The performance achieved in a proton beam experiment is shown below:

- Bias voltage $U_{bias} = 200$ V
- Rise time $(10\% - 90\%)$ 1.35 ns.
- Signal/RMS noise ratio: 30 : 1
- Expected timing precision: < 100 ps .
- Preamplifier power consumption: 1.65 mW/ channel, in total: 60 mW .
- Horizontal and vertical pixel resolution (σ) : 0.7 mm each.

CERBEROS detector

Two planes of sensitive silicon strip detectors (C1 and C2) are placed in the beamline between the production target and the HADES target, form the so-called CERBEROS system, see Fig. 2.10 [95]. Both detector are installed to measure the momentum of each beam particle. More details will be described in Section 3.2.

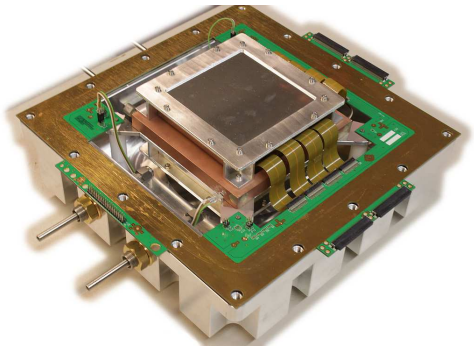

Figure 2.12: Photo of single tracking station with removed upper halve of the detector chamber with the silicon detector in the center [93].

2.6 HADES Data Acquisition Network and trigger

In 2011 the HADES trigger and data acquisition system was upgraded. The main purpose was to increase the event rate capability by a factor of up to 20 to reach 100 kHz in light collisions systems and 20 kHz in heavy-ion reaction systems. The total data rate written to storage is about 400 MByte/s in peak [96]. All the subdetectors use the same network setup to simplify integration, maintenance, and development. They are connected to the HADES Data Acquisition (DAQ) network, all electronics are based on platforms equipped with Field Programmable Gate Arrays (FPGA) with optical links inside the detector, and a commercial Gigabit Ethernet infrastructure to transport the data to the server farm. The registered data is transported in a common network based on the TrbNet protocol [97]. A sketch of the complete DAQ system is given in the left Fig. 2.13. The trigger and the read-out process are controlled by a central instance, the Central Trigger System (CTS). The CTS is supplied with fast input signals from different detector sub-systems. Based on these signals, a trigger decision is made. Based on the trigger decision, a total of four servers with two event builders analyzed and wrote the files in the local storage as HADES list-mode data (HLD).

Usually, a two-level trigger system is used in HADES experiments:

- 1^{st} First level trigger (LVL1) is a fast selection of central collisions by measuring the hit multiplicity in META systems.

- 2^{nd} The second level trigger (noted as LVL2) [98] is based on an online search for lepton candidates in the event. (ring in RICH and META matching)

Due to the low rate of interactions for the pion beam experiment, only LVL1 trigger was required, requiring a multiplicity with 2 hits in the META detector with a coincidence in START detector. In the last $\pi^- A$ beam time in 2014, which correspond to the current analysis in this thesis, the DAQ was recording with a trigger rate of 2 kHz and a data rate of 200 MByte/s.

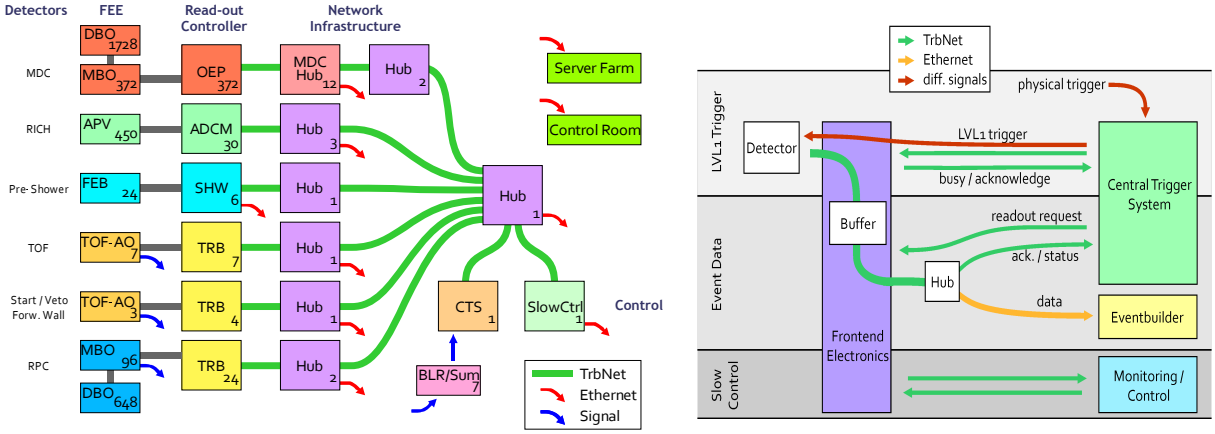

Figure 2.13: **Left**: A schematic view of the full network setup. The network has a tree-like structure, connecting all detector with the central control system. The numbers show the amount of boards of each type. **Right**: Several types of data and information are transported in parallel using one common network setup [99].

Chapter 3

Data analysis and particle reconstruction

Nowadays, experiments with heavy-ions collisions produced a high amount of data which has become a challenge in terms of processing and analyzing the obtained data. HADES can produce and record data with high event rates. This is possible because the analysis is made with the HYDRA framework (**H**ADES s**Y**stem for **D**ata **R**eduction and **A**nalysis) [100], which is completely based on the `C++` class package ROOT [101], an object-oriented data analysis framework. ROOT software was developed at CERN and become the standard software for nuclear and high energy physics; it provides a wide useful tool for retrieve store and displays the data in a very efficient way. HYDRA is a structure compounding many libraries that can be linked, and which basic unit is the *event* either simulated or experimental. It also contains a classes for the data analysis, event reconstruction, and for the detector specific duties. The parameters of the calibration, initialization, and geometry of the setup are stored in HADES data-based implemented ORACLE DB. In this chapter, it will be described the complete flow analysis from raw data to reconstructed track candidates for experimental and simulated events, see Fig. 4.5.

Experimental data

In the Section 2.6, it was mentioned already how the uncalibrated data is storage in HLD files. However, to reconstruct the events from experimental data, several steps needs to be accomplished. In the case of the experimental data, the data is first stored in the so called *Raw Level* in the HLD files. Also, when the values obtained from the detector are translated to physical values, the *Cal level* is reached. The information of the impact of a particle in a detector is given by the *Hit finder* and thats fill the *Hit level*. In the *Track level*, the following analysis steps will not modify the data but only enrich the additional physical information, such as the polarity, matching quality, momentum, and finally, the final particle identification.

Simulation data

Usually, simulated events are generated with Quantum Transport Models (BUU or UrQMD) [102], in my case it was done with a thermal model (PLUTO) [103], which is a Monte Carlo event generator. PLUTO provided information about energy, momentum, impact parameter and the identity of a particle. After, the events are tracked in the HADES detector by HGEANT, which is a HADES simulation package based on GEANT [104]. HGEANT include all the geometry, material budget, magnetic field interaction with HADES, production of secondary particles,

scattering, and energy losses by interaction with the material of the detectors. The signal obtained from the detector response on the interaction with a detected particle is smeared in the simulation with the *Digitizers* simulating the calibrated real detector readout. This information fills the so-called *Sim Cal level* which is the corresponding to the *Cal level* to the experimental data. Subsequently, the experimental and simulated reconstructed events are saved as data summary tapes (DST), which are used as input for event reconstruction. After this stage, both experimental and simulation data are used in the same way besides the steps of the analysis. The realistic simulated data can be used also to improve the efficiency corrections of the real data.

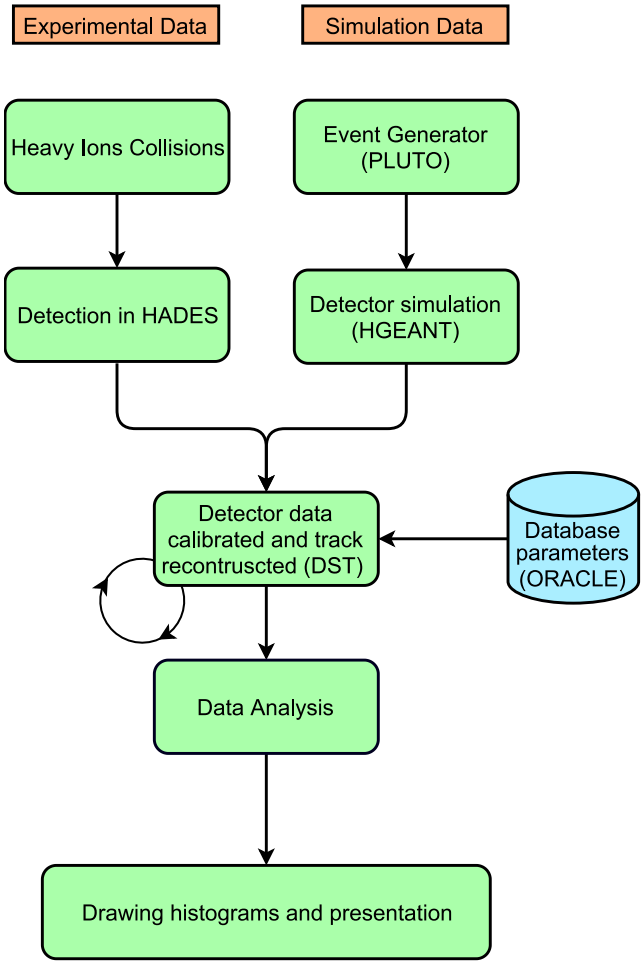

Figure 3.1: Flow analysis of experimental and simulation data.

3.1 Beam Time Facts and Numbers

In July and August of 2014 HADES experiment was effectuated with $2 \cdot 10^5$ pions per spill on the HADES polyethylene (PE) and carbon (C) target produced by a few 10^{10} primary nitrogen ions. Events have been processed with data rates of 2 kHz and a 50% duty cycle. We needed 36 shifts with an average of 14 h beam on target per day. At a pion momentum of 0.7 GeV/c it was obtained 500 reconstructed e^+e^- pairs in the channel $\pi^- p \to n e^+ e^-$, and 1000 from quasi-free reactions on carbon in the PE target. The collected statistics for the July/August 2014 pion

beam run are summarized in Table 3.1.

Target	p_{π^-} [MeV/c]	Events (10^6)	Data Taken (h)
Polyethylene (PE)	690	774.7	175.56
Polyethylene (PE)	748	76.5	11.61
Polyethylene (PE)	656	42.4	14,08
Polyethylene (PE)	800	52.4	7,48
Carbon (C)	690	115,7	13,06
Carbon (C)	800	41,2	6,27
Carbon (C)	748	42,2	6,8
Carbon (C)	656	41,9	14,75

Table 3.1: Collected statistics for beam time Aug14/Sep14.

3.2 Pion beam momentum reconstruction

For the analysis of exclusive channels, the precise measurement of pion beams momentum is essential since it determines the missing mass resolution. As we mentioned already in Section 2.5.1, two sensitive silicon detectors were placed in the beam line before the HADES target point for track reconstruction of the pion beam, the so-called CERBEROS system [95]. The method to reconstruct the pion observables is an event-by-event basis. The beamline between the production target and the HADES target is called pion chicane, see Fig. 2.10. Measuring the particle positions using the dedicated CERBEROS tracking system at two locations along with the chicane, and removing third-order effects, the transport equation can be solved by an iterative method and the position of the pion at the HADES target can be obtained. The pion momenta were reconstructed with a resolution from 0.1% to 0.3% over the acceptance window. In the first and second tracking stations, the effect of multiple hits due to high beam load and noise becomes visible and needs to be removed, see left of Fig. 3.2.

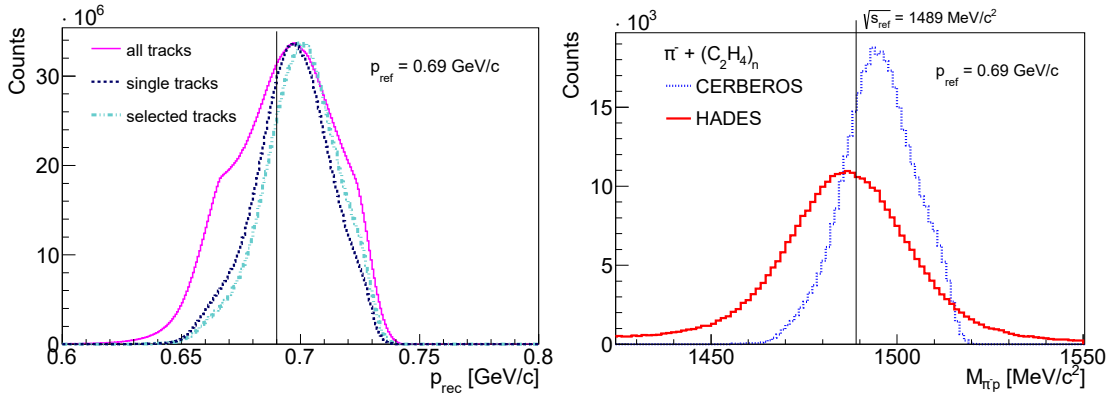

Figure 3.2: **Left**: Momentum reconstruction distributions for tracks from all hit combinations (purple), for single hit tracks (dark blue), and for selected tracks (light blue) at a a central beam of 0.69 GeV/c. The curves are normalized to the same peak maximum value. **Right**: Energy $\sqrt{s}$ distributions obtained for elastically scattered pion-proton pairs (red) and from pion beam momenta (blue) assuming a nominal central beam momentum of 0.69 GeV/c [93].

The suppression of fake tracks becomes essential because the measurement of the pion momenta allows for a precise reconstruction of the total center of mass energy of pion nucleon

interactions. With the purpose of verify the reconstruction of the incident pion momenta, the elastic scattering of π^-p in the polyethylene target $(PE, (C_2H_4)_n)$ was used. First, the pion momentum is reconstructed using time of flight measurements from T_0 and META detectors, and hits from the MDC tracking system . In an elastic scattering process, the invariant mass of the π^-p measured from HADES detectors is the same as the center-of-mass energy $\sqrt{s}$. In that way, we can determine the pion momenta independently from the CERBEROS tracking system. In Fig. 3.2 it is shown the center-of-mass energy $\sqrt{s}$ from π^-p elastic scattering and from pion beam momenta with a nominal momentum of 0.69 GeV/c. Mean value of the invariant mass is $M_{\pi p} = 1487$ MeV/c^2 with a width of $\Delta\,(M_{\pi p}) \simeq 33$ MeV/c^2(FWHM), we observer a high value from ($\sqrt{s} = 1496$ MeV) with a width distribution of ($\Delta(\sqrt{s}) \simeq 18$ MeV(FWHM)), a factor 2 smaller, which is a 1.7% of pion momenta, the simulations using transport coefficients expected a value of 1%. The differences may come from the vertical transport coefficients, which could not be measured. Also, it has to be mention that both distributions were obtained for a short period within good beam time conditions. Moreover, systematic discrepancies are due to the vertical or horizontal shift of the beam positions, adjustments of the dipoles, or energy loss effects. Simulations done with GEANT4 do not explain the discrepancies with an energy loss scenario. The difference may come from a shift of the reference momentum due to an error in the relation current in magnets and the integrated magnetic field, which provides the invariant mass spectrum obtained from HADES, that it is an independent measure of the pion beam momentum. The absence of a shift in the 1.7 GeV/c corroborates this interpretation. The offset observed in the pion beam momentum reconstructed has been corrected in the further data analysis, and gives a pion momentum average of 0.684 GeV/c. For the carbon target, the correction was introduced in the uncertainty on the center-of-mass energy with a value of 5 MeV/c^2.

3.3 Track reconstruction

The reconstruction of the tracking particles is done by the Mini Drift Chambers (MDC) and the super-conducting toroidal magnet called as Iron Less Superconducting Electron magnet (ILSE), explained in Section 2.3.2. When a charged particle entry an MDC drift cells, it ionizes the gas and produces electron/positive ion pairs along its trajectory, which moves towards the anode and cathode wires of the drift chamber. That is the general working concept to define just one hitting point on an MDC plane, which does not describe the full tracking reconstruction. The combined mode of the two inner (MDC I/II) and outer (MDC III/IV) planes, produces two hitting points for each charged particle traversing the detector in each MDC plane. As a result, interpolating the two points, a straight track appears, called segment. Additionally, the many MDC wires can lead to a fake combination of hit points, so it is necessary to employ a selection criteria method to avoid fake tracks. Finally, using the information about the two segments and the magnetic field strength, the momentum and the particle track can be reconstructed.

3.3.1 Clusters Vertex

The first to determine it is the hitting points in the inner (MDC I/II) segment, which will define the vertex position of the particle to be tracked. Using the projection of the wired distribution from MDC I and II, the cluster vertex is defined. In that process, many wires are fired, so in order to find the accurately hitting point in the MDC, the projection with the best size and amount of cluster is defined as a cluster vertex, as we can observe in Fig. 3.4. Only the z-vertex position in the target is defined. With the aim to improve the resolution about the fired drift cells, the drift time is also used. In principle, the tracking reconstruction procedure

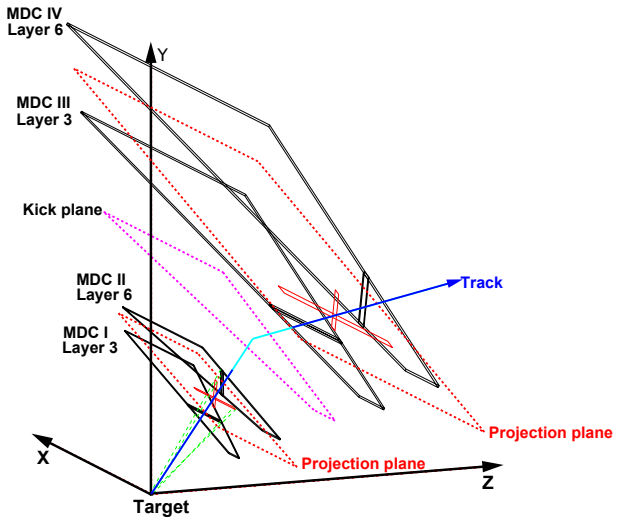

Figure 3.3: Track candidate search procedure. Only one layer out of six is shown per each MDC module. Four MDC and two projection are shown between the kick plane [46].

search for one hitting point in the inner (MDC I/II) segment and one or more in the outer (MDC III/IV) defining two projection planes.

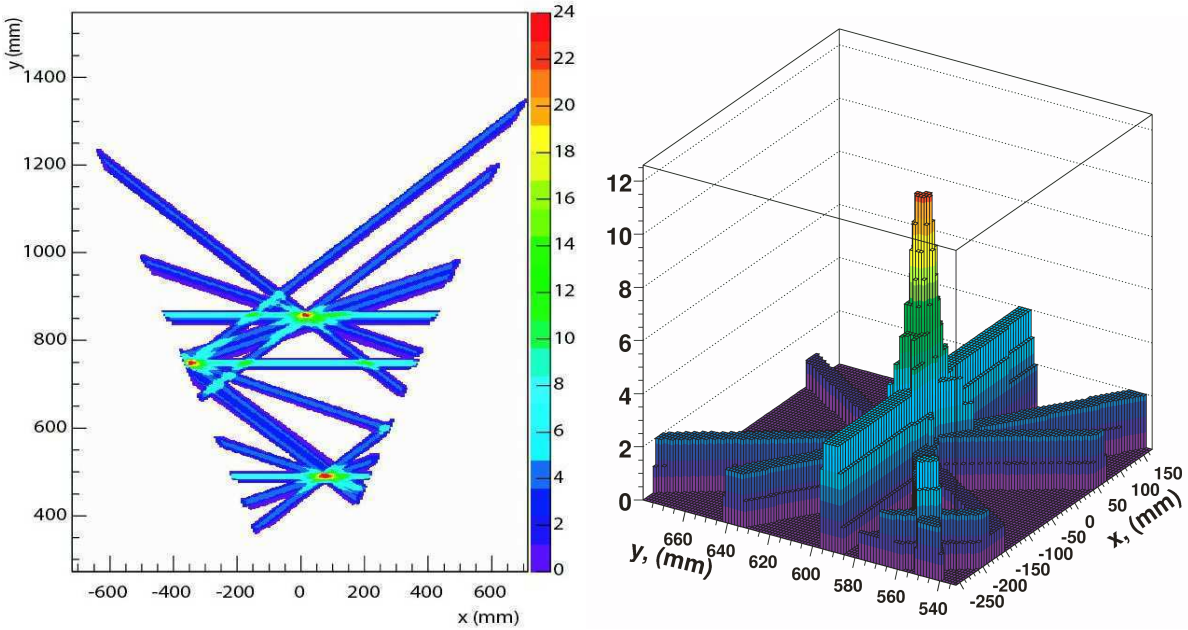

Figure 3.4: **Left:** Projection in $x-y$ coordinates for MDC layers in the cluster finder procedures. **Right:** Projection of the cluster in the $x-y$ plane where the local maximum clearly emerges like a cluster [46].

3.3.2 Inner segment

Once the cluster vertex is defined, the clusters from the inner MDC (I/II) are reconstructed. In that process, many wires are fired, so to find the accurately hitting point in the MDC,

the projection of the volume of a drift cell, which is defined as the space volume between the anode and the cathode wires, are projected between the common plane of MDC I and II. The correlated wire positions will emerge as a local maximum, also referred to as a cluster. Using these criteria, fake contributions are already removed from the real cluster vertex. After, the projections of the produced clusters are compared with an imaginary straight line segment, and the emerging tracks from the clusters which deviate less from this straight line are selected, this selection is called as the pre-fit procedure. At that point, there is no information about a vertex position included. A better segment is obtained by the segment fitter procedure, which will be described in Section 3.3.4, which improves the spatial resolution using the drift time information. A segment obtained from a cluster produced with at least nine layers is accepted for the track reconstructing procedure. Finally, the inner segment is defined connecting the two points from the clusters projecting plane of MDC (I/II) and the cluster vertex.

3.3.3 Outer segment

The procedure to determine the outer segment is similar to the inner segment, with the difference that the vertex position in the target can not be used as the initial viewpoint for the projection of the MDC planes. Instead, the so-called kick plane is obtained. The deflection of a charged particle moving in the influence of a magnetic field can be defined by a one-point momentum kick, the virtual plane that contains this point between the MDC (I/II) and MDC(III/IV) is defined as the kick plane. Once the hit point is defined in the kick plane, it is used as a vertex for the projections of the clusters between the MDC(III/IV). Also, at this stage, fake tracks are removed. Similarly to the pre-fit procedure for the inner segments, the tracks closer with a imaginary straight line are used within the information of the drift times to finally select them as track candidates.

3.3.4 Segment fitter

The segment fitter procedure can improve the spatial distribution of the track candidates from a few mm to 0.1 - 0.2 mm using the drift time information from each drift cell. The coordinates of the track can be fitted to a track model, where the drift time is converted into a distance to the sense wire. This distance-time correlation is obtained from Garfield simulations [89]. The drift cell inis modelede in two dimensions, and the track of a particle is described by the minimum distance to the anode wire d_{min} and the impact angle θ. The segments obtained in the previous analysis are fitted to the drift time information using a function $F = (d_{min}, \theta)$, which is minimized for each drift cell.

3.3.5 Matching MDC-META detectors

Matching algorithms are used to enrich the information about the reconstructed tracks. Information obtained from the Multiplicity Electron Trigger Array (META) detectors, including TOF and RPC, is combined with the MDC track information from the outer and inner segments. From a track reconstructed segment from the outer MDC, one can build a straight line, assuming that there is no effect from the magnetic field outside the tracking system. Hit position from the META detectors can be combined and compared with the intersection of the straight line from the reconstructed outer segments of the MDC, see Fig. 3.6. Using that information, the matching quality parameter `MetaQa`, is defined as the squared deviation between the reconstructed track

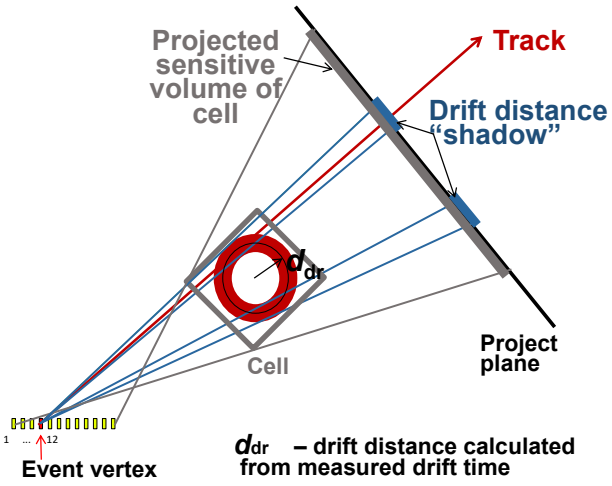

Figure 3.5: Scheme of the improvement in the resolution using the drift time measurement. It is shown the size comparison between the full size of the cell and the cell using the drift distance. The drift time information translates to drift position using Garfield simulation decrease the size of the projection and as a consequence increase the resolution of the measurement [46].

from MDC and the hit in the META detectors normalized by their errors.

$$\texttt{MetaQa} = \sqrt{\left(\frac{x_{TOF} - x_{Int} - x_{shift}}{\sigma_x}\right)^2 + \left(\frac{y_{TOF} - y_{Int} - y_{shift}}{\sigma_y}\right)^2} \tag{3.1}$$

where x_{TOF} and y_{TOF} are the coordinates of the TOF hits, x_{Int} and y_{Int} are the coordinates of the intersection from the outer MDC segment and TOF module, σ_x and σ_y resolution of TOF hits, and the parameter x_{shift} and y_{shift} are introduced to center around zero the residuals.

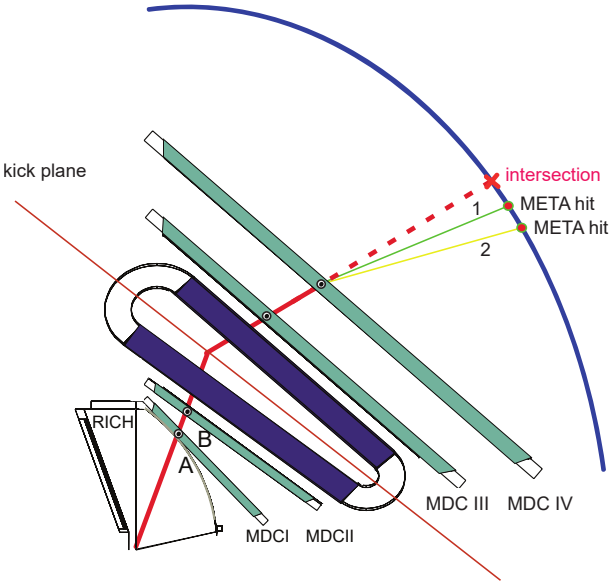

Figure 3.6: Track candidates matching with META detector [46].

In y-direction the measurement in META detectors is uniform and is taken as a boundary condition. It is restricted to straight lines to the dimension of the rod or cell of 4 mm which

scales inverse to the momentum of the particle, for low momenta particles this reduce Eq. 3.1 to:

$$\texttt{MetaQa} = \frac{x_{TOF} - x_{Int} - x_{shift}}{\sigma_x} \tag{3.2}$$

3.4 Momentum reconstruction

Once the particle track is obtained, the momentum can be reconstructed using the particle's trajectory and its deflection due to the magnetic field, based on the Lorentz force:

$$\vec{F}_L = q(\vec{v} \times \vec{B}) \tag{3.3}$$

where $\vec{v}$ is the particle velocity and $\vec{B}$ is the magnetic field. The total momentum change of the particle $\Delta\vec{p}_{tot}$, is given by the difference between the incoming $\vec{p}_{in}$ and $\vec{p}_{out}$:

$$\Delta\vec{p}_{tot} = \vec{p}_{out} - \vec{p}_{in} = \int d\vec{p} = \int \vec{F} dt = \int q\left(\vec{v} \times \vec{B}\right) ds = -q \int \vec{B} \times d\vec{s} \tag{3.4}$$

where the reflection angle is given by:

$$\sin\left(\frac{\Delta\Theta}{2}\right) = \frac{\Delta\vec{p}_{tot}}{2\,|\vec{p}_{tot}|} \tag{3.5}$$

One can see that the difference of the momentum is dependent only on the magnetic field.

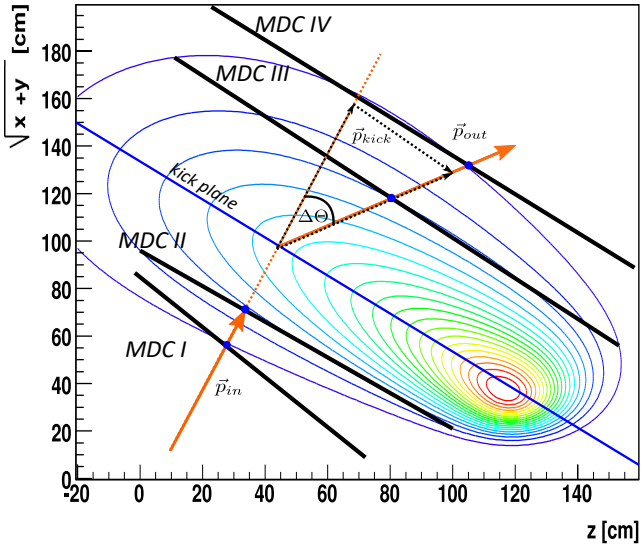

Figure 3.7: Schematic sectional drawing of the magnetic spectrometer and the deflection of a particle affected by the magnetic field. In the realistic case the particle trajectory indicated by the orange line gets deflected in the full magnetic field area, also in between the MDC planes I/II and III/IV, respectively. The kick-track method neglects this continuous deflection; instead, a one-point deflection at the kick surface is assumed. Also, the spline procedure only describes a step-less deflection between MDC II and III. The most accurate is provided by the Runge-Kutta method where the particle trajectory is reconstructed iteratively by solving the equation of motions with a variable step size. [46; 105].

HADES analysis used three algorithms to reconstruct the particle momentum; the main differences come from computing time and momentum resolution. The fastest is the kick plane method, already mentioned in Section 3.3.5. This method supposed the deflection of the particle in a single kick, in the kick plane, after, the track of the particle follows a straight line before arriving the META detectors. The kick plane offers the simplest and fastest computing time, moreover, one of the advantages is that the momentum reconstruction can be done with only the META position information, the momentum resolution σ_p/p goes from about 2% for 0.15 GeV/c electrons, up to $15-18\%$ for 1.4 GeV/c electrons. The *spline method* use the track candidates from the outer segments and apply a cubic spline function in the $(z, r = \sqrt{x^2+y^2})$ plane that match the trajectory of the particle passing the detector using hits coordinates from the MDC's. The cubic spline function is minimize and the momentum of the particle is estimated. The momentum resolution σ_p/p obtained with this method goes from from 1.5% to 4.5% for 0.15 GeV/c electrons in the θ range $[20^\circ - 80^\circ]$, decreasing to values ranging from 1% to 2.8% for 1.4 GeV/c electrons in the given angular range [46]. The *Runge-Kutta* method solves the differential equation of motion of the particle for the Lorentz force numerically. It requires initial conditions from the *spline method* like the momentum, polarity, vertex, and direction. The parameters are iteratively optimized to fit the hit measured points in the MDC's, the procedure it is repeated and as a result the momentum, direction and length it is obtained. Moreover, a χ^2_{RK} value which can be used as a quality factor for identification and particle selection. The Runge-Kutta method was chosen for the data analysis of this thesis, which takes into account the effect of a magnetic field through the detector and provides the highest momentum resolution of 4% of a particle trajectory.

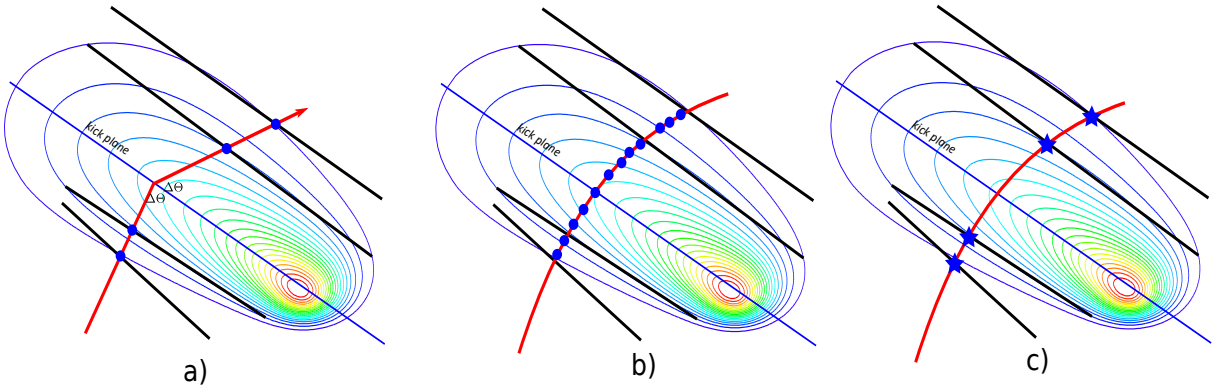

Figure 3.8: Momentum reconstruction algorithms for HADES: **a)** Kick-plane method. **b)** Cubic spline method. **c)** Runge-Kutta method.

3.5 Ring Reconstruction in RICH Detector

The **R**ing **I**maging **CH**erenkov RICH detector plays a significant role in the dilepton analysis as its main propose is the e^+/e^- identification by analyzing the photon rings created by Cherenkov emission in the pad planes, see Section 2.2. With the aim to recognize the formed rings in the photon-detector, two "ring finder" algorithms were developed to identify the position of the rings. A labeling and cleaning procedure is applied before the ring finder algorithm is executed. The cleaning procedure is required to reduce the induced signal on the pad-plane from other effects aside from the Cherenkov emission. Group of pads with at least one pad with high amplitude are removed, small charged amplitude pads distant to the next pad of 7 units

are also removed. In this way, 99.7% of the total signals from direct hits or electronic noise are removed. Only 1% of the pad occupancy is left, so the computing time is reduced significantly. Once the cleaning procedure is done, the labeling is followed, where an image is decomposed into smaller parts, and after is labeled following the previous criteria. The two algorithms developed to identify the position of the ring are the pattern mask (PM) and the Hough transform (HT).

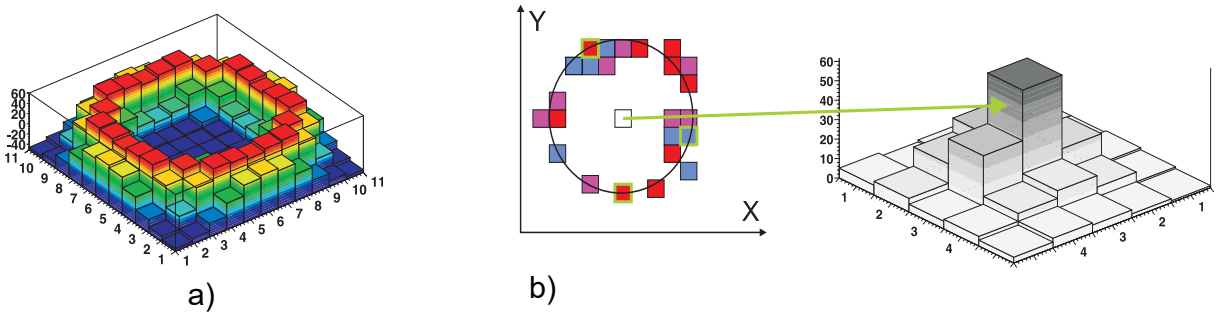

Figure 3.9: **a)** Pattern matrix representation in 3D .**b)** Schematic illustration of the Hough transformation method [106].

The (PM) is a circular mask of 11 x 11 pads symmetric and normalized to 0, where each cell of the pad has assigned a different weight which depends on the position on the ring mask, positive for cells contained in the ring and negatives for cells outside the fired pad. The mask matrix is scanned overall ring candidates, the weights of the matrix are add up to the measured charged resulting in a quality factor *Pattern Matrix Quality* (PM quality). If the quality factor is above a defined threshold value, the ring position is accepted. The Hough transform use a circle parametrization using as an input x, y coordinates and the radius r. The defined ring, maps all the possible pixels, (fired pads), combined with at least three fired pads, if the defined ring match with the fired pads forming a circle, the coordinates x and y are saved. In order to decrease the computing time and since a fixed radius is defined, there is a minimum distance condition between two pixels of half a ring radius. The values of the coordinates are accumulated in a two-dimensional array; the centers of the rings are located as a local maximum from the previous distribution. The patter mask algorithm is faster than the Hough transformation, but in case of close pairs or distorted rings, the accuracy is low while the Hough transformation is independent of the radius of the circle and has better efficiency when the electronic noise is high. In order to increase the detection of the real signal from electronic noise and fake contributions, both algorithms are used in parallel.

3.5.1 Matching RICH-MDC detectors

A similar procedure of matching the outer segments from MDC to the META detector, see Section 3.3.5, is done with the inner segments and RICH detector. The polar and the azimuthal angles from the inner segments of the MDC detector and the ring candidates must be matched. In other words, each ring from RICH is correlated to an inner segment from MDC and from META hits. A quality factor `RichQA` is defined as well, which is very crucial for discrimination between hadrons and leptons define as:

$$q\phi = \frac{(\phi_{\mathrm{RICH}} - \phi_{\mathrm{MDC}} - \phi_{\mathrm{shift}}) \cdot \sin(\theta_{\mathrm{MDC}})}{\sigma_{\mathrm{RICH}}} \tag{3.6}$$

$$\Delta\theta = \theta_{\mathrm{RICH}} - \theta_{\mathrm{MDC}} \tag{3.7}$$

$$\texttt{RichQA} = \sqrt{(\Delta\theta)^2 + (q\phi)^2} \tag{3.8}$$

Where θ_{RICH} and ϕ_{RICH} are the polar and azimuthal angles of a ring in the RICH detector in the laboratory frame θ_{MDC} and ϕ_{MDC} are the angular coordinates [107]. The difference in the azimuthal angle between the hits is multiplied by $\sin(\theta)$ to keep the solid angle spanned constant. If the conditions $q\phi < q\phi_{\max}$ and $\theta_{\min} < \Delta\theta < \theta_{\max}$ are satisfied the RICH-MDC matching is realized. The values $q\phi_{\max}$, $\theta_{\max}$ and $\theta_{\min}$ are defined beforehand by plotting the distributions. In a first analysis step, a broad window in the azimuthal and polar angle of $\Delta\phi\sin(\theta) = \pm 10^{\circ}$, $\Delta\theta = \pm 10^{\circ}$ is applied to the matched rings from RICH and the inner segments from MDC [107]. The resolution can be increase decreasing the window of the azimuthal and polar angle as a function of the particle momenta. This procedure needs a well define vertex position, which is not the case for our pion beam experiment, because the vertex position cannot be obtained with a high resolution due to low multiplicity.

3.6 Event reconstruction

Once the track candidates are reconstructed, physical quantities like, momentum, energy loss and time of flight are obtained. Also the quality factors which are useful for selection criteria, like `MetaQa`, see Section 3.1, are stored in the produced Data Summary Tape (DST) with a tree data structure. DST files can be handle by different users with various physics interests. However, the selected track candidates may not come from the desire event. Besides to the selection parameters mentioned above used for the selection of the track candidates, an event selection is required to refuse contaminated events from unwanted reactions, as a result, the quality of the data is improved. Following, the event selection criteria is described, which is based on fully reconstructed tracks, see Section 3.3.

3.6.1 Event selection

The reconstructed dilepton pairs may not come only from the reaction of the pion beam in the target, but also with the materials besides. Also, wrong information from a reaction in START detector will produce a miss identification of the particle, increasing the background events. To obtain clean events, contaminated events from the reaction with the surrounding materials of the target has to be removed from the analysis. Contaminated events are mainly removed using information from the reconstructed reaction vertex. The following selection criteria was applied in the current analysis:

- `selectStart`: For a time of flight calculation, a coincidence with a single hit in START detector is required.
- `selectStartNoPileUp`: If a second hit is found in START detector, the event is rejected.
- `isClusterVertex`: The procedure to reconstruct the event vertex was done in Section 3.3.1. The cluster vertex has a good resolution z direction. To make sure that the reaction came from the target and not from START detector a selection in the target extend was made from -100 mm $< z_{vertex} <$ 50 mm.
- `isCandVertex`: To improve the accuracy of the estimated vertex, at least two fully reconstructed tracks are required.

During the event selection the original number of events is reduced due to the restricted reaction vertex. In Fig. 3.10 it is shown the primary vertex distribution before and after vertex selection for polyethylene and carbon target. In the case of the carbon target, the peaks of the distribution reflect the segmented structure of the target. The Fig. 3.11 shows the primary vertex distributions in the $x - y$ plane for at least one fully reconstructed charged particle.

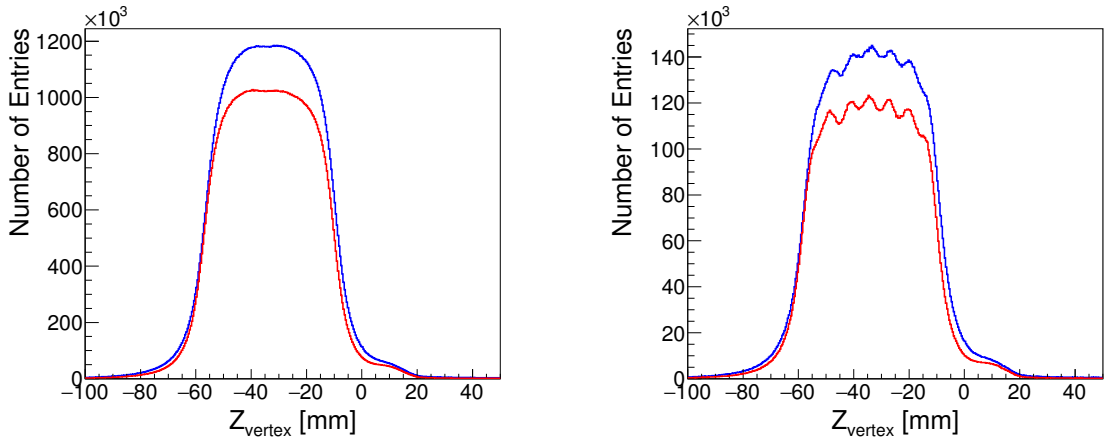

Figure 3.10: Vertex reconstructed in the beam direction (blue) before and (red) after event selection. **Left:** Polyethylene target. **Right:** C target.

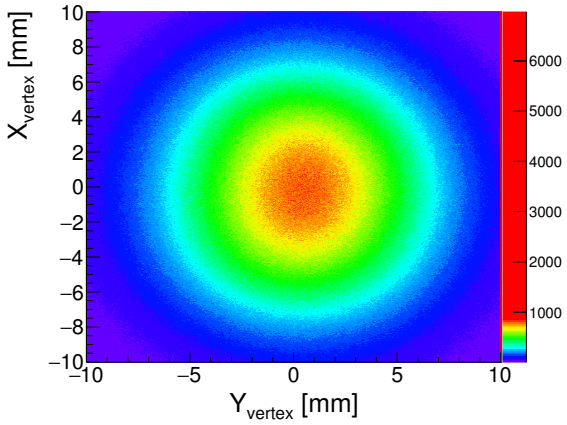

Figure 3.11: Vertex reconstructed in the $x - y$ plane. The diameter of 12 mm from the PE target is visible.

3.6.2 Track sorting routine

DST files stored information from all track candidates since the reconstruction of the trajectory of the particle is based on matching hits in the MDC-RICH detectors, it is possible that many tracks candidates shared one or more track segments. During the analysis, one ring RICH can be combined up to three hits in the META detectors. Therefore, different combinations of track segments can produce the same track candidates. Ideally, one electron should be produced by the match between one ring in RICH one hit in the inner MDC, one in the outer MDC,

and one in any of the time of flight detector, either TOF or RPC. Additionally, fake candidates can be produced by photon conversion into electron pairs inside the detector, typically at small opening angles lower than 9°, but after they pass the magnet they are bent in opposite directions and can be identified in the outer MDC as two individual segments, in that case, the tracks can be rejected as they are produced by pair conversion. To reduce the fake combinations, a sorting procedure algorithm is applied. Every track candidate requires one inner and outer segment. However, every inner segment can be used with combinations of many outer segments. The sorting algorithm store all segments in a list. After, the segments candidates are compared, and if it finds several tracks candidates sharing the same inner segments, a track quality χ^2_{RK}, is used as a discriminator. Only the track candidates with the smallest χ^2_{RK} are taken into account. The quality requirements of the track sorting procedure are listed below:

- Track reconstruction procedure avoid fake tracks with the minimum requirement of a MDC track matched to a META hit detector (see Section 3.3).
- A limit in the $\chi^2_{\mathrm{RK}} < 500$ from the Runge-Kutta fitting procedure.
- `MetaQa`$_x < 3\sigma$: Spatial matching of TOF signal and track position has to be lower than three along the rod.
- `MetaQa`$_y$: Only signals of the TOF rod at which the reconstructed track is pointing to are selected. A spacial match to the meta cell in y coordinate makes use of a match in y in within 3 mm (`setUseYMatching(kTRUE)`).
- `isAtAnyMDCEdge(kFALSE)`: Tracks at the detector edges are removed by a fiducial volume cut.

3.7 Particle identification

The identification of charged particles produced in the reaction is made using physical observables from the particle track reconstruction. In HADES, there are two relevant methods to identify the specific particle specie; using the information on the momentum reconstructed with measurements of time-of-flight, or with the energy losses in the MDC's, both methods can be used together.

Identification by TOF and momentum

The first method relates the velocity of the particle expressed as β with the momentum p. The polarity q of the particle is given by the curvature of the track after the magnet. The velocity of the particle is measured using the time-of-flight Δt and the path s from the track reconstructed already described in Section 3.4. The START detector gives the t_0 initial time (see Section 2.5.1), and one of the META detector TOF or RPC (see Section 3.3.5) gives the final time t_1. The difference between the time measurements gives the time-of-flight $\Delta t = t_1 - t_0$ of a particle. The Runge-Kutta method provided the path of a particle s. Therefore, the β velocity and the relativistic Lorentz factor is:

$$\beta = \frac{v}{c} = \frac{\frac{s}{\Delta t}}{c} \tag{3.9}$$

$$\gamma = \frac{1}{\sqrt{1-\beta^2}} \tag{3.10}$$

The mass of the particle can be deduced from:

$$m = \frac{p}{\beta\gamma} \tag{3.11}$$

And equaling to the centrifugal force F_z and the Lorentz force F_L the relation between mass and the charged is obtained:

$$\frac{m}{q} = \frac{p/q}{\beta\gamma c} \tag{3.12}$$

The resolution in the time-of-flight measurements can induced an error in the measurements Δt, identifying particles with velocities ($\beta > 1$) and as a consequence, appears unphysical imaginary mass. In order to avoid this problem m^2 is calculated instead:

$$\frac{m^2}{q^2} = \frac{p^2/q^2}{\beta^2\gamma^2 c^2} \tag{3.13}$$

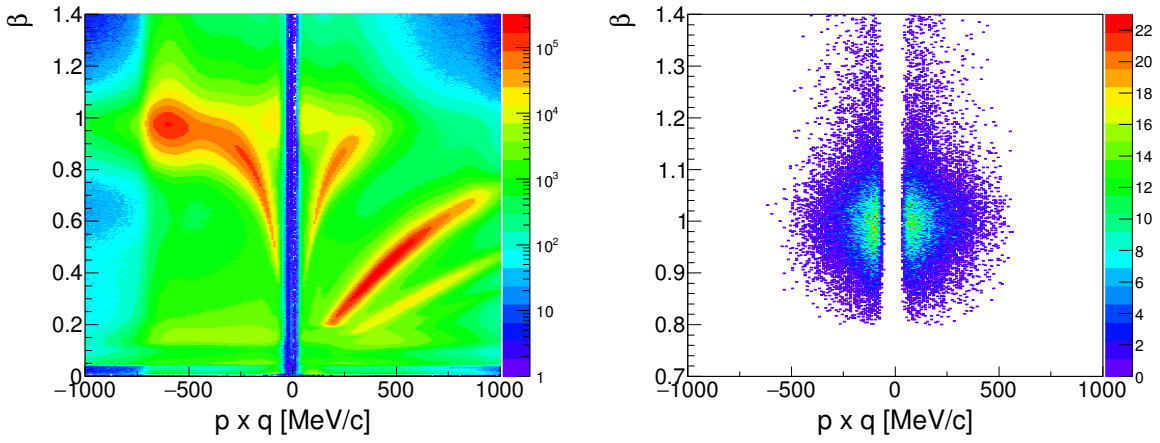

Figure 3.12: **Left:** Distribution of the velocity of the particle vs. momentum times charge before lepton identification. **Right:** Distribution of the velocity of the particle vs. momentum times charge after lepton identification.

We can observe in Fig. 3.13 that the number of positive reconstructed leptons with momenta lower than 250 MeV/c is smaller than for negative, either for the Backtracking or the RICH ring finder procedures. Positrons are bent towards beam axis and electrons outwards, the absence of acceptance at forwards angles explains that losses in the positrons identification.

Identification by energy loss

The TOF and the mini-drift-chambers MDC can measured also the specific energy loss dE per unit length dx of a charged particle when transverse a material. This information is used to identify a particular charged particle using the Bethe-Bloch formula, which describe the dependence between the mean energy loss per unit length $\langle dE/dx \rangle$ and the velocity β:

$$-\left\langle \frac{dE}{dx} \right\rangle = 4\pi N_A r_e^2 m_e c^2 z^2 \frac{Z}{A}\frac{1}{\beta^2}\left[\frac{1}{2}\ln\left(\frac{2m_e c^2\beta^2\gamma^2 T_{\max}}{I^2}\right) - \beta^2 - \frac{\delta}{2}\right] \tag{3.14}$$

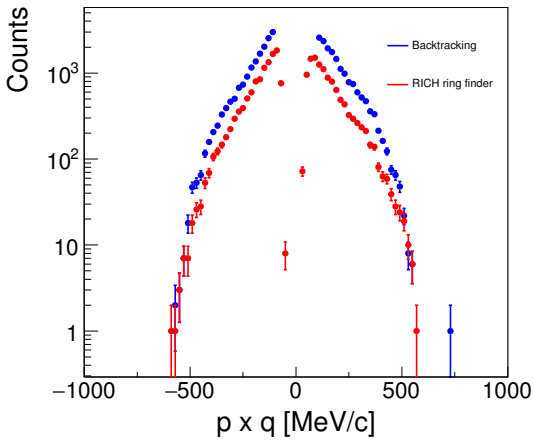

Figure 3.13: Mometum times charge distribution after single electron identification using Backtracking (blue) and RICH ring finder procedure (red).

where β is the speed, N_a Avogadro number, r_e classical electron radius, m_e electron mass, z atomic number of incident particle, Z atomic number, A atomic mass of absorber, I characteristic ionization constant, δ density effect correction and T_{max} maximum kinetic energy transfer.

3.8 Lepton identification

The lepton identification was made using two methods. The principle is based on RICH ring finder, see Section 3.5.1, which is a powerful selection criteria since electrons below 1800 MeV/c, are the only particles that produce Cherenkov radiation and consequently a ring in the RICH detector. Particularly, the `RichQa` matching quality factor is an excellent observable, which provides the angular distance between the RICH ring center and the MDC track. A value of `RichQa` < 4 was applied in the current analysis. Removing the tracks with the large matching distance, the electrons are identified. Unfortunately, ring finder procedure reconstructs only one ring instead of two when the opening angle between two electrons is smaller than 4°. Therefore, only one electron is identified, missing the other one, which contributes to the background signal. In order to improve the efficiency of this procedure, another method called Backtracking was developed for the Au+Au HADES 1.23 AGeV analysis [108]. The main idea is among the ring finder procedure, Backtracking uses tracking information from the MDC, energy losses, and time-of-flight detectors to predict the areas of interest where a RICH ring is produced. In other words, before the signal produced by an electron in RICH is measured, Backtracking algorithm uses the selection criteria for electrons with an specific energy losses and velocity, as it was described in Section 3.7. The tracking information of those pre-select electrons, gives an estimate position where a ring would be produced in RICH detector. Strictly speaking it is a backward process. The pre-selection procedure is used to select leptons from hadrons. To guarantee a good track quality, a limit in the $\chi^2_{\mathrm{RK}} < 500$ from the Runge-Kutta fitting procedure is required. A piece of crucial information to select electrons is the velocity, $\beta \approx 1$, since hadrons with similar momenta have lower velocity. A cut in TOF ($\beta > 0.87$) and RPC ($\beta > 0.9$) system was used, see Fig. 3.12. At our momentum range, the electrons have much more energy losses than pions, so a cut in $dE/dX < 10$ MeV/c$^2/g$ is applied to reject the pions. Also, a momentum cut of $p >$ 100 MeV/c was applied.

Chapter 4

TOF performance study

During the commissioning of the pion-beam experiment in 2014, one of my duties among the shifts in the counting room checking the data acquisition system of the HADES detector, was the calibration of the TOF detector. The calibration is necessary to optimize the lepton identification. In Section 2.4.1 it was already introduced the basic mechanism of TOF. In this section, a more detailed description of the time-of-light measurement and the calibration procedure will be presented.

4.1 Time of flight and hit position

When a charged particle goes throw a scintillator rod in TOF detector, it creates a signal due to the de-excitation mechanism of the molecules of the scintillator material. The signal is collected in both sides of the rod by the photomultipliers providing raw data. The goal of the hit finder procedure is to transform raw data extracted from the time and amplitude of the created pulse into physical information, i.e. particle hit time, position, energy loss, etc. In Fig. 4.1, we can observe the geometry of the TOF scintillator rod in the coordinate system. From both side of the rod the time and amplitude measured on left (right) t_L (t_R) and a_L (a_R) are used to obtain the time of flight t_{hit} and its position x_{hit}, see Eq. 4.1 and Eq. 4.2. Where the t_{off} and x_{off} are constant called time and position offset, the v_{eff} is the velocity of the light signal throw the scintillator rod and t_{start} is the time of START detector signal.

$$t_{hit} = \frac{(t_L + t_R)}{2} - t_{off} - t_{start} \tag{4.1}$$

$$x_{hit} = -\left(\frac{v_{eff}}{2}(t_L - t_R) - x_{off}\right) \tag{4.2}$$

Since the obtained signals are provided by a TDC, a slope parameter it is needed to transform the channel units to nanoseconds, see Eq. 4.3 and Eq. 4.4.

$$t_L = k_L^{TDC} \cdot t_L^c \tag{4.3}$$

$$t_R = k_R^{TDC} \cdot t_R^c \tag{4.4}$$

where $k_{L/R}^{TDC}$ is the slope parameter of left (right) TDC and $t_{L/R}^c$ is left (right) time measured in channel TDC units. Therefore, the Eq. 4.1 and Eq. 4.2 become :

$$t_{hit} = \frac{\left(k_L^{TDC} \cdot t_L^c + k_R^{TDC} \cdot t_R^c\right)}{2} - t_{off} - t_{start} \tag{4.5}$$

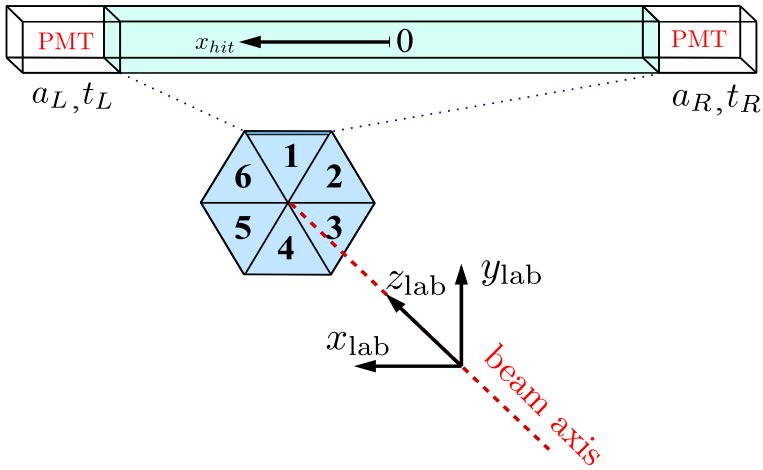

Figure 4.1: Geometry of the TOF scintillator rod in rod coordinate system. The orientation of HADES base coordinate system is shown for comparison. The z-axis of HADES base coordinate system and the axis of the beam are parallel. The orientation of the z-axis is in the direction of the beam. Numbering convention for the six sectors is shown.

$$x_{hit} = \left(\frac{v_{eff}}{2} \left(k_L^{TDC} \cdot t_L^c - k_R^{TDC} \cdot t_R^c \right) - x_{off} \right) \tag{4.6}$$

Finally, We end up with five independent parameters, i.e $v_{eff}(mm/ns)$, $k_{L/R}^{TDC}(ns/ch)$, $x_{off}(mm)$ and $t_{off}(ns)$ that are needed to reconstruct the hit time and position. The $k_{L/R}^{TDC}$, x_{off}, t_{off} have to be established from the calibration procedure.

4.2 Energy loss

Charged particle crossing a scintillator material produced a signal which its amplitude is proportional to the energy deposited in the scintillator rod $a_{hit} \sim \Delta E$. The amplitude is proportional to $a_{hit} \sim z^2/\beta^2$ according to Bethe-Bloch formula. Amplitude calibration is done in a way that the amplitude is set to one[1], also called MIP (Minimum Ionizing Particle). The amplitude of the signal for both sides of the rod is given by:

$$a_L = a_{hit} \exp\left\{ -\frac{\frac{l}{2} - x_{hit}}{l_{att}} \right\} \tag{4.7}$$

$$a_R = a_{hit} \exp\left\{ -\frac{\frac{l}{2} + x_{hit}}{l_{att}} \right\} \tag{4.8}$$

where l is the length of the rod an l_{att} is the attenuation length. Similar to the time of flight calculations, we can obtain the hit amplitude a_{hit} and the position along the rod $x_{hit}^{\mathcal{A}}$ with:

$$a_{hit} = \sqrt{a_L a_R} \exp\left\{ \frac{l}{2 l_{att}} \right\} \tag{4.9}$$

[1]More exactly the particle energy deposit 3.8MeV in 20mm thick rods and 5.7MeV in 30mm thick rods will correspond to amplitude $a_{hil} = 1$

$$x_{hit}^{A} = \frac{l_{att}}{2} \ln\left\{\frac{a_L}{a_R}\right\} \tag{4.10}$$

The position has been calculated using ADC data, so the amplitudes a_L and a_R needs to be converted to ADC channels using:

$$a_L = k_L^{ADC}\left(a_L^c - p_L\right) \tag{4.11}$$

$$a_R = k_R^{ADC}\left(a_R^c - p_R\right) \tag{4.12}$$

where p_L, p_R are the ADC pedestals, a_L^c, a_R^c are amplitudes in channel units, and k_L^{ADC}, k_R^{ADC} are ADC slopes. After introducing the so-called modified amplitudes:

$$a_{L/R}^m = a_{hit} \exp\left\{\frac{x_{hit}}{l_{att}}\right\} \tag{4.13}$$

which do not include the rod length parameter and the modified ADC slope parameters:

$$k_{L/R}^{ADC,m} = k_L^{ADC} \exp\left\{\frac{l}{2l_{att}}\right\} \tag{4.14}$$

the final amplitude is calculated as $a_{hit} = \sqrt{a_L^m a_R^m}$:

$$a_{hit} = k_A\sqrt{\left(a_L^c - p_L\right)\left(a_R^c - p_R\right)}, \quad \text{where} \quad k_A = \sqrt{k_L^{ADC,m} k_R^{ADC,m}} \tag{4.15}$$

4.3 Time of flight corrections

There are dependencies of time of flight on its amplitude and position which needs to be taken into account. The dependence of the time of flight calculation at a certain position along the scintillator rod is given by:

$$t_{hit}(x) = t_{hit}(0) - c_x \cdot x_{hit}^2 \tag{4.16}$$

Where $t_{hit}(0)$ is the time of flight of a particle crossing the center of the rod and c_x is regularly evaluated using LED discriminator (Leading Edge Discriminator). A time-walk effect in the amplitude is found out if we measured two times of flight signal with different height, the pulse with the bigger height will trigger the threshold before than the small one. The correction is chosen as:

$$t_{\text{corrTW}} = \frac{c_{twL}}{\sqrt{a_L^m}} + \frac{c_{twR}}{\sqrt{a_R^m}} \tag{4.17}$$

where c_{twL}, c_{twR} are constants and a_L^m, a_R^m are the modified amplitudes calculated in Eq. 4.13. This correction improves the time resolution of TOF about $\sim 12\,ps$. Including all the corrections the Eq. 4.5 become:

$$t_{hit} = \frac{\left(k_L^{TDC} \cdot t_L^c + k_R^{TDC} \cdot t_R^c\right)}{2} - t_{off} - t_{start} + c_x.x_{hit}^2 + \frac{c_{twL}}{\sqrt{a_L^m}} + \frac{c_{twR}}{\sqrt{a_R^m}} \tag{4.18}$$

which is the complete formula used for the time of flight reconstruction.

4.4 TOF calibration procedure

First, the time of flight and hit position is calculated using Eq. 4.5 and Eq. 4.6. Once the hit position is known, the corrections for time of flight dependencies obtained from Eq. 4.16 are used to calculate the time of flight with the position dependencies in Eq. 4.18. To calibrate the TOF measurement, we need to find out the values of a set of parameters $k_{L/R}^{TDC}$, x_{off} and t_{off} which are defined in Section 4.1. The calibration of the slope parameters $k_{L/R}^{TDC}$ can be calculated introducing a known delay $\Delta_{\text{delay}} \approx 50\ ns$, hence, the time peak position from the spectrum will be shifted with the known delay. Therefore, the ratio between the time peak position and the delay will give us the slope parameter.

$$k_{L/R}^{TDC} = \frac{\Delta_{\text{delay}}}{t_{L/R}^{c} - t_{L/R,\Delta}^{c}} \tag{4.19}$$

The position offset x_{off} can be evaluated using beam data without a magnetic field, and selection correlated hits between TOF and MDC. According to track reconstruction from MDC one can find out the corresponding hit in TOF detector, x_{MDC}. The position offset x_{off} will be the displacement of the mean $D = x_{hit} - x_{\text{MDC}}$ equal to zero, see Fig. 4.2.

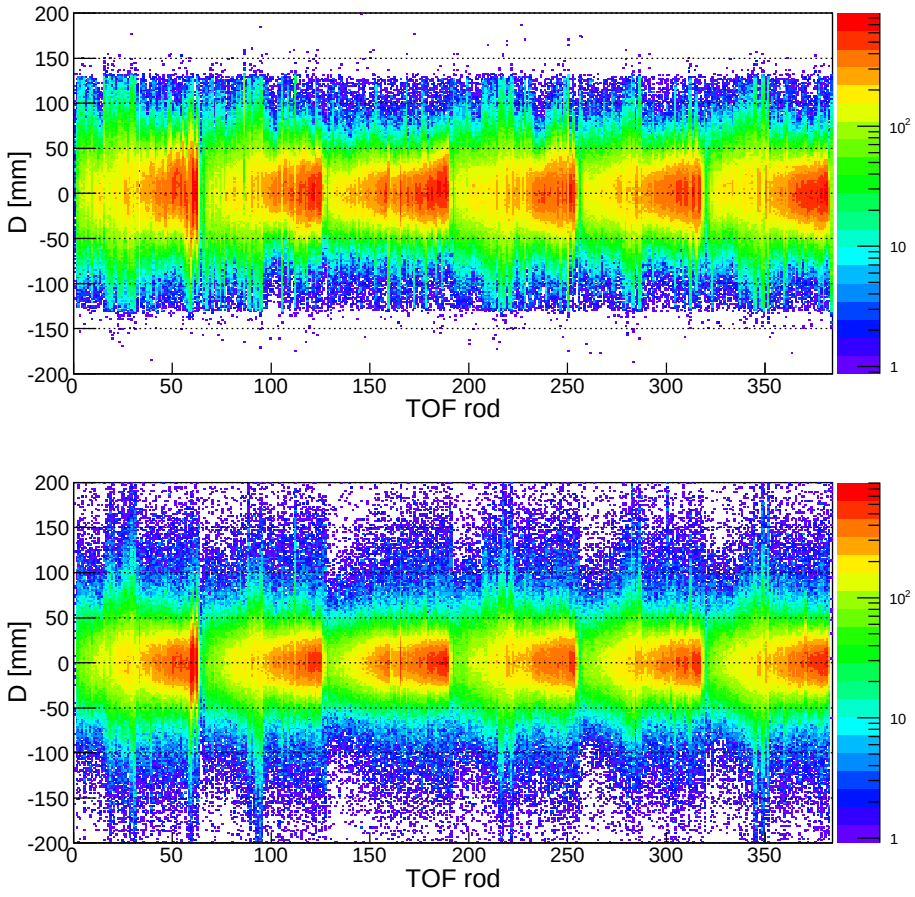

Figure 4.2: Position calibration of TOF. The plot shows $D = x_{hit} - x_{\text{MDC}}$ versus a consecutive number of TOF rod. Top figure without calibration and bottom figure after calibration.

To get the time offset t_{off} we need to select a known reference peak from experimental data.

In my case, I choose energetic pions moving practically at the speed of light, hitting the middle point of the rod. Setting the value of time of flight to zero in Eq. 4.5, we obtain the time offset, see Fig. 4.3.

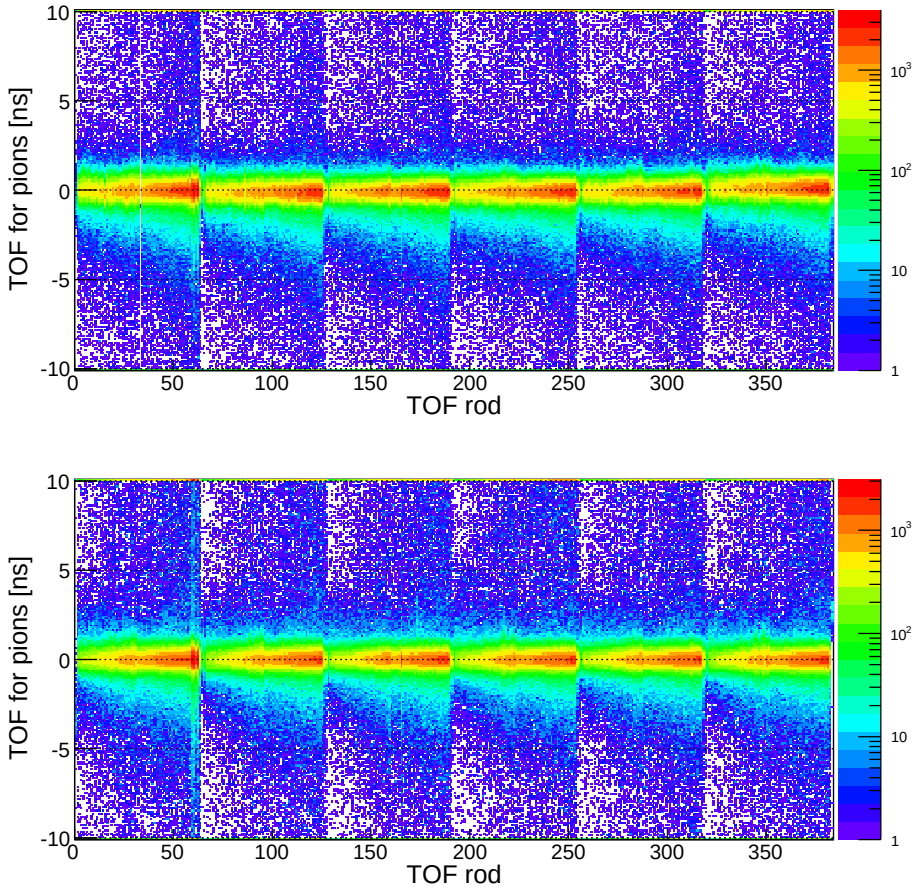

Figure 4.3: Time calibration of TOF. The plot shows time of flight of pions candidates versus a consecutive number of a TOF rod. Top figure without calibration and bottom figure after calibration.

Concerning energy deposited in the scintillator rods, I use information from Eq. 4.15 and Eq. 4.10. Using experimental data we can scale the position of the amplitude peak to a minimum ionizing particles MIP equal to one in all the rods, see Fig. 4.4.

The group velocity v_g and the attenuation length l were known from previous runs. In Fig. 4.5 it is shown a flow diagram of the calibration procedure. It is started with a non calibrate sample file called "be14188_hist.root" which contains all the observables given by already reconstructed measurements. They are improved iteratively since, in each newly calibrated data, the quality of the data is enhanced. The first calibration is done applying the caliboff_pos.C analysis macro which calibrates the data using the amplitude/energy deposited information discussed before. This macro will generate a text file with parameters that will be used as an input to generate a new DST file; the "HADESparam.txt" contains all the calibration parameters of HADES sub detector except TOF. This new file will be calibrated for the amplitude called "be14188_a_hist.root". This procedure is repeated for position and time of flight calibration with the respective macro analysis caliboff_pos.C and caliboff_pim.C. Resulting in a final DST file

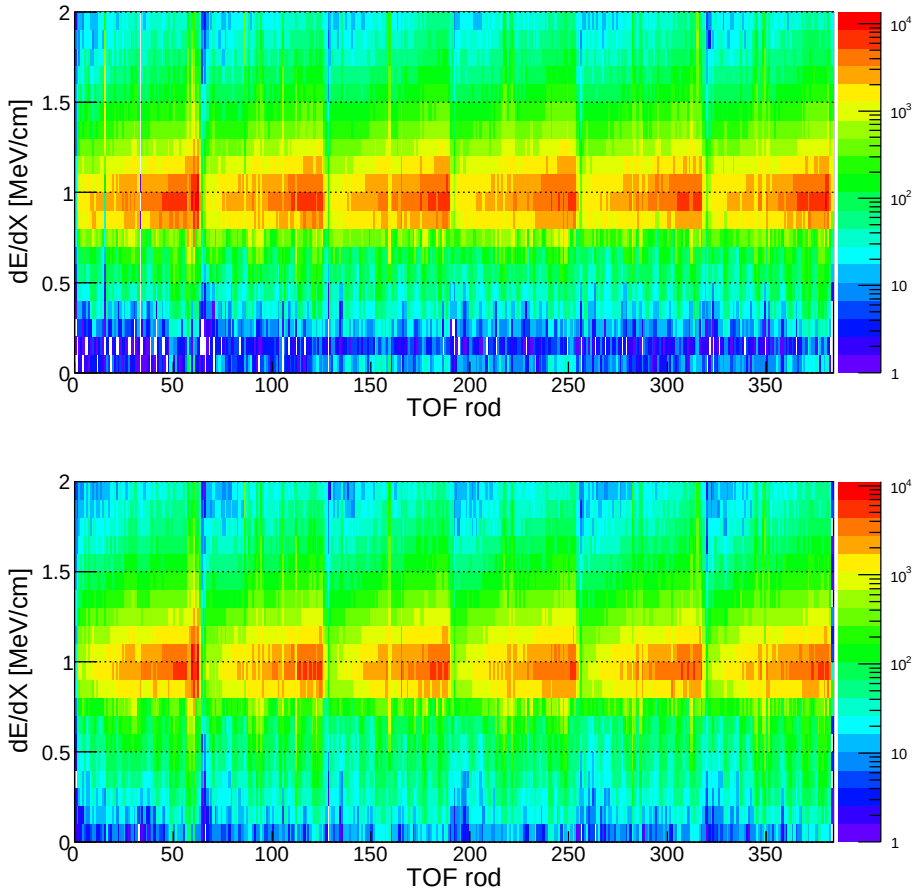

Figure 4.4: Energy loss calibration of TOF. The plot shows pion energy loss at MIP versus a consecutive number of a TOF rod. Top figure without calibration and bottom figure after calibration.

called "be14188_t_hist.root" which will be calibrated for the three methods mentioned above. The output parameters generated from this file are upload to ORACLE database and used for the final reconstructed experimental/simulated data.

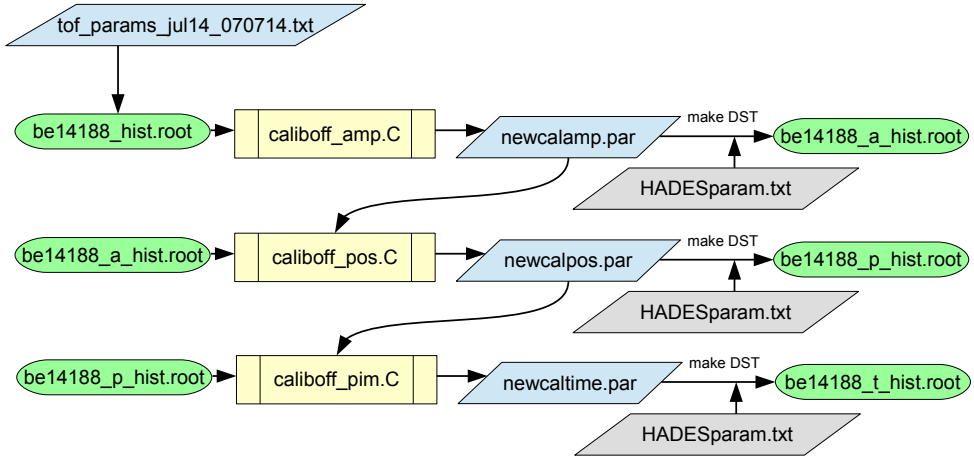

Figure 4.5: Diagram flow of TOF calibration procedure.

Chapter 5

Efficiency corrections and errors estimation

To compare our results with other experiments or theoretical predictions, the raw spectra described in Section 6.3 needs to be corrected for the imperfection of the detector acceptance and inefficiency. The **acceptance** corrections take into account the confined geometry of the detector and characterize if the particle goes or not throw the active volume, also a restriction in the opening angle ($\alpha > 9°$) and momentum size $100 < p < 1100$ MeV are considered in this level. The **efficiency** losses are because all the particle detection mechanisms are based on a statistical process which leads to an efficiency lower than 100%; also the track reconstruction, detector response, and restrictions applied in the analysis, like track quality or topology cuts affect the efficiency substantially.

5.1 One-dimensional efficiency correction for dilepton pair

In the "one-dimensional efficiency corrections" procedure the final spectra (invariant mass, missing mass, transverse momentum, etc.) is multiplied by a non-constant factor which corrects the losses due to inefficiency, the problem of this method is that the spectra may not show only a real physical distribution, but also non-physical distribution from the model used to calculate the correction factor. First, simulated events from Pluto are generated in 4π full solid angle, those leptons needs to go throw our restriction in the opening angle ($\alpha > 9°$) and momentum size $100 < p < 1100$ MeV. The pairs that survive are used to reconstruct the signal ($N_{4\pi}$). The next step is to process the previous simulations with the usual analysis chain, see Fig. 5.1. The tracks are propagated throw the detector using HGEANT [104] to get a real detector response as well the HADES acceptance. The obtained events are analyzed in an identical procedure as experimental ones. The pairs obtained after the analysis chain are already corrected for HADES acceptance, (N_{Reco}). The N_{Acc} represented the number of acceptance tracks. The acceptance factor ϵ_{Acc} and efficiency factor ϵ_{Eff} are defined as follow:

$$\epsilon_{Acc} = \frac{N_{4\pi}}{N_{Acc}} \tag{5.1}$$

$$\epsilon_{Eff} = \frac{N_{Acc}}{N_{Reco}} \tag{5.2}$$

Therefore, the final correction factor ϵ_{Total} will be a combination of an acceptance and efficiency correction factor defined as:

$$\epsilon_{Total} = \epsilon_{Acc} \cdot \epsilon_{Eff} = \frac{N_{4\pi}}{N_{Reco}} \tag{5.3}$$

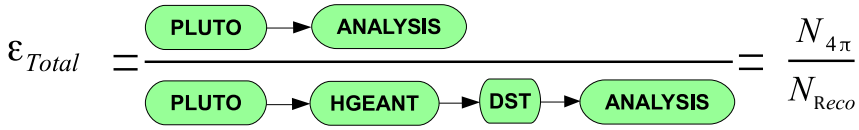

Figure 5.1: Flow analysis chain of the efficiency and acceptance factor estimation.

The ratio between $N_{4\pi}$ and N_{Reco}, see Fig. 5.2, gives the factor ϵ_{Total}.

$$N_{4\pi} = N_{\text{Reco}} \cdot \epsilon_{Total} \tag{5.4}$$

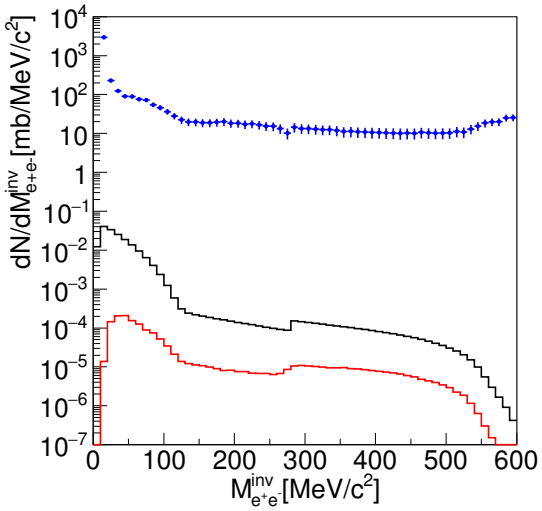

Figure 5.2: Invariant mass distribution simulations in 4π full solid angle (black line) and trough a full HADES response simulation and acceptance (red line). ϵ_{Total} is the ratio between the number of initial particles generates by Pluto in 4π full solid angle $N_{4\pi}$, and the reconstructed pairs N_{Reco} (blue dots)

Hence, to correct the yield by the efficiency in the 4π full solid angle, the experimental data has to be multiplied by ϵ_{Total}. The effect of the acceptance and efficiency correction is shown as a function of invariant mass in, Fig. 5.3. The efficiency correction method is used identical for different observables like the missing mass, transverse momentum, etc.

5.2 Estimation of systematic errors

In an experiment, the uncertainties arise from statistical and systematic errors. The statistical errors originate in the probability distributions used in experiments that involve counting. Systematic errors are inaccuracies of the data experiment that are consistently off in the same direction and often during the whole experiment. Therefore, it is also needed to add the systematic errors to our analysis to compare experimental results with theoretical models. The

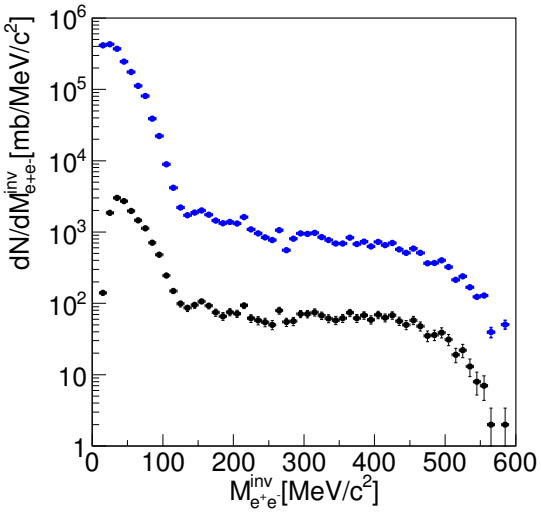

Figure 5.3: Invariant mass spectrum for the uncorrected (black dots) and the efficiency corrected spectra (blue dots).

systematic errors were calculated for correlated and uncorrelated events, see Section 6.1. The total systematic errors of our efficiency and acceptance corrected data comes mainly from:

- Event selection cuts: Relative difference between experimental results and simulations give a value of 15% for correlated systematic error and 10% for uncorrelated.
- Combinatorial background: Subtraction of the combinatorial background brings a systematic error of 5%·S/B. It is obtained from PLUTO + HGEANT simulations, studying the ratio of the reconstructed and true signal after background subtraction.
- Normalization: The data normalization was done using the elastic scattering events from where the cross section was obtained as well. A value of 10% was obtained due to the precision of this method.
- MDC tracking: Efficiency of tracking reconstruction procedure is affected by 10% for correlated and uncorrelated systematic errors.
- Backtracking/RICH algorithms: 15% for the correlated and 10% for the uncorrelated uncertainty for the Backtracking method. In the case of the RICH finder procedure, it was found out a value of 10% for the correlated and uncorrelated errors.

The errors of the cross section displayed for proton contribution in Table 9.2 are obtained directly from the knowledge of these cross sections, except for the η production where the uncertainty of pion beam momenta was used. The cross section for the carbon target is obtained by superposition of interactions with protons, taking into account the number of participant protons in the reaction, this factor denotes by R will introduced an extra uncertainty. Therefore, the carbon cross section will have two errors, the first one introduced by the proton cross section and the second by the uncertainty of the R factor, see Table 5.1:

$$(\Delta\sigma)_C = R' \cdot (\Delta\sigma)_H \pm \Delta R' \cdot \sigma_H \tag{5.5}$$

The errors for polyethylene target are a combination of the ones obtained from proton and carbon targets values normalized as $\sigma_{CH2} = \sigma_H + 1/2\sigma_C$, and also from the factor R.

$$(\Delta\sigma)_{CH2} = \sqrt{(\Delta\sigma + \frac{1}{2}(R' \cdot (\Delta\sigma)_H))^2 + \frac{1}{4}(\Delta R' \cdot \sigma_H)^2} \tag{5.6}$$

The correlated and uncorrelated systematic errors presented above are all independent in each in their group, and therefore they can be added quadratically to obtain the total systematic error (ΔN_{Sys}):

$$\frac{\Delta N_{Sys.Corr}}{N_{Tot}} = \sqrt{\left(\frac{\Delta N_{BG}}{N_{Bg}}\right)^2 + \left(\frac{\Delta N_{Eff}}{N_{Eff}}\right)^2 + \left(\frac{\Delta N_{Norm}}{N_{Norm}}\right)^2 + \left(\frac{\Delta N_{ES}}{N_{ES}}\right)^2} = 20 - 23\% \tag{5.7}$$

$$\frac{\Delta N_{Sys.UnCorr}}{N_{Tot}} = \sqrt{\left(\frac{\Delta N_{BG}}{N_{Bg}}\right)^2 + \left(\frac{\Delta N_{Eff}}{N_{Eff}}\right)^2 + \left(\frac{\Delta N_{Norm}}{N_{Norm}}\right)^2 + \left(\frac{\Delta N_{ES}}{N_{ES}}\right)^2} = 14 - 15\% \tag{5.8}$$

The final results presented in Section 9.3 are shown with the statistical and systematic errors.

5.3 Relative carbon and proton contribution to polyethylene target

The pion reaction on carbon target is treated as a superposition of interactions with protons, also called participant-spectator model, see Section 9.1.4. The ratio of the e^+e^- invariant mass between carbon and polyethylene target is shown in Fig. 5.4.

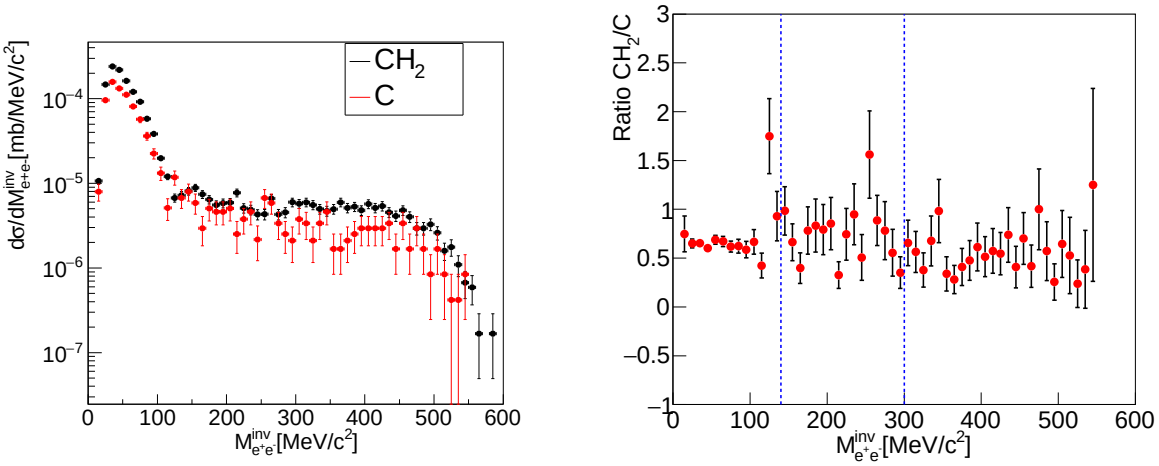

Figure 5.4: **Left:** Comparison of differential cross section as a function of invariant mass for polyethylene and carbon targets. **Right:** Ratio of both spectra.

From Eq. 5.9 is obtained the ratio between carbon and polyethylene distribution denoted as R.

$$R = \frac{\sigma_C}{\sigma_{PE}} = \frac{\frac{\sigma_C}{2}}{\frac{\sigma_C}{2} + \sigma_H} \tag{5.9}$$

The Eq. 5.10 shows the ratio R', which is the relative number of participant protons in the carbon nucleus. As it was discussed in Section 1.5.2, at pion beam momenta of 0.69 GeV/c the ratio between both reactions equal to $\sigma_{\pi^- p}/\sigma_{\pi^+ p} = 3$ indicates the $\pi^{-12}C$ reaction it is dominated by $\pi^- p$ interaction rather than $\pi^- n$. The small collected statistics from carbon target does not allow a proper subtraction at larger invariant mass. That is the reason why the trend of the ratio decrease specially at $M_{e^+e^-} > 300$ MeV/c^2. This ratio is not constant for the whole range of the spectra. In Table. 5.1 the ratio is shown into three different regions corresponding to the main dilepton sources.

$$R' = \frac{\sigma_C}{\sigma_H} = \frac{2R}{1-R} \tag{5.10}$$

Ratio	0-140 MeV/c^2	140-300 MeV/c^2	300-600 MeV/c^2
R=σ_C/σ_{CH2}	0.64 ± 0.06	0.65 ± 0.08	0.48 ± 0.07
R$'$=σ_C/σ_H	3.60 ± 0.90	3.70 ± 1.30	1.84 ± 0.52

Table 5.1: Ratio of cross section for carbon and polyethylene target (R), carbon and proton nuclei (R$'$)for three invariant mass regions

For the e^+e^-invariant mass region between $M_{e^+e^-} < 140$ MeV/c^2 which correspond to the π^0 region the number of participant protons in carbon target is $R' = N_{\text{part}} = 3.60$. The main contributions for the region between 140 MeV/c^2 $< M_{e^+e^-} <$ 300 MeV/c^2 are the resonances N(1520), N(1535), $\Delta(1232)$ and the η meson with a factor of 3.70. Last, for invariant mass region above $M_{e^+e^-} > 300$ MeV/c^2 the ρ contribution is more reduced with a factor of 1.84. Despite, the differences of the ratio at high invariant mass range, the distribution is consistent with a participant-spectator model with $\frac{\sigma_C}{\sigma_H} \approx 3.3$ for each range, as well with the relation $Z^{\frac{2}{3}}$. Finally, the factor $\frac{\sigma_C}{\sigma_H} \approx 3.3$ will be use for the scaling of the simulations in the full mass region.

Chapter 6

Reconstruction of dielectron signal

In Section 3, it was described the single identification of the electrons, the next step is to identify the electron pairs e^+ and e^- coming from the same virtual photon vertex. The reconstruction of dilepton pairs give access to probe nuclear matter under extreme conditions, also they allow studies of their mass and decay width, see Section 1.2.3. Unfortunately, many pairs are combined from different primary sources, creating a large combinatorial background. Hence, it is necessary a detailed analysis of the background, in order to subtract the produced background and to obtain the true signal pairs. The invariant mass of the lepton pair is defined by the following equation:

$$M_{e^+e^-} \cdot c^2 = \sqrt{(E_{e^+} + E_{e^-})^2 - (\vec{p}_{e^+} \cdot c + \vec{p}_{e^-} \cdot c)^2} \tag{6.1}$$

where the total energies of the positron/electron are E_{e^+}, E_{e^-}, the momenta in the laboratory system are p_{e^+}, p_{e^-}, c is the velocity of light (and $|\vec{p}| = p$). If the leptons have energies $E_{e^\pm} \gg m_{e^\pm}$= 0.511 MeV/c^2 the Eq. 6.1 can be written as:

$$M_{e^+e^-} \cdot c^2 = \sqrt{2 \cdot c^2 p_{e^+} p_{e^-} (1 - cos\theta_{e^+e^-})} = 2c \cdot sin(\theta_{e^+e^-}/2) \cdot \sqrt{p_{e^+} p_{e^-}} \tag{6.2}$$

where $\theta_{e^+e^-}$ is the opening angle of the pair. In HADES, the main sources of lepton pairs are the electromagnetic decay of π^0 mesons, and the photon conversion in the target or detector material, (like the radiator and carbon shell of RICH):

- external conversion, i.e. pair creation: $\pi^0 \rightarrow \gamma\,(\gamma \rightarrow e^+e^-)$
- Dalitz decays of the π^0 meson: $\pi^0 \rightarrow \gamma e^+e^-$
- η Dalitz: $\eta \rightarrow \gamma e^+e^-$
- Δ Dalitz, N^* Dalitz, ω Dalitz$\rightarrow \gamma e^+e^-$
- pn Bremsstrahlung
- Vector meson decays: ρ, ω, $\phi\rightarrow \gamma e^+e^-$

6.1 Combinatorial background

Unfortunatly, not all the dilepton reconstructed are originated in the hot and dense matter. One of the main sources is the background produced by photon conversion in the material detector or in the target, the background from an external pair conversion from photons, and the

dilepton pair combination of a lepton and a misidentified hadron. Besides the sources mentioned before, one has to distinguish between correlated and uncorrelated background. ***Correlated*** background correspond to the leptons originated from the same electromagnetic vertex, and ***uncorrelated*** background is everything else. The left part of Fig. 6.1 shows an example of uncorrelated background with the combination of dielectron pair coming from two different sources. In Fig. 6.2 the correlated background is coming from the π^0 Dalitz decay into two dielectrons pairs originated from a different photon conversion, or by the $\pi^0 \to \gamma\gamma$ decay.

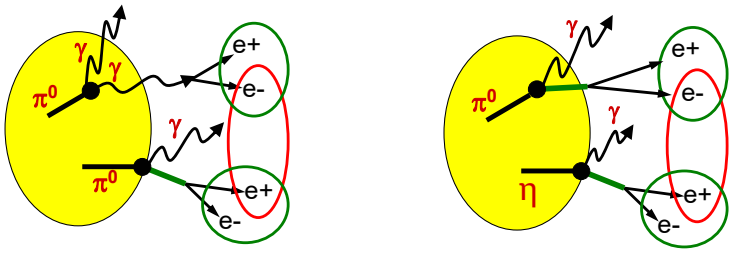

Figure 6.1: Example of sources of uncorrelated combinatorial background created by combining tracks coming from the π^0 Dalitz and η Dalitz decays which happen inside one event [109].

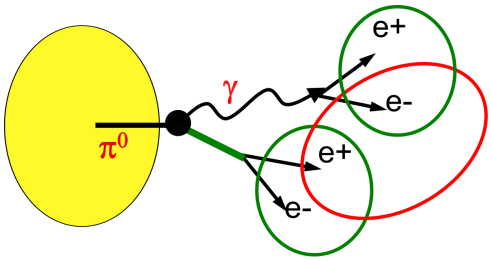

Figure 6.2: Correlated combinatorial pair created by a single π^0 Dalitz decay. Green circles represent the real signal pair and the red circles the combinatorial background [109].

6.1.1 Same-event like-sign background

In principle, it is not possible to know the origin of the decay particles, in other words, if the dileptons came from the same electromagnetic vertex. Therefore, all possible combinations have to be calculated, and subtract the spectral distribution of the true pairs , the pairs which are combined by tracks from different mother particles. To accomplish this, all possible combinations of electron-positron (e^+e^-, e^+e^+ and e^-e^-) from the same event are grouped, see Fig. 6.3. Over all events, the spectra of unlike-sign and like-sign pairs are obtained. The unlike-sign pairs $N^{tot}_{e^+e^-}$, is formed by true pairs of interest, S_{+-}, and the uncorrelated pairs which are the combinatorial background $CB_{e^+e^-}$, see Eq. 6.3.

$$S_{+-} = N^{tot}_{e^+e^-} - CB_{e^+e^-} \tag{6.3}$$

The *same-event like-sign* method was used to determine the $CB_{e^+e^-}$, it is based on the assumption that the combinatorial background of the like-sign pairs is a good approximation of the combinatorial unlike-sign background, taking into account the lack of combinatorial background from physics origin. From the same event all like-sign pairs ($N_{e^+e^+}, N_{e^-e^-}$), are combined and the geometrical mean is calculated:

$$CB^{geom}_{+-} = 2\sqrt{N_{e^-e^-}N_{e^+e^+}} \tag{6.4}$$

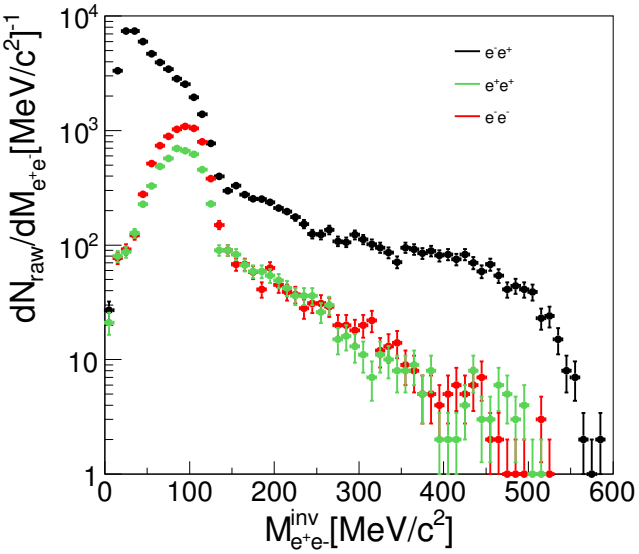

Figure 6.3: Invariant mass distribution for PE target of like-sign and unlike-sign pairs.

Another method frequently used is *the mixed-event technique*, in contrast with the *same-event technique* it mixed all particles from different events to created the unlike-signal background. Those pairs are uncorrelated and give higher statistical precision since the event can be mixed with many others, but for my analysis where most of the background is correlated, this method is useless. Hence, the present analysis will be done with the *same-event technique* using the geometric average to obtain the combinatorial background.

6.2 Background rejection procedure

Since the signal pairs are obtained from the subtraction of the combinatorial background pairs from all the pairs measured, a good ratio signal over background is necessary to obtain a precise measurement. Therefore, the strategy of the analysis, is to apply conditions in the reconstructed pairs to reject the background, but at the same time keep most of the signal one. It is clear that one of the main contributions of uncorrelated pairs and combinatorial background are due to photon conversion. Lepton pairs are produced by the decay of an intermediate virtual photon, studying their decay kinematics it is observed that the opening angle between leptons pairs is very small. As a result, those pairs will be close and detected as one ring in RICH, what is so-called "close pairs", if the two separate rings are identified in RICH, the pairs are classified as "open pairs". The background rejection procedure is done in two steps:

- ***Direct*** cut removes a single lepton pairs which do not fulfil the condition cut. However, the tracks from such pair can still be combined with other pairs in the event.

- ***Recursive*** cut removes the single lepton pair and also all the two segment tracks which compound the pair, which eventually can be combined with other segments. Recursive cuts are based in the opening angle cut, if lepton pairs do not survive this cuts, is almost like it is a pair coming from photon conversion or π^0 Dalitz decay and the should not contribute in other lepton pair. Also, due to the resolution in MDC and RICH, two leptons can be

identified as one. The RICH ring finder procedure only can resolve rings with an angular resolution of 4°. Those tracks should be excluded from the analysis.

Bases in PLUTO simulations and opening angle cut $\theta_{e^+e^-} > 9°$ has been applied. With this cut, it removes contribution from π^0 and η Dalitz decay as one can see in the left of Fig. 6.4. This threshold cut is crucial to removed the γ conversion pairs, which, as we mentioned before, are one of the main sources of combinatorial background which affects the invariant mass region below $\left(M_{e^+e^-} < 140\ MeV/c^2\right)$. This is a "direct" cut, which means that the excluded tracks can still be combined. Two more cuts in a single track level are applied. Leptons with momentum below 50 MeV/c are bent by the magnetic field and described a curling path without reaching the outer chambers of the MDC. As a consequence, the track reconstruction is not done, and those tracks need to be removed. To guarantee this selection, a **momemtum cut** of $p > 100$ MeV/c is applied in order to reject those slow leptons. And last, a cut in the "angle to the nearest track candidate α_C" is applied. This cut is applied to tracks that survived the previous cut with only one segment reconstructed in the inner MDC. Those segments are searched for their vicinity within an angle previously defined, α_C, if the segment in their neighborhood, either fitted or unfitted falls in this angle, the track is removed. This method reduced the combinatorial background substantially. A detailed study of "angle to the nearest track candidate α_C" is described in Section 6.3.2. The distribution of the angle to the closest non-fitted lepton is shown in the right of Fig. 6.4

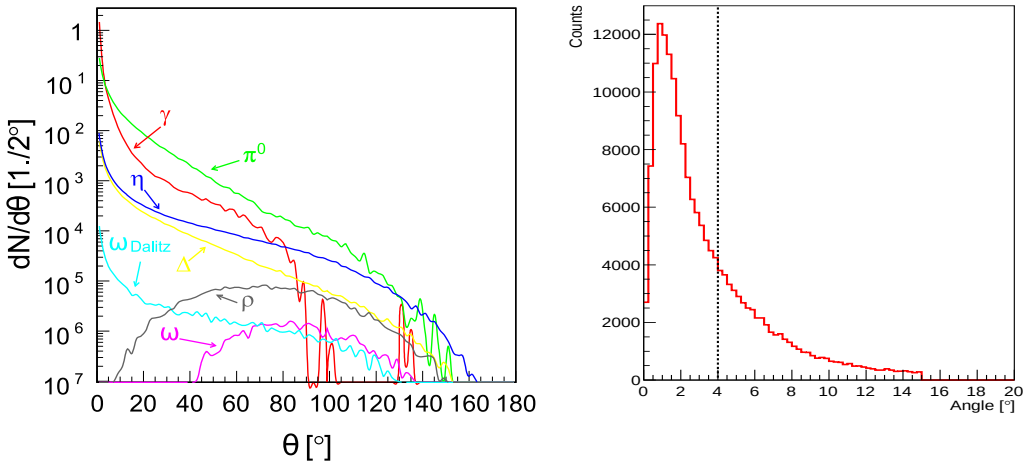

Figure 6.4: **Left:** Opening angle distribution of various lepton sources. **Right:** Opening angle distribution between a lepton pair and closest not fitted lepton.

6.3 Inclusive dielectron production

The inclusive dielectron production for polyethylene (PE) and carbon (C) target at pion beam momenta of 690 MeV/c will be shown in the following section. First, a description and comparison between the two methods of lepton identification, RICH ring finder and Backtracking analysis, see Section 3.8. After, the different results from cuts in "angle to the nearest track candidate α_C" in the analysis will be shown for the case of Backtracking analysis.

6.3.1 RICH ring finder analysis vs. Backtracking method

For the reaction $\pi^- PE \rightarrow Xe^+e^-$ the inclusive invariant mass distribution of e^+e^- pairs with an opening angle cut $\theta_{e^+e^-} > 9°$ is shown in Fig. 6.5. The left part for RICH ring procedure and right part for Backtracking analysis. The "Signal" of true pairs of interest is shown as black dots, the the uncorrelated pairs which are the "Combinatorial background" $CB_{e^+e^-}$ as green dots, see Section 6.1, and last, the unlike-sign pairs $N_{e^+e^-}$ formed by "Signal" and "Combinatorial background" as red dots. For the invariant masses $\left(\mathrm{M}_{e^+e^-} > 100\ \mathrm{MeV/c^2}\right)$ the "Combinatorial background" $CB_{e^+e^-}$ has no structure but a smooth shape due to random combination of like-sign pairs from photon conversion of two different π^0, creating an uncorrelated background, see Fig. 6.1. It is observed in both methods that there is a peak between $110\ \mathrm{MeV/c^2} < \mathrm{M}_{e^+e^-} < 120\ \mathrm{MeV/c^2}$, which corresponds to the correlated background of π^0, see Fig. 6.2. Same conclusion are obtained from the $\pi^- C \rightarrow Xe^+e^-$, see Fig. 6.6. It is clear that the efficiency of the lepton reconstruction is improved with the Backtracking algorithm in contrast with the RICH ring finder procedure. This conclusion was already obtained for a single electron identification in Fig. 3.13.

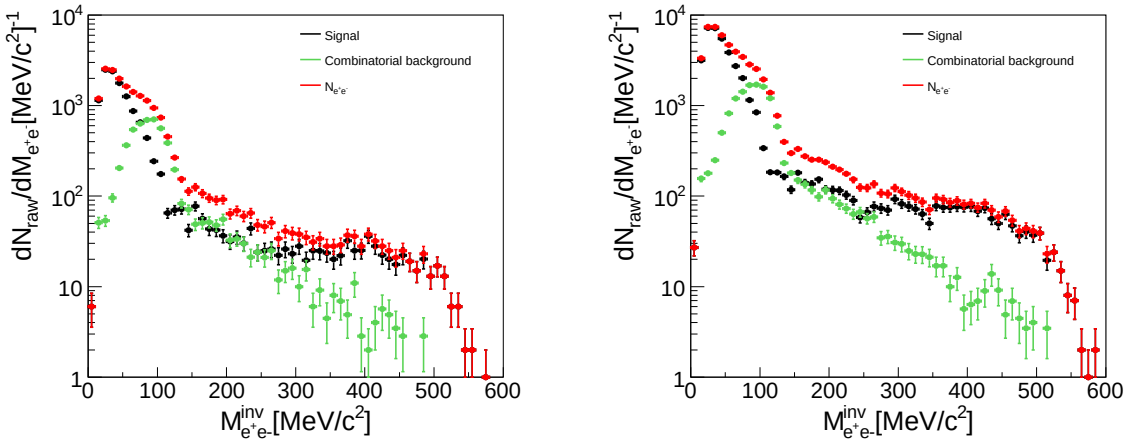

Figure 6.5: Inclusive invariant mass distribution of e^+e^- pairs for the $\pi^- PE \rightarrow Xe^+e^-$ reaction with an opening angle $\theta_{e^+e^-} > 9°$. **Left:** RICH ring finder procedure. **Right:** Backtracking analysis.

6.3.2 Closed-pair candidate rejection

In order to see the effect of the background in the final spectra, the ratio signal over background is shown in left part of Fig. 6.7. A minimum of the $S/CB_{e^+e^-}$=0.5 is obtained for $\mathrm{M}_{e^+e^-} = 110\ \mathrm{MeV/c^2}$. For invariant mass below 90 MeV/c^2 or larger than 90 MeV/c^2 the value of $S/CB_{e^+e^-}$ is larger than 1. Once the close neighbor cut α_C is applied, the reduction of the yield for the different values goes up to a factor 3 in the total yield. The yield is compared with and without the cut of α_C in the right part of Fig. 6.7. There is no much difference between the angles applied in the reduction of the yield between 3° and 7°.

Left part of Fig. 6.8 shows the inclusive invariant mass distribution with different cuts in α_C. Apart from the first cut at 3°, the difference between the different angles does not change much in the yield. The right part of Fig. 6.8 shows the significance calculated with Eq. 6.5. Studies in the significance of the different values of α_C do not show much difference between them.

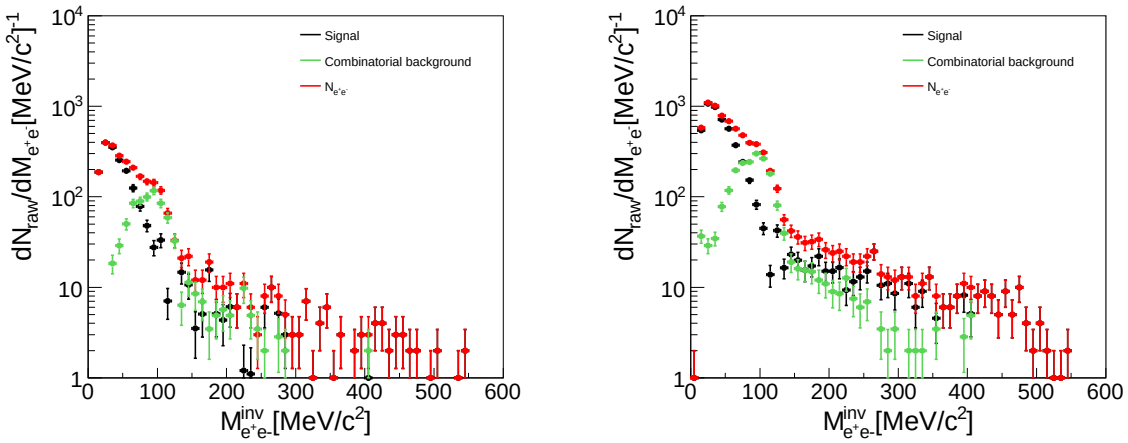

Figure 6.6: Inclusive invariant mass distribution of e^+e^- pairs for the $\pi^- C \to X e^+ e^-$ reaction with an opening angle $\theta_{e^+e^-} > 9°$. **Left:** RICH ring finder procedure. **Right:** Backtracking analysis.

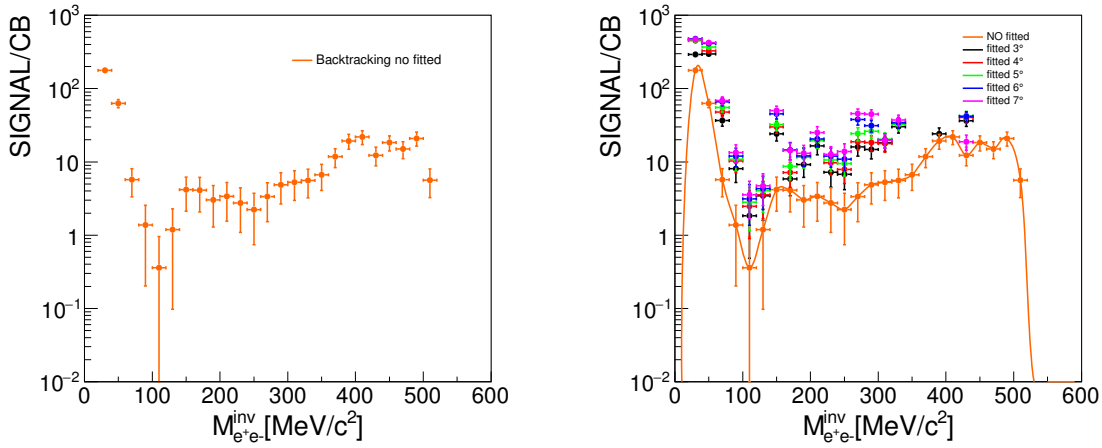

Figure 6.7: Ratio signal over background for the inclusive invariant mass distribution of e^+e^- pairs for the $\pi^- PE \to X e^+ e^-$ reaction with an opening angle $\theta_{e^+e^-} > 9°$ and Backtracking analysis. **Left:** No angle to close neighbor cut α_C. **Right:** Comparison with different values of the angle to close neighbor cut α_C.

$$\text{Sign} = \frac{S}{\sqrt{S+B}} \tag{6.5}$$

Based on the previous studies, we set a value of $\alpha_C = 6°$, which correspond to the largest S/BC. In Fig. 6.9 the inclusive invariant mass distribution for carbon and polyethylene targets are shown in left and right respectively, with an opening angle of $\theta_{e^+e^-} > 9°$ and α_C=6°. The shape is similar in both spectra, with a dominant peak at π^0 region for low invariant mass; also the uncorrelated $CB_{e^+e^-}$ is highly reduced once the cut in α_C=6° is applied, in contrast with Fig. 6.5 and Fig. 6.6 where no cut in an angle α_C was introduced. It can also be noticed the lower statistics obtained with the carbon target, something that will complicate the subtraction of carbon contributions from polyethylene target.

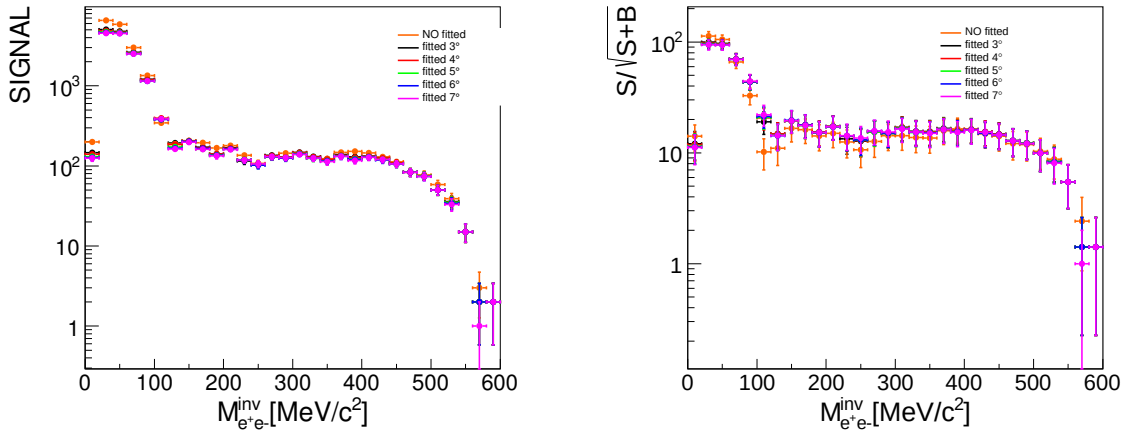

Figure 6.8: **Left:** Inclusive invariant mass distribution of e^+e^- pairs for the $\pi^- PE \to Xe^+e^-$ reaction with an opening angle $\theta_{e^+e^-} > 9°$ compared with different values of α_C for Backtracking analysis. **Right:** Significance.

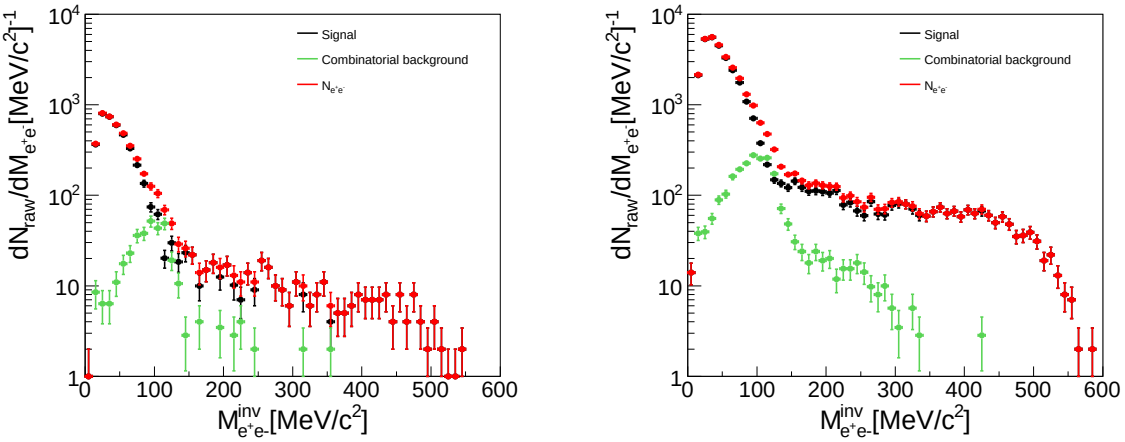

Figure 6.9: **Left:** Inclusive invariant mass distribution of e^+e^- pairs for the $\pi^- C \to Xe^+e^-$ reaction with an opening angle $\theta_{e^+e^-} > 9°$ and α_C=6° for Backtracking analysis. **Right:** Same for $\pi^- PE \to Xe^+e^-$ reaction.

6.4 Exclusive dielectron production

Besides the inclusive, the exclusive invariant mass distribution $\pi^- p \to ne^+e^-$ is also interesting because we can characterize better the production mechanism and compare later with the simulations. Since HADES at that time was not able to measure neutral particles, the neutron will be selected with the one dimensional cut in the missing mass distribution around neutron mass. However, there are more neutral particles in the final state despite neutrons. Based on the information extracted from the inclusive studies, we can notice that one of the main contributions at low invariant mass is the π^0 Dalitz decay $\left(\pi^0 \to \gamma e^+e^-\right)$. Therefore, the missing mass distributions should be a bit larger due to the photon from the π^0 Dalitz decay. Fortunately, the energy of the photon is usually small. Nevertheless, the missing mass spectra were obtained for an invariant mass larger than the π^0 of $M_{e^+e^-} > 140$ MeV/c^2, in order to remove the photon

contributions of π^0 Dalitz decay in the final state of e^+e^-. In Fig. 6.10 it is shown the missing mass distribution for invariant mass larger than $M_{e^+e^-} > 140$ MeV/c^2 for RICH ring finder procedure in the left part and Backtracking analysis in the right part. In both cases, emerges a clear peak around the neutron mass, also the higher efficiency of Backtracking analysis increase the tracks reconstructed about 40%. The combinatorial background is lower in the neutron peak region than for higher values. Once the contribution in the missing mass of π^0 Dalitz decay is removed, the only uncorrelated background comes from the $2\pi^0$, where at least two photons and two leptons are missing, and also from the η Dalitz decay where one photon is missing. It is observed in the missing mass distribution for polyethylene target that the peak does not match perfectly with the neutron mass. This shift of the neutron peak can be understood due to the energy loss of the bremsstrahlung electrons in the polyethylene target, also the interaction with bound protons can shift the neutron peak. This statement is confirmed in Fig. 6.11, where the neutron peak for the missing mass with the carbon target it is shift even towards values. Moreover, the description of the width peak can be described by the Fermi momentum of protons in carbon nucleus and the pion beam momenta distribution, see Section 3.2. In Fig. 3.2 it is shown that the resolution of the pion beam tracker is higher than the one we can obtain from HADES, but the lower efficiency forces to use average the pion beam momenta distribution. Based on the previous observations, the average pion beam momenta, the Fermi-motion of protons in carbon nucleus, and the bremsstrahlung effects, will be introduced in the simulations in order to include that effects.

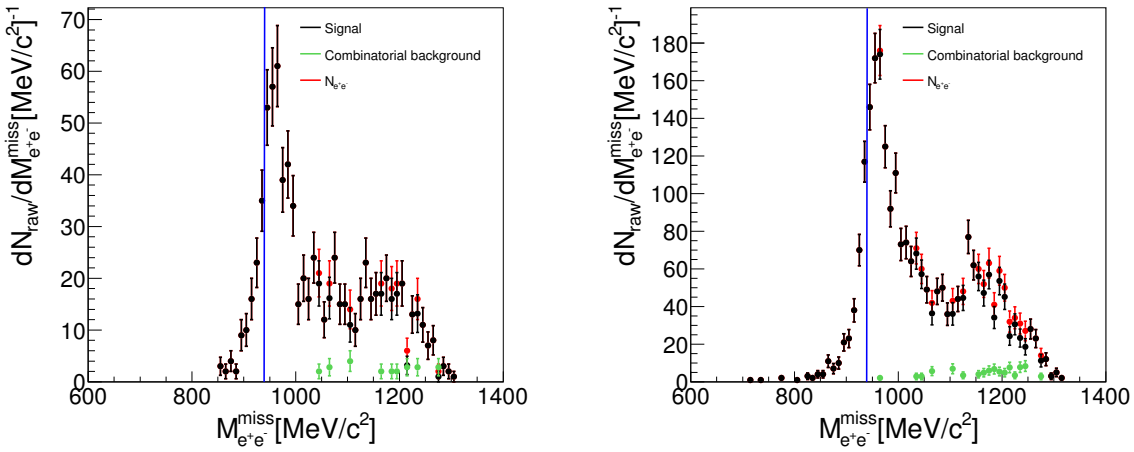

Figure 6.10: Missing mass distribution for $M_{e^+e^-} > 140$ MeV/c^2 in polyethylene target (blue line) represent the neutron mass. **Left:** RICH ring finder procedure. **Right:** Backtracking analysis

The exclusive invariant mass distribution obtained with a cut at 900 MeV/c^2 $< M^{miss}_{e^+e^-} <$ 1030 MeV/c^2 from the missing mass spectra is shown in Fig. 6.12 for carbon (left), and polyethylene (right). The combinatorial background is subtracted very efficiently, especially with the cut in the α_C=6°, which subtract very efficiently the peak in the π^0 region due to the uncorrelated background, see Fig. 6.13.

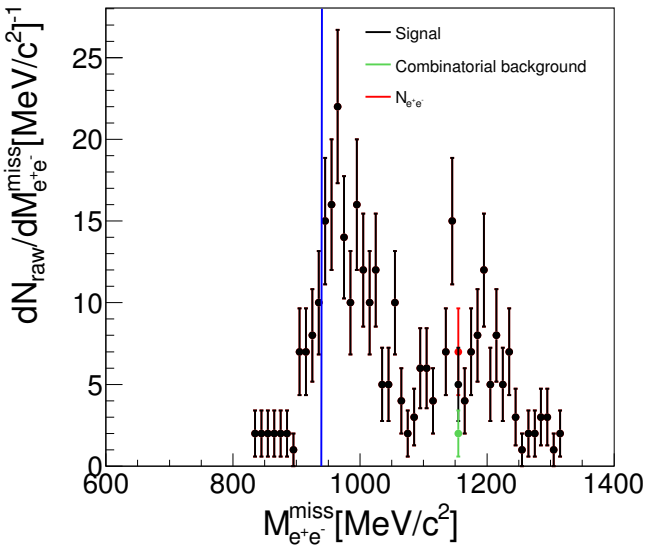

Figure 6.11: Missing mass distribution for $M_{e^+e^-} > 140$ MeV/c^2 in carbon target for Backtracking analysis. The (blue line) represent the neutron mass.

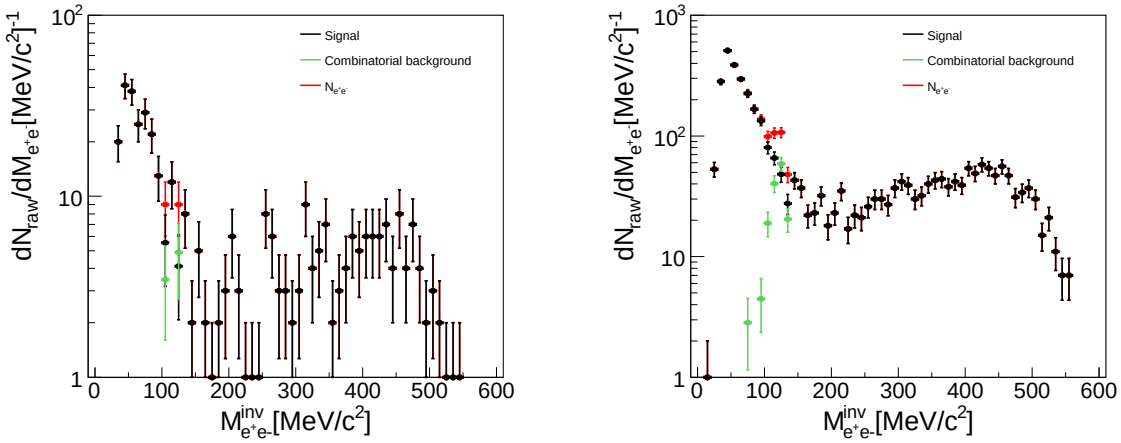

Figure 6.12: Exclusive invariant mass distribution after selection cut in the missing mass 900 MeV/c^2 $< M^{miss}_{e^+e^-} <$ 1030 MeV/c^2 with α_C=6° for Backtracking analysis. **Left:** Carbon target. **Right:** Polyethylene target.

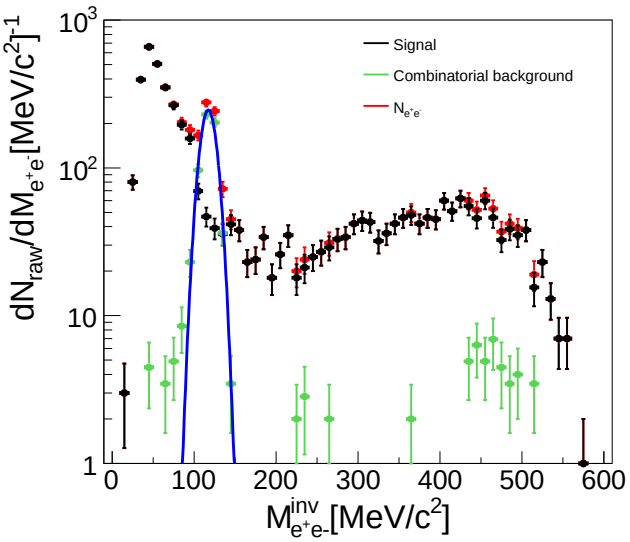

Figure 6.13: Exclusive invariant mass distribution after selection cut in the missing mass $900\,\mathrm{MeV/c^2} < \mathrm{M}^{\mathrm{miss}}_{e^+e^-} < 1030\,\mathrm{MeV/c^2}$ without cut in α_C for Backtracking analysis and Polyethylene target.

Chapter 7

Data normalization and carbon subtraction

In the beginning, the experiment was proposed to run with a liquid hydrogen target. Unfortunately, due to problems with the cooling system of the liquid hydrogen and also the produced background from the target holders, the liquid hydrogen target was substitute by a polyethylene target $(C_2H_4)_n$. The idea was to use also a (C) carbon target as a reference, and after to subtract the carbon contribution from the polyethylene target, and therefore, obtain the pure pion hydrogen interaction, see Section 7.2.1. The analysis of pion proton elastic scattering is very interesting for the current experiment since those results can be used also for the experimental yield normalization, this will be discussed in Section 7.2.2.

7.1 Normalization procedure

The normalization of the experimental measured yield to a well know reaction cross section is crucial, since allow us to compare the normalized e^+e^- spectra with the simulated model calculations. In principle, the absolute normalization of an experiment could be done using the number of beam particles from START detector N_{beam} and the properties of the target used. I could obtain the value of N_{beam} particles using the START detector, where the information is stored in so-called scalers. But there was electron contamination in the pion production target, (see Section 2.5), around 10%. Also, START detector area was larger than the target detector; simulation studies conclude that only a 66% of the pions hitting the START detector also hits the target. Therefore, due to technical problems mentioned above, this technique was refuse, and the yield was normalized by the $\pi^- p$ elastic scattering cross section.

7.2 Elastic scattering

The selection of $\pi^- p$ elastic scattering events from PE target is made with two selection cuts: The energy and momentum conservation gives the following condition for elastic scattering.

$$\Delta\varphi = |\varphi_\pi - \varphi_p| = 180^\circ \tag{7.1}$$

Where φ is the azimuthal angle between a pion and a proton. The particle selection of π^- and p is done by its mass reconstruction from Eq. 3.11, with a window in the velocity of $\beta = \pm 0.2$:

$$\left(\frac{p}{\sqrt{m^2+p^2}} - 0.2 < \beta < \frac{p}{\sqrt{m^2+p^2}} + 0.2 \right) \tag{7.2}$$

Finally, I can isolate the pions and the protons from the elastic scattering of PE target to further normalize the yield with the number of pions.

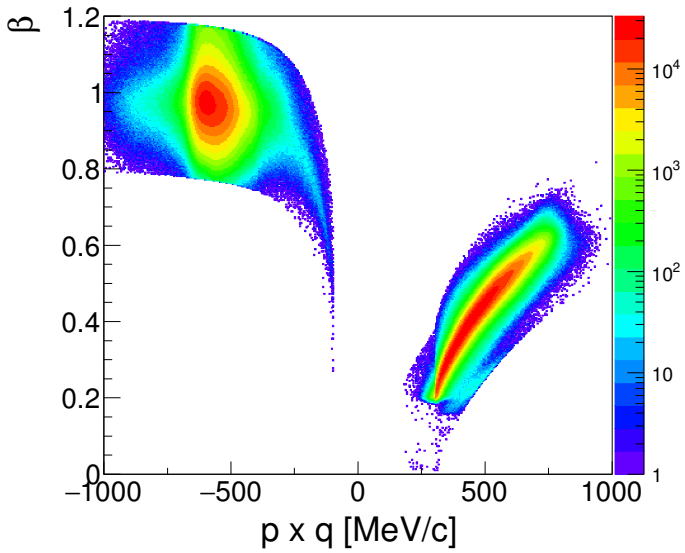

Figure 7.1: Final selection of $\pi^- p$ candidates from pion induced reactions with PE target at a pion beam momenta of 690 MeV/c.

7.2.1 Subtraction of carbon contribution

In order the subtract the carbon contribution from polyethylene; first I need to know the number of elastic events in the HADES acceptance $\mathbb{N}_{el}^{acc}$ for each reaction. As we mentioned before, the known reaction kinematics impose certain constraints on the angles of the scattered protons in an elastic process. We need to distinguish between elastic scattering

$$\pi^- + p \rightarrow \pi^- + p \tag{7.3}$$

and quasi-elastic scattering

$$\pi^- + C \rightarrow \pi^- + p + X \tag{7.4}$$

I can use the difference between azimuthal angle φ of pion and proton since due to momentum conservation, the ideal conditions of elastic scattering in Eq. 7.3 is that the difference $\Delta\varphi = |\varphi_\pi - \varphi_p| = 180°$, which at that value emerges as a Diracs $\delta-$function. For the quasi-elastic scattering in Eq. 7.4 it produces a flat distribution due to residual particles rather than a δ peak at $\Delta\varphi = 180°$. In a real experiment, this δ distribution should be smeared to normal distribution due to finite spatial resolution and random fluctuations. Another option to select elastic scattering events is to calculate the missing mass spectrum of $\pi^- p$ pair, see Eq. 7.5.

$$m^2_{\text{miss}} = g_{\mu\nu} \left(P_{\text{out}} - P_{\text{in}}\right)^\mu \left(P_{\text{out}} - P_{\text{in}}\right)^\nu \tag{7.5}$$

where $g_{\mu\nu} = diag(0, -1, -1, -1)$ is the metric tensor, the four-momentum vector will be $P = (E, \vec{p})$ and for the magnitude of three-vector $p = |\vec{p}|$. The Lorentz vector for the incoming pion from the beam and the proton from the target P_{in} (neglecting the thermal motion of nucleons) is:

$$P_{\text{in}} = \left(\sqrt{m_\pi^2 + p_{\text{beam}}^2} + m_p, \vec{p}_{\text{beam}} \right) \tag{7.6}$$

The Lorentz vector P_{out} from the outgoing pion and proton:

$$P_{\text{out}} = \left(\sqrt{m_\pi^2 + p_\pi^2} + \sqrt{m_p^2 + p_p^2}, \vec{p}_\pi + \vec{p}_p \right) \tag{7.7}$$

For the elastic scattering events should have a value of the missing mass $m_{miss}^2 = 0$ MeV/c^2 because all the particles that participated in the reaction are detected. Properties of the targets need to be taken into account to subtract the number of events from elastic and quasi-elastic scattering. A description of the targets is shown in Fig. 2.2. The number of elastic events is obtained from

$$\mathbb{N}_{events} = N_{\text{beam}} \cdot \sigma \cdot n_{\text{target}} \cdot l_{\text{target}} \tag{7.8}$$

where N_{beam} is the number of incoming pions from the beam, σ is the cross section of the reaction, n_{target} is density of the target and l_{target} is the length of the target. The n_{target} is defined as:

$$n_{\text{target}} = \frac{\rho \cdot N_A}{M} \tag{7.9}$$

where ρ is the mass density of target, N_A is Avogadro constant and M is the molar mass of the target. All the values are known for both targets, see Table 2.1. The relation between $\mathbb{N}_{events}^{PE}$ number of interactions of pion with polyethylene and the $\mathbb{N}_{events}^{C}$ number of interactions of pion with a carbon target to the number of pion proton elastic scattering events $\mathbb{N}_{events}^{H}$ is obtained by the following relation:

$$\mathbb{N}_{events}^{H} = \mathbb{N}_{events}^{PE} - f \cdot \mathbb{N}_{events}^{C} \tag{7.10}$$

The N_{beam} is the only value we need to obtain, but unfortunately it was not possible to obtain a correct value of the number of beam particles due to the problems mentioned before. Considering the technical issues, a promising solution was to introduce a free parameter k. This parameter will adjust the data by multiplying the measured number of detected pions to get the correct number of events of elastic scattering. Once the k parameter is obtained, the scaling factor f can be calculated and therefore, extract the real number of elastic scattering events $\mathbb{N}_{events}^{H}$, see Eq. 7.10. The f factor can be decomposed by the product of the f_1 scaling factor which is related to the measurement of the number of events in START detector corrected with the death time $1 - t_{\text{dead}}$, see Eq. 7.11, and the f_2 scaling factor related to the properties of targets, see Eq. 7.12. The polyethylene molecule consists of two carbon atoms, so the value 2 needs to be introduced in the numerator of Eq. 7.12. The value k from Eq. 7.11 is the unknown parameter.

$$f_1 = \frac{k^{\text{PE}} \cdot N_{\text{START}}^{\text{PE}} \cdot \left(1 - t_{\text{dead}}^{\text{C}}\right)}{k^{\text{C}} \cdot N_{\text{START}}^{\text{C}} \cdot \left(1 - t_{\text{dead}}^{\text{PE}}\right)} \tag{7.11}$$

$$f_2 = \frac{l_{\text{target}}^{PE} \cdot \frac{2\rho^{PE}}{M^{PE}}}{l_{\text{target}}^{C} \cdot \frac{\rho^{C}}{M^{C}}} \tag{7.12}$$

The value of the scaling factor $f_2 = 0.7823$ is calculated with the measured values extracted from Table 2.1.

	Polyethylene target	Carbon target
p_{beam} [MeV/c]	690	690
N_{trigger} $[\cdot 10^7]$	101.267	13.404
N_{START} $[\cdot 10^9]$	47.118	6.431
$1 - t_{\text{dead}}$	0.767	0.834

Table 7.1: Values of the scaling variables for each target and beam momentum.

To obtain the scaling factor f_1 it is needed first, to extract the unknown factor k. For that the following method will be use :

- First, in the spectrum of $\Delta\varphi$, see Fig. 7.2, there is a peak corresponding from elastic scattering between angles $(175°, 185°)$. Therefore, the rest of the spectra represent quasi-elastic scattering, see Eq. 7.4, events due to interactions of pions with the carbon nuclei in the polyethylene target. That means I can scale the spectrum of $\Delta\varphi$ for the rest angles for polyethylene and carbon target in the range $\Delta\varphi \in (0°, 175°) \bigcup (185°, 360°)$. After, I can subtract the number of events and obtain the scaling factor f corresponding to the region $\Delta\varphi \in (175°; 185°)$.

- Same procedure can be done for the missing mass spectrum, see Fig. 7.3. In that case the peak due to elastic scattering events is in the range of $m^2_{miss} \in (-0.02; -0.01)$ GeV^2/c^2. Therefore, I can scale for the rest of missing mass range $m^2_{\text{miss}} \in (-0.6; -0.02)$ GeV^2/c^2, subtract the number of events and obtain the scaling factor f. We can observed that there is a second peak due to missing mass of π^0 at $m^2_{\text{miss}} \in (0.01; -0.06)$ GeV^2/c^2, and above that again contribution of pion carbon interaction.

- In the last method, I used both cuts, see Fig. 7.4. First into the $\Delta\varphi$ for $\Delta\varphi \in (175°, 185°)$) and with the obtained spectra another cut for $m^2_{\text{miss}} \in (-0.02, -0.01)$ GeV^2/c^2. As a result the final scaling factor $f_{m^2_{\text{miss}}|\Delta\varphi}$ is obtained. Results of all factors for the different methods are shown in the Table 7.2.

p_{beam} [MeV/c]	690
$f_{\Delta\varphi}$	5.068
$\left(k^{\text{PE}}/k^{\text{C}}\right)_{\Delta\varphi}$	0.962
$f_{m^2_{\text{miss}}}$	4.394
$\left(k^{\text{PE}}/k^{\text{C}}\right)_{m^2_{\text{miss}}}$	0.834
$f_{m^2_{\text{miss}}}/\Delta\varphi$	4.583
$\left(k^{\text{PE}}/k^{\text{C}}\right)_{m_{\text{miss}}\,|\Delta\varphi}$	0.870

Table 7.2: Numerical values of the factors f and the resulting ratio $k^{\text{PE}}/k^{\text{C}}$

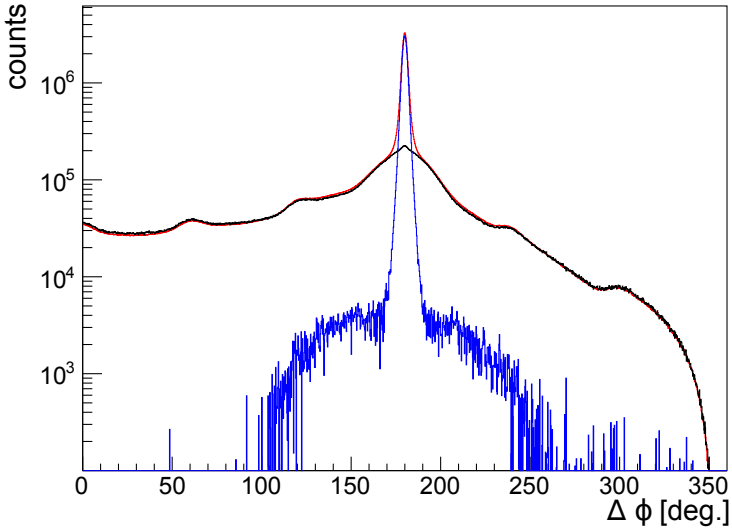

Figure 7.2: Measured $\Delta\varphi$ spectra with polyethylene target red line and scaled spectra for carbon target black line. The subtracted spectrum $PE - f_{\Delta\varphi} \cdot C$ is displayed with blue line.

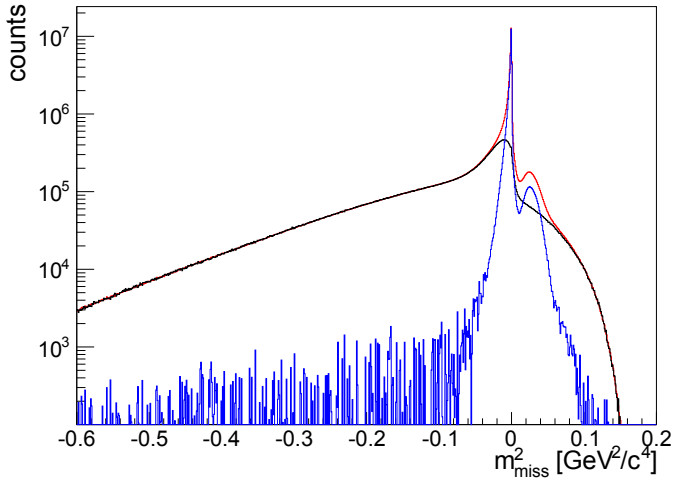

Figure 7.3: Measured m^2_{miss} spectra with polyethylene target red line and scaled spectra for carbon target black line. The subtracted spectrum $PE - f_{m^2_{\text{miss}}} \cdot C$ is displayed with blue line.

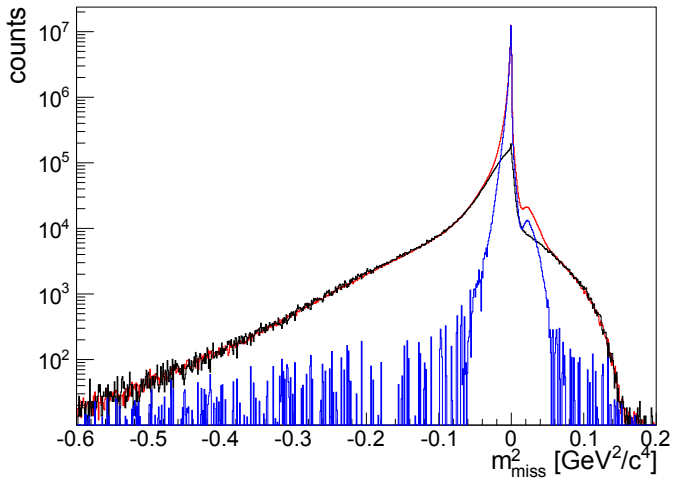

Figure 7.4: Measured m^2_{miss} spectra after cut $\Delta\varphi \in (175°, 185°)$ with polyethylene target red line and scaled spectra for carbon target black line. The subtracted spectrum $PE - f_{m^2_{miss}} \cdot C$ is displayed with blue line.

7.2.2 Normalization

The experimental angular distributions are compared to a simulation of elastic scattering from a Monte Carlo event generator for hadronic interaction called PLUTO [103]. For the input of the simulations, an angular distribution taken from [110] was used. In order to obtain the detector response, the simulated data is run throw usual chain of HGEANT (GEANT simulation with HADES geometry) and HYDRA (Hades System for Data Reduction and Analysis), afterwards, the reconstruct tracks are obtained. Comparison between the real and simulated data in 4π full solid angle, and in HADES acceptance allows to obtain the correction factor, see Fig. 7.5. This factor will be used to correct the elastic scattering events, see Eq. 7.13.

$$Correction(\theta) = \frac{N_{4\pi}(\theta)}{N_{\mathrm{HADES}}(\theta)} \tag{7.13}$$

In order to obtain the normalization factor F, see Eq. 7.14, I use the differential cross section as a function of pion polar angle in the centre of mass frame. First, carbon is subtracted from polythene using the scaling factor $f_{m^2_{\mathrm{miss}}}/\Delta\varphi$ from Table 7.2 and corrected for efficiency and HADES acceptance using the correction factor from Fig. 7.5.

$$F = \frac{\sigma_{acc}}{\mathbb{N}_{events}} \tag{7.14}$$

The differential cross section $d\sigma/d\Theta_{CM}$ as a function of pion polar angle in the center of the mass frame was compared with reference values of the differential cross section from the SAID [59] database, which is a Partial Wave Analysis of existing data. The values were calculated using the model WI08. The yield of the spectra was scaled with the simulated one in a way that there is the same cumulative differential cross section for $\Theta_{CM} \in (61° - 109°)$ as for the SAID database, see Fig. 7.6. In Fig. 7.6, we can observe that the reconstructed elastic scattering events from real data below $\Theta_{CM} < 60°$, are not well described. The reasons can be the discrepancies between the angular distribution used from [110], and the one from the SAID database, as well, the difference of the energy collisions in the scattering due to the broad spectrum of p_{beam}. The

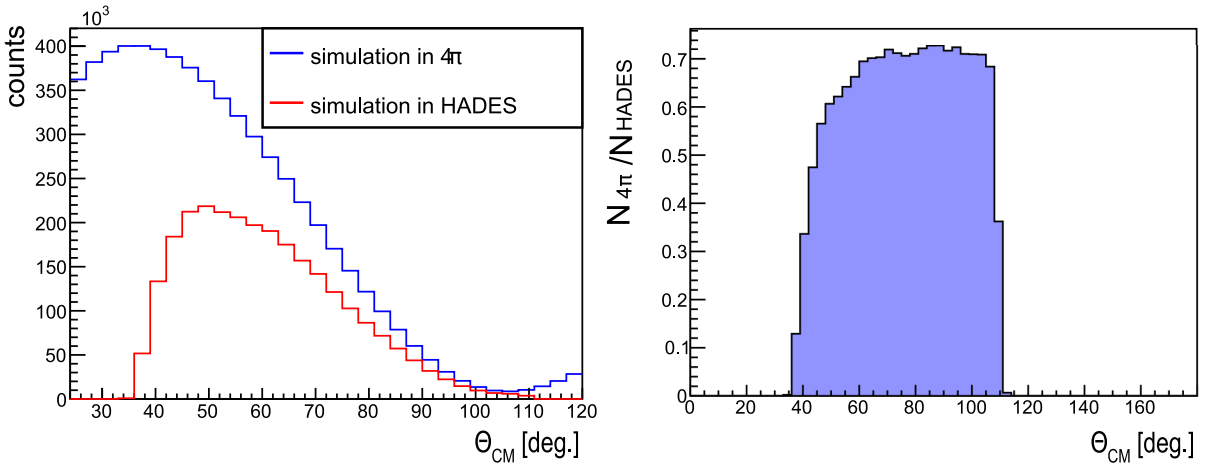

Figure 7.5: Correction factors simulations. **Left:** Comparision between simulations in 4π full solid angle (blue line) and after chain reconstruction HADES acceptance (red line). **Right:** Correction factors.

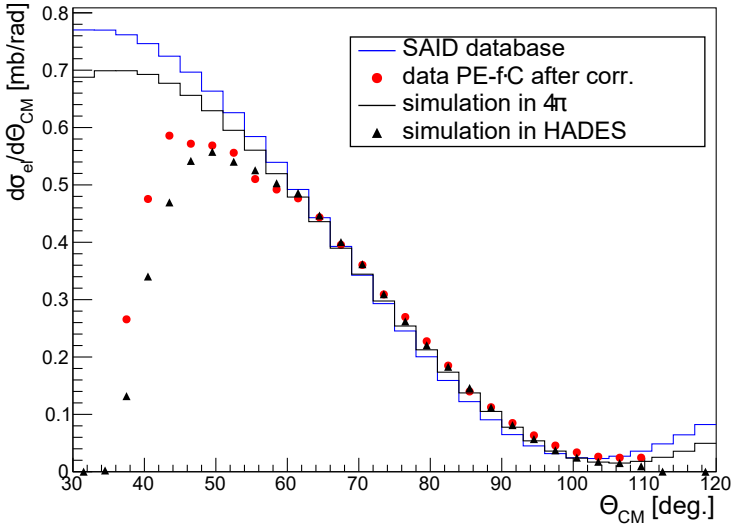

Figure 7.6: Spectra of differentail cross section $d\sigma/d\Theta_{CM}$ for $p_{beam} = 690$ MeV/c.

normalization factor F is calculated as the averaged ratio between the experimental data and the SAID predictions in the HADES acceptance. The final normalization factors for differential cross section and the corrected number of elastic scattering events per number of registered beam pions can be found in Table 7.3.

p_{beam} [MeV/c]	$\mathbb{N}^{PE}_{events} \cdot 10^6$	$\mathbb{N}^{PE}_{events}\,(61° - 109°)^{corr} \cdot 10^6$	$\sigma\,(61° - 109°)$ [mb]	$\frac{\sigma}{\mathbb{N}_{events}} \cdot 10^{-7}$ [mb]
690	776.82	31.01	3.007	0.97

Table 7.3: Normalization factors

Chapter 8

Theoretical background for pion-induced reaction

Based on hypotheses from Section 1.4, the theoretical approaches for the study of $\pi N \rightarrow Ne^+e^-$ reaction will be described in this chapter. One of the advantages of pion induced reactions is the ability to control the energy in a πN collision and sit on a particular resonance peak, which allows to excited particular resonance contribution. However, even in pion-induced reactions it is not possible to completely avoid the problem of overlapping resonance, therefore a detailed measurement of Partial Waves Analysis (PWA) of the pionic final state of 2π is necessary to allow the separation of the different resonance contributions [28; 111]. This measurement is crucial for the input of PWA. A described study of the PWA carried out by the Cracow team will be described as well in this chapter [111].

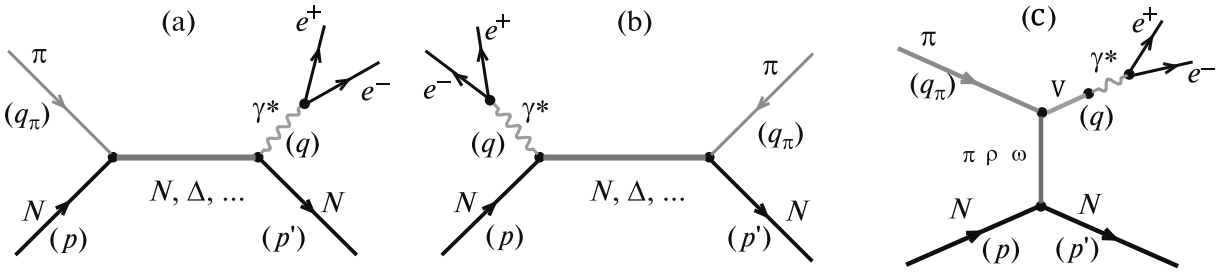

Figure 8.1: Feynman diagrams contributing to the process $\pi N \rightarrow Ne^+e^-$ in a) s-channel. b) u-channel. c) t-channel.

In Fig. 8.1 we can see the Feynman diagrams contributions to the process $\pi N \rightarrow Ne^+e^-$ in (a) the s-channel: Baryon resonance contributions decaying to dilepton pair and a nucleon. (b) t-channel: The dilepton decay is emitted before the meson-baryon vertex by a nucleon exchange. The (c) u-channel is the same as t-channel but the dilepton decay is mediated by a pion. Hence, studying studying the different channels we can have access to different electromagnetic form factors (eTFF).

8.0.1 Dalitz decay of baryonic resonances

In Fig. 1.31 is observed that the $\pi^- N$ reaction is dominated by resonance production among other sources which are described in Section 1.2.3. Therefore, it is necessary a detailed description of the Dalitz decay of baryonic resonance ($N^* \rightarrow Ne^+e^-$) to measure its dilepton contribution. The dilepton decay rate of a resonance N^* can be calculated using Eq. 8.1 [112].

$$d\Gamma\left(N^* \to Ne^+e^-\right) = \Gamma\left(N^* \to N\gamma^*\right) M\Gamma\left(\gamma^* \to e^+e^-\right) \frac{dM^2}{\pi M^4} \tag{8.1}$$

where $M\Gamma\left(\gamma^* \to e^+e^-\right)$ is the decay width of a virtual photon γ^* into the dilepton pair with invariant mass M given by Eq. 8.2.

$$M\Gamma\left(\gamma^* \to e^+e^-\right) = \frac{\alpha}{3}\left(M^2 + 2m_e^2\right)\sqrt{1 - \frac{4m_e^2}{M^2}} \tag{8.2}$$

Therefore, we only need to know the decay width $\Gamma\left(N^* \to N\gamma^*\right)$ which is described using the parametrization of Krivoruchenko [112], see Eq. 8.3, where γ^* is a massive virtual photon and the decay rate is in terms of magnetic (M), electric (E), and Coulomb (C) form factor.

$$\Gamma\left(N^*_{(\pm)} \to N\gamma^*\right) = \frac{9\alpha}{16}\frac{(l!)^2}{2^l(2l+1)!}\frac{m_\pm^2\left(m_\mp^2 - M^2\right)^{l+1/2}\left(m_\pm^2 - M^2\right)^{l-1/2}}{m_*^{2l+1}m^2} \times \left|G_T\left(q^2\right)\right|^2 \tag{8.3}$$

where m_* is the nucleon resonance mass, m the nucleon mass, $m_\pm = m_* \pm m$ and $M^2 = q^2$ the photon four-momentum. The sum of the total magnetic, electric and Coulomb form factors can be grouped in the so called effective form factor $\left|G_T\left(q^2\right)\right|^2$, see Eq. 8.4.

$$\left|G_T\left(q^2\right)\right|^2 = \left(\frac{l+1}{l}\left|G_{M/E}^{(\pm)}\right|^2 + (l+1)(l+2)\left|G_{E/M}^{(\pm)}\right|^2 + \frac{M^2}{m_*^2}\left|G_C^{(\pm)}\right|^2\right) \tag{8.4}$$

The signs $\pm$ are the natural parity $(1/2^-, 3/2^+, 5/2^-, \ldots)$ and abnormal parity $(1/2^+, 3/2^-, 5/2^+, \ldots)$ there is a symmetry between normal and abnormal parity: $m_+ \leftrightarrow m_-, G_M^{(+)} \leftrightarrow G_E^{(-)}, G_E^{(+)} \leftrightarrow G_M^{(-)}, G_C^{(+)} \leftrightarrow G_C^{(-)}$. The equation Eq. 8.3 is valid for $l > 0$, with $(J = l + 1/2)$.

For $l = 0 (J = 1/2)$, we obtain:

$$\Gamma\left(N^*_{(\pm)} \to N\gamma^*\right) = \frac{\alpha}{8m_*}\left(m_\pm^2 - M^2\right)^{3/2}\left(m_\mp^2 - M^2\right)^{1/2}\left(2\left|G_{E/M}^{(\pm)}\right|^2 + \frac{M^2}{m_*^2}\left|G_C^{(\pm)}\right|^2\right) \tag{8.5}$$

For $l = 1 (J = 3/2)$, we obtain the decay width of the $\Delta(1232)$ resonance [113], see Eq. 8.6.

$$\Gamma\left(\Delta \to N\gamma^*\right) = \frac{\alpha}{16}\frac{(m_\Delta + m_N)^2}{m_\Delta^3 m_N^2}\left((m_\Delta + m_N)^2 - M^2\right)^{1/2}\left((m_\Delta - m_N)^2 - M^2\right)^{3/2}\left(G_M^2 + 3G_E^2 + \frac{M^2}{2m_\Delta^2}G_C^2\right) \tag{8.6}$$

A detailed description about $\Delta(1232)$ resonance the will be given in Section 9.1.2

8.0.2 Form factors of baryonic Dalitz decay

The baryonic Dalitz decay width is described by Eq. 8.3, to gives a full description of the process the form factors need to be known. The electromagnetic form factors EMFF's tell us how different the interaction of a particle is if we treat it as a point-like or as a particle with a defined structure. Therefore, they give a powerful probe to study the internal structure of hadronic matter. There is much information about the form factors in the space-like region, even a new technique based on polarization can distinguishes between electric and magnetic EMFF's. Unfortunately, in the time-like region, the transition form factors are scare and restricted for $q^2 > 4m_p^2 \approx 3.6$ GeV^2 since where obtained in $p\bar{p}$ annihilation experiments [114]. Two models and interpretations for the nucleon EMFF's in the time-like region will be described below.

Photon-point "QED calculation"

The function $\left|G_T\left(q^2\right)\right|$ depends on the EMFF's given by Eq. 8.4. Those form factors are described as a function of the squared momentum transfer q^2. It is important to notice that the Eq. 8.3 vanish for $q^2 = (m_\star - m)^2$, which restrict the higher limit allowed of q^2 for the reaction occurred. Usually, the EMFF's in the time-like region are related to the experimental results of the form factor at the photon point $q^2 = 0$, this model implies that there is no q^2 dependence and use a fixed resonance masses, therefore, the EMFF's become constant. The model it is usually known as QED approximation or a constant form factor which describe a point-like particle. Using this description we can relate the decay width of a baryon resonance of a virtual photon to a real photon in the $q^2 = 0$ limit. Hence, the radiative decay can be obtained in the limit of vanishing virtual photon mass γ^*, when $M \to 0$ (real photon). In this limit we get $|G_T(0)|^2$ and therefore, Eq. 8.5 for $J = 1/2$ is equal to:

$$\Gamma^{N^*\to N\gamma} = \frac{\alpha}{4m_\star} m_\pm^{3/2} m_\mp^{1/2} \left|G_T(0)\right|^2 \tag{8.7}$$

and for $J > 3/2$:

$$\Gamma^{N^*\to N\gamma} = \frac{9\alpha}{8} \frac{(l!)^2}{2^l(2l+1)!} \frac{m_\mp^{l+1/2} m_\pm^{l+3/2}}{m_\star^{2l+1} m^2} \left|G_T(0)\right|^2 \tag{8.8}$$

Comparing Eq. 8.5 with Eq. 8.7 the Dalitz decay width of baryonic resonance with $J = 1/2$ can be written as follow:

$$\Gamma^{N^*\to N\gamma^*}\left(q^2\right) = \frac{\left(m_\pm^2 - M^2\right)^{3/2}\left(m_\mp^2 - M^2\right)^{1/2}}{m_\pm^{3/2} m_\mp^{1/2}} \frac{\left|G_T\left(q^2\right)\right|^2}{\left|G_T(0)\right|^2} \times \Gamma^{N^*\to N\gamma} \tag{8.9}$$

The same with Eq. 8.6 and Eq. 8.8 gives the Dalitz decay width of baryonic resonance with $J = 3/2$

$$\Gamma^{N^*\to N\gamma^*}\left(q^2\right) = \frac{\left(m_\mp^2 - M^2\right)^{l+1/2}\left(m_\pm^2 - M^2\right)^{l-1/2}}{m_\mp^{l+1/2} m_\pm^{l-1/2}} \frac{\left|G_T\left(q^2\right)\right|^2}{\left|G_T(0)\right|^2} \times \Gamma^{N^*\to N\gamma} \tag{8.10}$$

As a result the decay width for the resonance N(1520) with $\left(J^P = 3/2^-\right)$ is:

$$\Gamma^{N(1520)\to N\gamma^*}\left(q^2\right) = \frac{\left(m_+^2 - M^2\right)^{3/2}\left(m_-^2 - M^2\right)^{1/2}}{m_+^{3/2} m_-^{1/2}} \frac{\left|G_T\left(q^2\right)\right|^2}{\left|G_T(0)\right|^2} \times \Gamma^{N(1520)\to N\gamma} \tag{8.11}$$

and for the resonance N(1535) with $\left(J^P = 1/2^-\right)$:

$$\Gamma^{N(1535)\to N\gamma^*}\left(q^2\right) = \frac{\left(m_+^2 - M^2\right)^{3/2}\left(m_-^2 - M^2\right)^{1/2}}{m_+^{3/2} m_-^{1/2}} \frac{\left|G_T\left(q^2\right)\right|^2}{\left|G_T(0)\right|^2} \times \Gamma^{N(1535)\to N\gamma} \tag{8.12}$$

Based on the previous assumptions, the Dalitz decay width for small virtual photon mass can be approximate as:

$$\Gamma^{N^\star\to N\gamma^*} \sim \Gamma^{N^\star\to N\gamma} \tag{8.13}$$

and since the Dalitz decay width it depends only by the effective form factor $\left|G_T\left(q^2, W\right)\right|$ we obtain the following relation:

$$\left|G_T\left(q^2\right)\right|^2 \sim \left|G_T(0)\right|^2 \tag{8.14}$$

Therefore Eq. 8.11 and Eq. 8.12 are simplified to:

$$\Gamma^{N(1520)\to N\gamma^*}\left(q^2\right) = \frac{\left(m_+^2 - M^2\right)^{3/2}\left(m_-^2 - M^2\right)^{1/2}}{m_+^{3/2} m_-^{1/2}} \times \Gamma^{N(1520)\to N\gamma} \tag{8.15}$$

$$\Gamma^{N(1535)\to N\gamma^*}\left(q^2\right) = \frac{\left(m_+^2 - M^2\right)^{3/2}\left(m_-^2 - M^2\right)^{1/2}}{m_+^{3/2} m_-^{1/2}} \times \Gamma^{N(1535)\to N\gamma} \tag{8.16}$$

If we know the decay width of $\Gamma_{N^*\to N\gamma^*}$, using the factorization prescription from [115],[116] the dilepton rate can be related to its decay width to a virtual photon as follow:

$$\frac{d\Gamma^{N^*\to N\mathrm{e}^+\mathrm{e}^-}}{dM} = \frac{2\alpha}{3\pi}\frac{1}{M}\Gamma^{N^*\to N\gamma^*}(M) \tag{8.17}$$

therefore using the relation from Eq. 8.13 the Eq. 8.17 is transform to:

$$\frac{d\Gamma^{N^*\to N\mathrm{e}^+\mathrm{e}^-}}{dM} = \frac{2\alpha}{3\pi}\frac{1}{M^2}\Gamma^{N^*\to N\gamma}(M) \tag{8.18}$$

For $\Gamma^{N^\star\to Ne^+e^-}$ it will be given by integrating the function:

$$\Gamma'^{N^\star\to Ne^+e^-} = \frac{d\Gamma^{N^\star\to Ne^+e^-}}{dM} \tag{8.19}$$

as a consequence

$$\Gamma^{N^*\to Ne^+e^-}(m_\star) = \int_{2m_e}^{m_\star - m} \Gamma'^{N^*\to N\gamma}(M, m_\star)dM \tag{8.20}$$

Hence, the Dalitz decay width is given by the integral of Eq. 8.18 in the kinematic region $4{m_e}^2 \le q^2 \le (m_\star - m)^2$.

$$\Gamma^{N^*\to Ne^+e^-}(m_\star) = \int_{2m_e}^{m_\star - m} \frac{2\alpha}{3\pi}\frac{1}{M}\Gamma^{N^*\to N\gamma}(M, m_\star)dM \tag{8.21}$$

$$\Gamma^{N^\star\to Ne^+e^-} \sim \frac{2\alpha}{3\pi}\Gamma^{N^\star\to N\gamma}\ln\left(\frac{m_\star - m}{2m_e}\right) \tag{8.22}$$

For instance, with a resonance mass of $m_\star = 1520$ MeV/c^2, $m = 938$ MeV/c^2 and $m_e = 0.511$ MeV/c^2

$$\Gamma^{N^\star\to Ne^+e^-} \sim 1.35\alpha\Gamma^{N^\star\to N\gamma} \tag{8.23}$$

Using the relation given in Eq. 8.23 we can calculate the Dalitz decay branching ratio knowing the one from radiative decays. In Table 8.1 we can see the values of Dalitz decay width from PDG with large uncertainties and from Bonn-Gatchina PWA analysis, which will be described later in this Chapter.8.0.4. Also, values of effective form factors for N(1520) and N(1535) are calculated using formulas Eq. 8.11 and Eq. 8.12 respectively.

The Fig. 8.2 shows the differential invariant mass of Dalitz decay where the different spin and parity influence substantially in the mass spectrum. For instance, the resonance $J^P = 3/2^-$ resonance (e.g., N(1520)) gives the largest contribution at high invariant mass, while the $J^P = 5/2^-$ gives the smallest.

		$N(1520)^0$	$N(1535)^0$
PDG	BR (N* $\to n\gamma$)	$0.3 - 0.53\%$	$0.01 - 0.25\%$
Bonn-Gatchina	BR (N* $\to n\gamma$)	0.23%	0.35%
	Total width (MeV)	114	116
	Partial width (MeV)	0.26	0.4
	BR (N* $\to ne^+e^-$)	$2.3 \cdot 10^{-5}$	$3.5 \cdot 10^{-5}$
	$G_T(0)$	10^3 MeV	0.33

Table 8.1: The second row gives the PDG branching ratios for the N(1520) and N(1535) radiative decays. The next rows concern the Bonn-Gatchina PWA and display the radiative branching ratio, total width, radiative partial width, effective form factor, and Dalitz decay branching ratios.

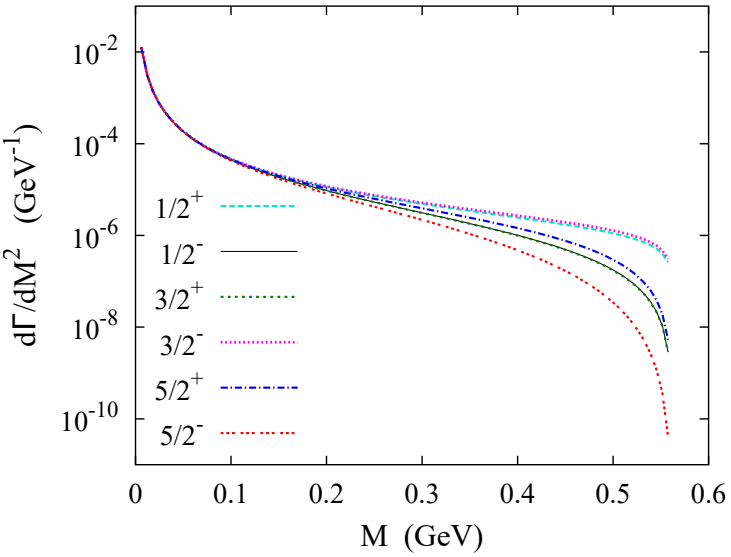

Figure 8.2: Differential Dalitz decay width of hypothetical baryon resonances with mass $m_* = 1.5$ GeV, photonic width $\Gamma_{R\to N\gamma} = 0.006$ GeV and with various spin-parities [116].

Vector Dominance Model (VDM)

Another model to calculate the electromagnetic form factors EMFF's is the Vector Dominance Model (VDM), see Fig. 8.3, which was already introduced in the Section 1.2.2. This model treats the baryon electromagnetic current like a vector meson (ρ, ω, ϕ), having the same quantum number as the virtual photon $J^P = 1^-$. Therefore, electromagnetic form factors EMFF's of a baryonic Dalitz decay will be parametrize assuming a VDM throw vector meson.

The dilepton decay of a vector meson is determined by the decay width [117]:

$$\Gamma_{V\to e^+e^-}(M) = \frac{c_V}{M^3}\sqrt{1-\frac{4m_e^2}{M^2}}\left(1+\frac{m_e^2}{M^2}\right) \tag{8.24}$$

where c_V is related to the branching ratio at pole mass.

8.0.3 Partial waves analysis of $\pi^- p$ reaction

It is already known the importance of pion scattering on nucleon in the study of baryon resonance. However, also high precision experiments using electron and photon beams are able

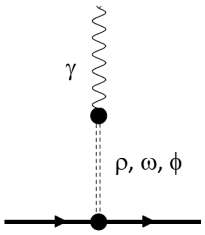

Figure 8.3: Vector Dominance Model. The electromagnetic interaction is mediated by vector mesons.

to produce resonances where the pion-nucleon scattering are not able due to the low coupling. This generation of experiment entailed of a scared database of pion-induced reactions since long time ago, even knowing the power of the $\pi^- N$ reaction to obtain direct information about branching ratios of the resonances and therefore, about their coupling constants. Also, the ρ meson-baryon coupling can be studied by the resonance decay into two pion final state since their branching ratios its close to 100%. Taking into account previous motivations, besides the e^+e^- dilepton production for $\pi^- N$ reaction at 690 MeV/c, which is the main task of the present work, HADES collected data for double pion production around the pole of $N(1520)D_{13}$ at (656, 690, 748 and 800 MeV/c) during the same run [118]. The $\pi^+\pi^- n$ and $\pi^-\pi^0 p$ two-pion data sample obtained from HADES experiment samples were included in the multichannel PWA developed by Andrey Sarantsev from the Bonn-Gatchina group [119; 120]. Among HADES data this multichannel PWA analysis included data world from Crystal Ball [121] and pseudoscalar meson photoproduction and photoproduction of vector mesons. HADES data is the only sample with charged double pion channels and therefore is sensitive to the ρ production.

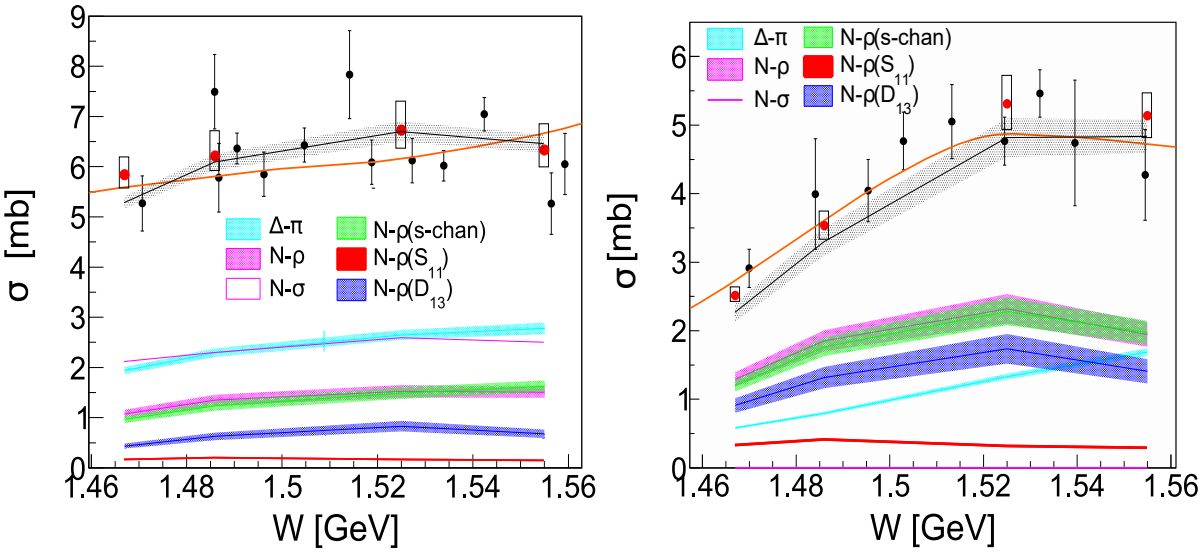

Figure 8.4: Total cross section for two pion production as a function of total energy $W = \sqrt{s}$ in the CM. **Left:** $\pi^- p \to n\pi^+\pi^-$. **Right:** $\pi^- p \to p\pi^0\pi^-$. Results are compared with other analysis, (black) world data, (red) HADES data (current analysis), (orange) PWA Manley analysis [122] and grey PWA Bn-Ga [111].

The total cross section as a function of $W = \sqrt{s}$ in the CM for two pion production is shown in Fig. 8.4. The total cross section is given as a sum of the cross section from PWA

with a defined total angular momentum and parity J^P. The decomposition into partial waves at HADES energies shows that they originate mainly by L = 0, 1, 2 (S, P, D) waves, and the amplitudes are associated with $J^P : 1/2^-(L = 0), 1/2^+, 3/2^+(L = 1)$ and $3/2^-, 5/2^-(L = 2)$ waves. We can observe that the N(1520)D_{13} resonance dominates the $p\pi^-\pi^0$ while the N(1440)P_{11} plays a similar role in the $n\pi^+\pi^-$. Also the $\Delta\pi$ contribution (cyan curve) is the most important contribution in the $n\pi^+\pi^-$. In conclusion, HADES collaboration measurements of two pion production in the exclusive $n\pi^+\pi^-$ and $p\pi^-\pi^0$ final states in πp reaction allows to the decomposition of the total cross section into partial waves width with a total J^P into $\Delta\pi, N\rho, N\sigma$ contributions. One of the primary goals of PWA analysis was to extract the cross section of ρ, which will be used in this analysis. Moreover, PWA allows also to obtain the branching ratios of the different $2\pi N$ of different baryons, in particular the N(1520), N(1535), and N(1440). For a detailed review of this analysis, see [111]. Results with the total cross section of $\pi^- p \to n\pi^0\pi^0$ from Crystal ball [65] shows the $\Delta\pi$ contribution a clear maximum at the mass of the N(1440), also results from CB-ELSA [123] for the $\gamma p \to n\pi^0\pi^0$ reaction it shows a $\Delta\pi$ dominance contribution, those results corroborate the $\Delta\pi$ production as intermediate state in HADES PWA.

The decomposition into partial waves allows us to separate the different contributions for the total cross section; the results from HADES PWA are shown in Fig. 8.5 as red dots. For the invariant mass distribution of $p\pi^0\pi^-$ final state we observed that the $N\rho$ gives the largest contribution originating from the N(1520)D_{13}. In the invariant mass distribution of $\pi^- n$, there is a clear peak around the $\Delta(1232)$ resonance pole, which indicates this contribution in the intermediate two-particle final state. In the $\pi^- p \to n\pi^+\pi^-$ we can observed a clear contributions from $\Delta\pi$ to the two-pion final state, with the $\Delta^+\pi^-, \Delta^0\pi^0$ and $\Delta^-\pi^+$. The obtained cross section for the $\Delta\pi$ charge states at pion beam momenta of 690 MeV/c is shown in Table 8.2. Finally only $\Delta^+\pi^-, \Delta^0\pi^0$ will be included in final dilepton production via Δ Dalitz decay process, which will be explained in Section 9.1.2.

	$\Delta^+\pi^-$	$\Delta^0\pi^0$	$\Delta^-\pi^+$
$\sigma(\mu b)$	0.779	1.041	2.009

Table 8.2: Cross sections for the different charge states of $\Delta\pi$ in $\pi^- p$ reaction at $\sqrt{s} = 1.487$ GeV

Among $\Delta\pi$ and N^* resonance, the ρ production is significant since they are linked to the time-like electromagnetic form factors via VDM of the baryon resonance decays. Results from the HADES PWA gives a ρ contribution at 690 MeV/c of 1.32 ± 0.16 (mb).

8.0.4 Photoproduction in $\gamma n \to \pi^- p$ reaction

At low energies, the interaction of a real photon with nucleons is dominated mainly by resonance excitations. In photoproduction experiments, the electromagnetic properties of baryonic resonance can be extracted with great detail, the reaction has been studied experimentally and theoretically, and many results have been published. An interesting point of this reaction is that it is linked with the $\pi N \to N e^+ e^-$ due to time inverse relation. Therefore, the $\pi^- p \to n\gamma^* (\gamma^* \to e^+ e^-)$ is related to the time inverse reaction $\gamma^* n \to \pi^- p$. Calculations are made neglecting the virtuality of the decay photon in $\pi N \to N e^+ e^-$ reaction. Consequently, the photon is on-shell $q^2 = 0$, and no form factors are taken into account, which is something that simplifies the process [56]. Results for photoproduction in our energy range were produced by Crystal Ball collaboration at BNL [124] and also by CLAS collaboration[125].

In left of Fig. 8.6 in the region of $\sqrt{s} = 1.5$ GeV, the main contribution are the meson exchange t-channel, and the $3/2^-$ and $1/2^-$, corresponding to N(1520) and N(1535) respectively.

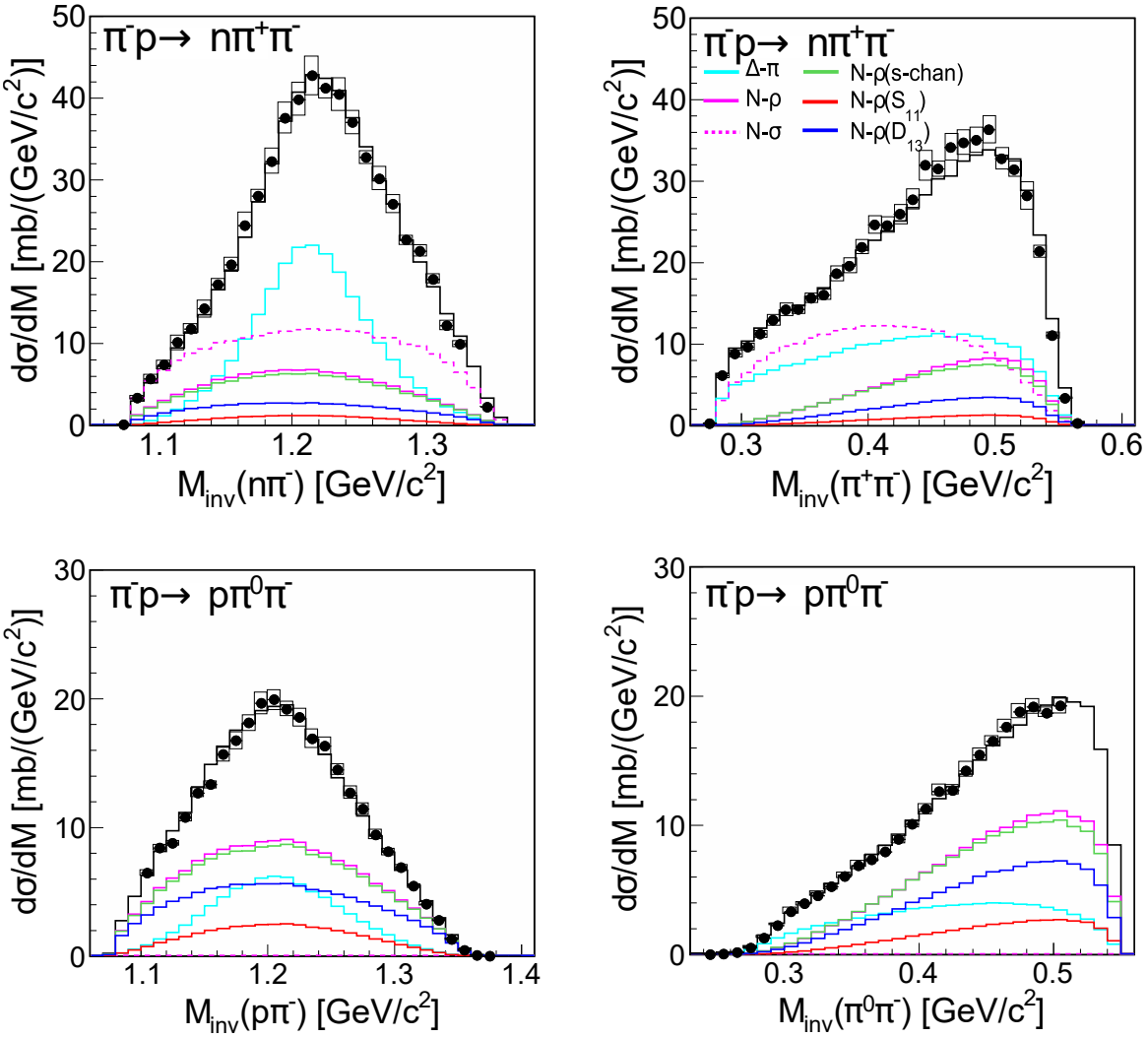

Figure 8.5: Invariant mass distributions of the πN (left column) and the 2π systems (right column) for the $\pi^- p \to n\pi^+\pi^-$ (upper row) and $\pi^- p \to p\pi^0\pi^-$ (lower row) reaction channels for $p_{\text{beam}} = 0.685$ GeV/c. Different contributions as (color lines) and total yield as (black line) [111].

Also, a small contribution from the $3/2^+$ corresponding to N(1440), which is negligible in the s-channel, and last the tail of the $3/2^+$ $\Delta(1232)$ resonance. The resonance N(1440), which contributes to the 2π channel, has a weak contribution in the photon-induced reaction due to low electromagnetic coupling. The $3/2^-$ partial wave solution shows a resonance peak at N(1520) coming from the s-channel, as we can see in the right of Fig. 8.6. That is not the case for the $1/2^-$ N(1535), where we cannot observe the resonance peak structure in the s-channel. Only 35% of the $1/2^-$ in the s-channel is due to the N(1535) resonance. In the left of Fig. 8.6 contributions of the entire cross section of N(1520) and N(1535) are similar, in contrast with the right part, (the s-channel), where the destructive interferences between s and u channel increase the N(1535) a factor 2. Assuming time-reversal invariant the $\pi^- p$ radiative decay is related to the π^- photoproduction by the detailed balance equation [124]:

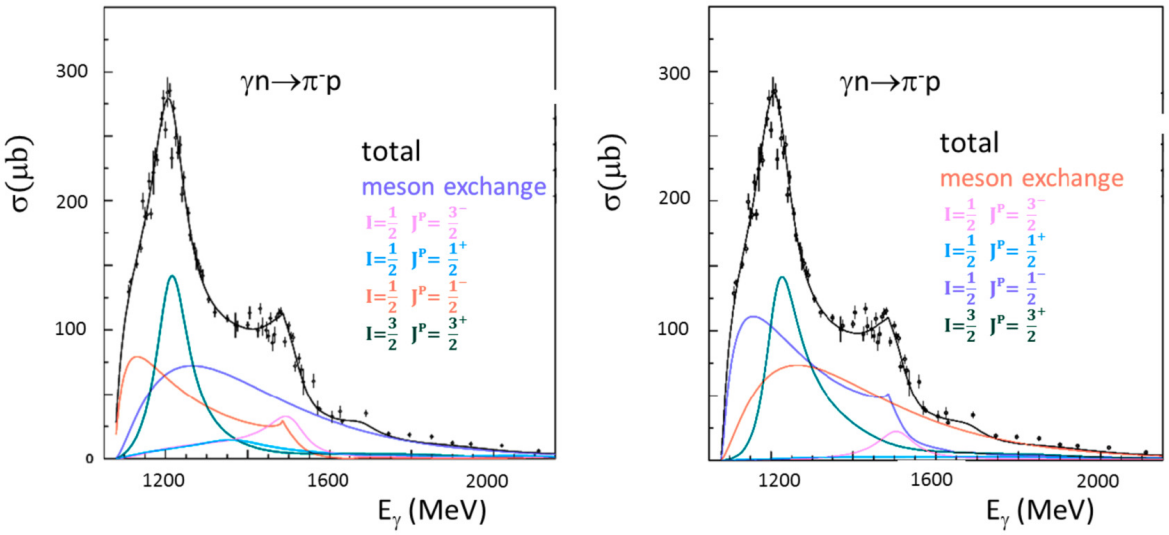

Figure 8.6: **Left:** Cross section of $\gamma n \to \pi^- p$ compared with solutions of PWA from Bonn-Gatchina group. **Right:** Same as left but only the s-channel contribution for each partial waves.

$$\mathrm{d}\sigma\left(\pi^- p \to \gamma n\right) = (2S_\pi + 1)\,(2S_p + 1)\,\frac{\left(p_\pi^*\right)^2}{v_i v_f}\overline{|\mathcal{M}_{if}|^2} \tag{8.25}$$

$$\mathrm{d}\sigma\left(\gamma n \to \pi^- p\right) = (2S_\gamma + 1)^2\,\frac{\left(p_\gamma^*\right)^2}{v_i v_f}\overline{|\mathcal{M}_{if}|^2} \tag{8.26}$$

Where v_i, v_f are the relative velocities, $\overline{|\mathcal{M}_{fi}|^2}$ is the spin average of the squared scattering $|\mathcal{M}_{fi}|^2$ and p_γ^* and p_π^* is the momentum in the CM at $\sqrt{s} = 1.49$ GeV.

$$p_\gamma^* = p_\gamma^{\mathrm{LAB}}\frac{m_n}{\sqrt{s}} = 0.448 \text{ GeV/c} \tag{8.27}$$

$$p_\pi^* = p_\pi^{\mathrm{LAB}}\frac{m_p}{\sqrt{s}} = 0.436 \text{ GeV/c} \tag{8.28}$$

The principle of detailed balance takes the form:

$$\overline{|\mathcal{M}_{if}|^2} = \overline{|\mathcal{M}_{fi}|^2} \tag{8.29}$$

Therefore the detailed balance relation is given by:

$$\sigma\left(\pi^- p \to n\gamma\right) = 2\left(\frac{p_\gamma^*}{p_\pi^*}\right)^2 \sigma\left(\gamma n \to \pi^- p\right) \tag{8.30}$$

substituting the values of p_γ^* and p_π^*:

$$\sigma\left(\pi^- p \to n\gamma\right) = 2.13 \cdot \sigma\left(\gamma n \to \pi^- p\right) \tag{8.31}$$

Results of cross section from $\gamma n \to \pi^- p$ reaction and $\pi^- p \to \gamma n$ using the relation in Eq. 8.29 are shown in Table 8.3.

	Cross sections (μb)	
Resonances	$\sigma(\gamma n \to \pi^- p)$	$\sigma(\pi^- p \to \gamma n)$
N(1520)	16.38	47
N(1535)	22.6	34
$\Delta(1232)$	8.67	18

Table 8.3: Total cross section contributions deduced from PWA for $\gamma n \to \pi^- p$ and $\pi^- p \to \gamma n$ reaction at $\sqrt{s} = 1.49$ GeV.

$$\sigma\left(\pi^- p \to N^*\right) = \frac{\sigma\left(\pi^- p \to N^*\left(N^* \to N\gamma\right)\right)}{BR\left(N^* \to N\gamma\right)} \tag{8.32}$$

Therefore, the partial contribution of the cross section can be deduced from Eq. 8.32. Cross section of resonance radiative decay and branching ratios are shown in Table 8.4.

Reaction	$\pi^- p \to N^*/\Delta$		
Resonance	N(1520)	N(1535)	$\Delta(1232)$
Cross section (mb)	20.4	9.7	3
Branching ratio	0.23%	0.35%	0.6%

Table 8.4: Cross sections and branching ratios of radiative decay for N(1520), N(1535) and $\Delta(1232)$ for $\pi^- p \to N^*$ reactions.

Chapter 9

Dilepton spectra results and discussion

The experimental results need to be compared with the simulated theoretical predictions in order to understand the dilepton production in $\pi^- N$ reactions. In this chapter the efficiency corrected spectra will be compared with the simulations produced from Pluto [103] Monte Carlo event generator, which is based in a thermal model. Simulations are a crucial part of any experimental program, either to gain information about the production or decay mechanism in a reaction and also to estimate the identification efficiency. With Pluto, the user can generate various particles and its decay channels which a corresponding angular distribution and certain momentum. Therefore, the pion beam momentum distribution is required to calculated the kinematics of the decay particles. The average cross section of the reaction is used to normalized the differential distributions. Using those inputs, a large number of events are generated from Pluto. The chain procedure from simple events generated from Pluto, to the final comparison with real experimental data is described in Section 3. The simulated events are generated in 4π full solid angle, after passed through the analysis chain they are restricted inside HADES acceptance. After the normalization process, they can be compared to raw data, which is not corrected by the efficiency. Other option is to compared the simulated events in 4π full solid angle to efficiency corrected data.

9.1 Dilepton spectrum composition: The cocktail

The incoherent sum of dilepton sources generated by Pluto composed the so-called "cocktail". In a simulation, the dilepton sources are the products of hadronic decays, in which the user gives a particular branching ratio and angular distribution. Explained already in Section 1.2.3 the mainly contribution to dileptons at low beam energy is due to **hadron decays** and **bremsstrahlung**. The hadron decays can be divided into two sub-categories (two-body) direct decays and Dalitz decays (three-body). In the Pluto simulations for $\pi^- N$ reactions at $\sqrt{s} = 1.49$ GeV the following hadronic decay modes are generated:

- Meson Dality decays:
  - π^0 Dalitz decay $\left(\pi^0 \to \gamma e^+ e^-\right)$
  - η Dalitz decay $(\eta \to \gamma e^+ e^-)$
- Baryonic Dalitz decay:

- N(1520) Dalitz decay (N(1520) $\rightarrow$ Ne^+e^-)
- N(1535) Dalitz decay (N(1535) $\rightarrow$ Ne^+e^-)
- Δ(1232) Dalitz decay ($\Delta \rightarrow$ Ne^+e^-)

• Direct decay:

- Off-shell ρ contribution ($\rho \rightarrow e^+e^-$)

These three categories contribute to the measured spectrum.

9.1.1 Dalitz decay of neutral mesons

The differential Dalitz decay width $P \rightarrow l^+l^-\gamma$ of pseoudoscalar meson, $P = \pi^0, \eta$, is treated with the parametrization from [30]

$$\frac{d\Gamma^{P\rightarrow l^+l^-\gamma}}{\Gamma^{P\rightarrow\gamma\gamma}dM} = \frac{4\alpha}{3\pi M}\sqrt{1-\frac{4m_e^2}{M^2}}\left(1+\frac{2m_e^2}{M^2}\right)\left(1-\frac{m_e^2}{M_P^2}\right)^3\left|F_P\left(M^2\right)\right|^2 \tag{9.1}$$

where $\Gamma^{P\rightarrow\gamma\gamma}$ is the partial width of the decay meson with values $\Gamma^{\pi^0\rightarrow\gamma\gamma} = 7.8{\cdot}10^{-6}$ MeV and $\Gamma^{\eta\rightarrow\gamma\gamma} = 5.11\cdot10^{-4}$ MeV. M_P correspond to the mass of the scalar meson. The complicated structure of hadrons modified the leptonic pair spectrum, either increasing or decreasing as compared with QED calculations obtained of point-like particles, see Eq. 9.2.

$$\frac{d\Gamma^{P\rightarrow l^+l^-\gamma}}{\Gamma^{P\rightarrow\gamma\gamma}dM} = [\text{QED}]\cdot\left|F_P\left(M^2\right)\right|^2 \tag{9.2}$$

The form factors for the different mesons Dalitz decays are given by:

$$F_{\pi^0}(M^2) = 1 + b_{\pi^0}M^2, \quad b_{\pi^0} = 5.5\ \text{GeV}^{-2} \tag{9.3}$$

$$F_\eta(M^2) = \left(1-\frac{M^2}{\Lambda_\eta^2}\right)^{-1}, \quad \Lambda_\eta = 0.676\ \text{GeV} \tag{9.4}$$

The dilepton decays of pseudoscalar meson follows an angular distribution given by:

$$\frac{\mathrm{d}\Gamma_{P\rightarrow\gamma e^+e^-}}{\mathrm{d}\cos\theta} \propto 1+\cos^2(\theta) \tag{9.5}$$

where θ is the angle between the dilepton momentum concerning the electron momentum.

π^0 production

The production channel of the π^0 Dalitz decay was discussed already in Section 1.5.1 and Section 1.5.1. The different production channels are listed below: The exclusive charge exchange of $\pi^-p \rightarrow n\pi^0$ reaction gives the largest π^0 production. In Table 1.4 the cross section from various experiments and SAID PWA are shown. Taking into account contributions from experiments at BNL [61], and theoretical solutions from WI08 SAID PWA solution, a cross section of 9.0$\pm$0.8 mb is used. Crystal Ball collaboration (CB) has measured the cross section for $\pi^-p \rightarrow \pi^0\pi^0n$. with a value of 1.880 ± 0.015 mb. Both π^0 can decay, therefore the effective cross section is multiplied by a factor 2. Results of $\pi^-p \rightarrow \pi^0\pi^-p$ cross section in our energy range from BNL [63] gives a cross section of 3.99 ± 0.5 mb with a precision about 10 %. We can observe in the exclusive charge exchange process that the angular distribution of the π^0 is strongly forward peak, see

Fig. 1.26. Unfortunately, the π^0 generated from Pluto do not include angular distributions, so the Cracow team from HADES collaboration formed by I. Sarantsev and I. Ciepal developed a new event generator for the π^0 using the angular distribution from SAID PWA WI08, see Fig. 1.26. Both event generator will be used and compared in my analysis,they are labeled by PLUTO and PWA.

9.1.2 Baryon Dalitz decay

Dalitz decay of baryonic resonances were included for the s-channel contribution in two modes. The direct decay of $\pi^- p \to N^* \to n e^+ e^-$ and the sequential decay mode $\pi^- p \to N^* \to \Delta\pi \to n e^+ e^-$.

Direct decay of baryonic resonance N*

For the first decay mode, the direct Dalitz decay of baryonic resonance, the PWA analysis were carried out from Bonn-Gatchina group of $\gamma n \to \pi^- p$. It revealed that the main resonance contributions to the final cross section are the N(1520) and N(1535) with the corresponding branching ratios calculated in Table 8.1. Therefore, using the detailed balance equation, Eq. 8.29, the cross section can be obtained for the inverse process $\pi^- p \to \gamma n$ reaction. Finally, the resonance production cross section is estimated from the radiative cross section using the Eq. 8.32, which results to 47 and 34 μb for N(1520) and N(1535), respectively, see Table 8.4. Unfortunately, the sum of both resonance contributions is not the total cross section of $\pi^- p \to \gamma n$ reaction which is 220 μb, see Fig. 8.6. The other contributions are due to non-resonant process in the s, t and u-channel which interference to the resonant contributions. Only models that takes into account all contributions can be used to described the total e^+e^- distribution, like in [56]. In Section 8.0.1 the obtained relation between the total Dalitz decay width of the baryon resonance to its decay width to a virtual photon, Eq. 8.23, can be used to obtained the relation between cross sections as follow:

$$\sigma\left(\pi^- p \to n e^+ e^-\right) \sim 1.35 \alpha \sigma\left(\pi^- p \to n\gamma\right) \tag{9.6}$$

This relation it is valid only for the Dalitz decay of baryonic resonance in the s-channel with a given mass. Using the Eq. 9.6, and the total cross section from the radiative decay $\pi^- p \to \gamma n = 220\ \mu b$, we obtain a value of $\sigma\left(\pi^- p \to n e^+ e^-\right) = 2\ \mu b$ which can be counted as a total cross section including resonant and non-resonant process. However, we only know the decay width for resonant process in the s-channel, which is given by Eq. 8.3, and it generates the e^+e^- invariant mass distribution. Considering the approach of using the total effective cross section derived from the radiative decays, also called as effective cross section, we can attempt to describe the dilepton assuming that all the contributions comes either from N(1520) or from N(1535) with a cross section given by:

$$\sigma\left(\pi^- p \to N^\star\right) = \frac{\sigma\left(\pi^- p \to n\gamma\right)}{BR(N^\star \to n\gamma)} \tag{9.7}$$

With N*= N(1520) or N(1535). Unfortunately, as we can observe in Fig. 8.2, the $(1/2^+)$N(1520) will give an overestimation of the dilepton yield, especially at higher invariant mass, and if we assume that all the contribution is provided only by the $(3/2^-)$N(1535), we probably underestimate the dilepton yield at higher invariant mass. In order to avoid this problem and gives a proper description of the dilepton yield, we can used both of the contribution but weighting the dilepton yield with the relative contribution of each one in the the resonant s-channel. Those

relatives contributions are 58% for N(1520) and 42% for N(1535). Finally, the cross section calculations are:

$$\sigma\left(\pi^- p \to N(1520)\right) = 0.58 \times \frac{\sigma\left(\pi^- p \to n\gamma\right)}{BR(N(1520) \to n\gamma)} = \frac{0.220}{0.0023} = 51 \text{ mb} \tag{9.8}$$

$$\sigma\left(\pi^- p \to N(1535)\right) = 0.42 \times \frac{\sigma\left(\pi^- p \to n\gamma\right)}{BR(N(1520) \to n\gamma)} = \frac{0.220}{0.0035} = 26 \text{ mb} \tag{9.9}$$

with branching ratio for $N(1520)^0 \to Ne^+e^-$ of $2.3 \cdot 10^{-5}$ and for $N(1535)^0 \to ne^+e^-$ of $3.5 \cdot 10^{-5}$ obtained from Table 8.1. All the values of the cross section are obtained from the photoproduction reaction $\gamma n \to \pi^- p$ with a precision about 10% which is uses as an uncertainty. Other option is to take into account only the cross section deduced from PWA from the resonant part of the $\pi^- p \to n\gamma$ reaction, see Table 8.3, unfortunately, this option will let the dilepton yield underestimate as it only represents 40% of the total cross section.

Sequential decay of baryonic resonance $\Delta(1232)\pi$

In Section 8.0.3 it was found out that the $\Delta\pi$ state had a reasonable contribution to the $n\pi^+\pi^-$ and $p\pi^-\pi^0$ final state. Mainly, by the sequential decay throw the N(1440) or N(1520) resonance to $\Delta(1232)\pi$. Therefore, the N(1440) resonance which is banished in the exclusive channel of the e^+e^- can contribute due to the coupling to the $\Delta(1232)$ resonance and its following Dalitz decay. The cross section of the sequential decay of $\Delta\pi$ to the Δ Dalitz decay can be found in Table 8.2. Only the $\Delta^+\pi^-$ and $\Delta^0\pi^0$ are admitted for the dilepton production. The differential decay width is treated with the Krivoruchenko parametrization [113] used in Eq. 8.6, with the point-like form factor equal to $|F_\Delta(0)| = G_M = 3.03$.

9.1.3 Off-shell ρ contribution

Two options generate the off-shell ρ production: The first one uses a simple Breit-Wigner distribution from Pluto event generator. The second option is to use the distribution of $\pi^+\pi^-$ from PWA, see Fig. 9.1, and relate it with the e^+e^- production channel using a VDM formalism using Eq. 9.10 which is derived from Eq. 8.24. Each invariant mass bin from $\pi^+\pi^-$ production is converted to e^+e^- invariant mass using the relation:

$$\frac{d\sigma}{dM_{e^+e^-}} \propto \frac{d\sigma}{dM_{\pi^+\pi^-}} \cdot \left(\frac{M_\rho}{M_{e^+e^-}}\right)^3 \tag{9.10}$$

The factor $(1/M_{e^+e^-})^3$ strongly increase the small invariant masses. In that option, the form factor in the time-like region is considered using the VDM model. The off-shell ρ production cross section is obtain from PWA of two pion channels in Section 8.0.4, resulting with a value of 1.65 ± 0.2 mb

9.1.4 Treatment of carbon reaction

In Section 1.5.2, it was mentioned that pion induced reactions on ^{12}C can interact either with protons or neutrons. In our energy range, at pion beam momenta of 0.690 GeV/c the ratio between cross on pion-proton and pion-neutron is equal to $\sigma_{\pi^- p}/\sigma_{\pi^+ p} = 3$, which indicates that the π^{-12}C reaction it is dominate by $\pi^- p$ interaction rather than $\pi^- n$. Consequently, we will consider the π^{-12}C reaction as a superposition of interactions with protons. The description of interactions with ^{12}C nuclei in CH_2 target is described with a quasi-free participant-spectator

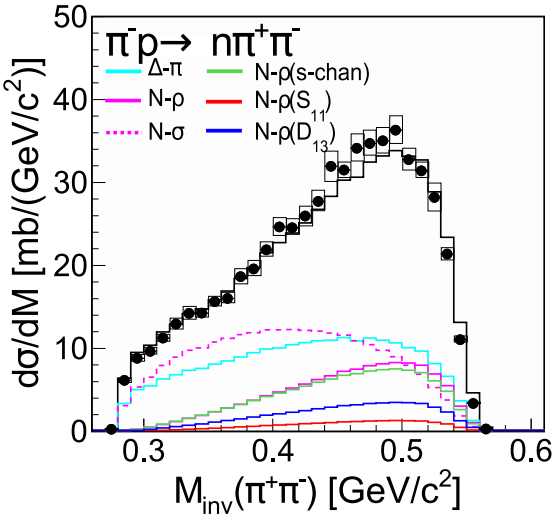

Figure 9.1: Invariant mass distributions of the 2π systems for the $\pi^- p \to n\pi^+\pi^-$ reaction channel at $p_{\text{beam}} = 0.685$ GeV/c. Different contributions as (color lines) and total yield as (black line) [111]

model. The ^{12}C nuclei are compound by a participant off-shell proton moving in the carbon nucleus with a Fermi momentum $\vec{p}_F$, becoming the original carbon nucleus into ^{11}B with Fermi momentum in the opposite direction with the proton, see Eq. 9.11.

$$M_{12C} = \sqrt{M_{\text{part}}^2 + (\vec{p}_F)^2} + \sqrt{M_{11B}^2 + (\vec{p}_F)^2} \tag{9.11}$$

The CM energy between the pion and the participant nucleon is (carbon target):

$$\sqrt{s_{\pi part}} = \sqrt{(W_\pi + W_{part})^2 - (\vec{p}_\pi + \vec{p}_F)^2} \tag{9.12}$$

If the participant nucleon is a free proton (proton target):

$$\sqrt{s_{\pi p}} = \sqrt{(W_\pi + M_p)^2 - (\vec{p}_\pi)^2} \tag{9.13}$$

In Fig. 9.2 it is shown the probability density of the reaction as a function of $\sqrt{s}$

η production cross section

Most of our production channels like one pion, two pions, and baryonic Dalitz decay, are well above the threshold. Therefore an average pion beam momenta can be assumed to obtain the cross section of each reaction. Unfortunately, for the η production threshold, our CM energy ($\sqrt{s_{th}} = 1.487$ GeV) is below the threshold, also the cross section increases significantly above the threshold.

In that case, from the total cross section of $\pi^- p \to \eta n$ reaction calculated by the Giessen group, see Fig. 1.30, I extract discreet values of the cross section in our energy range. The result is shown in Fig. 9.3. The corresponding $\sqrt{s}$ bins are multiply with the corresponding probability distribution for pion-proton or pion-carbon reaction obtained in Fig. 9.4 resulting as:

$$\Delta\sigma(\sqrt{s}) = \sigma(\sqrt{s})\mathcal{P}(\sqrt{s})\Delta(\sqrt{s}) \tag{9.14}$$

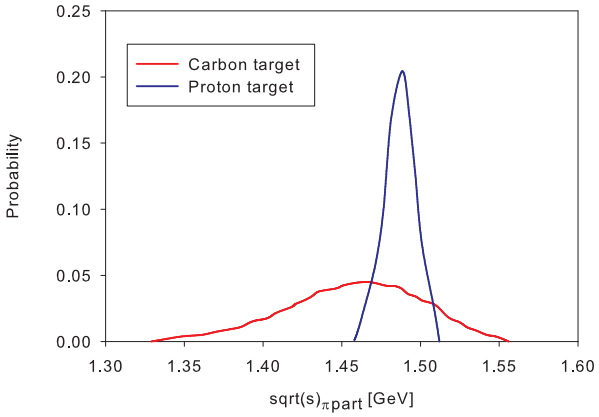

Figure 9.2: Probability density as a function of $\sqrt{s}$ for pion reaction on a free proton (blue-proton target) and bound proton (red-carbon target) using participant-spectator model. Pion beam distribution is taken into account

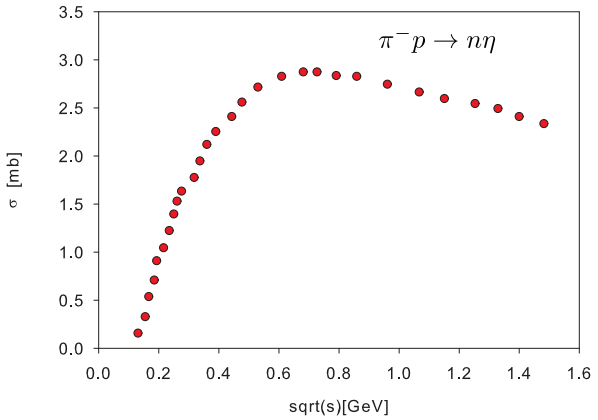

Figure 9.3: Cross section as a function of $\sqrt{s}$ for $\pi^- p \to n\eta$ reaction obtained from [28].

The total cross section is calculated as:

$$\sigma = \sum_{\Delta(bins)} \Delta\sigma(\sqrt{s}) \tag{9.15}$$

Values of the cross section obtained from Eq. 9.15 are summarized in Table 9.1

9.2 Dilepton cocktail for Pluto simulations

To generate events for a particular reaction in Pluto, it is also necessary to give the branching ratios and cross section, which can be extracted from theoretical calculations or experiments. The input of cross sections and branching ratios used for Pluto simulations for the different dilepton sources are summarized in Table 9.2. The cross section of CH_2 target is obtained by $\sigma_{CH2} = \sigma_H + \frac{1}{2}\sigma_C$. The first errors of the cross section are related to the uncertainty of the data and the second one by the factor R, which was explained in Section 5.2.

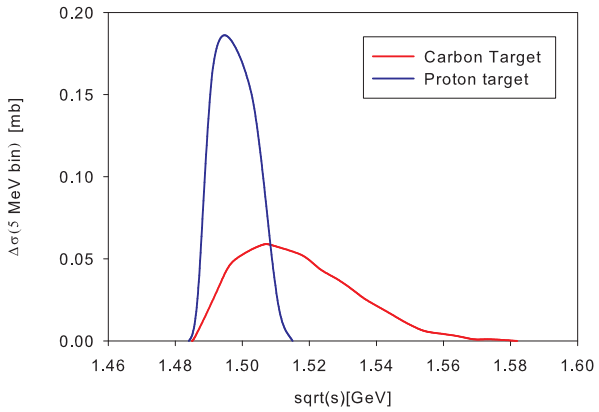

Figure 9.4: Cross section distribution in bins of 5 MeV for pion reaction on proton target (blue) and carbon target (red). Pion energy distribution is taken into account

Reaction	σ (mb)
$\pi^- p \to \eta n$	0.63 ± 0.2
$\pi^- C \to \eta n$	0.5 ± 0.05

Table 9.1: Cross section of η production in $\pi^- p$ and $\pi^- C$ reaction. The carbon reaction is assuming a participant-spectator model

Production channel	σ(mb)		
	$\pi^- p$	$\pi^- C$	$\pi^- \mathrm{CH_2}$
$\mathrm{n}\pi^0$	9.00 ± 0.8	$32.00 \pm 2.84 \pm 0.41$	25.00 ± 2.23
$\mathrm{n}\pi^0\pi^0$	1.90 ± 0.1	$6.76 \pm 0.36 \pm 0.05$	5.28 ± 0.28
$\mathrm{p}\pi^-\pi^0$	4.00 ± 0.1	$14.22 \pm 1.78 \pm 0.26$	11.11 ± 1.39
$\mathrm{n}\eta$	0.63 ± 0.2	$2.34 \pm 0.74 \pm 0.24$	1.80 ± 0.58
$\Delta^+\pi^-$	0.78 ± 0.08	$3.71 \pm 0.30 \pm 0.16$	2.86 ± 0.24
$\Delta^0\pi^0$	1.00 ± 0.1	$2.90 \pm 0.37 \pm 0.20$	2.23 ± 0.30
$\mathrm{n}\rho$	1.30 ± 0.20	$4.83 \pm 0.74 \pm 0.41$	3.71 ± 0.61
N(1520)('mixed')	51.00 ± 5	$189.43 \pm 18.57 \pm 10.20$	145.71 ± 15.17
N(1535)('mixed')	26.00 ± 3	$96.57 \pm 11.14 \pm 6.12$	74.29 ± 9.10
Decay Channel	Branching ratio		
$\pi^0 \to \gamma e^+ e^-$	0.012		
$\eta \to \gamma e^+ e^-$	$6.9 \cdot 10^{-3}$		
$\Delta^0\pi^0 \to \mathrm{N}e^+e^-$; $\Delta^+\pi^- \to \mathrm{N}e^+e^-$	$4.2 \cdot 10^{-3}$		
$\rho \to e^+e^-$	$4.7 \cdot 10^{-3}$		
$\mathrm{N}(1520)^0 \to \mathrm{n}e^+e^-$	$2.3 \cdot 10^{-3}$		
$\mathrm{N}(1535)^0 \to \mathrm{n}e^+e^-$	$3.5 \cdot 10^{-3}$		

Table 9.2: Cross sections and branching ratios of dilepton contributions for $\pi^- p$, $\pi^- C$ and $\pi^- \mathrm{CH_2}$ reactions.

9.3 Comparision of HADES data with Pluto event generator

In this section, the simulations obtained from Pluto will be compared with the experimental results. The experimental spectra, after all the analysis cut is normalized, see Section 7.2.2, and corrected by the efficiency calculations, see Section 5.1. The experimental data points shows the statistical errors (black bars) and the systematic errors calculated in Section 5.2 by (red bars). The corrected experimental spectra is compared with PLUTO simulations in 4π full solid angle.

9.3.1 Inclusive e^+e^- production

The inclusive invariant mass distribution is displayed in two energy ranges in order to described more into detail the π^0 region corresponding to $\left(M_{e^+e^-} < 140\ \mathrm{MeV/c^2}\right)$, later on, the complete mass range will be shown where baryonic resonance populates higher invariant mass distribution.

In Fig. 9.5, the inclusive efficiency corrected e^+e^- invariant mass distribution for π^-CH_2 reaction is compared with Pluto simulations, in that case, the π^0 and 2π contributions are generated with Pluto event generator, which do not take into account angular distributions as it mentioned in Section 9.1.1. The rest of the cocktail η, $\Delta(1232)$, N(1520) and N(1535) is included based in assumptions from Section 9.2. We can observe that the main contribution is from π^0 and 2π production following by a small contribution from η meson and baryonic resonance. Baryonic resonances start to dominate the invariant mass region above $\left(M_{e^+e^-} > 100\ \mathrm{MeV/c^2}\right)$. The right part of Fig. 9.5 shows the transverse momentum distribution for invariant mass $\left(M_{e^+e^-} < 140\ \mathrm{MeV/c^2}\right)$, it is observed that the region below $p_T < 100\ \mathrm{MeV/c^2}$ is not well described. This seems to be because the efficiency corrections extrapolate the experimental data inside HADES acceptance to 4π full solid angle, and introduce an artificial factor which do not correspond with any physical observable.

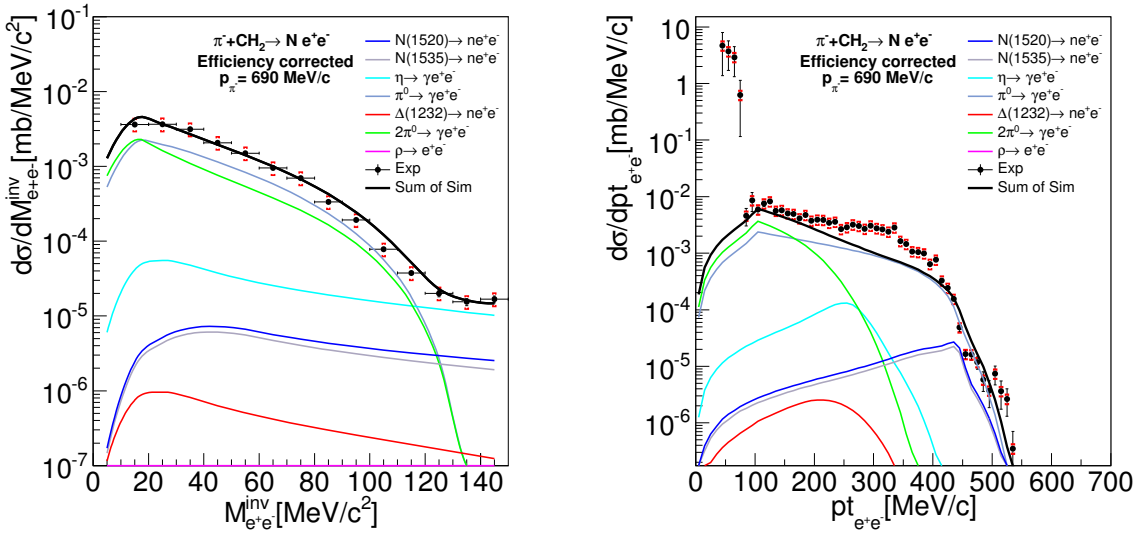

Figure 9.5: **Left:** Inclusive efficiency corrected e^+e^- invariant mass distribution for π^-CH_2 reaction compared with cocktail simulation from Pluto event generator in the π^0 region $\left(M_{e^+e^-} < 140\ \mathrm{MeV/c^2}\right)$. Contributions from π^0 and 2π production generated from Pluto. **Right:** Same as left but transverse momentum distribution.

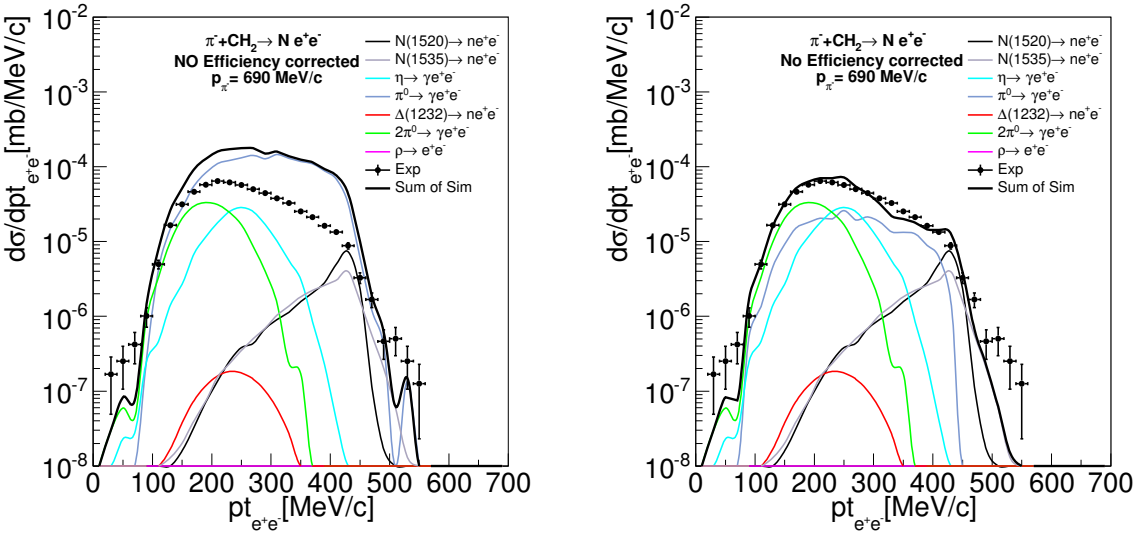

Figure 9.6: Inclusive no efficiency corrected e^+e^- invariant mass distribution for π^-CH_2 reaction compared with cocktail simulation from Pluto event generator. Contributions from π^0 produced with . **Left:** Pluto event generator. **Right:** Event generator based in PWA inputs.

However, in Fig. 9.6, the same distribution is compared for raw experimental spectra, i.e no efficiency corrections. This uncorrected data, is inside HADES acceptance and reproduce very well the shape of the transverse distribution specially in the right figure with the PWA option, which will be described below. The region between 200 MeV/c^2 $< p_T <$ 400 MeV/c^2 is underestimate by a factor 2 due to the π^0 contribution. The high transverse momentum is populated mainly by the baryonic contributions.

In Fig. 9.7, it is shown the same results as in Fig. 9.5, but with the difference that the π^0 contributions are generated with an event generator based in PWA, which take into account the angular distributions. In that case the simulations are more consistent with the experimental data than in Fig. 9.5, and despite the region below $p_T <$ 100 MeV/c^2, the traversal momentum distribution is very well reproduce. In the left part of Fig. 9.7, the inclusive invariant mass distribution, the π^0 region is in a better agreement. The π^0 produced with the event generator based in PWA gives a lower contribution due to the forward peak angular distribution, see Fig. 1.26. The behaviors of the angular distributions are reproduced in the p_T distribution. Consequently, at high p_T, the region between 200 MeV/c^2 $< p_T <$ 400 MeV/c^2 now is well reproduced with the new event generator that incorporated angular distributions in comparison with (right Fig. 9.5). That is because at high p_T, the yield corresponding with large polar angles is suppressed. We found the right consistency using the PWA generator, which includes real inputs for the angular distributions. The discrepancy between efficiency corrected data, and raw data, see Fig. 9.6, could be because the non corrected data reproduce a wider phase space region, that also can explain the inconsistency for $p_T <$ 100 MeV/c^2 in the efficiency corrected data.

In Fig. 9.8 it is shown the e^+e^- invariant mass distribution in the full invariant mass range. The region between 0 MeV/c^2 $<$ M$_{e^+e^-}$ $<$ 140 MeV/c^2 was discussed above, and it is compound mainly by contributions from π^0 and $2\pi^0$ production using the PWA option. The yield in the region between 100 MeV/c^2 $<$ M$_{e^+e^-}$ $<$ 300 MeV/c^2 is very well reproduced by the η and Dalitz decay of baryonic resonance N(1520) and N(1535). As well, the $\Delta(1232)$ contribute one order of

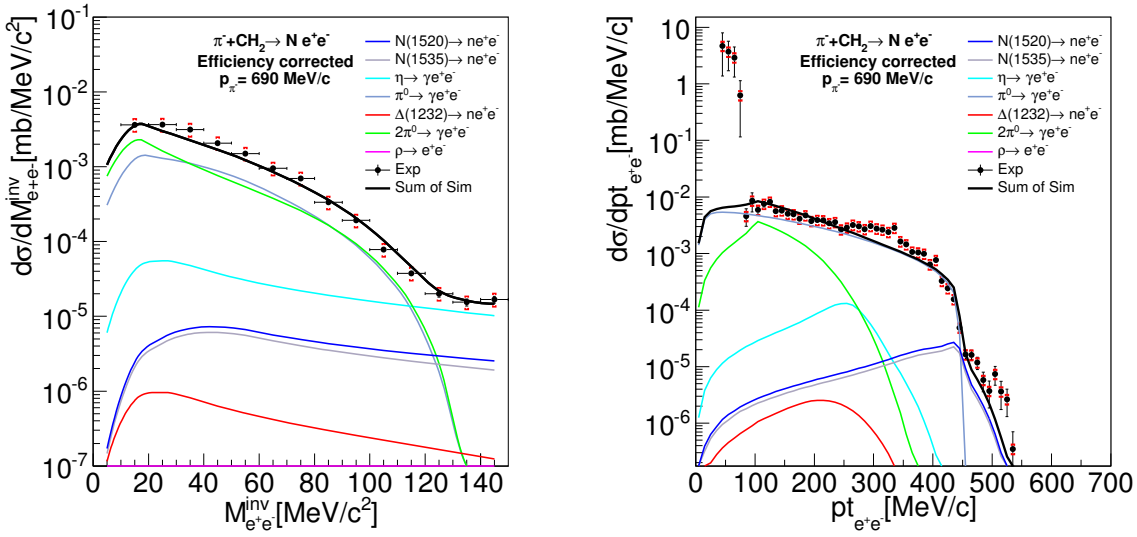

Figure 9.7: **Left:** Inclusive efficiency corrected e^+e^- invariant mass distribution for π^-CH_2 reaction compared with cocktail simulation from Pluto event generator in the π^0 region $\left(M_{e^+e^-} < 140\ MeV/c^2\right)$. Contributions from π^0 and 2π production with event generator based in PWA inputs. **Right:** Same as left but transverse momentum distribution.

magnitude lower. The η contribution decrease very fast at invariant mass $M_{e^+e^-} = 300\ MeV/c^2$. For invariant mass $M_{e^+e^-} > 300\ MeV/c^2$ its very clear that there is an excess in the yield that cannot be reproduce with the contributions of the Dalitz decay of baryonic resonances treated as point-like. Anyway, the point-like approach gives a reasonable description of the dilepton yield below $M_{e^+e^-} < 300\ MeV/c^2$ where the π^0 and η Dalitz decay dominates.

In Fig. 9.9 it is displayed the inclusive efficiency corrected e^+e^- transverse momentum distribution for invariant mass between $140\ MeV/c^2 < M_{e^+e^-} < 300\ MeV/c^2$ for π^-CH_2. We can observe two peaks, the first one by the η production and the second one by contributions from baryonic resonances N(1520) and N(1535), in general the transverse momentum distribution is well described despite at very low p_T, where we can perceive contributions from unknown sources.

In Fig. 9.8 it was found out an excess in the yield for invariant mass $M_{e^+e^-} > 300\ MeV/c^2$, which could not be explained by the baryonic resonances treated as a point-like. What it suggest that the excess in the yield it is a direct consequence of the time-like electromagnetic form factors (EMFF's) of the baryonic transitions, and therefore, they need to be implemented.

The VDM is a usual instrument to take into account the time-like electromagnetic form factors; therefore the off-shell ρ contribution is introduced in the simulations using a Breit-Wigner mass distribution, see Section 9.1.3. As well, the cross section was obtained from PWA analysis $\pi\pi$ of HADES data, which gives a better consistency with the data. As shown in Fig. 9.10 it is observed that the off-shell ρ contribution described very well the excess of the yield for invariant mass $M_{e^+e^-} > 300\ MeV/c^2$ which validates our previous statements.

In Fig. 9.11 it is displayed the inclusive efficiency corrected e^+e^- transverse momentum distribution with invariant mass between $300\ MeV/c^2 < M_{e^+e^-} < 600\ MeV/c^2$. The ρ contribution dominates the whole p_T range in a very good agreement, which support the statement of the description of the excess yield with the off-shell ρ contribution using a VDM model.

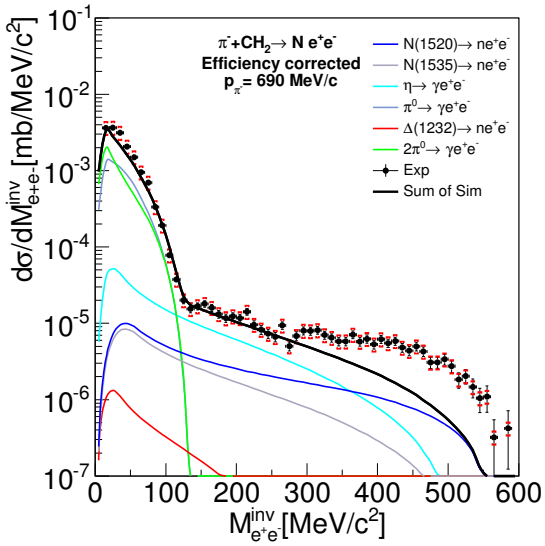

Figure 9.8: Inclusive efficiency corrected e^+e^- invariant mass distribution for π^-CH_2 reaction compared with cocktail simulation from Pluto event generator. Contributions from π^0 produced with event generator based in PWA inputs. The off-shell ρ contribution is not included

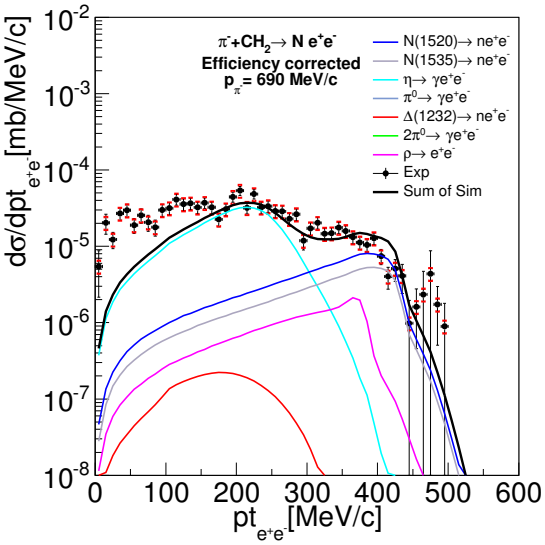

Figure 9.9: Inclusive efficiency corrected e^+e^- transverse momentum distribution with invariant mass 140 MeV/c^2 $<$ M$_{e^+e^-}$ $<$ 300 MeV/c^2 for π^-CH_2 reaction compared with cocktail simulation from Pluto event generator.

9.3.2 Exclusive e^+e^- production

Additionally to the inclusive, the exclusive invariant mass distribution $\pi^-p \to ne^+e^-$ is crucial to characterize better the production mechanism and compared later with the simulations, see Section 6.4.

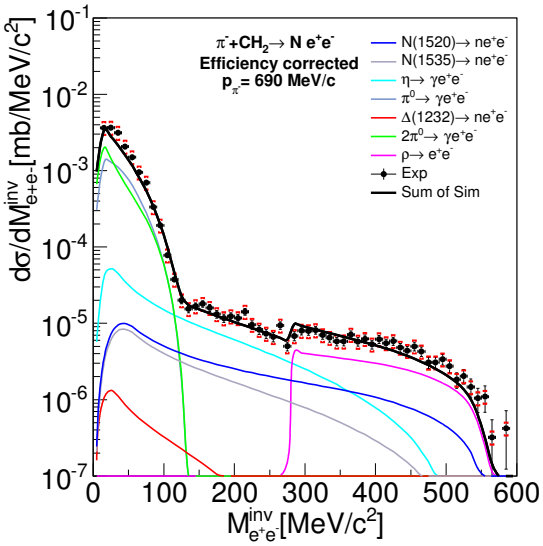

Figure 9.10: Inclusive efficiency corrected e^+e^- invariant mass distribution for π^-CH_2 reaction compared with cocktail simulation from Pluto event generator. Contributions from π^0 produced with event generator based in PWA inputs. The off-shell ρ contribution is included

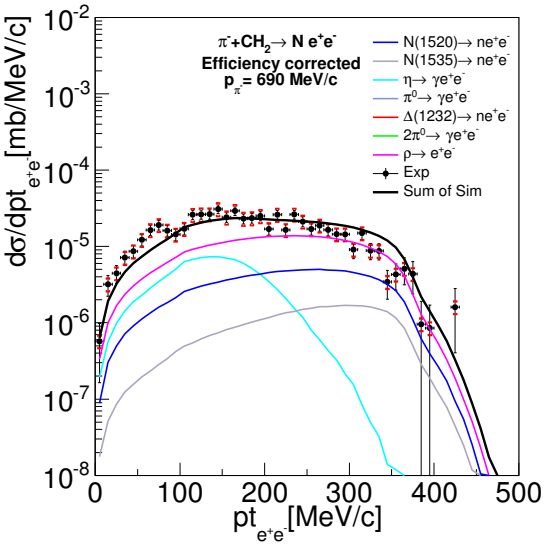

Figure 9.11: Inclusive efficiency corrected e^+e^- transverse momentum distribution with invariant mass 300 MeV/c^2 $<$ M$_{e^+e^-}$ $<$ 600 MeV/c^2 for π^-CH_2 reaction compared with cocktail simulation from Pluto event generator.

In order to remove the photon contributions of π^0 Dalitz decay in the final state e^+e^-, the missing mass spectra is obtained for a invariant mass larger than the π^0 mass, i.e. M$_{e^+e^-}$ $>$ 140 MeV/c^2. In Fig. 9.12, the efficiency corrected missing mass distribution is compared with simulations from Pluto. The neutron peak's width is well described only by the N(1520), N(1535) resonances, and the ρ contributions. However, those contributions overestimate the yield around

the neutron peak. The neutron peak region can be understand as a exclusive $\pi^- p \rightarrow n e^+ e^-$ reaction on a free proton or bound proton in ^{12}C nuclei, see Section 9.1.4. Above the neutron peak region, $M^{miss}_{e^+e^-} > 1000$ MeV/c^2 the trend of the experimental data is described by the η Dalitz decay where a photon is emitted, this contribution overestimate the yield. This excess in the experimental data could be related to the underestimated yield shown in Fig. 9.9.

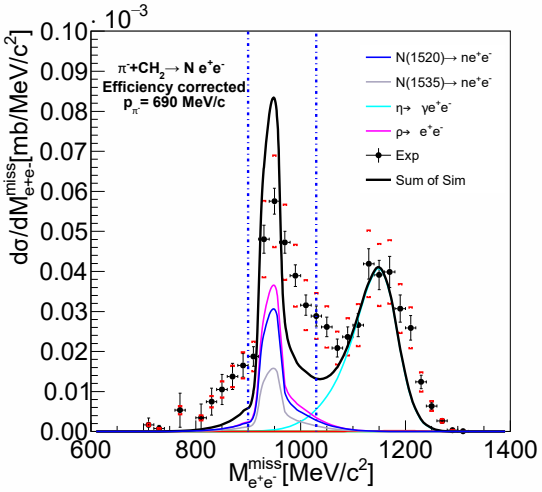

Figure 9.12: Efficiency corrected e^+e^- missing mass distribution with invariant mass $M_{e^+e^-} <$ 140 MeV/c^2 for $\pi^- CH_2$ reaction compared with cocktail simulation from Pluto event generator the (blue line) indicates the neutron mass region.

The misidentify neutron in the final state is selected with a one dimensional cut in the missing mass distribution around the neutron mass (900 MeV/c^2 $< M^{miss}_{e^+e^-} <$ 1030 MeV/c^2). In Fig. 9.13 and Fig. 9.14 it is displayed the missing mass vs. invariant mass distribution for all the decay channels simulated with Pluto. Contributions with a photon in their final step will be removed in the neutron selection, but also it is important to remark the advantage in contrast with the inclusive analysis since the η production is suppressed almost completely, therefore we can compare directly the baryonic resonances contributions and the off-shell ρ production with the models based in pion induced reaction.

In Fig. 9.15 it is shown the exclusive efficiency corrected e^+e^- invariant mass distribution compared with cocktail simulations from Pluto. In order to remove the π^0 contribution a threshold in the missing mass of $M_{e^+e^-} > 140$ MeV/c^2 was applied. Unfortunately, due to the missing mass resolution the π^0 contributions was not well suppressed. However, this does not represent a big issues since description of the baryonic Dalitz decay and the time-like electromagnetic form factors (EMFF's) of the baryonic transitions manifest an excess in the yield for invariant mass $M_{e^+e^-} > 300$ MeV/c^2. Therefore, the inclusion of the π^0 contribution in the spectra is used as a consistency check of the simulations. The η Dalitz decay and the $\Delta(1232)$ contributions is very well suppressed, similarly to Fig. 9.8 the yield in the region between 0 MeV/c^2 $< M_{e^+e^-} <$ 250 MeV/c^2 is well reproduced by π^0 and Dalitz decay of baryonic resonance N(1520) and N(1535) using the point-like approach. At high invariant mass, again emerges an even more remarkable excess in the yield which cannot be reproduce with the contributions of the Dalitz decay of baryonic resonances treated as point-like, (i.e QED approach). This, strengthens the need to include the time-like electromagnetic form factors (EMFF's) using the VDM formalism described in Section 9.1.3.

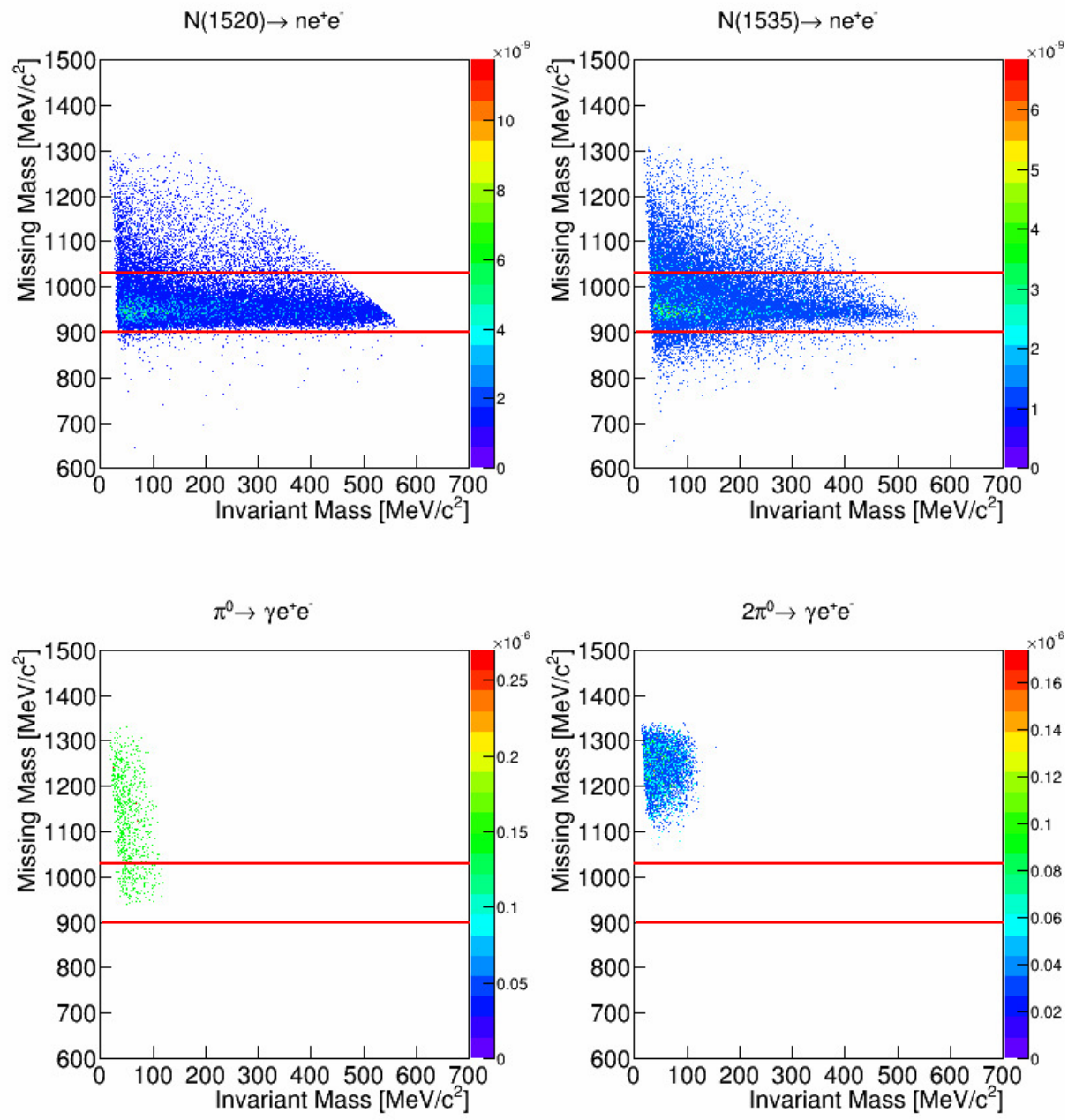

Figure 9.13: Missing mass vs. invariant mass distribution for $\pi^- CH_2$ reaction of cocktail source produced by Pluto event generator. Red lines correspond to the selection cut in the neutron mass between 900 MeV/c^2 < $M^{miss}_{e^+e^-}$ < 1030 MeV/c^2.

The two different off-shell ρ contribution using a Breit-Wigner mass distribution and the one using the PWA of two pion production is shown Fig. 9.16. The ρ production cross section is the same in both cases, but it can be observed that the yield of the e^+e^- invariant mass is different. According to PWA results, the main difference comes due to the strong coupling of the N(1520) resonance to the off-shell ρ. Also, the dependence of the branching ratio with the invariant mass, see Eq. 9.10.

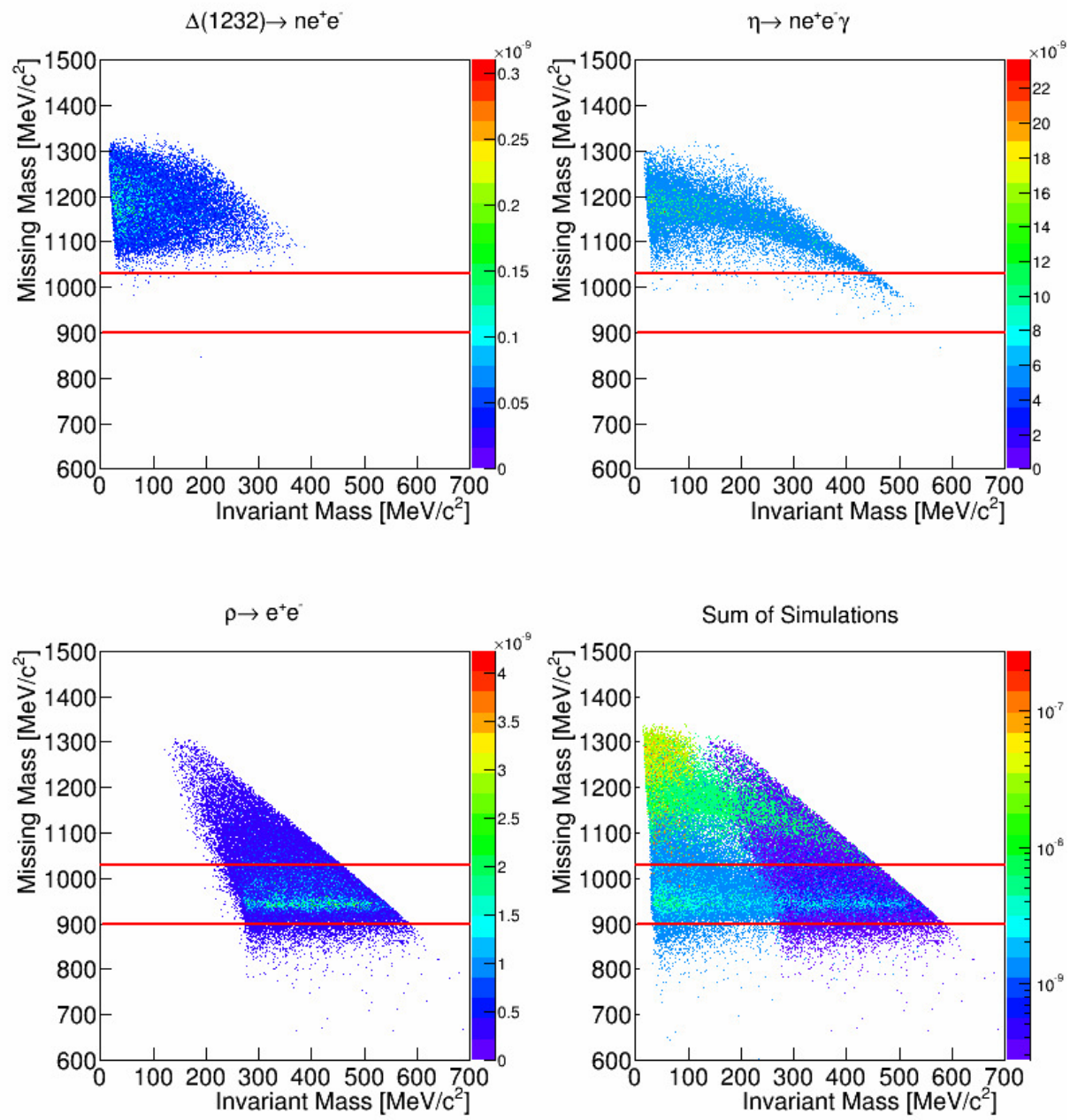

Figure 9.14: Missing mass vs. invariant mass distribution for $\pi^- CH_2$ reaction of cocktail source produced by Pluto event generator. Red lines correspond to the selection cut in the neutron mass between 900 MeV/c^2 < $M^{miss}_{e^+e^-}$ < 1030 MeV/c^2.

In Fig. 9.17 it is displayed the exclusive invariant mass distribution compared with cocktail simulations from Pluto, including the off-shell ρ production for both methods described above. In left part, is compared with the off-shell ρ contributions obtained from a "Breit-Wigner" mass distribution, which improves the description of the spectra for invariant mass above $M_{e^+e^-}$ > 250 MeV/c^2 for $\pi^- CH_2$, and it is consistent with the results obtained from the inclusive analysis, see Fig. 9.10. The off-shell ρ obtained from PWA of two pion production is compared in the

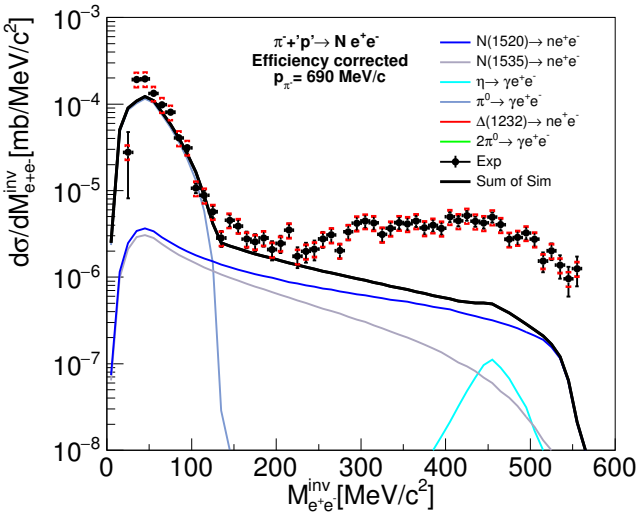

Figure 9.15: Exclusive efficiency corrected e^+e^- invariant mass distribution compared with cocktail simulation from Pluto event generator. Contributions from π^0 produced with event generator based in PWA inputs. The off-shell ρ contribution is not included.

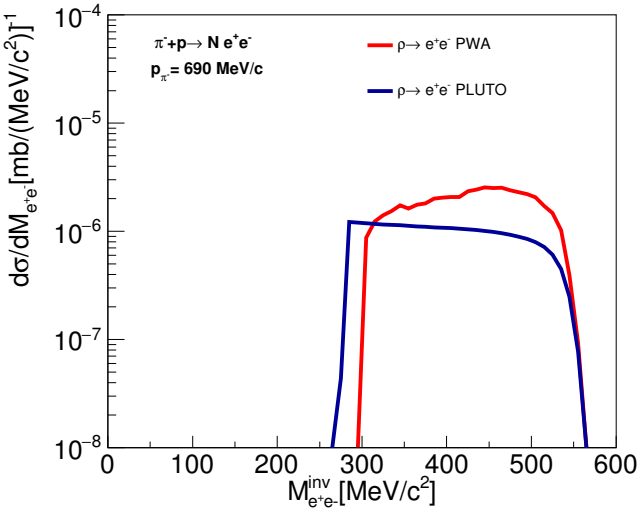

Figure 9.16: Comparison of simulated exclusive e^+e^- invariant mass of off-shell ρ contribution with "Breit-Wigner" mass distribution (blue line) and ρ deduced from PWA of two pion production (red line).

right part, this contribution is more realistic because it is obtained directly from experimental data, giving a consistency in the results.

In conclusion, the ρ obtained from PWA of two pion production gives a more realistic description of the spectra for invariant mass above $M_{e^+e^-} > 300$ MeV/c^2 than the one produced with a "Breit-Wigner" mass distribution. Therefore, the results confirm experimentally the validity of the VDM formalism which is a way to take into account the effect of time-like electromagnetic transition form factors using the distribution of $\pi\pi$ from PWA and to relate it with the e^+e^-

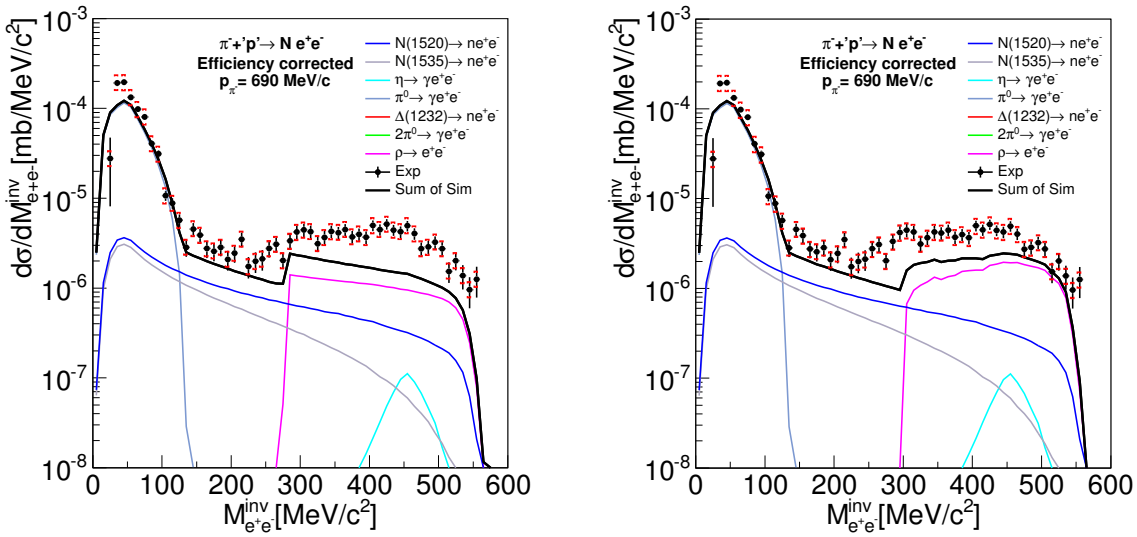

Figure 9.17: Efficiency corrected exclusive invariant mass distribution compared with simulations from Pluto event generator. **Left:** ρ contribution from "Breit-Wigner" (Pluto). **Right:** ρ contribution from PWA of two pion production.

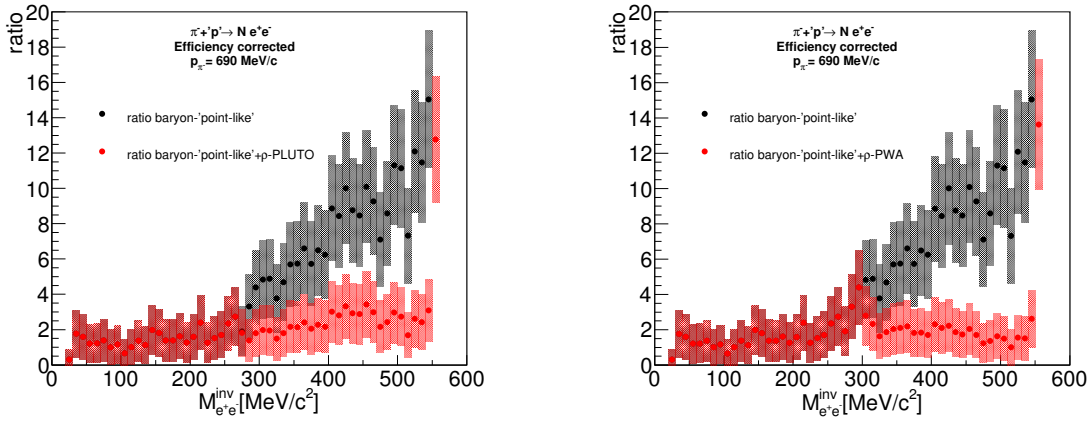

Figure 9.18: Ratio of exclusive invariant mass distributions to the point-like baryonic resonance N(1520), N(1535) (i.e QED approach), and the same with the ρ contribution. **Left:** ρ contribution from a "Breit-Wigner" distribution (PLUTO). **Right:** ρ contribution from PWA of two pion production.

In Fig. 9.18 it is shown with black dots the ratio between the experimental exclusive invariant mass and the baryonic sources N(1520) and N(1535) treated as point-like (i.e QED approach). The ratio shows the excess of the dilepton spectra from the baryonic sources treated with the point-like approach. It is observed than for invariant mass above $M_{e^+e^-} > 300$ MeV/c^2 the ratio deviates from the expected point-like behaviors, showing clear evidence of the need for the inclusion of a form factor. With red dots it is displayed the ratio between the experimental exclusive invariant mass with the baryonic sources, N(1520) and N(1535), and the off-shell ρ

contribution obtained from PWA of two pion production (right) and with the PLUTO simulation using a "Breit-Wigner" distribution (left). Therefore, the consistency of the ratio using the off-shell ρ contribution verify once again the VDM approach.

Part II

Electromagnetic CALorimeter (ECAL)

Chapter 10

Electromagnetic CALorimeter for HADES (ECAL)

Electromagnetic calorimeter (ECAL) was developed to complement dilepton spectrometer HADES currently operating on the beam of the SIS18 heavy-ion synchrotron at GSI Helmholtzzentrum für Schwerionenforschung, Darmstadt, Germany. In the future, the HADES spectrometer will be placed in front of the Compressed Baryonic Matter (CBM) experiment, to continue its physics program at collision energies from 2 to 11 AGeV. ECAL will enable in the future the HADES@FAIR experiment to measure data on inclusive photons, gamma pairs from neutral meson decays (π^0 and η) and also ω vector mesons reconstructed via their decay channel $\pi^0\gamma \rightarrow \gamma\gamma\gamma$, see Table 10. The combination of charged particles detected by HADES and the photons detected by ECAL will allow the investigation of neutral hyperon and resonances like $\Lambda(1405)$ and $\Sigma(1385)$ in elementary and heavy-ion reactions. Special interest lies in the measurement of neutral meson production in this energy range since the cross sections are still unknown, and might open the window to a new interpretation of the dilepton spectra. The ECAL will also significantly improve electron/pion separation at large momenta over 400 MeV/c.

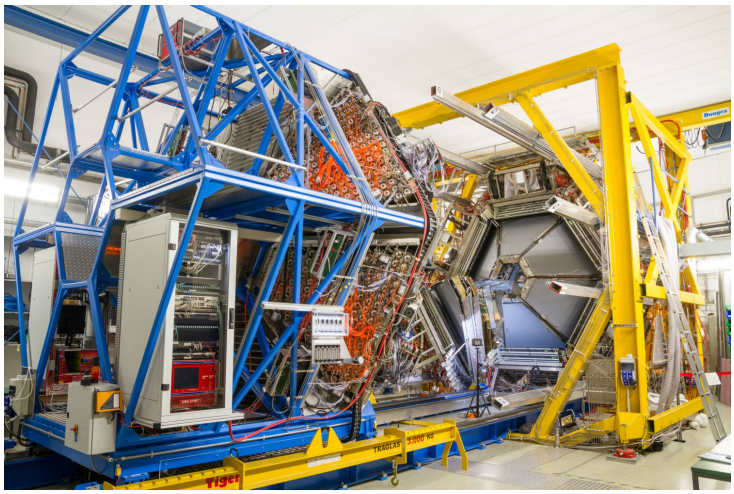

Figure 10.1: The HADES set-up at GSI Helmholtzzentrum für Schwerionenforschung GmbH in Darmstadt while it is extended to a service position. The new ECAL detector is mounted on a blue movable support structure (picture taken in January 2019).

Meson	Decay Mode	Fraction
Neutral modes		
π^0	2γ	98.8%
η	2γ	39.4%
ω	$\pi^0\gamma \rightarrow 3\gamma$	8.4%
Charged modes		
π^0	γe^+e^-	1.2%
η	$\pi^0\pi^+\pi^-$	22.92%
ω	$\pi^0 e^+e^-$	$7.7{\cdot}10^{-4}$

Table 10.1: Branching ratio decay of neutral mesons [15].

10.1 Calorimeter design

The goal is to cover a total area around of 8.3 m^2, corresponding to HADES polar angles between 12° and 45° with almost full azimuthal coverage. The modules of the electromagnetic calorimeter are based on the lead glass serving both as an absorber for developing of an electromagnetic shower and as an active volume for Cherenkov light generation. This light is read out by the PMT coupled to the glass. HV divider is mounted directly on the PMT socket and is also inside of the module. The modules are reused from the end-cap EM calorimeter of the OPAL experiment [126]. As the size of the modules were fixed, the lead glass dimension determines the properties of the calorimeter. The electron and energy resolution for the given calorimeters is $\approx 5\%/\sqrt{E}$ which is enough for the η meson reconstruction. The calorimeter consist of 978 modules divided into six trapezoidal sectors, each sector include 15 rows of modules. With a total weight of about 15 tons. ECAL is mounted on a movable support structure, shown in Fig. 10.2 [127].

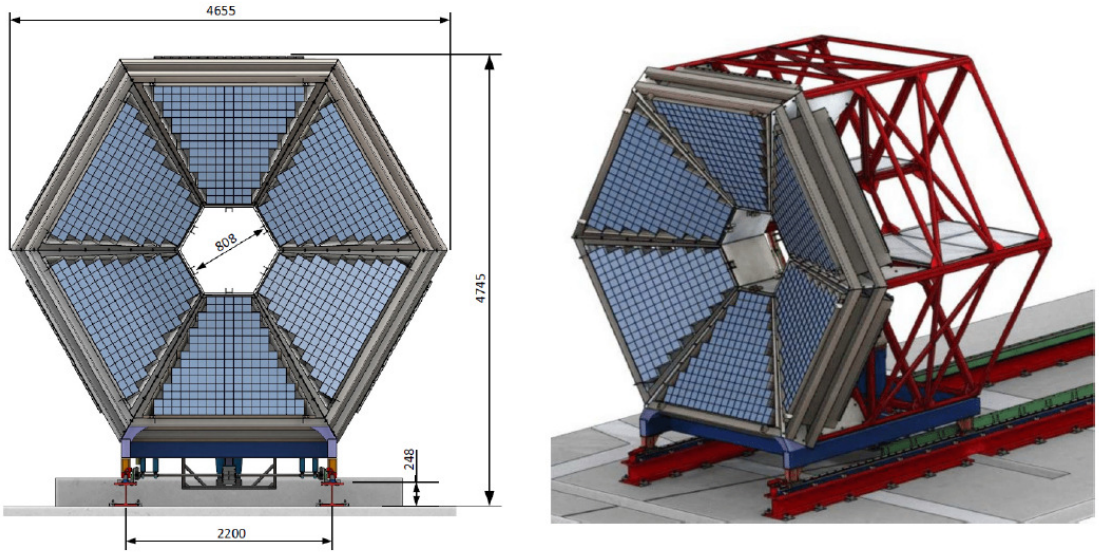

Figure 10.2: **Left**: Dimensions of the HADES electromagnetic calorimeter, front view. **Right**: Final assembly of the drive system and detector modules [127].

10.2 Physics of calorimeter detectors

In high energy physics experiments a calorimeter is a detectors used to measure the energy and position of a particle by total absorption. In contrary with other detectors, the measurement is destructive because all the energy needs to be deposited in the detector, also they can detect neutral particles by detecting the secondary charged particles. Electromagnetic calorimeters are used to detected particles which interact via the electromagnetic force (i.e. electrons, positrons and photons). When a high-energy electron/positron interacts with matter the main energy losses are due to bremsstrahlung, and for photons pair production. Therefore, the initial particle will lose energy due to those processes leading to a cascade of $e^{\pm}$ and photons. The amount of light produced in the detection material is proportional to the ionization charge deposited in the detector. In our case, ECAL lead glass will works both as the absorber and the active medium. The glass is coupled to a photomultiplier which will measure the energy deposited. For instance, when a high energy photon (E > 1 MeV) interacts with the lead glass it will create a pair production $e^{\pm}$, consequently, it will by bremsstrahlung process emit again photons. With sufficient energy available, the photons can produce can produce again $e^{\pm}$, therefore a electromagnetic shower is produced. The energy is deposited mainly via the interaction of a primary or secondary gamma with the medium and subsequent ionization loses within the EM shower. Small part of the energy is transfered into the light. The light is generated through Cherenkov effect, which describes a light generated by charged particles moving through some medium with higher velocity than is a phase velocity of light in that medium.

10.3 Module Properties

As already mentioned, the modules are reused and modified from the OPAL end cap electromagnetic calorimeter. Each module consist of 92 x 92 x 420 mm^3 lead glass CEREN 25 used as Cherenkov radiator and also as a medium for EM shower development. A schematic view of the module is displayed in Fig. 10.3. Modules are inside a brass container of 0.49 mm wrapped with white synthetic paper (Tyvek) which increase the energy resolution by up to 10% in comparison with other reflector materials like aluminum or mylar reflector. All the surfaces were cleaned and polished to increase the reflectivity of the glass. The rear side of the lead glass serves as an attachment surface for the PMT, which is centered with a plastic plate with a hole in the middle. The centering plate and the PMT together with the HV divider are hold in place and protected by a special housing. This housing consists of and aluminum case and a brass plate with tapped holes for attaching to the module casing (thus also securing the glass against movement), upper round hole for PMT cap and square hole for LC simplex optical connector. The cap presses the PMT towards the glass and also allows the access to the divider and possibly also optical fiber. The optical components mentioned without context in the previous sentence are part of the optical monitoring system. This system allows to inject defined amount of light into the lead glass. The light is transfered to the glass, via a multi-mode optical fiber with ceramic ferule with diameter of 2.8 mm on one side and standard LC type connector on the other. The laser LED based system will be used to generate light pulses with the same output from the detector as from the cosmic muons which are used for the initial setting of the HV. The HV power supply is provided by the CAEN multichannel HV system with SY4527 crates and combination of A1535N and A7435N modules providing negative voltage up to 3.5 kV and current up to 3.0 mA (3.5 mA for A7435N). For test the predecessor type of crate SY1527LC and only A1535N modules were used. However both systems are fully compatible.

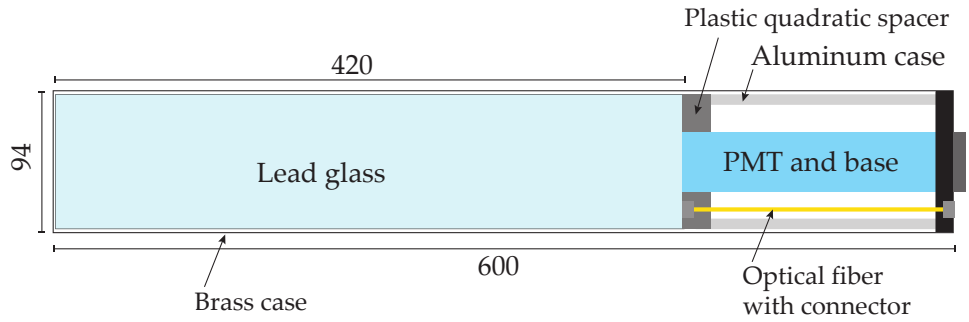

Figure 10.3: OPAL module with brass case, lead-glass, plastic spacer, aluminum case with the PMT and optical fiber with connector [128].

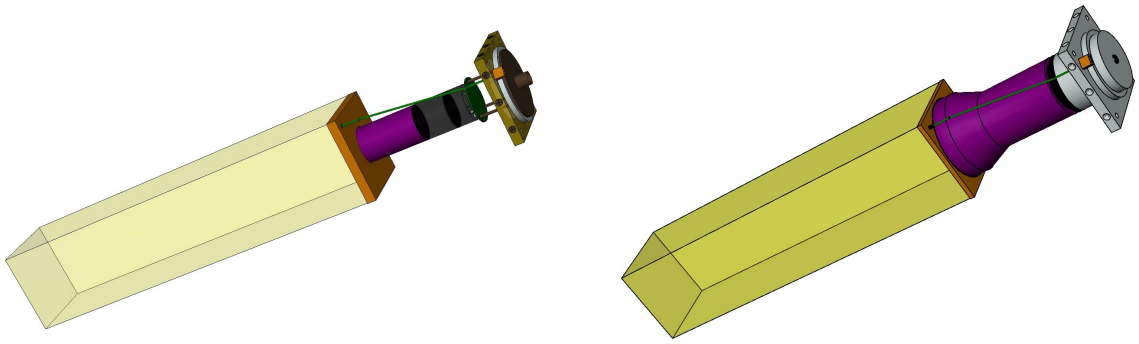

Figure 10.4: 3D design of the module mounted with **Left:** 1″ Hamamatsu R8619. **Right:** 3″ Hamamatsu R6091.

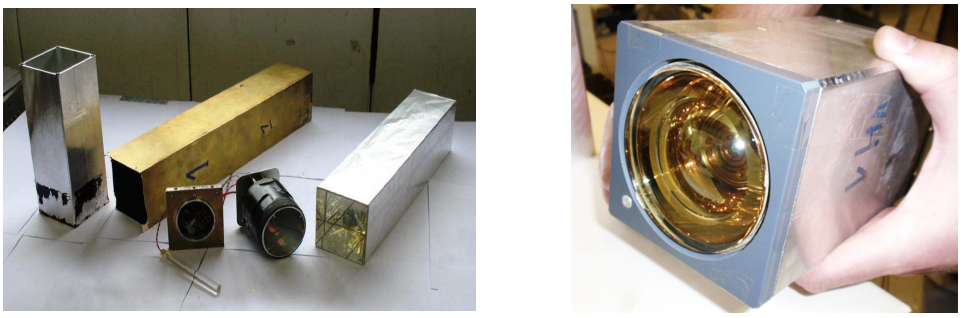

Figure 10.5: **Left:** OPAL end cap electromagnetic calorimeter modules disassembled. **Right:** Housing case for the Hamamatsu 3″ PMT with plastic spacer and optical connector.

10.3.1 Photomultiplier

During the development phase, three types of head-on PMT's were tested. The types were following: Hamamatsu R8619 (Fig. 10.6) with the head diameter of 1″, EMI (now ET Enterprises) 9903KB (Fig. 10.7) with the head diameter of 1.5″ and Hamamatsu R6091 (Fig. 10.8) with head diameter of 3″. The properties are listed in the Table 10.3.1. During the tests the R8619 PMT showed unsatisfactory results compared to the other two, see further. Because of budgetary and time reasons it was decided to use both R6091 and 9903KB in the initial setup of

the calorimeter and later upgrade the modules equipped with 9903 KB PMT's to R6091 PMT's. The time factor lied within the availability. The 9903KB were available in large quantity, covering two thirds of the calorimeter which is approximately 600 PMT's, obtained immediately from the MIRAC detector (WA80 and WA98) [129]. The R6091 had to be ordered and manufactured first. All 9903KB PMT's were tested using NaI(Tl) scintillator and radioactive source to asses their condition and to have some quantity in order to use the best ones. In order to cut the costs, in-house developed voltage dividers are used for R6091 PMT's.

ECAL modules	HM3 R6091	HM1 R8619	EMI 1,5 9903KB
Active diameter [mm]	65	22	32
Active area [cm^2]	33,1	3,8	8,0
Quatum efficiency at peak [%]	26	29	28
Wavelength at maximum QE	390	390	-
Spectral range [nm]	300-650	300-650	290-680

Table 10.2: Properties of used ECAL modules.

Figure 10.6: 1″ Hamamatsu R8619

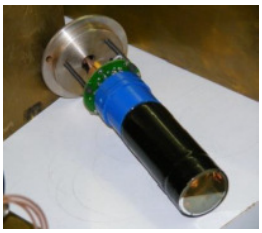

Figure 10.7: 1,5″ EMI 9903KB

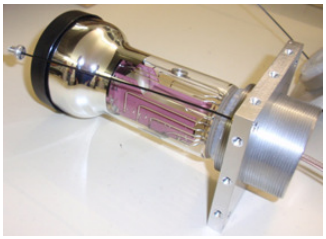

Figure 10.8: 3″ Hamamatsu R6091

10.3.2 Lead-glass

Lead-glass CEREN 25 is used as a Cherenkov radiator, the module properties of lead-glass CEREN 25 or (similar to SF_5) are summarized in Table 10.3:

Density	4,06 g/cm^3
Radiation length X_0	2,51 cm
Refractive index (at 400 nm)	1,708
Refractive index (at 587 nm)	1,673
Moliere Radius	3,6-3,7 cm
Nuclear collision length	21,4 cm
Critical energy	15,5 - 15,8 MeV
β_T threshold	0,5978
Electron kinetic energy at threshold	126,5 KeV

Table 10.3: The properties of lead-glass CEREN 25 or SF5.

10.4 Readout Scheme and Electronics

The general readout scheme is restrained by two conditions: one is the capacity to offer separate time and energy measurements with high resolution in the expected dynamic range. The second constraint is request for minimization of cost and effort needed for implementation to the existing HADES read-out and DAQ infrastructure. To fulfill the requirements, two front-end electronics (FEE) were considered and tested. The Cracow FEE was based on sampling ADC. The second FEE was based on the PaDiWa-AMPS and TDC (Time-to-Digital-Converter) on the TRB (Trigger and Read-out Board) [97]. The TRB was tested in its newest version TRB3. Also CAEN DT5742B digitizer was used as an independent read-out and ADC measurement. The PaDiWa-AMPS is a signal amplifier and discriminator based on the discrete analog amplification stage and an FPGA based discrimination. The amplitude measurements is achieved using the Time-over-Threshold (ToT) method in the connected TDC. The advantage of this solution is low cost and seamless implementation in the HADES DAQ. The Cracow FEE is based on already known nuclear electronics which haven been developed and improved for decades. On the other side it has an outstanding performance in terms of linearity, resolution and ability for pulse analysis in the FPGA.

10.5 Beam tests at the MAMI accelerator (Mainz)

Two tests were carried out in 2009 and 2010. First was conducted at MAMI(Mainz Microtron) facility of Johannes Gutenberg-Universität, Mainz in September 2009 in order to measure the energy resolution with different reflector and light collector using gamma beam. Second test was targeted to check the electron pion separation using a secondary e^-/π^- beam from T10 at CERN in May 2010. Since than, only measurements with cosmic muons and LED was carried out. In order to verify the technical solution developed in the meantime, another test with gamma beam at MAMI-C, Mainz was proposed, see Fig.10.9. The main motivation of the test was to asses the performance of the modules equipped with different types of PMT's. As mentioned earlier the PMT's were 3″ Hamamatsu R6091, 1″ R8619 and 1.5″EMI 9903KB. The 1″ R8619 PMT was included in the set in order to investigate a possibility to use it instead of the 3″ R6091 due to its significantly lower price. The second task which depended on the result of the PMT type assessment was to measure performance by means of energy resolution, deposited energy in one module for different lengths of the beam path in the glass and energy leakage to neighboring module. Third task was to test and asses the performance of the FEE which was so far newer used with a real beam. The test took place at MAMI facility in January 2014. Fig. 10.9 shows the arrangement of the experimental facility and also the secondary gamma beam production target with a tagging spectrometer. This spectrometer generates triggers which allows to select different gamma energies between 80 and 1400 MeV. One of my main task during my PhD was to participate on this test during the experiment on site, and later I was working on the analysis of the data to determine the relative energy resolution of modules with different PMT sizes, test the novel front-end electronics and to study the energy leakage of neighboring modules [130].

In Table 10.5 are the displayed the eight select channels from the tagging spectrometer with the corresponding gamma energies.

In the following the experimental setup is described, see Fig. 10.10. Four ECAL modules were placed on a remotely movable platform about 1 m to the target exit, the platform allowed us to select the different modules without entering the experimental hall. Using a collimator of 2 mm we were able to focus the beam in a spot of 6 mm at the front plate module. Description of the

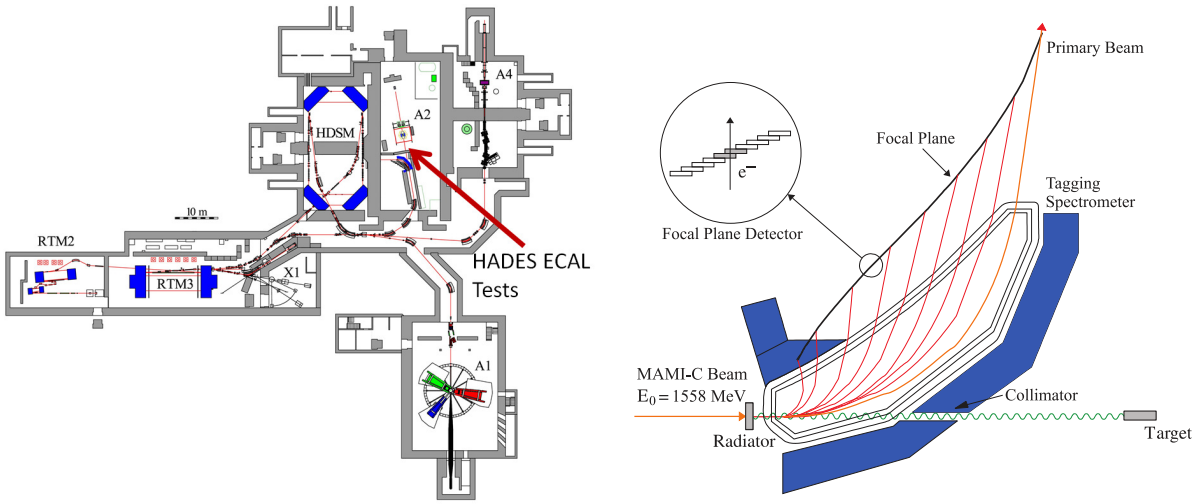

Figure 10.9: Schematic picture of the MAMI facility in Mainz (left panel) [131]. The HADES ECAL test were located in area A2 just in front of the the Crystal Ball Experiment. Electrons are accelerated in four microtrons stages, once they are accelerated they are drive on to a copper radiator where the secondary photons are generate in front of the tagging spectrometer. The tagging spectrometer gives triggers that allow the selection of gammas with energies between 80 and 1400 MeV. The ECAL modules were placed behing the beam collimator.

different configuration modules and position are shown in Table 10.5. The gap corresponding for position 3 between modules 2 and 4 are to allow the beam goes through our setup to a different experiment setup of the Bonn group.

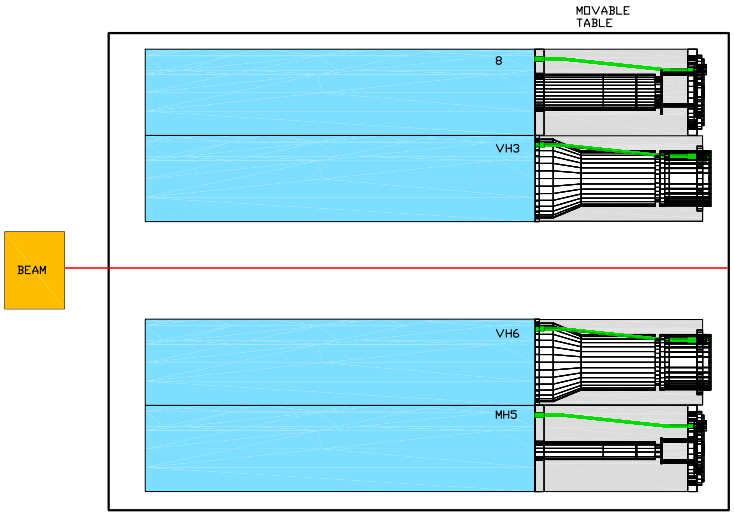

Figure 10.10: Schematic top view of the movable platform, equipped with four ECAL modules. The front plate of the modules were located 1 m downstream of the tagger exit window.

10.5.1 Energy resolution of ECAL modules

One of the goal of the beam time was to measure the energy resolution of the three PMT types using the Cracow FE and the PaDiWa-AMPS readout solution. CAEN DT5742 digitizer

Tagger channel	E_γ (mean) in MeV	E_γ (width) in MeV
2	1399,3	2,0
66	1217,8	3,3
121	1032,4	4,0
170	843,4	4,3
210	678,1	4,7
261	461,3	4,8
306	270,9	4,9
352	81,4	4,8

Table 10.4: Selected channels of the electron tagger, the corresponding mean photon energy and the trigger channel used in the setup.

Module name	PMT type	Operation HV in V	Table position
8	EMI 9903KB (1,5")	1400	1
VH3	Hamamatsu R6091 (3")	1650	2
VH6	Hamamatsu R6091 (3")	1750	4
MH5	Hamamatsu R8619 (1")	1300	5

Table 10.5: List of used ECAL modules. The photomultiplier type, the operation voltage and the position on the movable platform are listed.

with a pulses shaper (MA8000) and a high resolution Rhode Schwarz oscilloscope (RTO 1044) were used as a reference. The relative energy resolutions of the ECAL modules equipped with 1″, 1.5″ and 3″ PMT's are shown in Fig. 10.11. The relative energy resolution is comparable (5.8% at 1 GeV photon with 1.5″ EMI and 5.5% with 3″ Hamamatsu), in contrast with the 1″ Hamamatsu PMT which gives the energy resolution worse by 1.6% and a non-linear response.

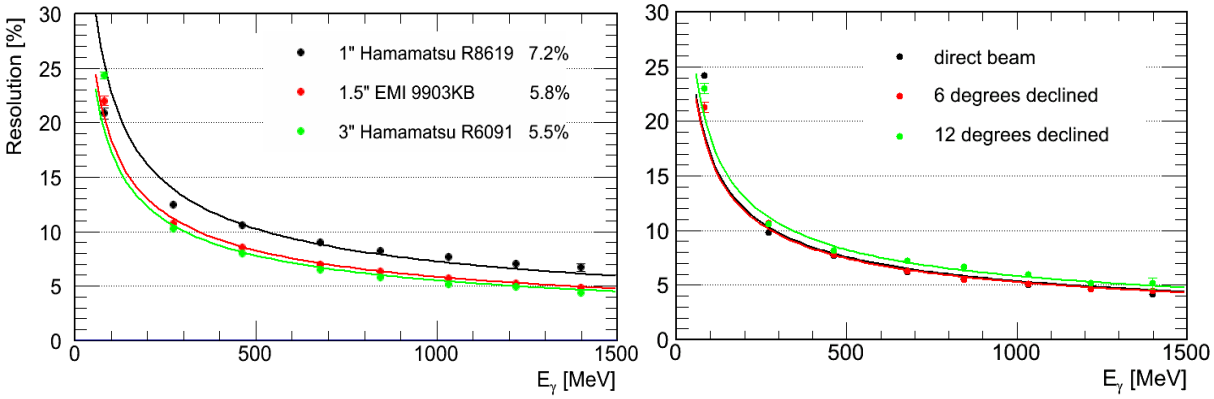

Figure 10.11: Comparison of relative energy resolution for modules with PMT's of different size (left). Relative energy resolution of the ECAL module equipped with 3″ PMT with respect to the various declination of the incident photon (combination of measurements with different angle) [132].

In Fig. 10.12 it is displayed the comparison of the response for the Cracow FE, PaDiWa-AMPS and the CAEN DT5742 readout in therms of energy resolution. The three read out solutions shows similar results. The relative energy resolution obtained with the Cracow ADC and PaDiWa-AMPS has an inappreciably better energy resolution than the CAEN + MA8000

setup. The difference may come because the CAEN+ MA800 setup is a commercial device and the other read out are optimized to the PMT pulse shapes.

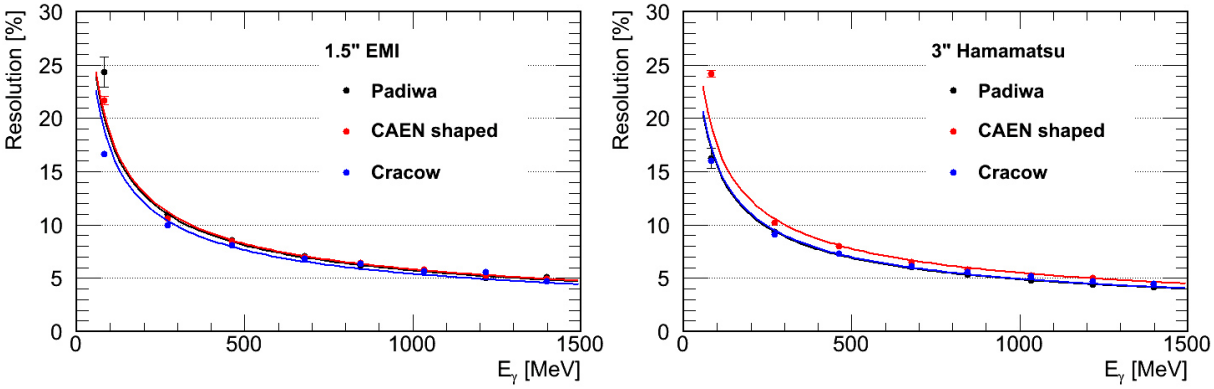

Figure 10.12: Relative energy resolution measured with the standard CAEN ADC and novel front-end boards "Cracow" and PaDiWa Amps. Data are measured using the module with 1.5″ photomultiplier (left) and 3″ photomultiplier (right)[132].

10.5.2 Energy leakage between the modules

The other objective of the beam test was to study the energy leakage between two modules. Two identical modules called as VH3 and VH6 equipped with 3″ PMT were placed on the movable table and irradiated with photon beam with energies ranging from 81 MeV up to 1399 MeV (eight different triggers were used), see Table 10.5.

Energy leakage into neighbor module parallel with the beam

In Fig. 10.13, the experimental layout is displayed for the parallel beam test. Two identical modules were placed parallel to the beam. The module VH6 was hit in the center at three horizontal positions (-4 cm, -2 cm and center of the module=0 cm). Most of the energy was still deposited in the hit module in the case of beam in the center or two centimeters far from the center of the module, see Fig. 10.14.

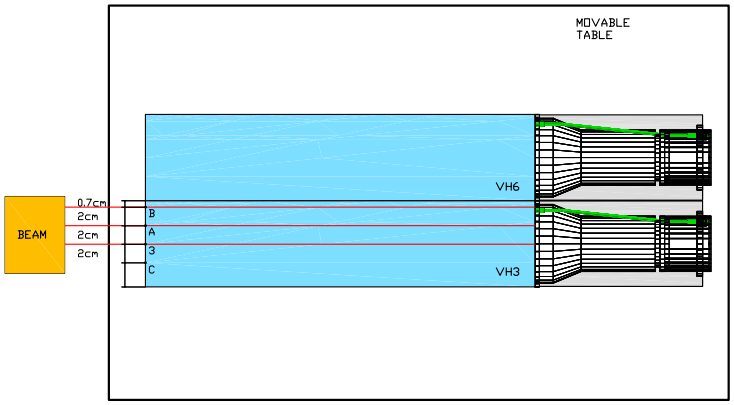

Figure 10.13: Schematic top view of the movable platform, equipped with two ECAL modules at 0° respect to the beam.

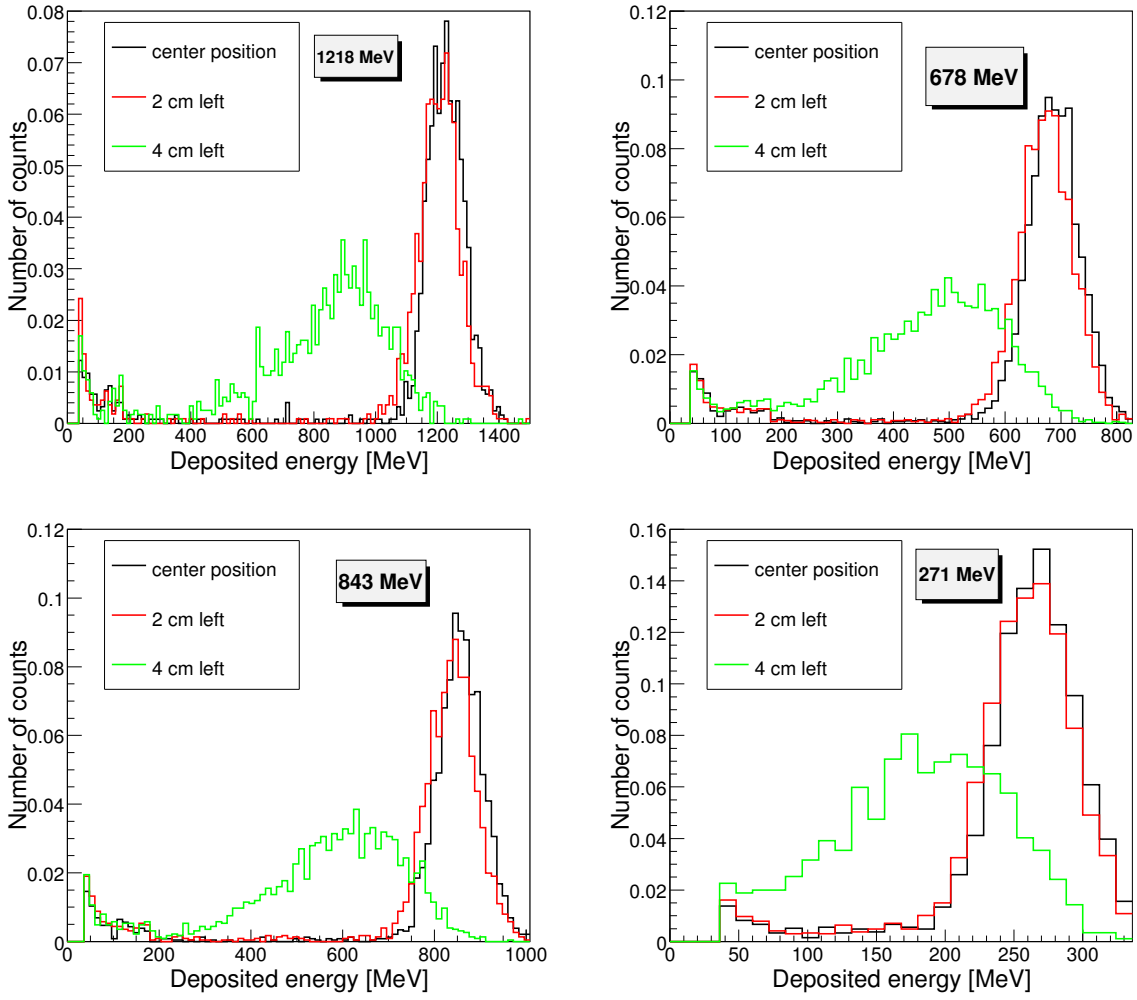

Figure 10.14: Energy deposited in first module VH3 for three beam position in the detector at different photon beam energies.

When summing the deposited energy in both modules, it was possible to fully recover original photon energy. Unfortunately, some energy is lost in the case of photon beam placed at 4 cm left from the center where the module border is located. Most probably because of the brass walls between the modules and also some of the secondary particles (mainly electrons) created in the gamma interaction interact with the non-active volume of the detector are lost, see Fig. 10.15.

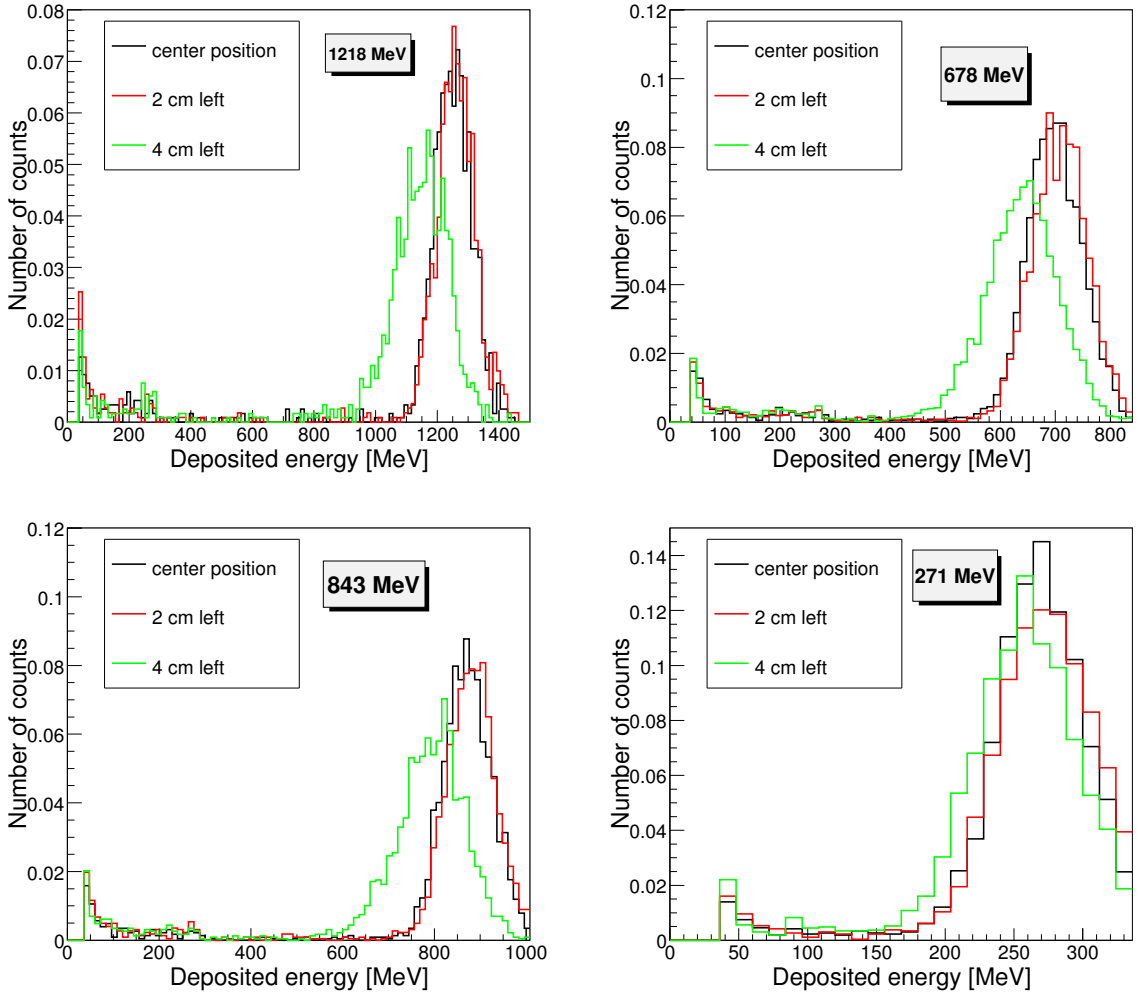

Figure 10.15: Sum of energy deposited in VH3 and VH6 modules for three beam position in the detector at different photon beam energies.

Energy leakage into neighbor module inclined 6° and 12° respect to the longitudinal axis

The response of the ECAL modules on photons coming under non-zero angle is very important as most of the modules will be declined with respect to the incoming particles. The photon beam hit the setup at four different positions (-4 cm, -2 cm, center of the module=0 cm, +2 cm) and under three inclinations (angles 0°, 6° and 12° with respect to the module's longitudinal axis), see Fig. 10.13, Fig. 10.16 and Fig. 10.17 [132]. Fig. 10.18 shows the top view of module VH3 with the corresponding path lengths for a given hit position and angle. In Fig. 10.19, the energy deposited in the VH3 module is displayed for different path lengths.

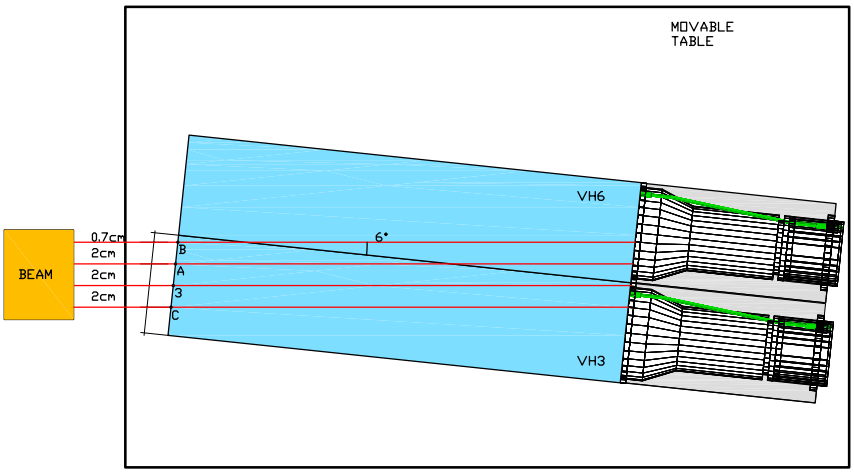

Figure 10.16: Schematic top view of the movable platform, equipped with two ECAL modules at 6° respect to the beam.

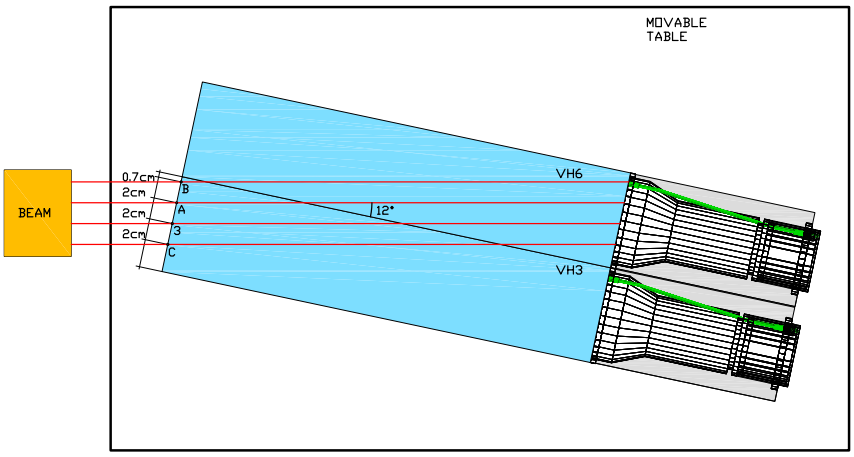

Figure 10.17: Schematic top view of the movable platform, equipped with two ECAL modules at 12° respect to the beam.

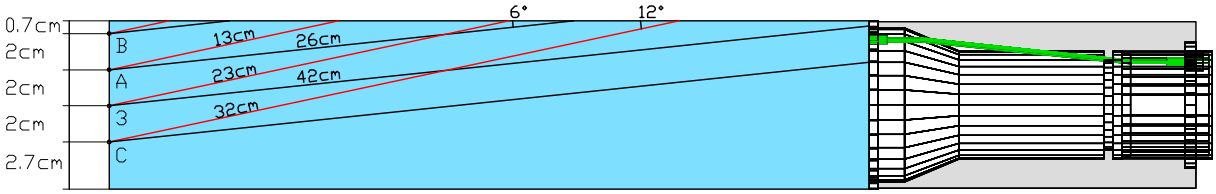

Figure 10.18: Schematic top view of VH3 module with the different path length.

We can observe that most of the original photon beam energy was recovered as a sum of energies stored in modules, VH3 and VH6, see Fig. 10.20. Even, for the length of 13 cm which correspond to 6° inclination and hit position 4 cm from the center, the original energy of the photon is recover almost completely. Therefore, it was demonstrated that almost no energy is lost between the modules VH3 and VH6 and therefore we are able to reconstruct the initial energy of the photon.

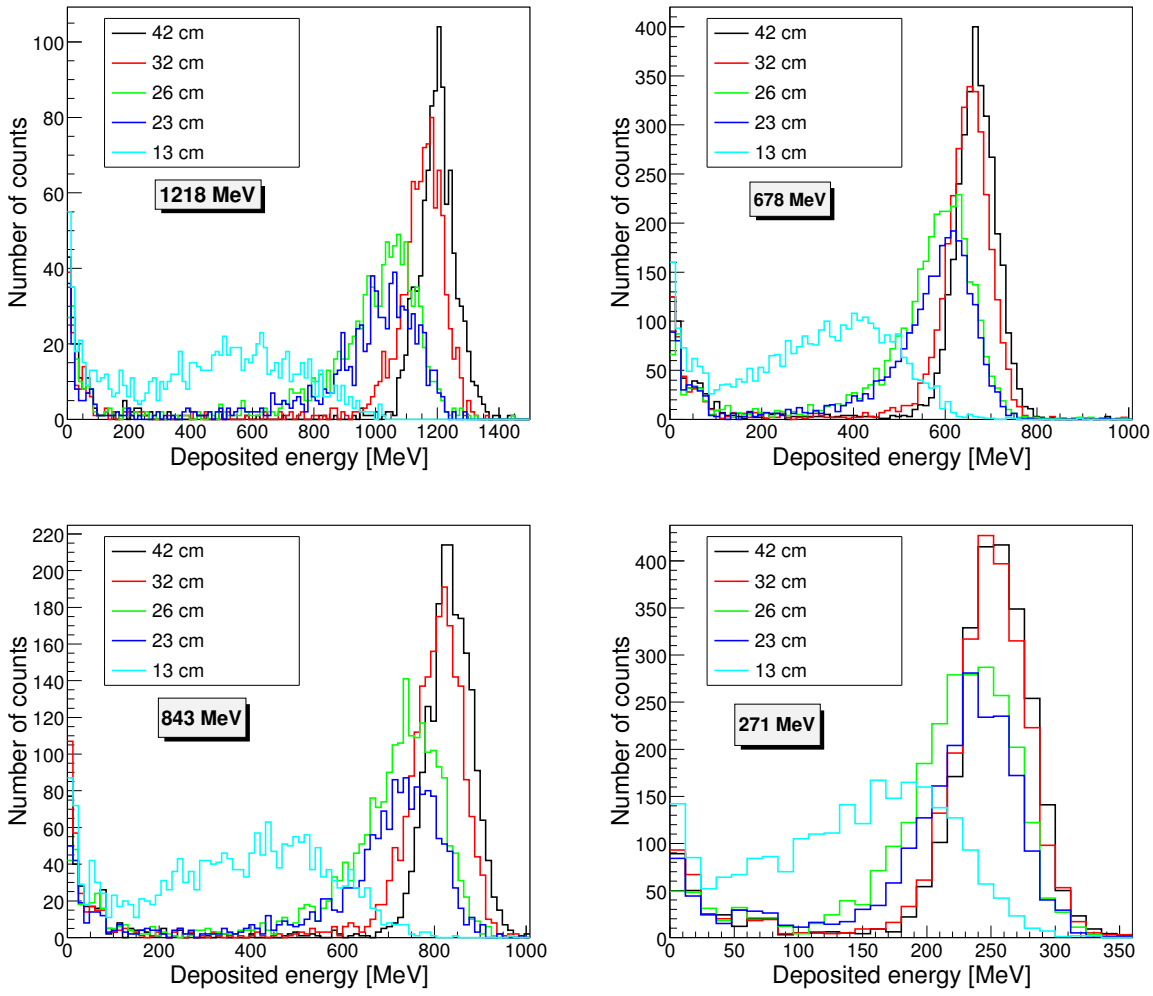

Figure 10.19: Energy deposited in first module VH3 for different path length corresponding to a photon beam angle of 6° and 12°. Results are shown for different photon beam energies.

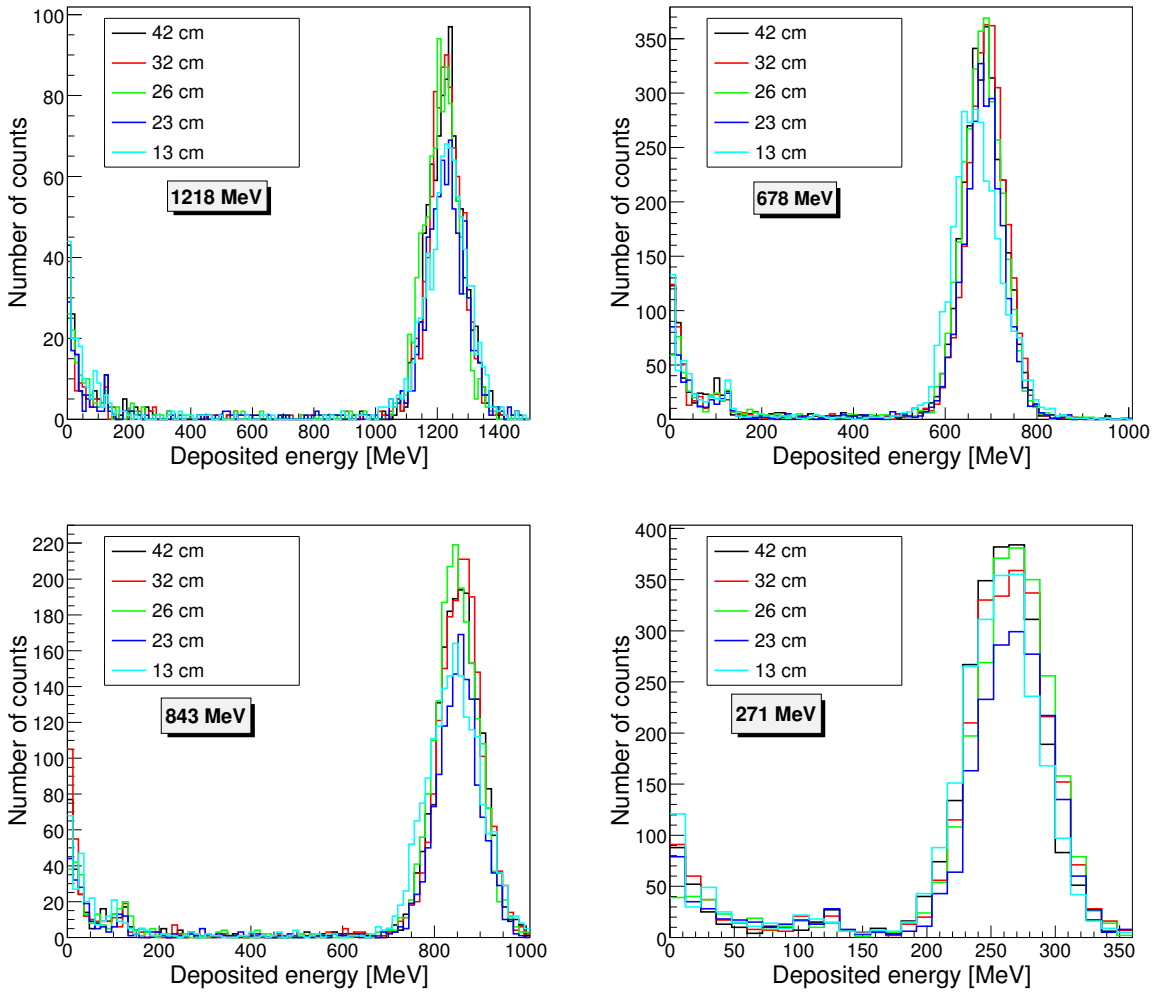

Figure 10.20: Sum of energy deposited in VH3 and VH6 modules for different path length corresponding to a photon beam angle of 6° and 12°. Results are shown for different photon beam energies.

Chapter 11

Conclusion

Part I: Pion induced reaction on carbon and polyethylene targets obtained by HADES-GSI

One of the main goal of HADES experiment is to study the microscopic structure of dense baryonic matter in the region of high net-baryon density and moderate temperature (T¡ 80 MeV). baryonic matter in the region of high net-baryon density. Experimental results from HADES experiments in the last year in nucleus-nucleus, proton-nucleus and nucleon-nucleon reaction reveals the importance of the coupling of ρ meson with baryonic resonances, which appears as an excess in the e^+e^- invariant mass distribution above usual sources below vector meson poles. The in-medium modifications of the ρ spectral function due to the coupling to baryonic resonance, can appear already in elementary nucleon-nucleon collisions (like pion-induced reactions) at low energy where the medium is cold and baryon rich. In that case, the ρ spectral function is modified via the production and decay of these baryonic resonances, with processes like the ($R \rightarrow N\rho \rightarrow Ne^+e^-$). Baryon resonance Dalitz decays are considered to study the electromagnetic structure of this baryonic transition and also to probes the role the role of vector mesons herein. The overlapping of the resonances produced in N-N or A-A collisions is better controlled using pion induced reactions since the energy in the collision can be modified with the pion beam energy, and therefore scan an specific resonance mass. In this PhD thesis it is presented the analysis of a commissioning experiment at HADES experiment using a pion beam momenta of 0.690 GeV/c in the second resonance region (N(1520)) using polyethylene $(C_2H_4)_n$ and carbon C targets. The calibration of the TOF detector was one of my duties during the commissioning of the pion-beam experiment in 2014. It is a crucial part of the experiment since it is necessary to optimize the lepton identification, and therefore the detection efficiency. For this, the parameters obtained from the TOF calibration procedure were upload to the HADES database and used for the final reconstructed/simulated data. The reconstruction of the dielectron signal was obtained successfully, one of the main sources of the background is produced by photon conversion in the material detector or in the target. In order to remove the combinatorial background originated by this mechanism, a detailed analysis was carried out using the the closed-pair candidate rejection. As well, the correlated pairs coming from photon conversion were rejected applying a threshold cut of 9° in the opening cut between the lepton pairs. Finally, the combinatorial background is calculated using the same-event like-sign method. The normalization of the yield was done with the elastic scattering of π^-p measured during the same experiment. Unfortunately, due to the lack of statistics in the carbon target, it was not possible to subtract the carbon contribution from the polyethylene target. The exclusive $\pi^-p \rightarrow ne^+e^-$ channel was obtained using the missing mass technique, detecting the e^+e^- pair with a missing neutron mass cut between 900 MeV/c^2 < $M^{miss}_{e^+e^-}$ < 1030 MeV/c^2. However, the

π^0 Dalitz decays $\pi^0 \to \gamma e^+ e^-$ can not be rejected, therefore the reaction can only be measured for the invariant e^+e^- mass larger than $M_{e^+e^-} > 250$ MeV/c^2. The efficiency corrections used to correct the raw experimental spectra are calculated using the one-dimensional method. Finally, the corrected experimental spectra is presented in full solid angle (i.e. 4π), with statistical and systematic errors mainly produced by the efficiency and normalization uncertainties. In order to described the experimental e^+e^- production in $\pi^- (C_2H_4)_n$ and π^-C reactions, I developed a cocktail simulations with Pluto event generator. For the π^0 and η meson Dalitz decay I used available information from pion-nucleon interactions. Based in the PWA of two pion production during the same experiment it was found out that the dominant resonant contributions in the s-channel are N(1520) and N(1535). Moreover, the e^+e^- contribution of the Dalitz decay of those baryonic resonances could be related from their radiative decay, using the point-like assumption. Therefore, the differential cross section were obtained from existing data from the Bonn-Gatchina PWA of $\gamma n \to \pi^- p$. The Dalitz decay of the $\Delta(1232)$ was implemented using the cross section extracted from PWA of two pion production during the same experiment. The carbon interactions were treated using the participant-spectator model, and the total simulated yield CH_2 of polyethylene target, was normalized using the cross section $\sigma_{CH2} = \sigma_H + \frac{1}{2}\sigma_C$ which takes into account the number of hydrogen and carbon atoms in polyethylene. As a results, the simulated dilepton yield was calculated as an incoherent sum of the contributions from the different resonances. The cocktail provides a reasonable description of the dilepton spectra for invariant mass below $M_{e^+e^-} < 300$ MeV/c^2. However, for higher invariant mass it was found out an excess in the yield, which could not be explained by the baryonic resonances treated as a point-like. What it suggest that the excess in the yield it is a direct consequence of the time-like electromagnetic form factors (EMFF's) of the baryonic transitions. In the exclusive $\pi^- p \to n e^+ e^-$ channel the excess is even more remarkable. Finally, the time-like electromagnetic form factors were introduced using a Vector Dominance Meson formalism, which generate the off-shell ρ production using the distribution of $\pi^+\pi^-$ from PWA, and relate it with the e^+e^- production channel. The experimental invariant mass distribution above $M_{e^+e^-} > 300$ MeV/c^2 either in the inclusive or exclusive channel, cannot be described without the introduction of the off-shell ρ contribution.

Part II: Electromagnetic CALorimeter ECAL

Electromagnetic calorimeter ECAL is being built to improve the experimental possibilities and physics program of the HADES experiment. The ECAL will allow us to measure gamma photons from the decay of neutral particle. The performance of the gamma beam test at MAMI-C Mainz determined that both two new front-end boards ("Cracow" and PaDiWa AMPS) have similar relative energy resolution and can operate under real beam conditions. The energy resolution was studied to decide the size of PMT taking into account physical and economic point of view. The ECAL modules equipped with $1.5''$ and $3''$ photomultipliers produce comparable relative energy resolution, 5.5% and 5.8% respectively for 1 GeV photon beam energy, whereas the module with $1''$ photomultiplier gives by 1.6% worse energy resolution and non-linear response, therefore it was discarded as not suitable for our purpose. The energy leakage between two neighbor modules VH3 and VH6 were tested with parallel and declined beams at 0°, 6°, and 12°. The energy of the original photon was successfully recovered as a sum of energies deposited in each of the modules. Some part of the original energy was lost only in the case of parallel gamma beam hitting close to module boarder. The design of a single ECAL module was settled and successfully verified in beam tests. Mass production of modules and final setup of the calorimeter depends on the completion of the CBM cave. In the second half of 2018 four sectors of the ECAL detector were assembled in the experimental hall and tested with Ag+Ag

collisions at 1.58A GeV.

Chapter 12

Outlook

Current results stimulate further experiments using pion beam to study the time-like baryon electromagnetic transitions in the third resonance region at $\sqrt{s} = 1.70$ GeV. At that energy many baryonic resonances are excited ($\Delta(1620)$, $\Delta(1700)$, (1650)...) [133]. It will be studied dielectron strange and non-strange meson production in $\pi^- p$ and $\pi^- C$ reactions. In this energy range the value of q^2 is very close to vector meson poles, therefore, theoretical predictions for $\rho-\omega$ mixing can be tested. Also the exclusive channels like $\left(\pi^0\pi^-\mathrm{n}, \pi^+\pi^-\mathrm{p}, \omega\mathrm{n}, \rho\mathrm{n}, \eta\mathrm{n}, \mathrm{K}\Lambda, \mathrm{K}\Sigma\right)$ will be measured with the aim to increase precision the existing data for these hadronic decay channels. Concerning the HADES collaboration program, the main goal for future experiments will be the improving information about $\rho - \mathrm{N}, \omega - \mathrm{N}$ and $\mathrm{K} - \Lambda$ couplings, which plays an important role in the dilepton emission, and can be calculated with unprecedented precision. The measurement of neutral meson (π^0, η) or real photons will be posible with the new Electromagnetic CALorimeter (ECAL), also the electron efficiency is increased in the RICH with a new CSI photon detector. This was part of the development to the HADES-CBM FAIR Phase-0 program. The updated detectors were tested already in a measurement of Ag+Ag collisions. In a long future, the fourth resonance region at center-of-mass energy $\sqrt{s} = 2.00$ GeV focusing on $\Lambda(1405)$ resonance. In the recent years, has become relevant the study of the hyperon-nucleon and hyperon-nucleon-nucleon interaction since they are connected with astrophysical objects like neutron stars. HADES collaboration plans to investigate the electromagnetic structure of the hyperon. The study of the Dalitz decay hyperons ($\mathrm{Y}' \to \mathrm{Y}e^+e^-$) at low q^2 makes a unique opportunity to measure the validity of VDM in the hyperon sector. Hyperons can be identified by pe^+e^- invariant mass of their decay products. therefore, pp reactions are unique due to their abundant production. The radiative decays will be measured with the ECAL detector, and also the improvement in the HADES acceptance with the new Forward Detector, will help to detect the forward emitted protons. This makes HADES able to study hadronic, radiative and Dalitz decay of hyperons. It will be interesting to study the baryonic electromagnetic structure containing strange quark in the time-like region with finitie q^2. This can be done comparing the N(1520) and $\Lambda(1520)$ Dalitz decay produced by HADES [133].

List of publications

Main author:

[1] P. Rodríguez-Ramos *et al.* [HADES], "Electromagnetic Calorimeter for HADES Experiment," EPJ Web Conf. **81** (2014), 06009. doi:10.1051/epjconf/20148106009

[2] P. Rodríguez-Ramos *et al.* [HADES], "Pion induced reaction with carbon and polyethylene targets obtained by HADES-GSI in 2014," J. Phys. Conf. Ser. **742** (2016) no.1, 012029 doi:10.1088/1742-6596/742/1/012029

Publications as co-author:
In impacted journal

[3] J. Adamczewski-Musch *et al.* [HADES], "Directed, Elliptic, and Higher Order Flow Harmonics of Protons, Deuterons, and Tritons in Au + Au Collisions at $\sqrt{s_{NN}} = 2.4$ GeV," Phys. Rev. Lett. **125** (2020), 262301 [arXiv:2005.12217 [nucl-ex]]. doi:10.1103/PhysRevLett.125.262301

[4] J. Adamczewski-Musch *et al.* [HADES], "Charged-pion production in Au+Au collisions at $\sqrt{s_{NN}} = 2.4$ GeV: HADES Collaboration," Eur. Phys. J. A **56** (2020) no.10, 259 [arXiv:2005.08774 [nucl-ex]]. doi:10.1140/epja/s10050-020-00237-2

[5] J. Adamczewski-Musch *et al.* [HADES], "Two-pion production in the second resonance region in $\pi^- p$ collisions with the High-Acceptance Di-Electron Spectrometer (HADES)," Phys. Rev. C **102** (2020) no.2, 024001 [arXiv:2004.08265 [nucl-ex]]. doi:10.1103/PhysRevC.102.024001

[6] J. Adamczewski-Musch *et al.* [HADES], "Proton-number fluctuations in $\sqrt{s_{NN}} = 2.4$ GeV Au + Au collisions studied with the High-Acceptance DiElectron Spectrometer (HADES)," Phys. Rev. C **102** (2020) no.2, 024914 [arXiv:2002.08701 [nucl-ex]]. doi:10.1103/PhysRevC.102.024914

[7] J. Adamczewski-Musch *et al.* [HADES], "Identical pion intensity interferometry at $\sqrt{s_{\rm NN}} =$ 2.4 GeV: HADES collaboration," Eur. Phys. J. A **56** (2020) no.5, 140 [arXiv:1910.07885 [nucl-ex]]. doi:10.1140/epja/s10050-020-00116-w

[8] J. Adamczewski-Musch *et al.* [HADES], "Probing dense baryon-rich matter with virtual photons," Nature Phys. **15** (2019) no.10, 1040-1045. doi:10.1038/s41567-019-0583-8

[9] J. Adamczewski-Musch *et al.* [HADES], "Sub-threshold production of K^0_s mesons and Λ hyperons in Au+Au collisions at $\sqrt{s_{NN}} = 2.4$ GeV," Phys. Lett. B **793** (2019), 457-463 [arXiv:1812.07304 [nucl-ex]]. doi:10.1016/j.physletb.2019.03.065

[10] J. Adamczewski-Musch *et al.* [HADES], "Strong absorption of hadrons with hidden and open strangeness in nuclear matter," Phys. Rev. Lett. **123** (2019) no.2, 022002 [arXiv:1812.03728 [nucl-ex]]. doi:10.1103/PhysRevLett.123.022002

[11] J. Adamczewski-Musch *et al.* [HADES], "Identical pion intensity interferometry in central Au + Au collisions at 1.23 A GeV," Phys. Lett. B **795** (2019), 446-451 [arXiv:1811.06213 [nucl-ex]]. doi:10.1016/j.physletb.2019.06.047

[12] J. Adamczewski-Musch *et al.* [HADES], "Centrality determination of Au + Au collisions at 1.23A GeV with HADES," Eur. Phys. J. A **54** (2018) no.5, 85 [arXiv:1712.07993 [nucl-ex]]. doi:10.1140/epja/i2018-12513-7

[13] J. Adamczewski-Musch *et al.* [HADES], "A facility for pion-induced nuclear reaction studies with HADES," Eur. Phys. J. A **53** (2017) no.9, 188. doi:10.1140/epja/i2017-12365-7

[14] J. Adamczewski-Musch *et al.* [HADES], "Deep sub-threshold ϕ production in Au+Au collisions," Phys. Lett. B **778** (2018), 403-407 [arXiv:1703.08418 [nucl-ex]]. doi:10.1016/j.physletb.2018.01.048

[15] J. Adamczewski-Musch *et al.* [HADES], "Analysis of the exclusive final state npe^+e^- in quasi-free np reaction," Eur. Phys. J. A **53** (2017) no.7, 149 [arXiv:1703.08575 [nucl-ex]]. doi:10.1140/epja/i2017-12341-3

[16] J. Adamczewski-Musch *et al.* [HADES], "$\Delta(1232)$ Dalitz decay in proton-proton collisions at T=1.25 GeV measured with HADES at GSI," Phys. Rev. C **95** (2017) no.6, 065205 [arXiv:1703.07840 [nucl-ex]]. doi:10.1103/PhysRevC.95.065205

In proceedings

[17] P. Salabura *et al.* [HADES], "Exploring time like tranistions in $pp, \pi p$ and AA reactions with HADES," EPJ Web Conf. **241** (2020), 01013. doi:10.1051/epjconf/202024101013

[18] B. Ramstein *et al.* [HADES], "Time-Like Baryon Transitions studies with HADES," EPJ Web Conf. **199** (2019), 01008. doi:10.1051/epjconf/201919901008

[19] O. Svoboda*et al.* [HADES], "Verification of Electromagnetic Calorimeter Concept for the HADES spectrometer," J. Phys. Conf. Ser. **599** (2015) no.1, 012026. doi:10.1088/1742-6596/599/1/012026

Bibliography

[1] Georges Aad et al. Observation of a new particle in the search for the Standard Model Higgs boson with the ATLAS detector at the LHC. *Phys. Lett. B*, 716:1–29, 2012.

[2] `https://commons.wikimedia.org/wiki/File:Standard_Model_of_Elementary_Particles.svg`.

[3] Torsten Dahms. *Dilepton spectra in p + p and Au + Au collisions at RHIC*. PhD thesis, 2008.

[4] G. Dissertori. *The Determination of the Strong Coupling Constant*, volume 26, pages 113–128. 2016.

[5] F. Klingl and W. Weise. Vector mesons in-medium. In *36th International Winter Meeting on Nuclear Physics*, pages 17–26, 2 1998.

[6] Volker Koch. Aspects of chiral symmetry. *Int. J. Mod. Phys. E*, 6:203–250, 1997.

[7] Anthony William Thomas and Wolfram Weise. *The Structure of the Nucleon*. Wiley, Germany, 2001.

[8] W. Cassing and E.L. Bratkovskaya. Hadronic and electromagnetic probes of hot and dense nuclear matter. *Phys. Rept.*, 308:65–233, 1999.

[9] `https://cds.cern.ch/record/2025215`.

[10] Y. Nambu and G. Jona-Lasinio. Dynamical model of elementary particles based on an analogy with superconductivity. ii. *Phys. Rev.*, 124:246–254, Oct 1961.

[11] S. Klimt, M. Lutz, and W. Weise. Chiral phase transition in the SU(3) Nambu and Jona-Lasinio model. *Physics Letters B*, 249:386–390, October 1990.

[12] G. E. Brown and Mannque Rho. Scaling effective lagrangians in a dense medium. *Phys. Rev. Lett.*, 66:2720–2723, May 1991.

[13] G.E. Brown, Guo-Qiang Li, R. Rapp, Mannque Rho, and J. Wambach. Medium dependence of the vector meson mass: Dynamical and/or Brown-Rho scaling? *Acta Phys. Polon. B*, 29:2309–2321, 1998.

[14] J. J. Sakurai. Theory of strong interactions. *Annals Phys.*, 11:1–48, 1960.

[15] K Nakamura and Particle Data Group. Review of particle physics. *Journal of Physics G: Nuclear and Particle Physics*, 37(7A):075021, 2010.

[16] Hendrik van Hees and Ralf Rapp. Dilepton Radiation at the CERN Super Proton Synchrotron. *Nucl. Phys. A*, 806:339–387, 2008.

[17] Ralf Rapp, Hendrik van Hees, and Trenton Strong. Melting rho Meson and Thermal Dileptons. *Braz. J. Phys.*, 37:779–781, 2007.

[18] Tetsuo Hatsuda and Su Houng Lee. QCD sum rules for vector mesons in the nuclear medium. *Phys. Rev. C*, 46(1):34, 1992.

[19] Robert D. Pisarski. Where does the rho go? Chirally symmetric vector mesons in the quark - gluon plasma. *Phys. Rev. D*, 52:3773–3776, 1995.

[20] Chungsik Song. Masses of vector and axial-vector mesons at finite temperature. *Phys. Rev. D*, 48:1375–1389, Aug 1993.

[21] R. Rapp and J. Wambach. Chiral symmetry restoration and dileptons in relativistic heavy ion collisions. *Adv. Nucl. Phys.*, 25:1, 2000.

[22] Ralf Rapp and Jochen Wambach. Low mass dileptons at the CERN SPS: Evidence for chiral restoration? *Eur. Phys. J.*, A6:415–420, 1999.

[23] R. Rapp, G. Chanfray, and J. Wambach. Rho meson propagation and dilepton enhancement in hot hadronic matter. *Nucl. Phys. A*, 617:472–495, 1997.

[24] W. Peters, M. Post, H. Lenske, S. Leupold, and U. Mosel. The Spectral function of the rho meson in nuclear matter. *Nucl. Phys.*, A632:109–127, 1998.

[25] R. Rapp, G. Chanfray, and J. Wambach. Medium modifications of the rho meson at CERN SPS energies. *Phys. Rev. Lett.*, 76:368–371, 1996.

[26] M. Post, S. Leupold, and U. Mosel. Hadronic spectral functions in nuclear matter. *Nucl. Phys.*, A741:81–148, 2004.

[27] P. Muehlich, V. Shklyar, S. Leupold, U. Mosel, and M. Post. The Spectral function of the omega meson in nuclear matter from a coupled-channel resonance model. *Nucl. Phys.*, A780:187–205, 2006.

[28] Janus Weil. *Vector Mesons in Medium in a Transport Approach.* PhD thesis, 2013.

[29] M. N. Rosenbluth. High energy elastic scattering of electrons on protons. *Phys. Rev.*, 79:615–619, Aug 1950.

[30] L. G. Landsberg. Electromagnetic Decays of Light Mesons. *Phys. Rept.*, 128:301–376, 1985.

[31] F. Klingl, Norbert Kaiser, and W. Weise. Effective Lagrangian approach to vector mesons, their structure and decays. *Z. Phys.*, A356:193–206, 1996.

[32] Christian Fuchs and Amand Faessler. Dilepton production in elementary and in heavy ion reactions. *Prog. Part. Nucl. Phys.*, 53:59–75, 2004.

[33] Gernot Eichmann, Helios Sanchis-Alepuz, Richard Williams, Reinhard Alkofer, and Christian S. Fischer. Baryons as relativistic three-quark bound states. *Prog. Part. Nucl. Phys.*, 91:1–100, 2016.

[34] M. Naruki et al. Experimental signature of medium modifications for ρ and ω mesons in the 12 GeV $p + a$ reactions. *Phys. Rev. Lett.*, 96:092301, Mar 2006.

[35] R. Nasseripour et al. Search for medium modifications of the ρ meson. *Phys. Rev. Lett.*, 99:262302, Dec 2007.

[36] M. Kotulla et al. Modification of the ω-meson lifetime in nuclear matter. *Phys. Rev. Lett.*, 100:192302, May 2008.

[37] M. H. Wood et al. Absorption of the ω and ϕ mesons in nuclei. *Phys. Rev. Lett.*, 105:112301, Sep 2010.

[38] A. Polyanskiy et al. Measurement of the in-medium phi-meson width in proton-nucleus collisions. *Phys. Lett.*, B695:74–77, 2011.

[39] T. Ishikawa et al. ϕ photo-production from Li, C, Al, and Cu nuclei at E(γ) = 1.5-GeV to 2.4-GeV. *Phys. Lett. B*, 608:215–222, 2005.

[40] G. Agakichiev et al. Enhanced production of low-mass electron pairs in 200 GeV/Nucleon S-Au collisions at the CERN Super Proton Synchrotron. *Phys. Rev. Lett.*, 75:1272–1275, Aug 1995.

[41] M. Masera. Dimuon production below mass 3.1-GeV/c^2 in p W and S W interactions at 200-A/GeV/c. *Nucl. Phys. A*, 590:93C–102C, 1995.

[42] R. J. Porter et al. Dielectron cross-section measurements in nucleus-nucleus reactions at 1-A/GeV. *Phys. Rev. Lett.*, 79:1229–1232, Aug 1997.

[43] R. Arnaldi et al. First measurement of the ρ spectral function in high-energy nuclear collisions. *Phys. Rev. Lett.*, 96:162302, Apr 2006.

[44] A. Adare et al. Detailed measurement of the e^+e^- pair continuum in $p+p$ and Au+Au collisions at $\sqrt{s_{NN}} = 200$ GeV and implications for direct photon production. *Phys. Rev. C*, 81:034911, 2010.

[45] L. Adamczyk et al. Measurements of Dielectron Production in Au+Au Collisions at $\sqrt{s_{\rm NN}}$ = 200 GeV from the STAR Experiment. *Phys. Rev.*, C92(2):024912, 2015.

[46] G. Agakishiev et al. The High-Acceptance Dielectron Spectrometer HADES. *Eur. Phys. J. A*, 41:243–277, 2009.

[47] Piotr Salabura et al. Hades experiments: investigation of hadron in-medium properties. *J. Phys. Conf. Ser.*, 420:012013, 2013.

[48] Q. Wan and F. Iachello. A unified description of baryon electromagnetic form factors. *Int. J. Mod. Phys. A*, 20:1846–1849, 2005.

[49] M. Bashkanov and H. Clement. On a Possible Explanation of the DLS Puzzle. *Eur. Phys. J.*, A50:107, 2014.

[50] G. Agakishiev et al. Origin of the low-mass electron pair excess in light nucleus-nucleus collisions. *Phys. Lett. B*, 690:118–122, 2010.

[51] G. Agakishiev et al. First measurement of proton-induced low-momentum dielectron radiation off cold nuclear matter. *Phys. Lett.*, B715:304–309, 2012.

[52] G. Agakishiev et al. Baryon resonance production and dielectron decays in proton-proton collisions at 3.5 GeV. *Eur. Phys. J.*, A50:82, 2014.

[53] G. Agakishiev et al. Study of dielectron production in C+C collisions at 1-AGeV. *Phys. Lett. B*, 663:43–48, 2008.

[54] G. Agakishiev et al. Dielectron production in Ar+KCl collisions at 1.76A GeV. *Phys. Rev. C*, 84:014902, 2011.

[55] J. Adamczewski-Musch et al. Probing dense baryon-rich matter with virtual photons. *Nature Phys.*, 15(10):1040–1045, 2019.

[56] Miklos Zetenyi and Gyorgy Wolf. Dilepton production in pion–nucleon collisions in an effective field theory approach. *Phys. Rev.*, C86:065209, 2012.

[57] Witold Przygoda. Resonance Production and Decay in Proton and Pion Induced Collisions with HADES. *JPS Conf. Proc.*, 10:010013, 2016.

[58] V. Shklyar, H. Lenske, and U. Mosel. 2π production in the Giessen coupled-channel model. *Phys. Rev.*, C93(4):045206, 2016.

[59] `http://gwdac.phys.gwu.edu/`.

[60] F. Bulos et al. Total cross sections and angular distributions for $\pi^- p$ charge exchange in the second and third resonance regions. *Phys. Rev. Lett.*, 13:558–562, 1964.

[61] F. Bulos et al. Charge exchange and production of η mesons and multiple neutral pions in $\pi^- p$ reactions between 654 and 1247 MeV/c. *Phys. Rev.*, 187:1827–1844, 1969.

[62] A. Starostin et al. Measurement of $\pi^- p \to \pi^0 n$ in the vicinity of the η threshold. *Phys. Rev. C*, 72:015205, 2005.

[63] R. A. Burnstein, G. R. Charlton, T. B. Day, G. Quareni, A. Quareni-Vignudelli, G. B. Yodh, and I. Nadelhaft. $\pi^- - p$ interactions at 683 MeV/c. *Phys. Rev.*, 137:B1044–B1052, Feb 1965.

[64] A. D. Brody. Experimental results on the reactions $\pi^- p \to \pi\pi n$ in the c.m. energy range 1400-2000 MeV. *Phys. Rev. D*, 5:2899–2899, Jun 1972.

[65] S. Prakhov et al. Measurement of $\pi^- p \to \pi^0\pi^0 n$ from threshold to $p_{\pi^-} = 750$ MeV/c. *Phys. Rev. C*, 69:045202, 2004.

[66] G. Penner and U. Mosel. Vector meson production and nucleon resonance analysis in a coupled-channel approach for energies $m_N < \sqrt{s} < 2$ GeV. Pion-induced results and hadronic parameters. *Phys. Rev.*, C66:055211, 2002.

[67] R. A. Arndt, W. J. Briscoe, T. W. Morrison, I. I. Strakovsky, R. L. Workman, and A. B. Gridnev. Low-energy ηn interactions: Scattering lengths and resonance parameters. *Phys. Rev. C*, 72:045202, Oct 2005.

[68] N. W. Tanner. Pions and nuclei. In Samuel Devons, editor, *High-Energy Physics and Nuclear Structure*, pages 346–366, Boston, MA, 1970. Springer US.

[69] Michael Thies. Quasielastic Pion Scattering on ^{16}O: A Comparison Between the Δ Hole Approach and a Standard First Order Calculation. *Nucl. Phys.*, A382:434–460, 1982.

[70] E. Oset, H. Toki, and W. Weise. Pionic modes of excitation in nuclei. *Phys. Rept.*, 83:281–380, 1982.

[71] J. W. Cronin, R. Cool, and A. Abashian. Cross sections of nuclei for high-energy pions. *Phys. Rev.*, 107:1121–1130, Aug 1957.

[72] M. Crozon, Ph. Chavanon, A. Courau, Th. Leray, J.L. Narjoux, and J. Tocqueville. Étude de la diffusion π-noyau entre 500 et 1300 MeV. *Nuclear Physics*, 64(4):567 – 584, 1965.

[73] J.D. Zumbro et al. Inclusive scattering of 500 MeV pions from carbon. *Phys. Rev. Lett.*, 71:1796–1799, 1993.

[74] R. J. Peterson, J. Ouyang, S. Hoeibraten, and L. B. Weinstein. 500 MeV pion single charge exchange on deuterium. *Phys. Rev.*, C52:33–37, 1995.

[75] B. L. Clausen, R. A. Loveman, R. J. Peterson, R. A. Ristinen, J. L. Ullmann, and F. Irom. Delta production by pion charge exchange on complex nuclei. *Phys. Rev.*, C35:1028–1036, 1987.

[76] J. Ouyang, S. Høibråten, and R. J. Peterson. Effective number of protons for quasifree (π^-,π^0) at 500 and 400 mev. *Phys. Rev.*, C47:2809–2811, 1993.

[77] R. J. Peterson et al. Quasifree pion single charge exchange at 500 MeV. *Phys. Lett.*, B297:238–242, 1992.

[78] A. Rahav et al. Measurement of the ^{12}C$(\pi,2\pi)$ reactions and possible evidence of a double-Δ excitation. *Phys. Rev. Lett.*, 66:1279–1282, 1991.

[79] N. Grion et al. Pion Production by Pions in the ^{16}O $(\pi^+, \pi^+\pi^-)$ Reaction at $T(\pi^+) =$ 280 MeV. *Nucl. Phys. A*, 492:509–528, 1989.

[80] P. Camerini et al. General properties of the pion production reaction in nuclear matter. *Nucl. Phys.*, A735:89–110, 2004.

[81] F. Bonutti et al. The $\pi\pi$ interaction in nuclear matter from a study of the $\pi^+\mathrm{A} \to \pi^+\pi^\pm\mathrm{A}'$ reactions. *Nucl. Phys.*, A677:213–240, 2000.

[82] A. Starostin et al. Measurement of $\pi^0\pi^0$ Production in the Nuclear Medium by π^- Interactions at 0.408 GeV/c. *Phys. Rev. Lett.*, 85:5539–5542, 2000.

[83] J.C. Peng. Eta meson production in pion induced reactions. In *17th INS International Symposium on Nuclear Physics at Intermediate Energy*, pages 233–247, 1988.

[84] B. V. Krippa and J. T. Londergan. Inclusive (π, η) reactions on nuclei. *Phys. Lett.*, B286:216–220, 1992.

[85] M. Kohno and H. Tanabe. Pion induced η production on nuclei. *Nucl. Phys.*, A519:755–772, 1990.

[86] B. V. Krippa and J. T. Londergan. Inclusive and exclusive production of η mesons by pions. *Phys. Rev. C*, 48:2967–2972, Dec 1993.

[87] K. Zeitelhack et al. The HADES RICH detector. *Nucl. Instrum. Meth. A*, 433:201–206, 1999.

[88] C. Muntz et al. The hades tracking system. *Nucl. Instrum. Meth. A*, 535:242–246, 2004.

[89] `https://garfield.web.cern.ch/garfield/`.

[90] C. Agodi et al. The HADES time-of-flight wall. *Nucl. Instrum. Meth. A*, 492:14–25, 2002.

[91] G. Kornakov et al. Time of flight measurement in heavy-ion collisions with the HADES RPC TOF wall. *JINST*, 9(11):C11015, 2014.

[92] A. Balanda et al. The HADES Pre-Shower detector. *Nucl. Instrum. Meth. A*, 531:445–458, 2004.

[93] J. Adamczewski-Musch et al. A facility for pion-induced nuclear reaction studies with HADES. *Eur. Phys. J. A*, 53(9):188, 2017.

[94] J. Diaz et al. Design and commissioning of the GSI pion beam. *Nucl. Instrum. Meth. A*, 478:511–526, 2002.

[95] J. Wirth, L. Fabbietti, R. Lalik, L. Maier, and A. Scordo. CERBEROS: A tracking system for secondary pion beams at the HADES spectrometer. *Nucl. Instrum. Meth. A*, 824:243–244, 2016.

[96] J. Michel et al. The upgraded HADES trigger and data acquisition system. *JINST*, 6:C12056, 2011.

[97] J. Michel, G. Korcyl, L. Maier, and M. Traxler. In-beam experience with a highly granular DAQ and control network: TrbNet. *JINST*, 8:C02034, 2013.

[98] M. Traxler, R. Becker, I. Frohlich, W. Kuhn, J. Lehnert, C. Lichtblau, E. Lins, M. Petri, Marc-Andre Pleier, and J. Ritman. The 2nd level trigger system of the HADES detector. *IEEE Trans. Nucl. Sci.*, 47:376–380, 2000.

[99] I. Fröhlich et al. A General Purpose Trigger and Readout Board for HADES and FAIR-Experiments. *IEEE Trans. Nucl. Sci.*, 55:59–66, 2008.

[100] Manuel Sanchez Garcia. *Momentum reconstruction and Pion Production Analysis in the HADES Spectrometer at GSI.* PhD thesis, 2003.

[101] I. Antcheva et al. ROOT: A C++ framework for petabyte data storage, statistical analysis and visualization. *Comput. Phys. Commun.*, 180:2499–2512, 2009.

[102] M. Bleicher et al. Relativistic hadron hadron collisions in the ultrarelativistic quantum molecular dynamics model. *J. Phys. G*, 25:1859–1896, 1999.

[103] I. Fröhlich et al. Pluto: A Monte Carlo Simulation Tool for Hadronic Physics. *PoS*, ACAT:076, 2007.

[104] René Brun and F. Bruyant. GEANT Detector Description and Simulation Tool. 10 1994.

[105] Timo Scheib. *Λ and K0 s Production in Au+Au Collisions at 1.23A GeV.* PhD thesis, 2017.

[106] Laura Fabbietti. *Study of the e^+e^- pair acceptance in the dilepton spectrometer HADES.* PhD thesis, 2003.

[107] Attilio Tarantola Peloni. *Dielectron analysis in pp collisions at 3 . 5 GeV with the HADES spectrometer : ω -meson line shape and a new electronics readout for the Multi-wire Drift Chambers Dissertation.* PhD thesis, 2010.

[108] P. Sellheim. Backtracking algorithm for lepton reconstruction with HADES. *J. Phys. Conf. Ser.*, 599(1):012027, 2015.

[109] Małgorzata Sudoł. *Measurement of low-mass e^+e^- pair production in 2 AGeV C-C collisions with HADES*. PhD thesis, 2007.

[110] A.D. Brody et al. $\pi^- p$ elastic scattering in the c. m. energy range 1400-2000 MeV. *Phys. Rev. D*, 3:2619–2637, Jun 1971.

[111] J. Adamczewski-Musch et al. Two-Pion production in the second resonance region in $\pi^- p$ collisions with HADES. *Phys. Rev. C*, 102(2):024001, 2020.

[112] Amand Faessler M.I. Krivoruchenko, B.V. Martemyanov and C. Fuchs. Electromagnetic transition form factors and dilepton decay rates of nucleon resonances. *Annals of Physics*, 296(2):299 – 346, 2002.

[113] M. I. Krivoruchenko and Amand Faessler. Remarks on Δ radiative and dalitz decays. *Physical Review D*, 65(1), Dec 2001.

[114] Earle L. Lomon and Simone Pacetti. Timelike and spacelike electromagnetic form factors of nucleons, a unified description. *Physical Review D*, 85(11), Jun 2012.

[115] Amand Faessler, C. Fuchs, and M. I. Krivoruchenko. Dilepton spectra from decays of light unflavored mesons. *Phys. Rev. C*, 61:035206, Feb 2000.

[116] M. Zétényi and Gy. Wolf. Dilepton decays of baryon resonances. *Acta Physica Hungarica A) Heavy Ion Physics*, 17(1):27–39, Feb 2003.

[117] Guo-Qiang Li, G.E. Brown, and C.M. Ko. Electromagnetic probes of dense matter in heavy ion collisions. *Nucl. Phys. A*, 630:563–570, 1998.

[118] Witold Przygoda. Production and decay of baryonic resonances in pion induced reactions. *EPJ Web Conf.*, 130:01021, 2016.

[119] A. V. Anisovich, E. Klempt, A. V. Sarantsev, and U. Thoma. Partial-wave decomposition of pion and photoproduction amplitudes. *The European Physical Journal A*, 24(1):111–128, Feb 2005.

[120] Andrey Sarantsev. Properties of Baryons from Bonn-Gatchina Partial Wave Analysis. *JPS Conf. Proc.*, 10:010005, 2016.

[121] S. Prakhov et al. Measurement of $\pi^- p \to \eta n$ from threshold to $p_{\pi^-} = 747$ MeV/c. *Phys. Rev. C*, 72:015203, Jul 2005.

[122] D. M. Manley and E. M. Saleski. Multichannel resonance parametrization of πn scattering amplitudes. *Phys. Rev. D*, 45:4002–4033, Jun 1992.

[123] U. Thoma et al. N^* and Δ^* decays into $N\pi^0\pi^0$. *Phys. Lett. B*, 659:87–93, 2008.

[124] A. Shafi et al. Measurement of inverse pion photoproduction at energies spanning the N(1440) resonance. *Phys. Rev. C*, 70:035204, 2004.

[125] P.T. Mattione et al. Differential cross section measurements for $\gamma n \to \pi^- p$ above the first nucleon resonance region. *Phys. Rev. C*, 96(3):035204, 2017.

[126] P.W. Jeffreys et al. Development Studies for the Opal Endcap Electromagnetic Calorimeter Using Vacuum Photo Triode Instrumented Lead Glass. *Nucl. Instrum. Meth. A*, 290:76, 1990.

[127] W. Czyzycki et al. Electromagnetic Calorimeter for HADES. 9 2011.

[128] Behruz Kardan. Centrality Determination and HADES ECAL readout-electronics.

[129] T.C. Awes et al. The Midrapidity calorimeter for the relativistic heavy ion experiment WA80 at CERN. *Nucl. Instrum. Meth. A*, 279:479–502, 1989.

[130] P. Rodríguez-Ramos et al. Electromagnetic Calorimeter for HADES Experiment. *EPJ Web Conf.*, 81:06009, 2014.

[131] H.J. Arendsa. The Mainz Microtron MAMI. In *9th International Conference on Hypernuclear and Strange Particle Physics*, pages 1–5, 2007.

[132] O. Svoboda et al. Verification of Electromagnetic Calorimeter Concept for the HADES spectrometer. *J. Phys. Conf. Ser.*, 599(1):012026, 2015.

[133] J. Adamczewski-Musch et al. Proposals for experiments at SIS18 during FAIR Phase-0. (HADES):102 p., 2017.

List of abbreviations

CB - Combinatorial Background
CTS - Central Trigger System
DAQ - Data Acquisition
DST - Data Summary Tape
FAIR - Facility for Antiproton and Ion Research
GEANT - Toolkit for the simulation of particles in matter
HADES - The High-Acceptance Dielectron Spectrometer HADES
HLD - HADES List-mode DATA
HYDRA - HADES sYstem for Data Reduction and Analysis
MDC - Mini drift chamber detector
META - Multiplicity Electron Trigger Array
METAQa - META matching Quality
PLUTO - Simulation framework for heavy-ion and hadron reactions
PT3-Particle Trigger 3
QCD- Quantum Chromo Dynamics
QED -Quantum Electro Dynamics
QGP- Quark Gluon Plasma
RICH -Ring imaging cherenkov detector
RIChQa -RICH matching quality
RK -Runge Kutta
ROOT - Data Analysis Framework
RPC -Resistive plate chamber
SIS100 -Schwerionensynchrotron 100
SIS18- Schwerionensynchrotron 18
TOF- Time-of-flight Detector
TRB- Trigger Readout Board
VDM- Vector Dominance Model

List of Figures

List of Tables